THE UNIVERSITY OF HULL

Growth and spectroscopic studies of CdS/CdSe single layers and superlattice structures

being a thesis submitted for the degree of

DOCTOR OF PHILOSOPHY

in the University of Hull

by

Matthew Peter Halsall, BSc (Sheffield)

February, 1990

Summary of Thesis submitted for Ph.D degree

by M.P.Halsall

on

Growth and spectroscopic studies of CdS/CdSe single layers a superlattice structures

Epitaxial layers of CdS and CdSe were grown on various substra by metallo-organic chemical vapour deposition. The substrates used growth were GaAs, InP and InAs with differing crystallograp orientations. The effect of growth conditions on the surface morphol of the epitaxial layers was studied. Reflection high energy elect diffraction was also used to determine the crystalline phase of resulting epilayers. It was found that the CdS grew as high qual wurtzite epilayers only on GaAs (111)A out of the substrates tried. CdSe in contrast tended to grow as either cubic or mixed phases. It found that the alloys $CdS_{1-x}Se_x$ tended to grow hexagonal on the G (111)A face.

Photoluminescence studies of the single epilayers confirmed high quality and purity of the CdS grown on GaAs (111)A relative that grown on other substrates. Similar studies of the CdSe epilay grown on this face showed lower quality material, the luminesce being dominated by a defect band (the 'Y' band). Evidence is presen linking this emission with twinning in the layers. The quality of CdSe epilayers improved with increased growth temperatures.

CdS/CdSe wurtzite superlattice structures were subsequently gr on GaAs (111)A substrates, the first reported. The luminescence f these superlattices was dominated by deep near infra-red emiss unlike that observed from other II-VI superlattices. A piezoelect model is presented to account for the observed luminescence. Using t model we find good agreement between theory and experiment if assume a type II conduction band offset of approximately 0.23 eV. conclude that the band structure of this superlattice is dominated the presence of strain induced piezoelectric fields.

ACKNOWLEDGEMENTS

I would like to thank my supervisors Dr. J.E.Nicholls an Professor J.J.Davies of the University of Hull along with Professo B.Cockayne and Dr. P.J.Wright of R.S.R.E for their interest and exper guidance throughout my research. I would also like to thank Dr A.G.Cullis of R.S.R.E for performing the TEM measurements on th superlattice samples. I must also acknowledge the contribution made b the late Dr. G.J.Russell in supervising the RHEED experiments. M thanks go to Professor F.J. Bryant and Professor P.E.Dyer for the us of laboratory facilities, to the workshop staff for maintaining th cryostats in working order and to Dr. C.P.Hilton for the spectromete control system used to prepare the spectra for this thesis. Finally thank SERC for its financial support and R.S.R.E for awarding the CAS studentship.

CONTENTS

1. PROPERTIES OF CdS AND CdSe AND INTRODUCTION TO LOW DIMENSIONAL STRUCTURES

Introduction

This thesis describes the growth and assessment of epitaxial CdS and CdSe. The principal objective of the project was the growth and spectroscopic assessment of the first CdS/CdSe strained layer superlattices. The study of such artificial semiconductor structures is an area of research which has shown an explosion of interest in recent years. This field promises the production of novel semiconductor materials with properties tailored to the requirements of the user. One technology which has been influenced by the production of superlattices is that of optoelectronic devices. New growth techniques have allowed the production of semiconductor lasers operating at efficencies and wavelengths previously unobtainable. The study of such structures containing large bandgap II-VI compounds is of particular interest as these promise the production of blue light emitting solid state devices, the subject of considerable technological interest. CdS and CdSe are both large bandgap II-VI semiconductors which have previously not been grown into such epitaxial structures. The growth and optical studies of such CdS/CdSe superlattices is therefore clearly of great interest. This thesis describes the growth of, and spectroscopic studies conducted on, the first reported wurtzite CdS/CdSe superlattices grown by MOCVD.

To enable the superlattices studied here to be grown many studies of single layers of CdS, CdSe and the alloy $CdS_{1-x}Se_x$ had to be undertaken. Therefore, this thesis contains work relating to many areas

of the growth and assessment of epitaxial CdS/CdSe and other compound semiconductors. The studies contained in the subsequent chapters are concerned with the structure, growth and photoluminescence of CdS and CdSe. Hence, in order to provide a background to the work in this thesis, these aspects of CdS, CdSe and other II-VI compounds are reviewed here in this chapter. Also in this chapter is a review of the field of semiconductor superlattices. The final section puts the CdS/CdSe system into the perspective of other II-VI semiconductor superlattice systems.

1.1 II-VI semiconductors

The II-VI semiconductors are, as the name suggests, composed of elements from groups II and VI of the periodic table. Figure 1.1 shows the elements of interest. As semiconductors, these compounds are direct gap materials with large band gaps of between 1.5 and 3.8 eV (table 1.1). It is this latter property which provides most of the interest in these compounds. The energy of a photon of visible light lies in the range 1.8-2.8 eV. Therefore, in principle, the band to band recombination emission from these compounds can be anywhere in the visible spectrum. This property makes the compounds of interest for technological applications in light emitting solid state devices. However, this single advantage is somewhat offset by the difficulties associated with the preparation of these compounds, which include the presence of two stable crystal phases and the lack of controlled n and p doping. Most II-VI compounds can conveniently be doped only one type; i.e. either p-type or n-type. This restriction prevents the production of efficent p-n junctions and the associated light emitting devices. The study of II-VI compounds, however, is still important as, to date,

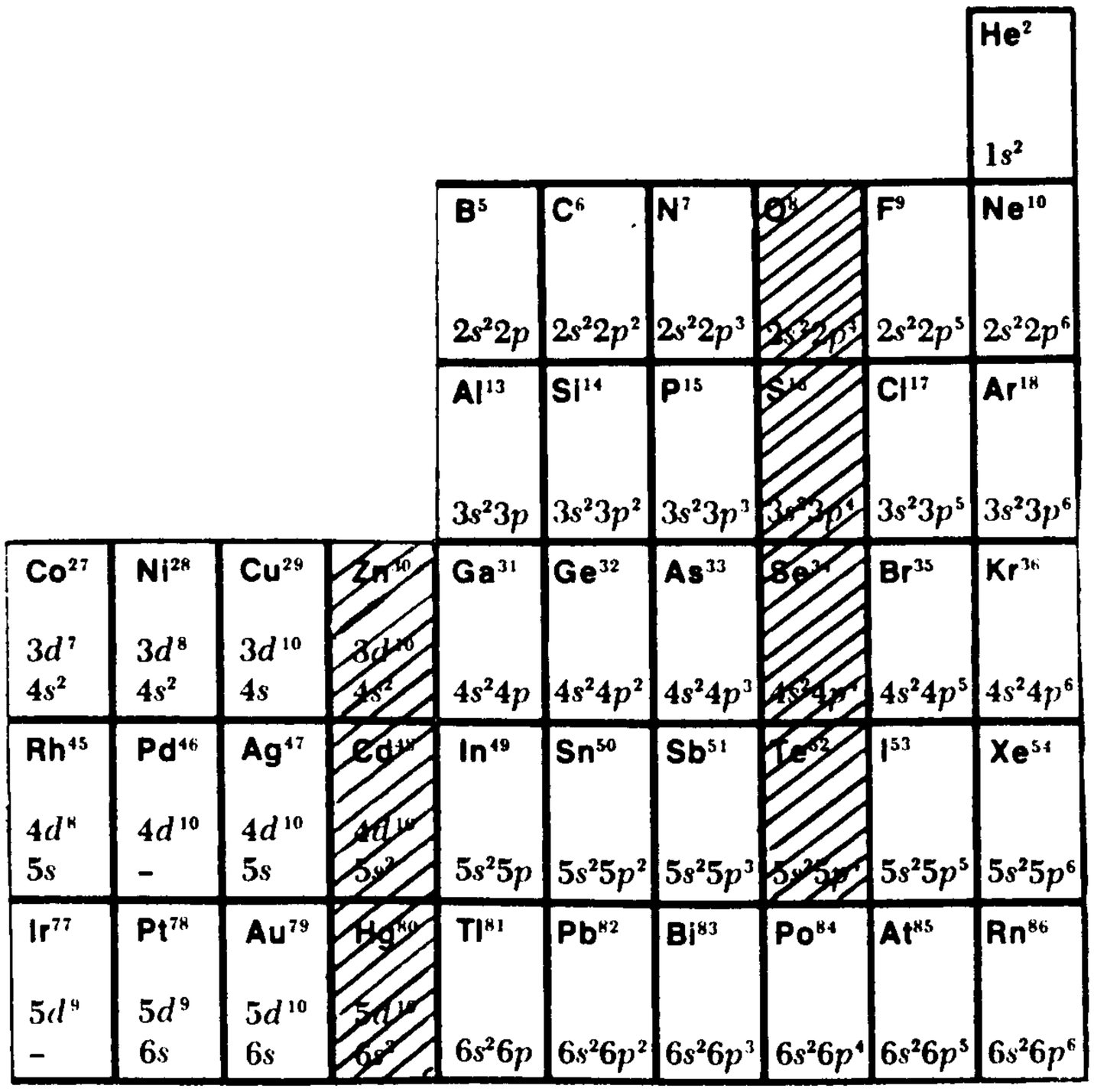

Figure 1.1. Periodic table showing elements used as components in II-VI semiconductors (hatched areas).

Compound	Band gap (eV)
ZnO	3.436
ZnS	3.91
ZnSe	2.823
ZnTe	2.391
CdS	2.582
CdSe	1.840
CdTe	1.607

Table 1.1. Band gaps of major II-VI semiconductors at 0 K.

they present the only realistic possibility of efficent blue-light emitting solid state devices.

With the advent of precision epitaxial growth techniques the field of II-VI compounds has shown a surge in interest. It has been suggested that by appropriate control of the growth and the use of semiconductor microstructures efficent p-n junctions might be grown. Cadmium sulphide and cadmium selenide are both large band gap II-VI semiconductors with a long history of previous study. Consequently the study of their epitaxial growth is of considerable interest.

1.2 Crystal structure and lattice defects

In common with the other II-VI semiconducting compounds, both CdS and CdSe can be grown with either the hexagonal 'Wurtzite' or the cubic 'Zincblende' crystal structures, the phase of the material being determined by the growth conditions. However, unlike the other II-VI semiconductors, the most stable phase for CdS and CdSe is the hexagonal one. The two structures are closely related and it is important that the similarities between the two are understood, as this has a bearing on the origin of lattice defects in the two compounds.

1.2.1 Wurtzite structure

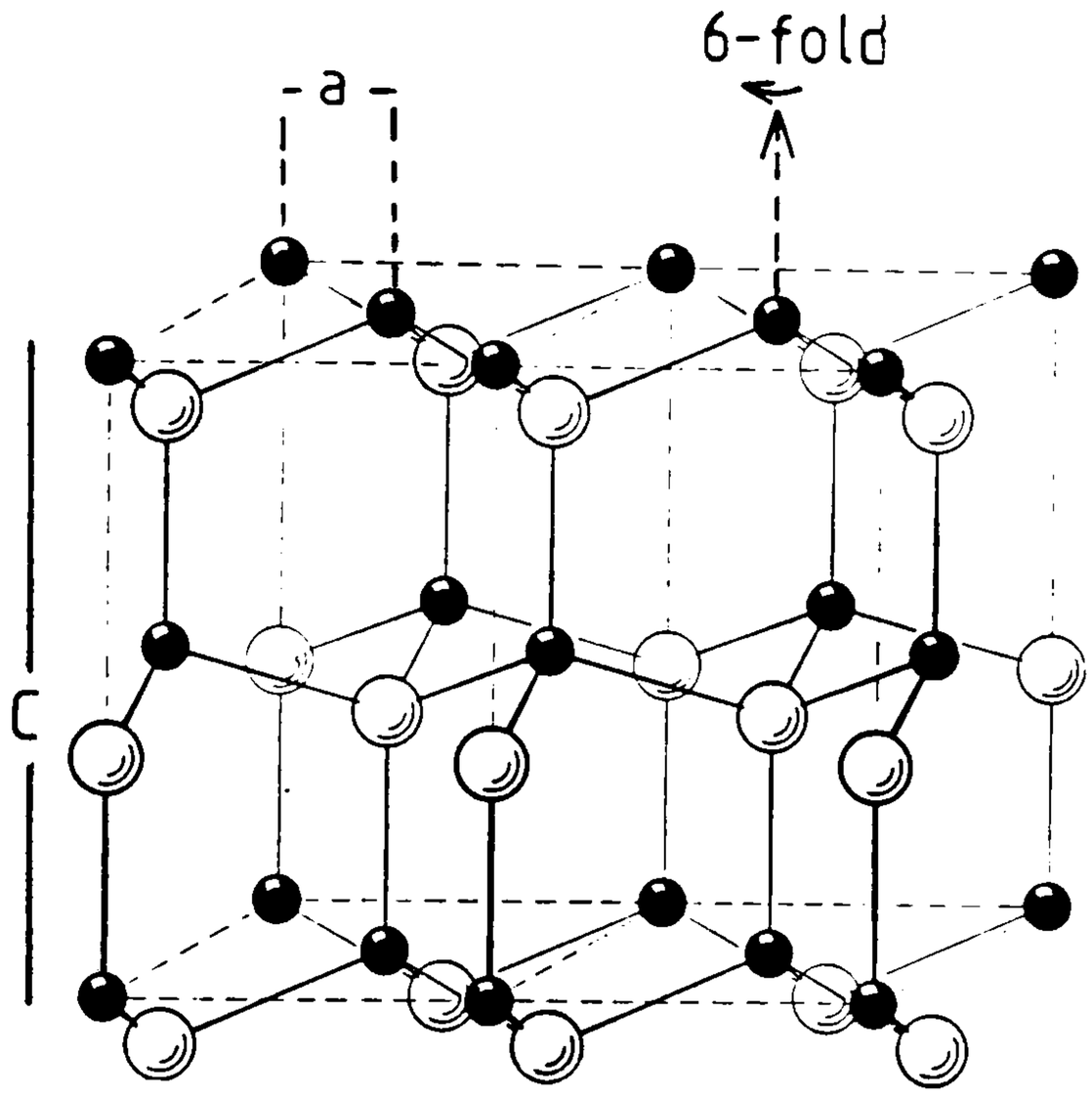

Figure 1.2. Wurtzite atomic arrangment; a and c are the wurtzite lattice constants.

Figure 1.2 shows the wurtzite atomic arrangment with the hexagonal lattice constants a and c indicated. The underlying Bravais lattice for this structure is the simple hexagonal. The structure can be considered to be composed of two interpenetrating hexagonal close packed lattices, one for the anions and one for the cations. The successive alternating layers of Cd (or S) are displaced horizontally so as to lie over the hollows in the preceding layer. For this structure there exists an 'ideal' ratio of c/a given by

$$c = a\sqrt{8/3} \qquad \text{(i)}$$

This ratio represents the optimum packing density of spheres for such an arrangment. The lattice constants and ratio c/a are given in

table 1.2 for the II-VI compounds known to crystallize in this phase.

As indicated on the figure, there exists a six fold axis of rotational symmetry about the [0001] axis. It is important to note that the atoms possess tetrahedrally orientated bonds in this structure. Such bonding is characteristic of covalent materials and is common to all II-VI, III-V and group IV semiconducting compounds. Also note that there is no centre for inversional symmetry along the [0001] axis and consequently there is a polar axis parallel to the [0001] axis. The group II and group VI ions can be seen as forming a network of dipole moments. A distortion of the lattice will thus produce a net field. As a result, wurtzite crystals are piezoelectric.

1.2.2 Zincblende structure

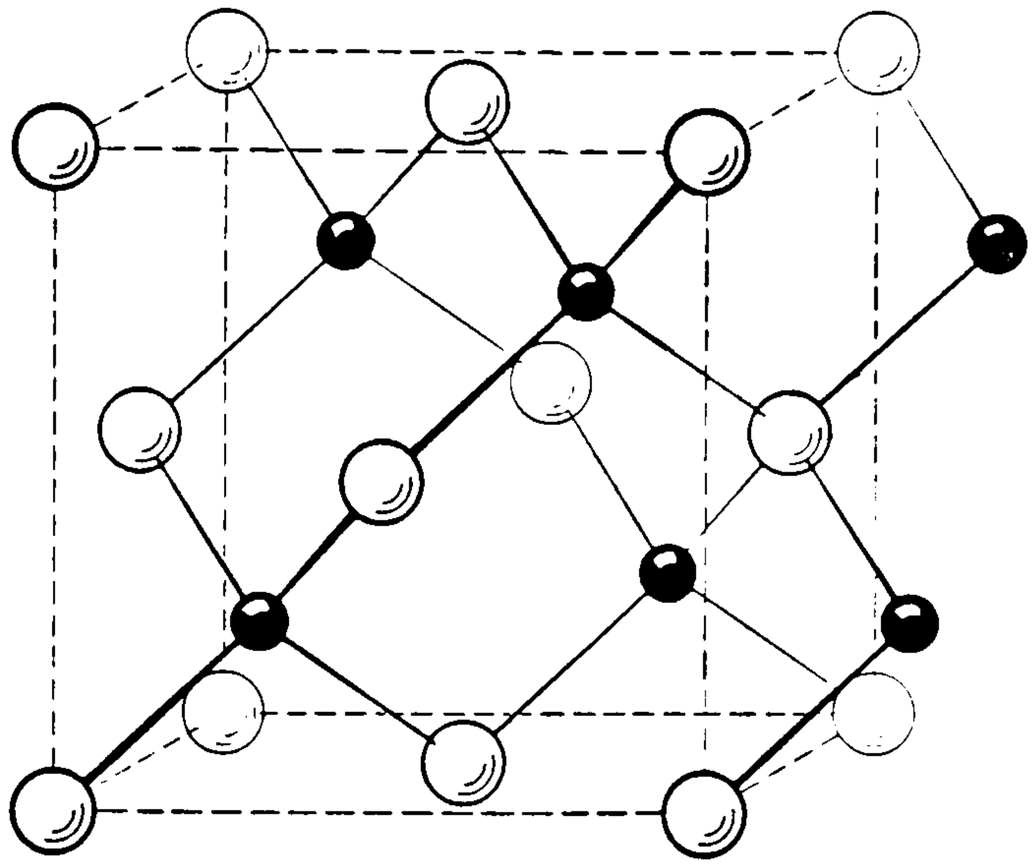

Figure 1.3. Zincblende atomic arrangment.

Figure 1.3 shows the zincblende atomic arrangement. This structure is by far the most common amongst the II-VI, III-V and group IV semiconductors. The underlying Bravais lattice for this structure is

Compound	a	c	c/a	a $\sqrt{2}$
ZnO	3.250	5.206	1.602	4.600
ZnS	3.814	6.257	1.641	5.393
ZnSe	4.003	6.540	1.634	5.661
CdS	4.136	6.713	1.623	5.849
CdSe	4.299	7.011	1.631	6.080

Table 1.2. Lattice constants of II-IV compounds known to crystallize in the wurtzite structure. The values are in Angstroms and at room temperature. The a $\sqrt{2}$ value is the equivalent crystal parameter to the cubic lattice constant (see section 1.2.3).

face centred cubic. The atomic positions consist of two interpenetrating face centred cubes, displaced along the body diagonal by one quarter the length of the diagonal, one cube represents the positions of the anions, the other the cations. The atoms in the structure possess tetrahedral bonds. Table 1.3 shows the lattice constants of a number of II-VI compounds which can be crystallized in this structure

It is important to note that, as for wurtzite, there is no centre of inversional symmetry in the zincblende structure. Consequently the [111] axis is a polar axis and zincblende compounds are piezoelectric. Another result of the lack of inversional symmetry is that the [111] axis and the $[\bar{1}\bar{1}\bar{1}]$ are not equivalent. A crystal can be cleaved to produce two (111) facets parallel to each other (i.e. a bottom and top face). These faces will not be equivalent, as one will be composed of metal ions and the other non-metal. These faces are referred to as the (111)A and (111)B respectively and they frequently possess different physical and chemical properties [1].

1.2.3 Relationship between structures

The wurtzite and zincblende structures are closely related. Figure 1.4 shows the two structures aligned with the [0001] and [111] axis vertical. It can be seen that, along these directions, the structures are composed of tetrahedrally bonded layers that repeat in a given sequence, the sequence for wurtzite being ABAB and for zincblende being ABCABC, where the letters refer to the layers on the diagram.

Compound	a
ZnS	5.4102
ZnSe	5.6687
ZnTe	6.100
CdO	6.100
CdS	5.825
CdSe	6.052
CdTe	6.481

Table 1.3. Lattice constants of II-VI compounds known to crystallize in the zincblende phase. The values are in Angstroms and at room temperature.

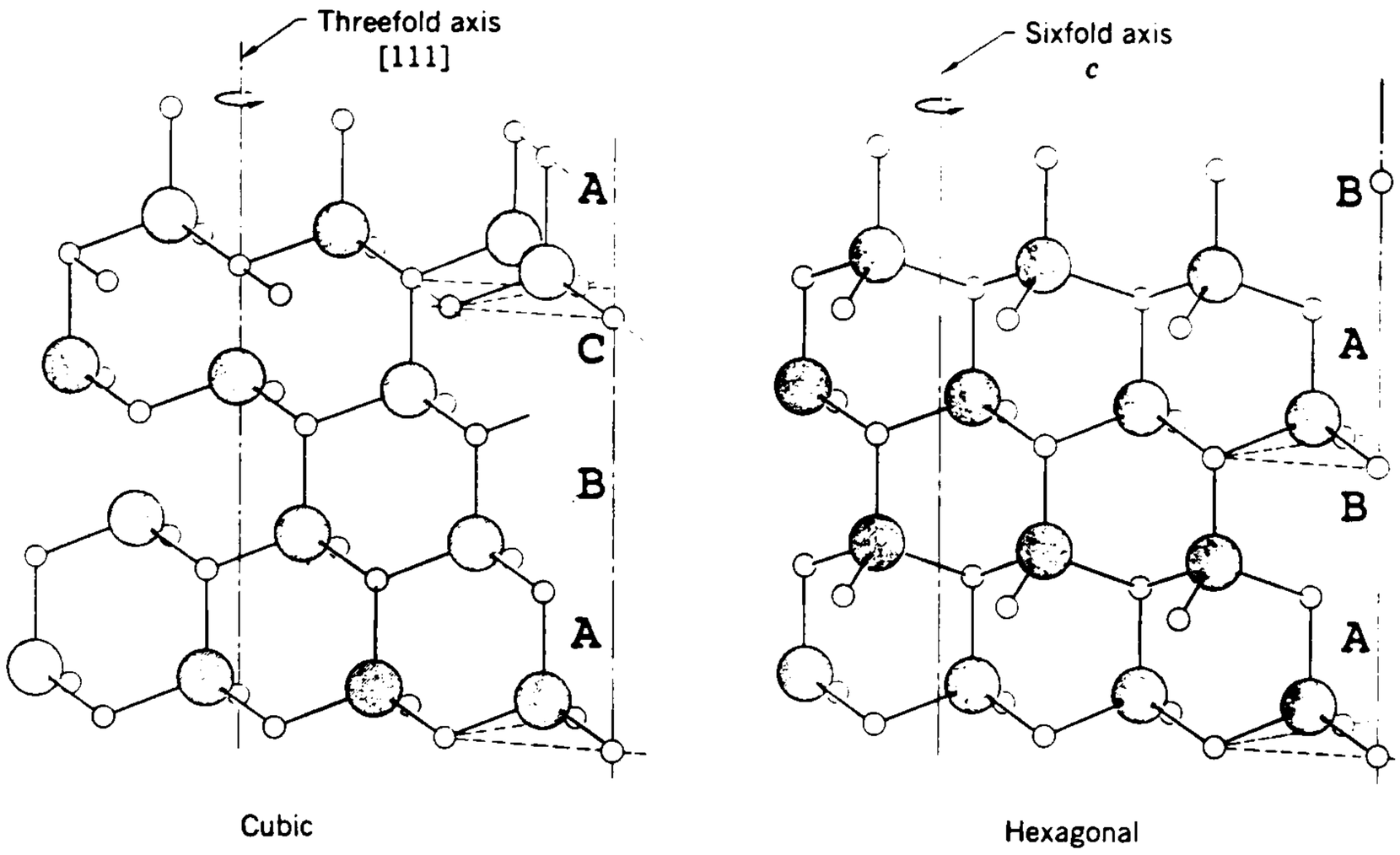

Figure 1.4. Stacking sequence of tetrahydral layers in zincblende and wurtzite compounds. The large atoms are the group VI elements.

The actual layers are identical for the two structures only their sequence is different. In consequence the structures are identical out to nearest neighbour atoms, and the arrangement of the twelve next nearest neighbour atoms is very similar.

It is possible to relate the two structures by defining transformation relations. We do this by defining the [111] and [0001] axis as equivalent. By comparing the (0001) and (111) facets we find that the $[20\bar{2}0]$ hexagonal and [110] cubic axis are equivalent. The lengths of these two lattice vectors are 2a and $a\sqrt{2}$ for the hexagonal and cubic systems respectively. By using this and the ideal c/a ratio (see above) we can obtain the relationships

$$a' = a/\sqrt{2} \qquad \text{(ii)}$$

$$c' = a\sqrt{4/3} \qquad \text{(iii)}$$

Where the primed letters are the hexagonal constants. The full coordinate transformations between the cubic miller indices a_{1-3} and the hexagonal a'_1, a'_2 and c are now [2]:-

$$a'_1 = a_1 - a_3 \qquad \text{(iv)}$$

$$a'_2 = -a_1 + a_3 \qquad \text{(v)}$$

$$c = a_1 + a_2 + a_3 \qquad \text{(vi)}$$

These relationships are used throughout this thesis to obtain the equivalent cubic and hexagonal axes. Also, the lattice mismatches between hexagonal epilayers and cubic substrates were calculated using relation (ii).

It was mentioned above that some II-VI compounds will readily crystallize in either phase. In particular, ZnS, CdS and CdSe tend to grow in a mixture of the two phases. The similarity in the two structures means that the difference in their formation energy is small. The wurtzite structure has a slightly larger Madelung constant than the zincblende (1.641 compared to 1.638 [3]). This probably explains the propensity for the more highly ionic compounds to crystallize in this structure. For example, CdS has a c/a ratio that strongly deviates from the ideal (table 1.2); such a deviation will enhance the Madelung constant even more [4].

The closeness of the structures in energy terms in some compounds leads to polytypism. This is where the stacking sequence has a longer repeat sequence than the ideal ones mentioned above. ZnS has been shown to exhibit polytypes and amongst the sequences observed have been ABAC, ABCACB and ABACBABC. This behaviour is closely related to the problem

of twinning in these compounds

1.2.4 Twinning

Twins are large two dimensional crystalline defects. Their presence can have serious effects on the electronic and luminescent properties of a semiconductor. In wurtzite or zincblende compounds twins are almost invariably caused by layers being added in the wrong stacking sequence and thus lie in the plane perpendicular to the [111]/[0001] axes. Such a fault in a hexagonal crystal results in a cubic layer one double layer thick, the stacking sequence proceeding

ABABABCBCBC

Correspondingly the same fault in the zincblende structure produces a hexagonal double layer

ABCABABC

These double layers are referred to as lamellas. They give the twins their name -'lamella twins'.

The twins formed are referred to as p type, n type or neutral depending on where the change in stacking sequence occurs. The most likely to occur is the neutral, as this has the lowest formation energy. In general lamella twins are very common in II-VI compounds grown along a [111] axis as a result of their low energy of formation. Twins are highly undesirable in semiconductor materials; they enhance impurity diffusion and trap carriers, causing non radiative recombination.

1.3 Crystal growth

The production of pure and defect free semiconductor crystals is essential for the study of their electrical or optical properties. The growth of II-VI semiconducting compounds is a well studied problem. As this thesis describes the epitaxial growth of CdS and CdSe by MOCVD, it it useful first to consider the other growth techniques that have been applied to II-VI compounds. This section describes briefly the basic techniques used for the preparation of samples by either bulk or epitaxial techniques.

1.3.1 Bulk growth

The principal technique used to produce spectroscopy quality crystals of CdS (and other II-VI compounds) has been vapour growth. The most commonly used apparatus for this growth is that developed by Greene et al [5]: figure 1.5 shows the growth apparatus.

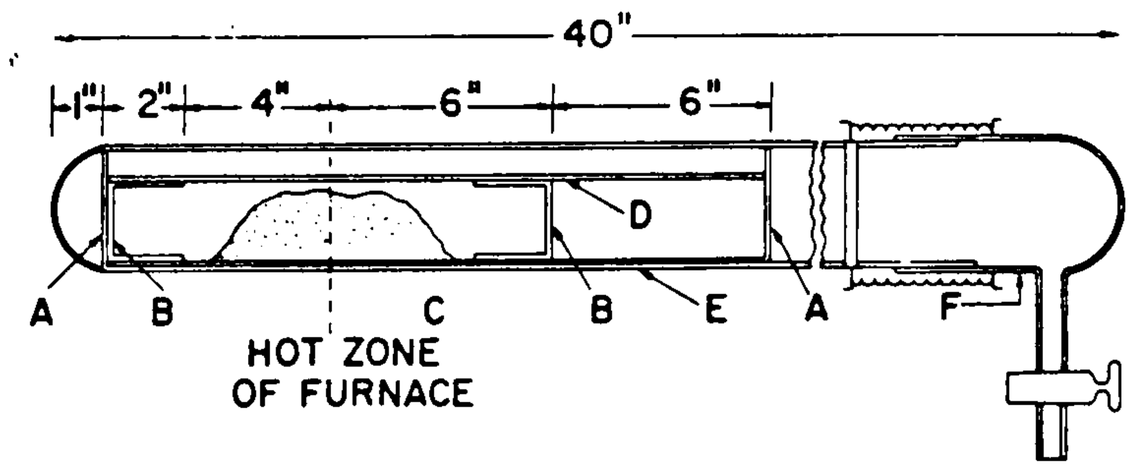

Figure 1.5. Vapour growth apparatus used by Greene et al for the growth of CdS (taken from [5]).

The growth occurs in a silica tube (E) heated at the centre to the sublimation temperature of the compound. The compound simply evaporates from the reservoir (C) and condenses on to the seed crystal on an endplate (B). Using this technique, large samples of crystalline CdS and other II-VI compounds have been prepared. Much of the pioneering work on the spectroscopy of II-VI compounds was done on samples grown by this simple method. The main disadvantage of the technique is the high growth temperature, up to 1200 ^{o}C for CdS growth. At such a high temperature indiffusion of impurities from the metal plates and silica tube is inevitable.

Other bulk growth techniques have been used for the preparation of II-VI crystals. A similar technique to sublimation is vapour phase transport, in which a reversible reaction is used to transport the compound to the growing crystal. For CdS and ZnS a commonly used transport agent is iodine, the reaction proceeds thus:-

$$CdS + I_2 \rightleftharpoons CdI_2 + S_2$$

This technique has all the disadvantages of the vapour technique with the additional one of the transport agent being incorporated into the crystal. However, the growth temperature is somewhat lower than for straight sublimation techniques.

Growth from the melt is possible for the II-VI compounds with lower melting points, such as CdTe, ZnTe and CdSe. However, this material is usually unsuitable for spectroscopic purposes owing to the high concentration of intrinsic and extrinsic defects in such material.

1.3.2 Epitaxial techniques

An alternative to bulk growth is the growth of epitaxial layers. There are a number of such epitaxial techniques. In these processes the semiconductor is deposited on to the surface of another crystal (the substrate) with a similar structure and lattice constant. For spectroscopic and optoelectronic applications such techniques have proved invaluable in recent years. The advantages of epitaxy stem from the low growth temperatures and the accurate growth control that these techniques provide. Three such techniques are briefly discussed here, vapour phase epitaxy (VPE), metallorganic chemical vapour deposition (MOCVD) and molecular beam epitaxy (MBE).

VPE is the simplest of the epitaxial techniques and involves simple sublimation of the compound on to the substrate. The closed space technique is an example of this approach and has been applied to CdS [6]. The substrate temperatures involved for the growth of CdS are in the range 500-800^{o}C. Thus the growth temperature is still quite high and impurity diffusion occurs.

MOCVD is a more advanced technique which relies on the thermal instability of some metallo-organic compounds which carry the elemental components of the semiconductor to the substrate. MOCVD is described fully in chapter 2. Its principle advantage is the low growth temperature, which is typically in the range 250-450^{o}C. At these temperatures impurity diffusion is considerably restricted and high purity growth can be achieved. Control of the reagent flow can be very precise allowing the production of superlattice type structures (see section 1.6). MOCVD has been used to grow a large number of II-VI compounds including ZnSe, ZnS [7], CdTe, $Cd_xHg_{1-x}Te$ [8] and, in this present work, CdS and CdSe [9]. The only real disadvantage of the technique is the highly reactive and toxic nature of some of the

reagents.

The final epitaxial technique mentioned is molecular beam epitaxy. MBE is the most advanced epitaxial technique developed, requiring the use of complex apparatus, although the principle is simple. Figure 1.6 shows, schematically, an MBE machine. The machine is evacuated to ultra-high vacuum conditions (typically 10^{-11}torr). The component elements are projected at the heated substrate from cells arranged around the periphery of the machine. The epitaxial layer grows on the substrate under very closely controlled conditions. In addition the use of an evacuated apparatus allows the in situ characterisation of the growing layer by RHEED. As MBE was not used for the material studied in this thesis it is not described in detail. It is useful to note, however, that the MBE technique allows the growth of semiconductor superlattices with great precision. The growth temperature is typically very low (200-300 ^{o}C). Compounds grown by this technique include $Cd_xMn_{1-x}Te$, $Cd_xZn_{1-x}Te$ and ZnSe [10,11,12].

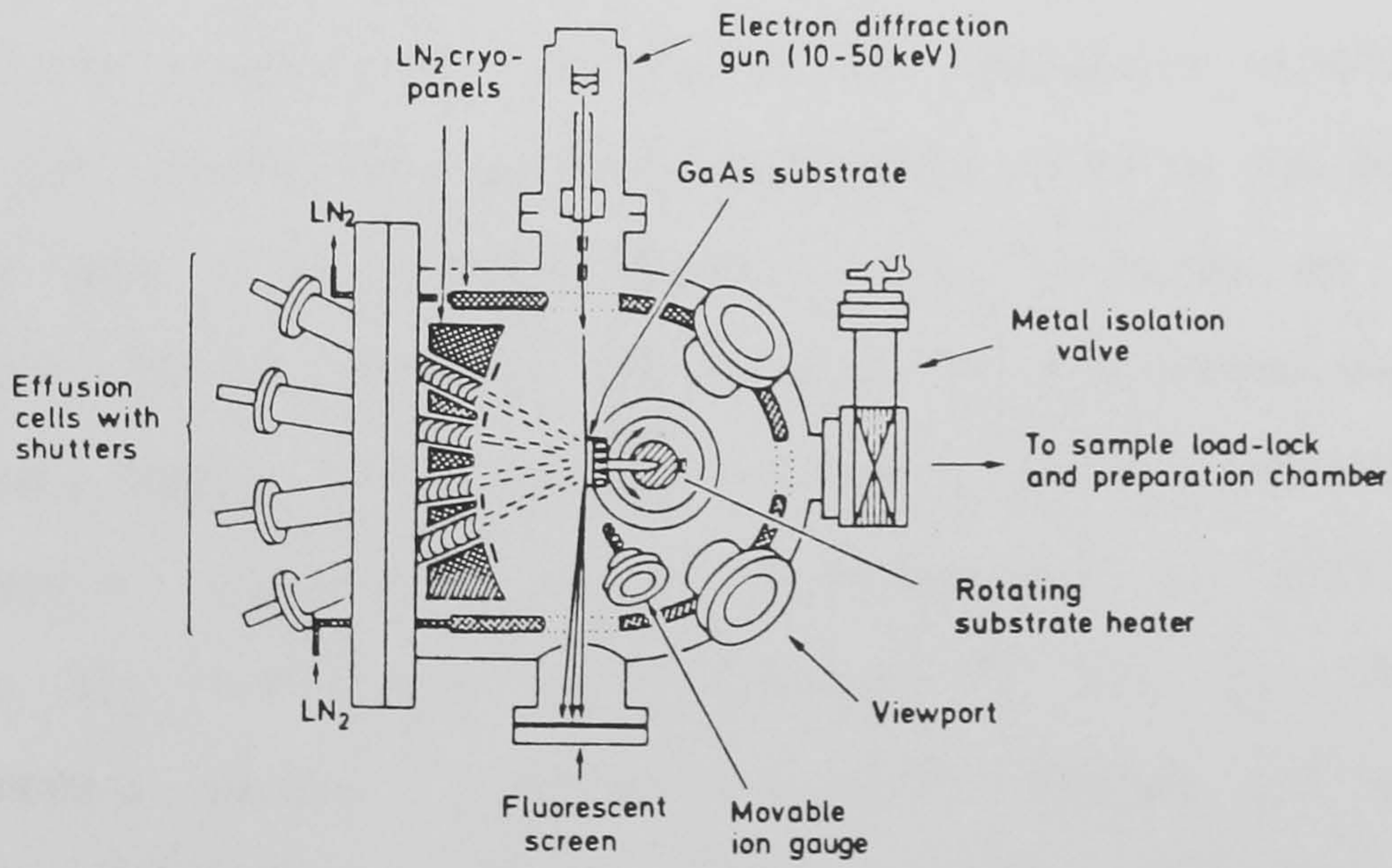

Figure 1.6. Schematic diagram of molecular beam epitaxy (MBE) machine of the type used for the growth of III-V epitaxial material [36].

Epitaxial techniques allow the growth of crystalline layers of semiconductor with great precision and purity. The key to the production of good quality material lies in the choice of a suitable substrate and growth conditions. It is, therefore, important that the quality of the material grown can be assessed by as many techniques as possible to allow the optimization of these parameters

1.4 Wurtzite band structure

The band structures of the wurtzite II-VI compounds have been calculated theoretically. These calculations have been found to be in good agreement with experiment (for a review see [13]). In the tight binding approximation the bands at the Γ point are considered to be composed of linear combinations of atomic wavefunctions. For CdS the bottom of the conduction band is assumed to be formed from the 5s levels of the cadmium atoms and the top of the valence band from the 3p levels of the sulphur. In the case of the sphalerite structure the p levels in the valence band would be degenerate owing to the equivalence of the x,y and z directions. However, for wurtzite an important modification occurs owing to the presence of a principal axis (along the z-axis). Hence, in the absence of the spin-orbit interaction, the valence band at the centre of the Brillouin zone is split into two bands with the irreducible representations Γ_1 and Γ_5. The cadmium s-levels form a single Γ_1 conduction band. Figure 1.7 shows the calculated energy bands for a wurtzite crystal along the Γ-A axis (i.e. the c-axis of the reciprocal lattice), in the absence of spin orbit coupling [13].

The presence of spin-orbit coupling produces a splitting of the Γ_5

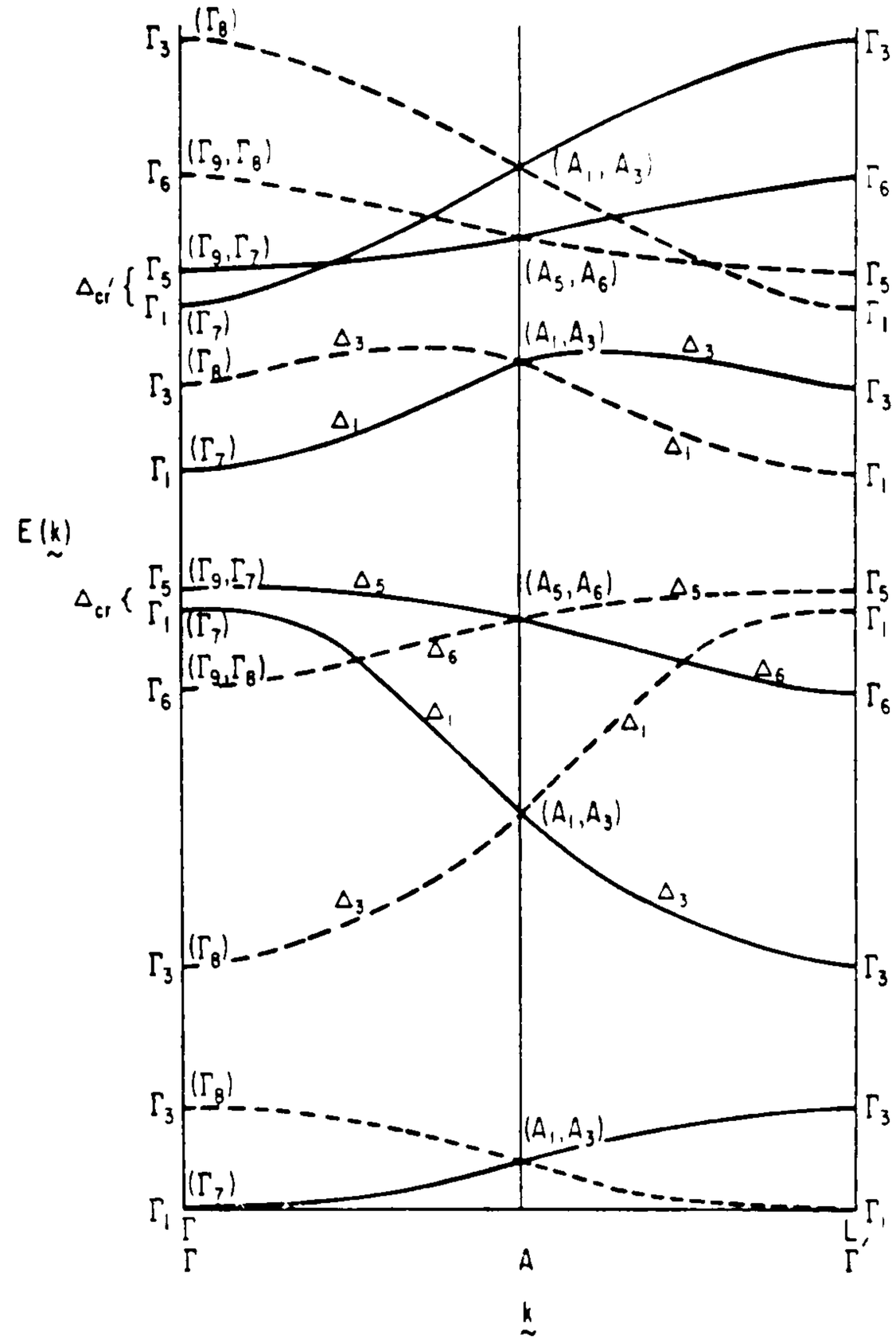

Figure 1.7. Wurtzite band structure in the absence of spin orbit coupling [13].

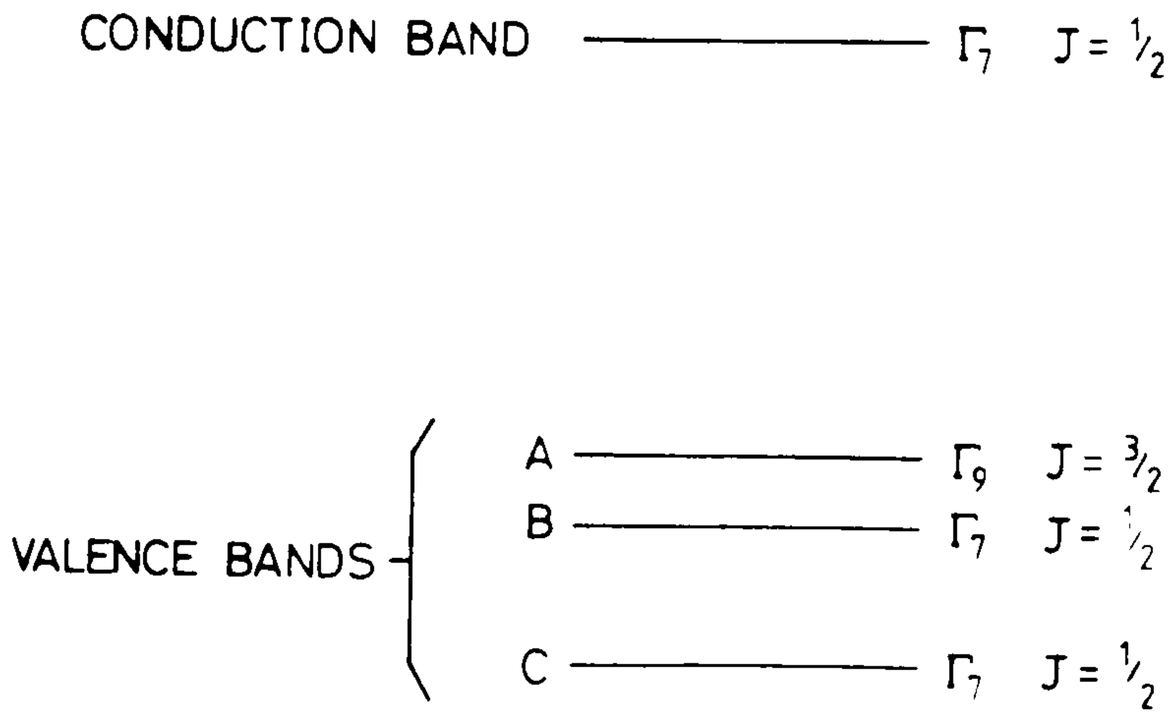

Figure 1.8. Composition of wurtzite conduction and valence bands at k=0 [14]. The valence bands are referred to as A, B and C for convenience.

band into a Γ_9 and a Γ_7 bands, the Γ_1 band is also reduced to a Γ_7 band [14]. The resulting band structure in the region of k=0 is shown in figure 1.8. The holes from the three valence bands have the spins indicated. It can be seen that the effect of the wurtzite structure is to lift the degeneracy of the valence bands that occurs for the zincblende structure. The effect of this splitting is important in optical studies, as recombination can be observed involving holes from any of these bands. For convenience the bands are referred to as the 'A','B' and 'C' bands, as indicated on the diagram.

Table 1.4 shows the important band parameters amd effective masses for the wurtzite forms of CdS and CdSe. It is important to note that the mass of the 'A' band hole is highly anisotropic with a much larger mass along the c-axis of the crystal. This anisotropy is the result of the presence of a principal axis. The values of the hole effective mass along this axis are (as indicated) uncertain. Cardona [15] calculated a series of band parameters for CdS and CdSe using k.p theory. The value obtained for the mass $m^{*\parallel}_a$ was 2.5 m_o for both CdS and CdSe. The values calculated for m^*_e,$m^{*\perp}_a$ and m^*_b were in close agreement with experiment. In the light of the difference between the measurement and calculation of the $m^{*\parallel}_a$ parameter a large uncertainty must be applied for its measured value (as indeed the experimenters themselves acknowledged [16,17]). As the value of the $m^{*\parallel}_a$ parameter for CdSe is important for the work in chapter 4, we will here ascribe limiting values to it. The measured value of $m^{*\parallel}_a$ is greater than or equal to m_o [16], and the calculated value is 2.5 m_o. Therefore for the moment we will assume that the value lies in the range 1-2.5 m_o. Notice that the calculated and measured value of $m^{*\parallel}_a$ for CdS are in agreement (both 2.5 m_o) [15,18]. The implications of the uncertainty in this value are discussed in chapter 4.

	CdS	CdSe
E_g^a	2.582	1.841
E_g^b	2.599	1.866
E_g^c	2.655	2.274
Δ_{cf}	0.028	0.039
Δ_{so}	0.068	0.420
$M_h^{a\perp}$	0.7	0.45
$M_h^{a\parallel}$	2.5 [18]	>1 [16]
M_h^b	1.1	0.9
M_e	0.2 [19]	0.13 [20]

Table 1.4. Band parameters and effective masses of wurtzite CdS and CdSe. The masses are in units of m_o and the energies in electron volts. The sources from some of the more important parameters are indicated.

1.5 Luminescence properties of II-VI compounds

One of the most technologically useful effects exhibited by semiconductors is that of radiative recombination. The origin of such recombination can reveal a great deal about the relative purity and structural quality of a semiconductor crystal. The origins of the various luminescence bands observed from the II-VI compounds have been studied for many years. Here, a brief overview of low temperature radiative recombination in these compounds is given.

The luminescence technique described in this thesis is photoluminescence. In photoluminescence a sample of semiconductor is excited with photons of light, usually with a greater energy than the materials forbidden gap. This light produces a large number of electron-hole pairs in the sample. These carriers are thermally unstable (at the low temperature of the sample) and they will recombine, some radiatively. The process by which recombination occurs will reveal information about the presence of impurity or defect states within the forbidden gap. The general types of recombination process observed in II-VI semiconductors are described here.

1.5.1 Free excitonic recombination

Excitonic states in semiconductors arise as a result of the coulombic interaction between an electron in the conduction band and a hole in the valence band. The resulting exciton has hydrogen like energy states. These states are displaced in energy below that of the materials band gap by the excitonic binding energy given by :-

$$E_x = \mu^* e^4 / (4\pi (2\hbar^2 \epsilon_r^2)) \qquad \text{(vii)}$$

where ϵ_r is the dielectric constant of the material and μ is the reduced electron hole effective mass, the other constants have their usual values. It was observed above that the photocreated carriers must recombine. Free excitonic recombination is the simplest recombination process, and occurs when the exciton decays, the electron recombining with the hole. However, as the exciton is free to move within the crystal lattice it will, in general, possess a non-zero momentum. This momentum must be exactly removed by the emitted photon (for the zero-phonon line). Although this k-selection rule is relaxed by phonon emission, the free exciton emission is, in practice, usually weak compared to other processes. In general, although phonon assisted free exciton transitions are observed in high quality semiconductor crystals, the zero-phonon line is not [21].

1.5.2 Bound excitonic recombination

In a structurally perfect and totally pure semiconductor (the type only grown in theoretical treatments!) free excitonic recombination emission would be the only one observed. However, in impure material another type of excitonic process can occur. It was shown by Lampert [22] that it is possible for excitons in II-VI compounds to bind to shallow acceptor or donor defects. Bound excitons can best be considered by the analogy of the exciton with the hydrogen atom. Consider neutral donors: these are also analogous to the hydrogen atom with the donor centre holding an electron by coulombic attraction. An exciton can bind to this donor in the same manner as two hydrogen atoms can bind together to form a hydrogen molecule. A neutral acceptor can also trap a free exciton in a similar manner. Similar states exist for the ionized sites. The systems this time being analogous to the H^+ and

H^- ion for the ionized donor and ionized acceptor sites respectively.

The exciton bound in any of these states has no momentum, thus the exciton can recombine directly, without phonon assistance. This lack of lattice interaction results in a very narrow linewidth (as small as 0.04 meV [23]), the main broadening mechanism being the interaction of the bound exciton with impurities on lattice sites close by. Thus broadening of the bound exciton emission line can indicate the presence of high levels of impurities [24]. The energy of the photon emitted on recombination for an exciton bound to a neutral acceptor or donor is given by

$$E_R = E_g - E_{bx} - E_{xo} \qquad \text{(viii)}$$

Where E_{xo} is the binding energy of the free exciton, E_{bx} is the binding energy of the exciton to the impurity site and E_g is the materials band gap. E_{bx} can be calculated by using the analogy with the hydrogen molecule. However, without going into the calculation here, a simple rule (the so called 'Haynes rule' [24]) is found to hold for most semiconductors.

$$E_{bx} = k_d E_d \qquad \text{(ix)}$$

Where E_d is the binding energies of the donor and k_d is a constant dependant on the material. A similar relationship holds for the neutral acceptor bound exciton with a different constant. The value of these constants have been determined for a large number of impurities in most of the II-VI compounds. Measurements of the positions of the bound exciton emissions allows an assessment of the impurities present in a sample.

1.5.3 Impurity recombination

With the presence of high levels of impurities in a sample another kind of recombination becomes possible. This recombination involves the impurity levels lying within the forbidden gap of the semiconductor. Two types of emission are considered here; donor-acceptor pair and free to bound.

Donor acceptor pair recombination occurs when an electron bound to a neutral donor site recombines directly with a hole bound at a neutral acceptor site. This is illustrated in figure 1.9.

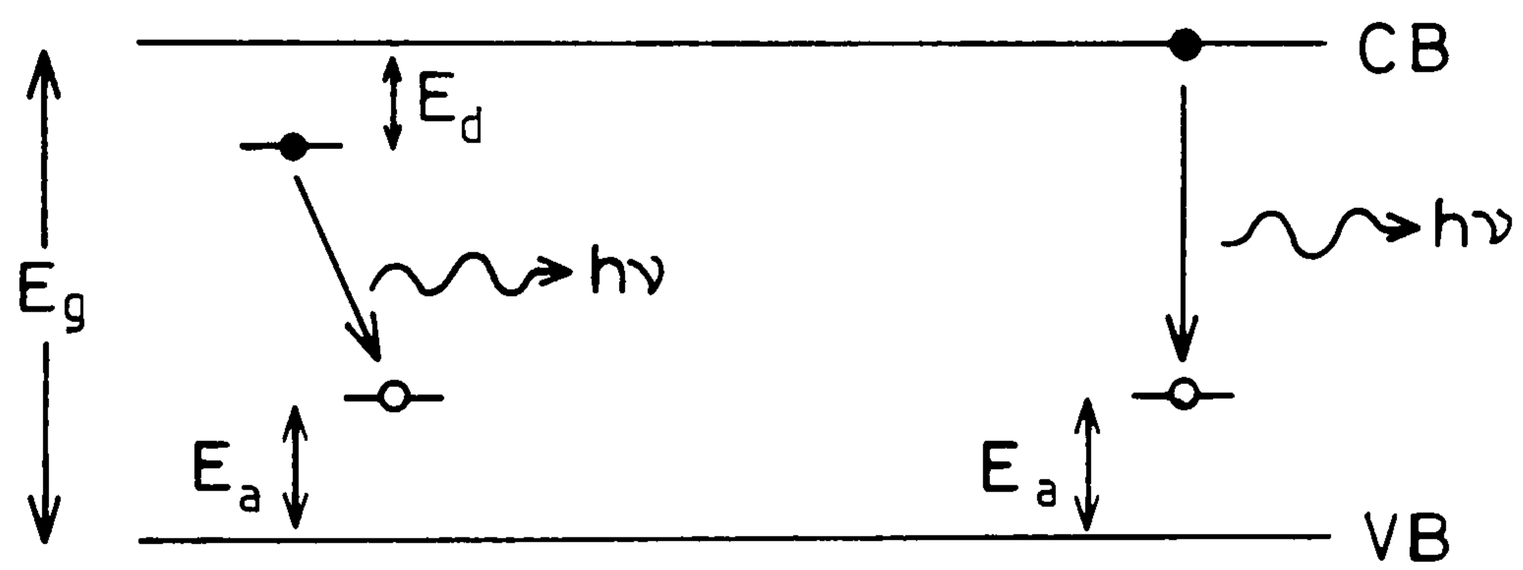

Figure 1.9. Mechanisms for donor acceptor pair (left hand side) and free to bound recombinations. E_a and E_d are the binding energies of the acceptor and donor respectively.

The energy of the emitted phonon for D–A pair recombination is given :-

$$E_p(r) = E_g - E_d - E_a + e^2/(4\pi\epsilon_r r) \qquad (x)$$

Where the E_a and E_d are the binding energies of the donor and acceptor respectively. The term on the righthand side is the coulombic

interaction energy between the ionized donor and acceptor present after the recombination has occured. This is dependent on the separation r of the two sites. Consequently the d-a pair emission is usually a broad band consisting of emission from pairs with differing separations. In general the d-a pair emission is strongly coupled to the lattice and is accompanied by phonon replicas.

Free to bound emission occurs when a free electron recombines with a hole bound at an acceptor, as illustrated on the right hand side of figure 1.9. The corresponding process in which a hole recombines with an electron bound at a donor is known (bound to free) but rarely observed [25]. The photon energy observed is given by [26]:-

$$E_p = E_g - E_a + kT_e \qquad \text{(xi)}$$

Where the kT_e term is the thermal energy of the recombining electron which can be obtained by curve fitting. As for the d-a pair emission; the free to bound couples strongly to the lattice and phonon repicas are usually observed. The relation (xi) can be used to derive the depth of the acceptor involved by estimating the kT_e term which is usually small anyway [27].

Both of the above processes produce similar emissions in the same region of the spectrum. In order to determine which, if either, is involved in a particular luminescence band other measurements may be necessary. One method that can be applied is the temperature dependance of the emissions. The free to bound, in general, persists to higher temperatures, the d-a pair emission decaying with the activation energy of the donor (the shallower defect).

1.6 Low dimensional structures and superlattices

Introduction

One of the most intensively studied areas of solid state physics in recent years has been that of semiconductor microstructures. Advances in the epitaxial growth techniques mentioned in section 1.3.2 have allowed the construction of semiconductor structures with unprecedented precision. These techniques have allowed the construction of devices on a scale comparable to the wavelength of the carriers in such devices. One of the most promising areas of research for such structures is that of solid state optical devices. The techniques have already been applied to the construction of visible light solid state lasers and such lasers have proved to be the most efficent light sources ever constructed [28].

In this section the field of epitaxial structures is reviewed. Special emphasis is given to the optical properties of semiconductor superlattices, as this is of relevance in chapter 4.

1.6.1 Compositional superlattices

The term superlattice is applied to semiconductor systems in which a larger scale periodicity is imposed on the usual lattice structure. If this periodicity is of sufficently small size than it can alter the band structure of the semiconductor. Because of the nature of epitaxial growth techniques the simplest way to impose such periodicity is by depositing alternating layers with different compositions. In such a system the imposed periodicity is essentially one dimensional. Such

compositional semiconductor superlattices were first suggested in 1970 by Esaki and Tsu [29], long before one was actually produced.

Consider a simple system in which both materials have the same lattice constant such as the GaAs/$Al_xGa_{1-x}As$ system. $Al_xGa_{1-x}As$ has a larger band gap than the GaAs (approx 2ev for $Al_{0.3}Ga_{0.7}As$ compared to 1.5 eV for GaAs). The simplest structure of interest is a simple 'quantum well' composed of a thin layer of GaAs sandwiched between thick $Al_xGa_{1-x}As$ cladding layers. We can consider the interface between the two semiconductors to produce a potential step in the conduction and valence bands of E_c and E_v respectively. It is clear that the sum of E_c and E_v must be equal to the difference in the band gap of the two materials. For the $Al_xGa_{1-x}As$/GaAs system E_v and E_c are both positive (i.e. the lower potential is in the GaAs). Figure 1.10 shows the electronic structure of such a quantum well along the z-axis (the growth direction).

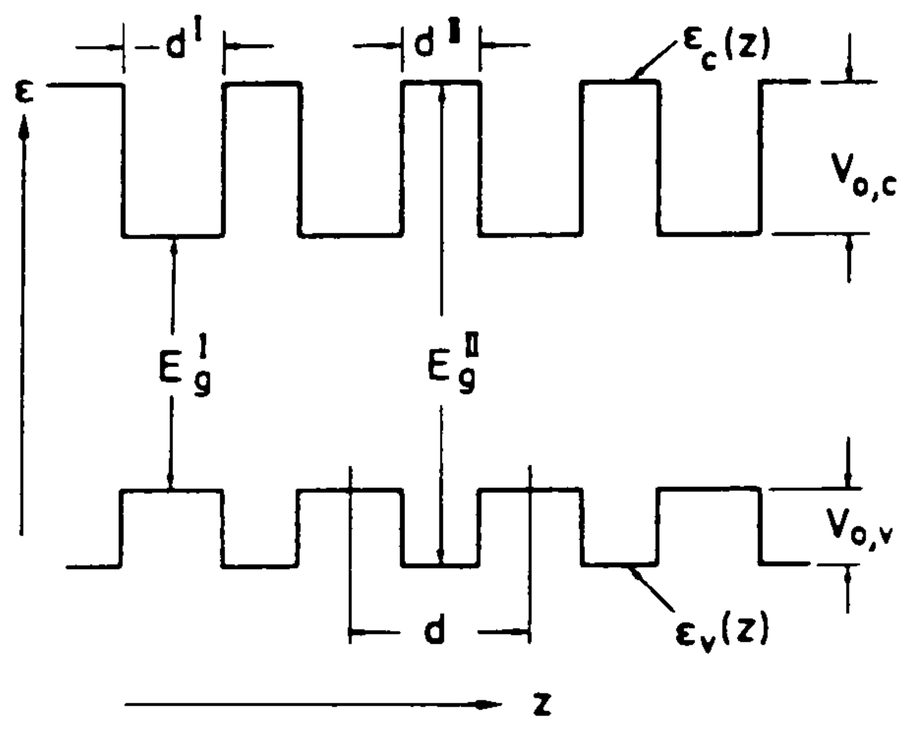

Figure 1.10. Electronic structure of GaAs/$Al_xGa_{1-x}As$ multiple quantum well structure. The I and II superscripts refer to GaAs and $Al_xGa_{1-x}As$ respectively.

It can be seen that the confinement of the carriers in the z-direction will produce a series of confined states in the conduction and valence bands. The problem of the carrier confined in the quantum well in figure 1.10 is analogous to that of the 'particle in a box' problem. The appropriate electron and hole wavefunctions can be calculated from the solutions of Schrodinger's equation for the problem. Here we will briefly review the calculation of the effective band gap in such a system.

The simplest approach is to assume that the well is infinitely deep (a good approximation for wide wells). Now the energy of the electron or hole is quantized into a set of discrete levels with energies trivially given by [30]:-

$$E_n = \hbar^2 n^2 \pi^2 / (2m^* L_w^2) + \hbar^2 (k_x^2 + k_y^2)/2m^* \qquad \text{(xii)}$$

Where L_w is the well width, m^* is the effective mass of the particle and the term of the right hand side is the dispersion term for motion in the x and y directions. The most important effect of this quantization is to alter the density of states in the conduction and valence bands of the semiconductor. For each value of n the density of states for the system described above is given by [31]:-

$$\rho(E) = nm^* / (\pi \hbar^2) \qquad \text{(xiii)}$$

Figure 1.11 shows the density of states of a 2 dimensional system compared with the 3 dimensional bulk. Instead of the usual parabolic density the 2 dimensional system has a stepped density, with the steps occuring at the confined energy levels of the carrier.

The most important changes in the optical properties of the

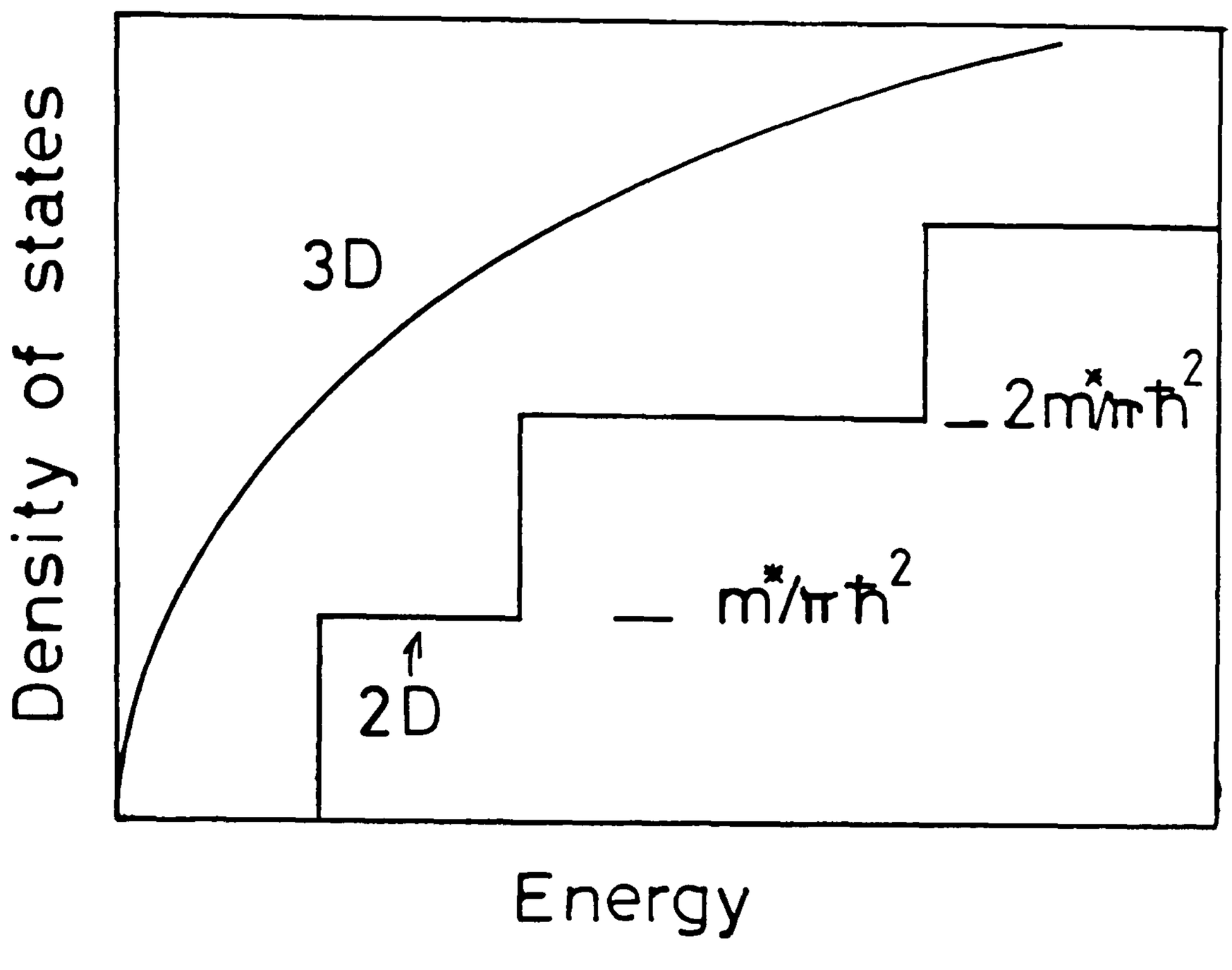

Figure 1.11. Density of states in three dimensional and two dimensional energy bands (assuming k perpendicular to the quantization direction is zero).

material in the quantum well can be understood in terms of the elementary theory described above. The first effect is the shift of the emission to higher energy as the well width is reduced. This is a result of the increase in band gap of the well material due to the confinement of the carriers. The optical transition occurs between the confined electron and confined hole ground states. Another effect arises out of the selection rule $\Delta n=0,2,4$ etc for optical transitions. This is seen in the absorption spectra, where only the these transitions are observed [31]. The presence of light and heavy holes can split the emission line as the confinement energy is a function of carrier mass. The most technologically interesting effect, however, is the enhancment of the radiative efficency. In the bulk semiconductor the density of states at the the Γ point is zero. Therefore any radiative recombination will, in general, be indirect and require some phonon assistance. In the 2 dimensional system this is not the case as there are a finite number of states at k=0. The result of this is that direct excitonic radiative recombination is enhanced in quantum well emission. It is observed in a number of systems that the luminescence from quantum wells can be brighter than that from bulk epilayers by several orders of magnitude [32].

The theory above assumed infinite potential barriers for the well. In practice the band offsets E_V and E_C are finite and sometimes unknown. It is therefore important that the modifications to the theory this gives are understood. In the case of a single quantum well with finite barriers the solution of Schrodingers equation for the confined carriers is again elementary. Using the definitions [30]:-

$$q^2=2m^*(V-E)/h^2 \qquad \text{(xiv)}$$

$$k^2=2m^*E/h^2 \qquad \text{(xv)}$$

we find the following quantization condition for the energy levels in the well.

$$k^2-q^2= 2qk\ \mathrm{Cot}(ka) \qquad \text{(xvi)}$$

where the constants have the same meaning as above and V is the height of the potential barrier. This relation can be solved numerically by computer as outlined in appendix 2. The energy levels occur at higher energy than those given by (xii). It is important to note that the density of states in this case is still stepped as in the infinite well case. The steps simply occuring at the positions given by (xvi). The selection rule $\Delta n=0$ still holds for optical transitions in this case.

The final modification we consider here is the interaction between adjacent wells. Figure 1.12 shows the potential experienced by the electron in a true 'superlattice'. The superlattice has a periodicity of d superimposed on the lattice constant.

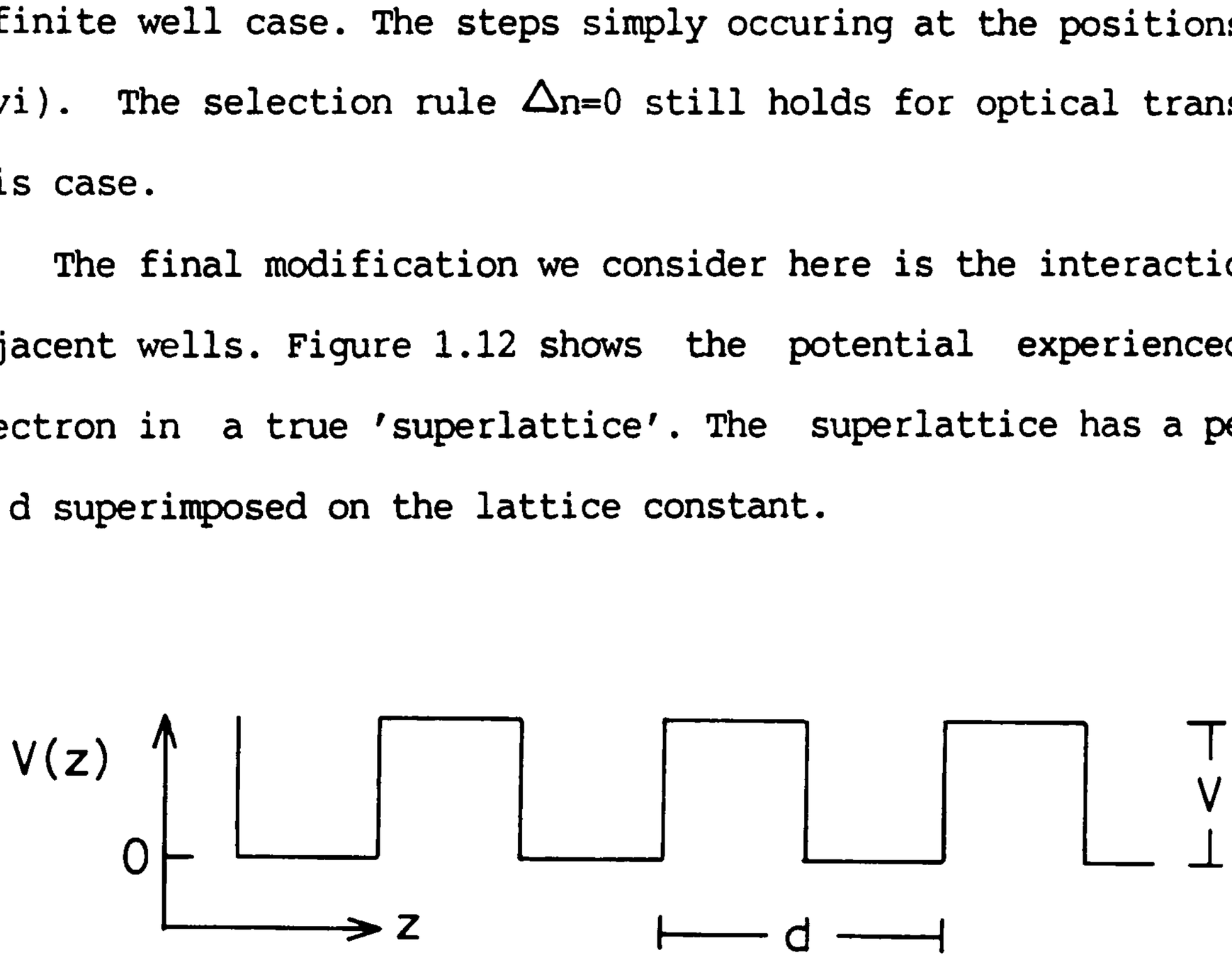

Figure 1.12. Periodic potential assumed in Kronig-Penney model.

The solution of Schrodinger's equation for this potential was derived by Kronig and Penney in 1936. They derived the well known Kronig-Penney dispersion relation [33]:-

$$\mathrm{Cos}(d\,k_{sl})=[(q^2-k^2)/2qk]\,\mathrm{Sinh}(qb)\,\mathrm{Sin}(ka)+\mathrm{Cosh}(qb)\,\mathrm{Cos}(ka) \quad \text{(xvii)}$$

where a and b are the thicknesses of the well and barrier respectively (d=a+b) and k_{sl} is the 'superlattice momentum vector'. The other values are the same as for the finite well solution. The left hand side of the equation only has real solutions in the range -1 to +1. Bastard [34] adapted this equation for superlattices in which the effective mass alters at the interface to derive the relations:-

$$k_a^2=2m_aE/\hbar^2-k^2 \quad \text{(xviii)}$$

$$k_b^2=2m_b(V-E)/\hbar^2-k^2 \quad \text{(xix)}$$

$$x=m_ak_b/m_bk_a \quad \text{(xx)}$$

$$\mathrm{Cos}(d\,k_{sl})=\mathrm{Cos}(a\,k_a)\mathrm{Cosh}(b\,k_b)-\tfrac{1}{2}[x-1/x]\mathrm{Sin}(a\,k_a)\mathrm{Sinh}(b\,k_b) \quad \text{(xxi)}$$

Where m_a and m_b are the effective masses along the z-direction in the barrier and well respectively and k is the term for the dispersion in the x and y directions. A computer program was written to solve this equation for a wide range of material parameters (see appendix 2). The resulting carrier states are referred to as subbands. Figure 1.13 shows the reduced zone scheme for the subbands in a semiconductor superlattice, superimposed on the usual parabolic dispersion. The effect of the interaction between wells is to reduce the confinement

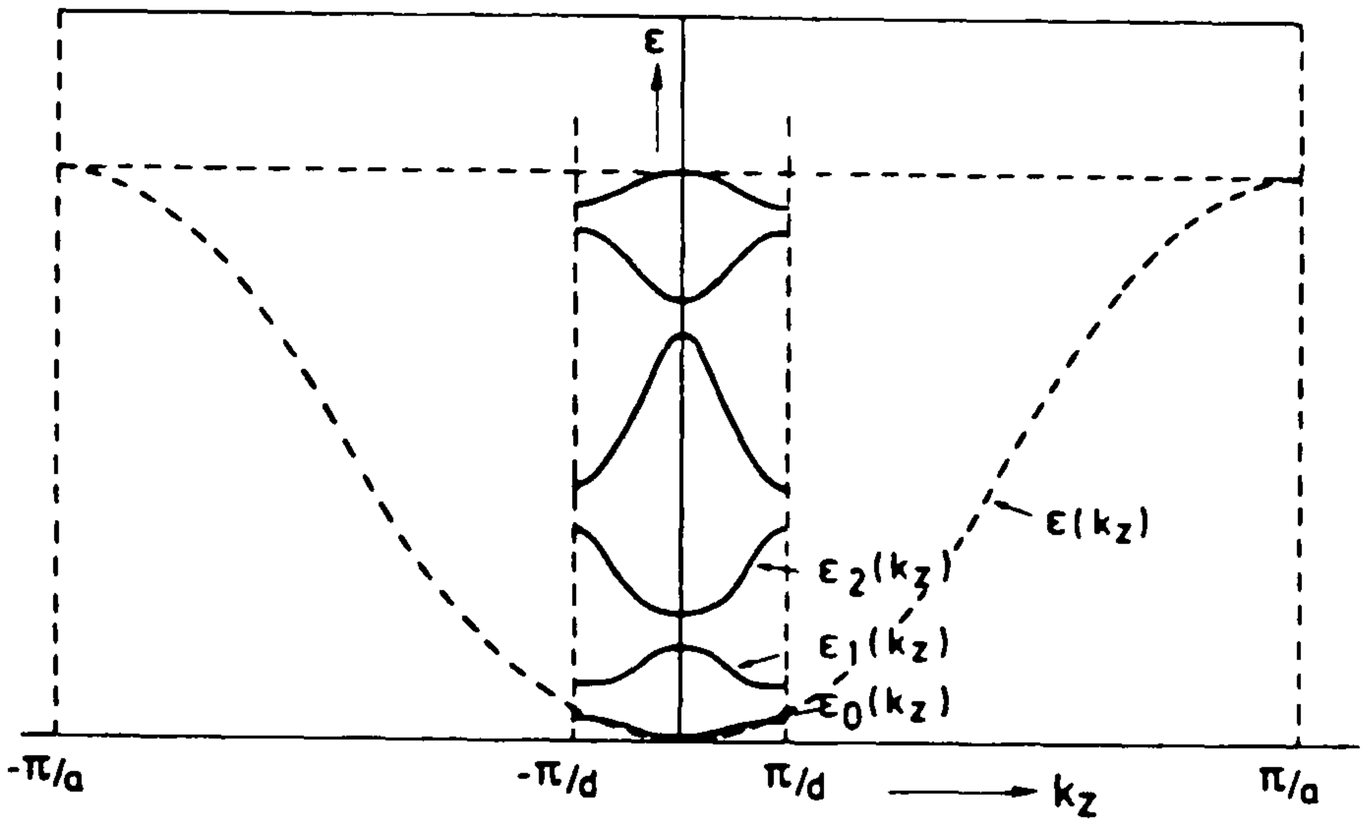

Figure 1.13. Dispersion relation obtained from Kronig-Penney model for superlattice of period d, where a is the lattice constant of the material.

energy below that of the finite well case. In addition the presence of a non-zero dispersion relaxes the $\Delta n=0$ transition rule [35].

Calculating the confinement energies using the theory above depends on a knowledge of band offsets. This is not always available. However, by measuring the transition energies accurately it is possible to estimate the band offsets. This approach has been taken for a series of systems. As a rule of thumb, the accuracy of such measurments increases as the number of electron and hole subbands observed increases; also the electron and holes must possess significantly different effective masses.

Before considering alternatives to compositional superlattices it is important to note that not all systems have band offsets with the same sign. The system described above is type I. An example of a superlattice with offsets of different signs is the $Ga_xIn_{1-x}As/GaAs_ySb_{1-y}$ system. The potential along the z direction for this system is illustrated in figure 1.14

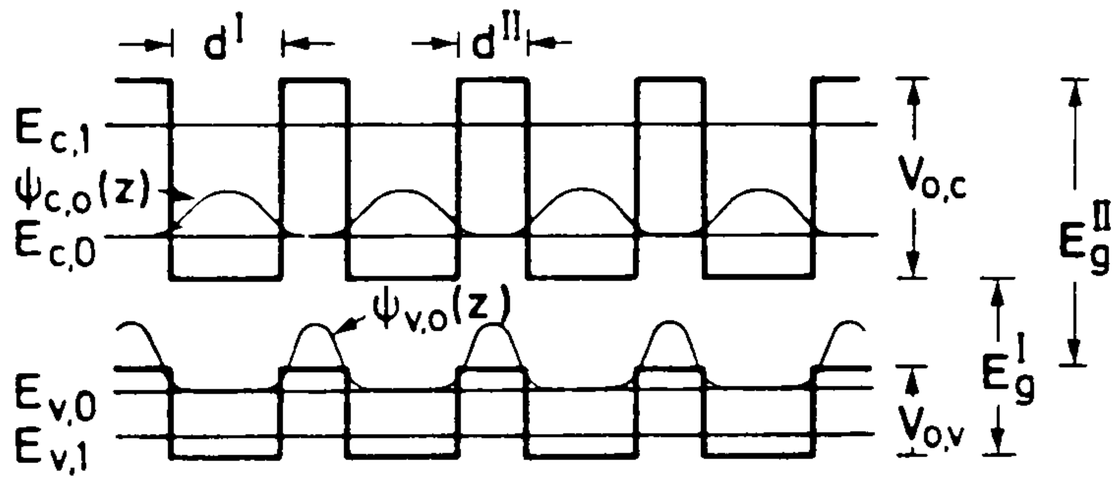

Figure 1.14. Type II superlattice in a $Ga_xIn_{1-x}As/GaAs_ySb_{1-y}$ compositional superlattice (taken from [36]).

In this system the electrons and holes are confined in different layers and such a system is referred to as type II. The confinement

energy of the electron and holes can be calculated in a type II superlattices as described above. However, the optical transition is indirect in real space and will occur with lower energy than the band gap of either component. The theory used to deal with this is discussed in section 4.4.3.

1.6.2 Doping superlattices

In addition to simple modulation of the composition of epitaxial material, an alternative 'doping' form of superlattice can be produced. A doping superlattice is formed when alternating layers of p and n doped semiconductor are deposited within an epitaxial layer. The layer compound itself remains the same throughout the superlattce. An example of a doping superlattice is the GaAs nipi structure. In a GaAs nipi structure layers of GaAs are deposited in the sequence n-type, insulating, p-type, insulating, hence the acronym nipi. The modulation produces a series of parabolic potential wells in the conduction and valence bands which are displaced relative to each other in space. Figure 1.15 shows the potential distribution along the growth direction of such a structure.

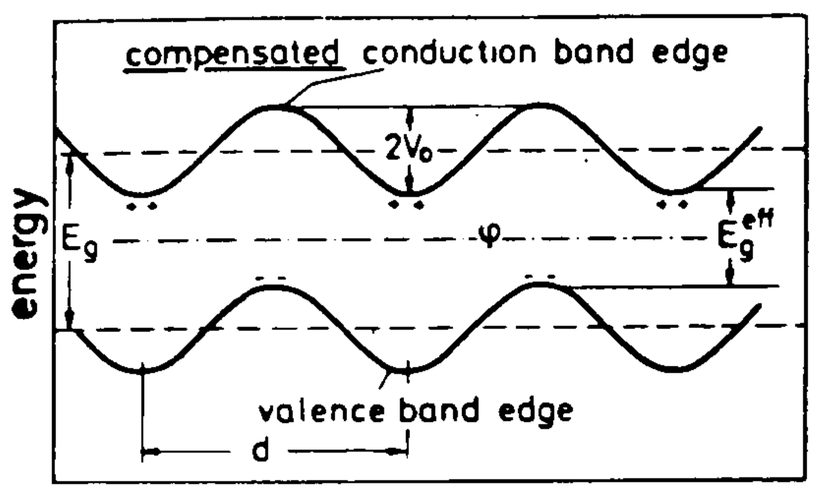

Figure 1.15. Potential distribution in a GaAs nipi doping superlattice.

GaAs nipi structures display a number of interesting properties associated with the spatial separation of the electrons and holes [36]. The theory of their band structure is not important for the present work and so is not discussed. However, comparisons are made between nipi structures and CdS/CdSe superlattices in chapter 4.

1.6.3 Strained layer superlattices

Strained layer superlattices are compositional superlattices. In the $Al_xGa_{1-x}As/GaAs$ system discussed in section 1.6.1 the two components of the superlattice had almost identical lattice constants. When the component materials of the superlattice have different lattice constants than the superlattice is described as 'strained layer'. Such a system can be considered in some ways to be an ordered alloy, with a lattice constant which is intermediate between those of the two component materials. The effect of the strain on the presence of defects in the lattice and on the band structure of the material can be significant. These aspects are discussed for CdS and CdSe in section 3.1. The lattice constants of the superlattice and the bulk compounds are related by the Matthews Blakeslee lattice matching condition [37]:-

$$a_{sl} = a_1 + (a_1 - a_2)/(1 + L_1/L_2) \qquad \text{(xxii)}$$

Where a and L refer to the lattice constant and the thickness of the materials 1 and 2 respectively and where a_{sl} is the lattice constant of the superlattice. Equation (xxii) relies on the superlattice being effectively infinite and the elastic constants of the two compounds being the same. The biaxial strain E of each layer can be obtained from (xxii) trivially as :-

$$E_1 = f/(1+L_1/L_2) \qquad \text{(xxiii)}$$

$$E_2 = f/(1+L_2/L_1) \qquad \text{(xxiv)}$$

Where the subscripts again refer to material 1 and 2, and f is the lattice mismatch between the two compounds. The periodic potential in such a superlattice is similar to that of other compositional superlattices, as outlined above. However, the presence of strain might alter the band structures of the compounds and this might have to be taken into account to when calculating the carrier energy levels in the system.

A modification to the periodic potential of such a superlattice by the piezoelectric effect was suggested recently [38]. It was found that for certain orientations of cubic substrates large strain-induced fields could be generated. Figure 1.16 is a diagram taken from [39] showing the periodic potential for the InGaAs/GaP system with a substrate orientated so that the [111] cubic axis is perpendicular to the epilayer. The internal fields have a number of effects on the electronic states in the system, these are discussed for the case of the CdS/CdSe system in chapter 4.

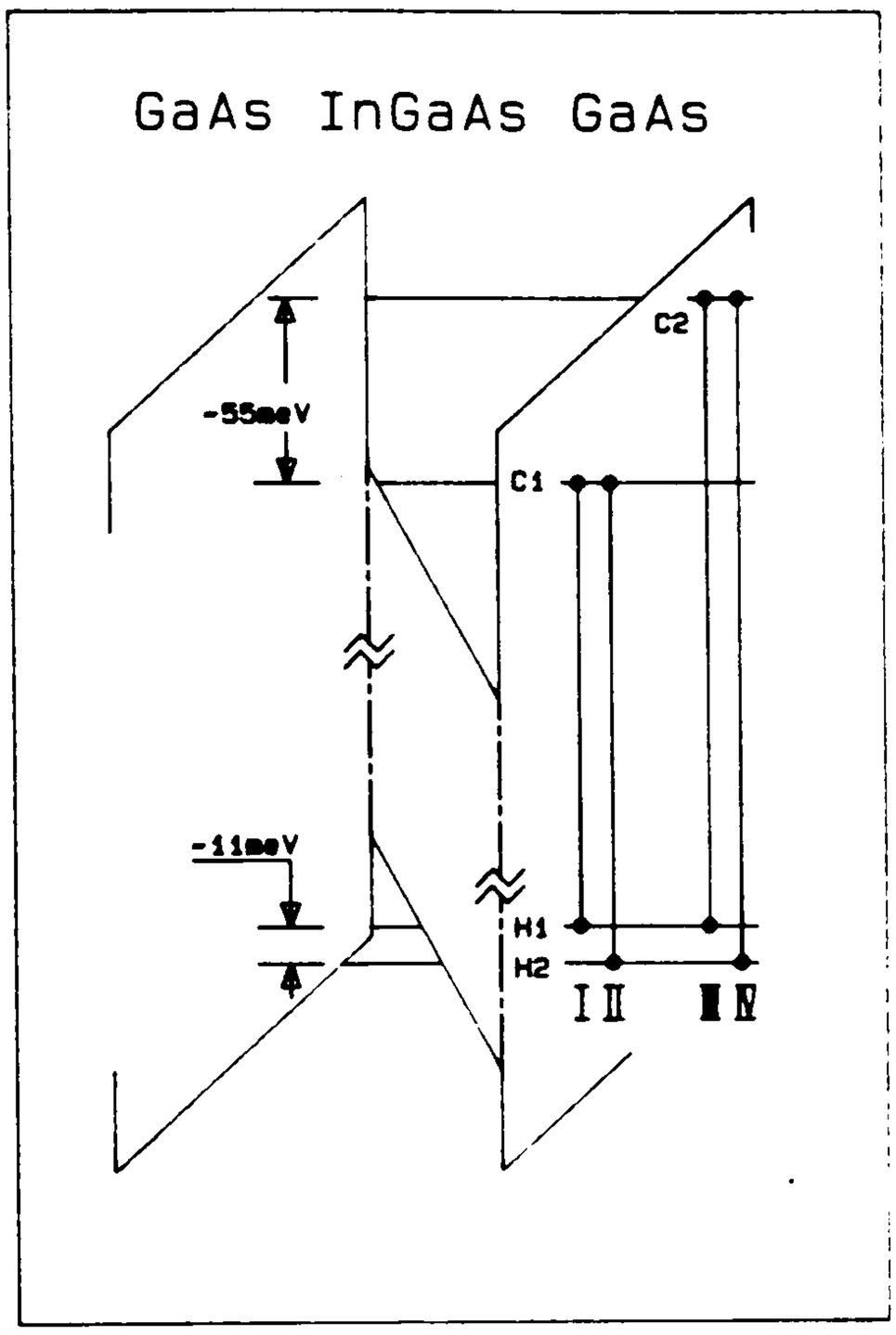

Figure 1.16. Effect of piezoelectric fields in the GaAs/$In_xGa_{1-x}As$ strained layer system [39].

1.7 II-VI superlattice systems and band offsets

A large number of compositional superlattices have been grown using II-VI semiconductor compounds. It is useful here to review the offsets found for these systems. Table 1.5 shows the systems studied along with the system type, the magnitude of the valence and conduction band offsets measured and the size of the mismatch between the components; the sources of the data are indicated. Some of the most intensively investigated systems are those based around the zinc cation. These systems include ZnS/ZnSe, ZnS/ZnTe and ZnSe/ZnTe. The zinc based superlattices are of technological interest as blue light emitting compounds. It has been found for these systems that intense excitonic emission dominates the luminescence at low temperatures. By studying this luminescence it has been concluded that the ZnS/ZnSe is type I and the ZnSe/ZnTe and ZnS/ZnTe systems are type II [46,41]. For any of these systems to be used in optoelectronic devices a knowledge of the band offsets is essential.

The measurement of band offsets is a problem frequently addressed in the study of semiconductor superlattices. There have been many theoretical attempts at predicting offsets (see for example [47,48,49]). However, most of these have proved unreliable. The simplest theoretical approach taken has been the so called common-anion rule [50]. This relies on the observation that for all the III-V and II-VI semiconductors the conduction band is derived from the s-levels of the cations and the valence band from the p-levels of the anion. It was therefore suggested that for common cation superlattices the conduction band offset should be very small. Correspondingly, for common anion systems the valence band offset should be vanishingly small. Table 1.5 is divided into common cation and common anion sections. It can be seen

II-VI COMPONENTS	TYPE	E_C	E_V	$\Delta a/a$ (%)	SOURCES
		COMMON CATION			
ZnS/ZnSe	I	<0.035	0.8	4.7	[40]
ZnTe/ZnSe	II	-0.67	1.1	7	[41]
ZnTe/ZnS	II	-0.64	1.9	13	[41]
		COMMON ANION			
ZnSe/$Zn_xMn_{1-x}S$	I	0.25	<0.02	0-1	(x=0.77 [42])
CdTe/$Cd_xZn_{1-x}Te$	I	0.325	0.025	0-6	(x=1.00 [43])
CdTe/$Cd_xMn_{1-x}Te$	I	0.71	0.07	0-0.5	(x=0.24 [44])
CdSe/ZnSe	I	?	'Small'	7	[45]
ZnS/CdS	I	?	'Small'	7	[45]

Table 1.5. II-VI semiconductor superlattices studied to date. The lattice mismatch between the components are given in percent. Recent measurements of valence and conduction band offsets are also included (in electron volts). Where alloys are involved the x values used in the measurements are included with the source of the data. All the systems were grown in the zincblende structure, with the [100] axis normal to the epitaxial layer.

that although this law holds for a number of systems there are noticeable exceptions (e.g. ZnSe/ZnTe).

Photoluminescence provides a convenient tool for assessing the band offsets of a new system. However, the accurate measurement of band line-ups requires the use of a combination of techniques and is not so simple. It can be seen from table 1.5 that, previous to the present work, no studies of CdS/CdSe superlattices have been reported. The parameters of this system are therefore of considerable interest.

REFERENCES FOR CHAPTER 1

[1] E.P.Warekois, M.C.Lavine, A.N.Mariano and H.C.Gatos
J. Appl. Phys. 33 (1962) 6901

[2] 'Physics and chemistry of II-VI compounds' edited by M.Aven and J.S.Prener North-Holland publishing, Amsterdam 1967, Chpt 3 pg 124.

[3] J.Sherman Chem. Revs. 11 (1932) 92

[4] F.Keffer and A.M.Portis J. Chem. Phys. 27 (1957) 675

[5] L.C.Greene, D.C.Reynolds, S.J.Czyzak and W.M.Baker
J. Chem. Phys. 29 (1958) 1375

[6] O.Igarashi Jap. J. Appl. Phys. 8 (1969) 642

[7] P.J.Wright and B.Cockayne, J. Cryst. Growth 59 (1982) 14

[8] J.B.Mullin, S.J.C.Irvine and D.J.Ashen, J. Cryst. Growth 55 (1981) 92

[9] M.P.Halsall, J.J.Davies, J.E.Nicholls, B.Cockayne, P.J.Wright and G.J.Russell, J. Cryst. Growth 91 (1988) 135.

[10] R.N.Bicknell, R.Yanka, N.C.Giles-Taylor, D.K.Blanks, E.L.Buckland and J.F.Schetzina Appl. Phys. Lett. 45 (1984) 92

[11] H.Mariette, F.Dal'bo, G.Lentz, N.Magnea, G.Lentz and H.Tuffigo
In press Phys. Rev. B

[12] T.Yao and T.Takedo Appl. Phys. Lett. 48 (1986) 160

[13] E.Jahne and E.Gutsche Phys. Stat. Sol. 21 (1967) 57

[14] J.L.Birman Phys. Rev. 114 (1959) 1490

[15] M. Cardona J. Phys. Chem. Solids 24 (1963) 1543

[16] R.G.Wheeler and J.O.Dimmock Phys. Rev. 125 (1962) 1805

[17] J.J.Hopfield and D.G.Thomas Phys. Rev. 122 (1961) 35

[18] P.Y.Yu and F.Evangelisti Solid State Commun. 27 (1978) 87

[19] G.P.Srivastava, G.P.Mathur, P.C.Kataria and S.Radhey
J. Phys. D 8 (1975) 523

[20] N.Miura, G.Kido and S.Chikazumi Proc. 14th Int Conf. Phys. Semicond. Edinburgh, UK 1978 11209

[21] C.J.Radford, W.E.Hagston and F.J.Bryant J. Lumin. 5 (1972) 47

[22] M.A.Lampert, Phys. Rev. Lett. 1 (1958) 450

[23] D.G.Thomas and J.J.Hopfield Phys. Rev. 128 (1962) 2135

[24] P.J.Dean, Luminescence of crystals, molecules and solutions Edited by F.E.Williams (Plenum press, New York, 1973). p 538

[25] P.J.Dean, R.N.Bhargava, B.J.Fitzpatrick, D.C.Herbert, and C.J.Werkhoven. Phys. Rev. B 23 (1981) 23

[26] J.M.Francou, K.Saminadayar, J.L.Pautrat, J.P.Gauillard, A.Million and C.Fontaine, J. Cryst. Growth 72 (1985) 220

[27] C.H.Henry and K.Nassau, Phys. Rev. B 1 (1970) 1628

[28] see for example H.Imamoto, F.Sato, K.Imanaka and M.Shimura Superlattices and Microstructures 5 (1989) 167

[29] L.Esaki and R.Tsu IBM J. Res. Develop. 14 (1970) 61

[30] see for example 'Quantum mechanics' L.I.Shiff (McGraw-Hill, New York 1955) Chpt II pg 38.

[31] R.C.Miller, D.A.Kleinman, W.A.Nordland and A.C.Gossard Phys. Rev. B22 (1980) 863

[32] H.Jung, A.Fischer and K.Ploog Appl. Phys. A 33 (1984) 97

[33] See for example C.Kittel 'Introduction to solid state physics' (5th Edition John Wiley & sons, New York 1976) chpt 7 pg 191

[34] G.Bastard, Phys. Rev. B24 (1981) 5693

[35] P.Voisin, G.Bastard and M.Voos Phys. Rev. B29 (1984) 935

[36] K.Ploog and G.Dohler Advances in Physics 32 (1983) 285

[37] J.W.Matthews and A.E.Blakeslee J. Vac. Sci. Technol. 14 (1977) 98

[38] D.L.Smith, Solid State Commun. 57 (1986) 919

[39] B.S.Yoo, X.C.Liu, A.Petrou, J-P.Cheng, A.A.Reeder, B.D.McCombe K.Elcess and C.Fonstad, Superlattices and Micro. 5 (1989) 363

[40] N.Teraguchi, Y.Takemura, R.Kimura, M.Konagai and K.Takahashi J. Cryst. Growth 93 (1988) 720

[41] H.Fujiyasu, K.Mochizuki, Y.Yamazuki, M.Aoki, A.Sasaki, H.Kuwabara, Y.Nakanishi and G.Shimaoka Surf. Science 174 (1986) 543

[42] L.A.Kolodzieski, R.L.Gunshor, N.Otsuka, S.Datta, W.M.Becker and A.V.Nurmikko IEEE J. Quantum Elect. 22 (1986) 1666

[43] H.Shtrikman and E.Finkman Superlattices and micro. 6 (1989) 55

[44] S.K.Chang, A.V.Nurmikko, J.W.Wu, L.A.Kolodziejski and R.L.Gunshor Phys. Rev. B37 (1988) 1191

[45] K.P.O'Donnel, P.J.Parbrooke, B.Henderson, C.Trager-Cowan, X.Chen, F.Yang, M.P.Halsall, P.J.Wright and B.Cockayne J. Cryst. Growth in press

[46] K.Shahzad, D.J.Olego and C.G.Van de Walle Phys. Rev. B38 (1988) 1417

[47] J.M.Langer and H.Heinrich. Phys. Rev. Lett. 55 (1985) 1414

[48] S.H.Wei and A.Zunger. Phys. Rev. Lett. 59 (1987) 144

[49] K.Kroemer. Surf. Science 174 (1986) 299

[50] J.O.McCaldin in 'Growth and optical properties of wide-gap II-VI low dimensional semiconductors' (T.C.McGill, C.M.Sotomayor-Torres and W.Gebhardt, Eds) Plenum NY and London (1989), 39.

2 GROWTH AND MICROSCOPY

Introduction

This chapter describes the growth of CdS and CdSe epitaxial material by atmospheric pressure metallo-organic chemical vapour deposition. All the growth was carried out using the facilities of the Royal Signals and Radar Establishment, Great Malvern (R.S.R.E). The surface morphology was also examined at R.S.R.E using both optical and scanning electron microscopy.

CdS and CdSe have been grown previously mainly by vapour phase techniques, as discussed in chapter 1. However, this study is the first detailed investigation of the growth of CdS and CdSe by MOCVD and includes the first reported growth of CdS/CdSe low dimensional structures, although for many electronic materials MOCVD is a well established epitaxial growth technique.

The initial problem was the choice and orientation of the substrate. It is known that CdS and CdSe can grow in either of two crystalline phases, cubic or hexagonal. Clearly any layer which contained more than one phase must contain large extended crystalline defects at the interface between phases (see section 1.2.4). It was therefore desirable that only one phase be present throughout the epilayer and this was found to be dependent on the substrate used.

The effect of growth parameters on the surface morphology was investigated. The surfaces of the material grown by MOCVD are compared to those of material grown by vapour phase epitaxy. In particular the appearance of hexagonal growth features is discussed in connection with growth mechanisms.

In this chapter the principal features of the growth process and the requirements of the reactor and gas flow system are discussed. The choice and preparation of the substrates for the growth of CdS and CdSe is described. Also included in the chapter is a study of the surface morphology of the layers grown. The adaption of the reactor gas-flow system to allow superlattice growth is also outlined.

2.1 Growth system

The use of MOCVD for the growth of electronic grade epitaxial material is well established. The principal advantages of MOCVD over other vapour phase epitaxy techniques stem from the use of an unstable organo-metallic compound as the source of the metallic elements. The reagents are mixed and passed into a reaction vessel where the reaction occurs over the heated substrate. Ideally, this reaction should only occur over the heated parts of the reactor. In this way impurities from the cooler parts of the system are not incorporated into the layer. Further, the use of volatile compounds allows precise control of the flow of reagents into the vessel, enabling the growth of multilayer structures. These aspects dictated the design of the MOCVD growth system.

The choice of reagents used for MOCVD growth is limited mainly by the availability of the high purity compounds. The principal requirements of the reagents are that they should only react at elevated temperatures and that they have adequate vapour pressures. If they react significantly at room temperature, material will be deposited throughout the system making effective growth control impossible. Such prereaction is a well recognized problem in MOCVD. The

other main requirement is that they must be available at high enough purities and not contain any elements which can be incorporated as defects in the layer.

The important features of the reaction vessel are relatively simple. To produce uniform layer thicknesses the reaction vessel should allow an isotropic flow of the reagents over a small heated region holding the substrate. The source of heating should be outside the vessel preventing contamination from heating elements.

2.1.1 Reagents

Table 2.1 lists the compounds commonly used as sources of group II and group VI elements for MOCVD growth [1]; included in the table are some physical properties relating to their suitability as such sources. It is important for the growth of good material to choose the best reagents. In order to do this we must consider the MOCVD growth process. The principal problems associated with MOCVD reagents are (a) prereaction and (b) precondensation. Both can interfere with the growth process. The former can be prevented by choosing reagents which do not react significantly at room temperature. The latter is most simply prevented by using compounds that are sufficently volatile so as not to condense in the pipework.

Previous investigations of MOCVD growth of CdS [2,3,4] have centred on the use of Dimethyl Cadmium and Hydrogen Sulphide. Dimethyl Cadmium (DMC) is already used as a source in the growth of CdHgTe [5] and as such has been in industrial use for some years. As a result DMC has the advantage of being readily available at the required high purities. DMC is a liquid at room temperature and so needs to be conveyed into the vessel by a carrier gas (hydrogen). This can most

Formula	Name	Melting point °C	Boiling point °C	Vapour pressure at 20 °C (torr)
Group II				
$(CH_3)_2Cd$	DMC	-2.4	105.7	28
$(C_2H_5)Zn$	DEZ	-28	118	22.5
$(CH_3)_2Zn$	DMZ	-29.2	44.0	300
$(CH_3)_2Hg$	DMH		92.5	
Group VI				
H_2S	Hydrogen sulphide		Gas at room temperature	
$(CH_3)_2S$	Dimethylsulphide	-83.2	37.3	400
$(C_2H_5)S$	Diethylsulphide	-103.3	92	
H_2Se	Hydrogen selenide		Gas at room temperature	
$(CH_3)_2Se$	Dimethylselenide		54	
$(CH_3)_2Te$	Dimethyltelluride	-10	82	
$(C_2H_5)Te$	Diethyltelluride		137	7

Table 2.1. Physical properties of some common II-VI MOCVD reagents. The missing values are unobtainable.

easily be achieved by a simple bubbler arrangement, as shown in figure 2.1.

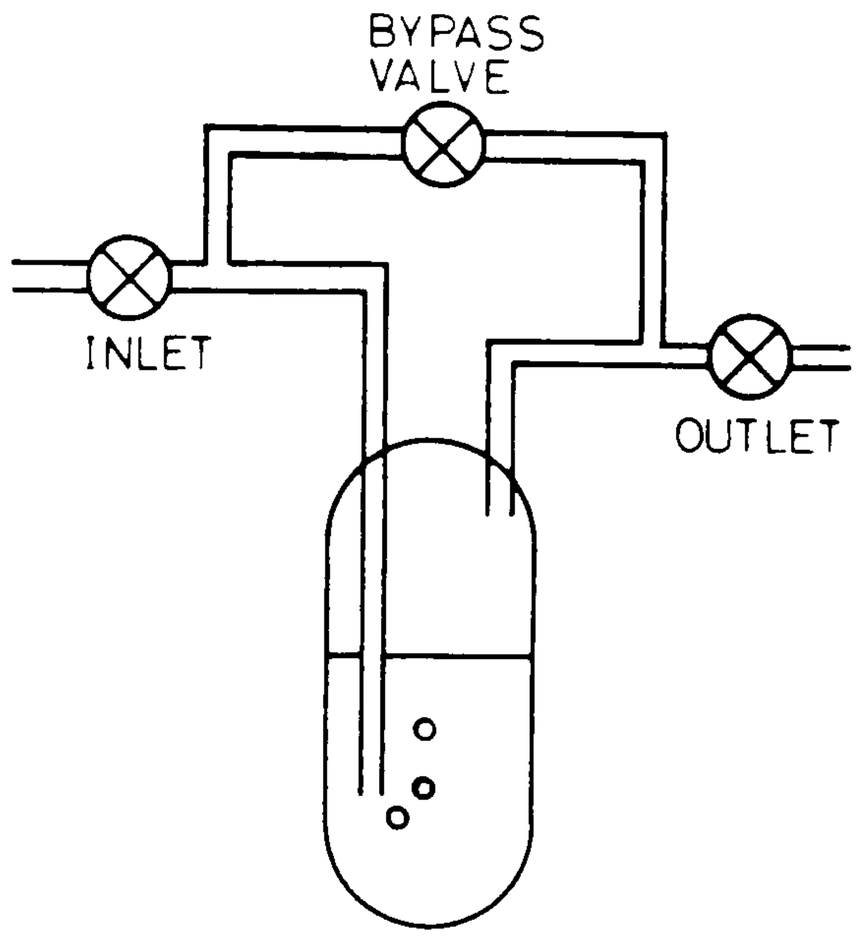

Figure 2.1. Gas bubbler used to convey liquid reagents into the reactor vessel.

There are two gas lines to the bubbler, the input line and the output line. The carrier gas is passed into the input line, through the liquid and out of the output line. The quantity of vapour carried out is essentially proportional to the flow rate of the carrier gas and the vapour pressure of the liquid. In order to produce consistent results the temperature and hence the vapour pressure of the compound should remain constant during a series of growths. If the compound has a high vapour pressure at room temperature it may prove necessary to control the temperature of the bubbler accurately. However, at 20 ^{o}C DMC has a vapour pressure of 28 torr and it proved unnecessary to control the temperature in this case. A high purity DMC bubbler supplied by Alfa products was used for the cadmium source in all growths.

The simplest sulphur and selenium sources available for use are the hydrides, hydrogen sulphide and hydrogen selenide. These are gases

at room temperature and therefore can be conveyed into the reactor from pressurised cylinders. Cylinders of high purity 5% H_2S and H_2Se in hydrogen were used as the sulphur and selenium sources respectively.

The reaction that occurs over the heated substrate can now be elucidated. As mentioned earlier, the reaction should occur only over the heated substrate. The simple (without catalysis) reaction that occurs can be written as [6] :-

$$Cd(CH_3)_2 + H_2S \longrightarrow CdS + 2CH_4$$

One part of this is the pyrolysis of the DMC to form free cadmium. This decomposition assists the lowering of the growth temperatures in MOCVD. It is possible to estimate the minimum reaction temperature by measuring the degree of DMC pyrolysis occuring as a function of temperature. Figure 2.2 shows a series of measurements performed in a reactor similar to the one used in this study with a DMC partial pressure of 7.3 Torr [7]. As can be seen, the decomposition increases between the temperatures of 350-380 ^{o}C. This temperature is high enough to prevent deposition of elemental cadmium in the growth system due to reevaporation. During growth the reactions occuring may be more complex as the pyrolysis is catalysed by the presence of the hydrides [8], which lowers the growth temperature further. This can have important consequences on both alloy growth and the possible formation of cadmium droplets at the surface (see sections 2.4.4). The reaction produces a supersaturated vapour of the growing compound over the substrate. This vapour will condense onto the surface of the substrate producing the desired epitaxial layer.

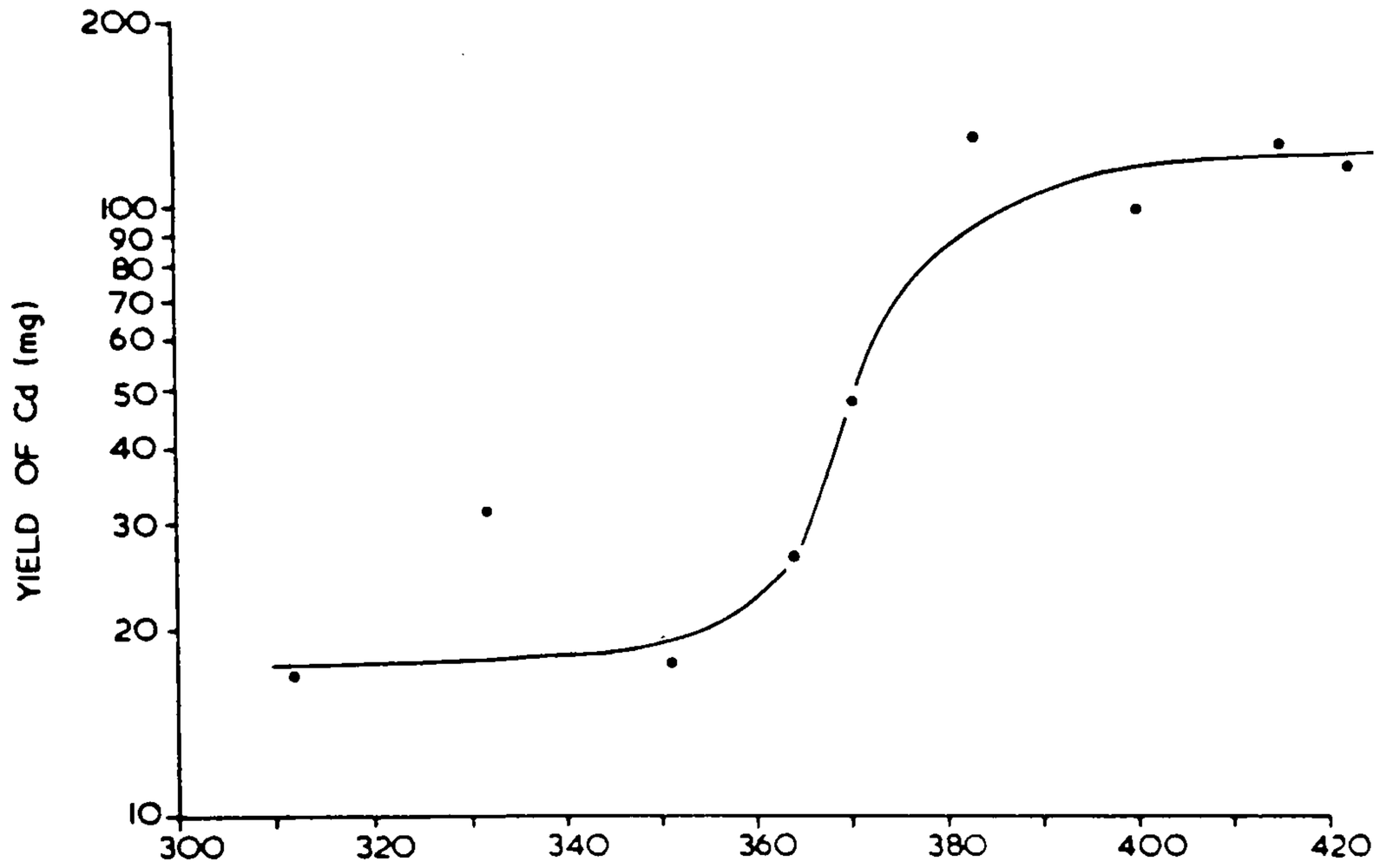

Figure 2.2. Yield of elemental cadmium from the pyrolysis of dimethyl cadmium as a function of temperature. The partial pressure of dimethyl cadmium was 7.3 torr (taken from [7]).

2.1.2 Reactor design

The reactor used for the growth of epitaxial CdS and CdSe is shown schematically in figure 2.3. The design is a development of that described by Bass [9] for the growth of III-V compounds. The reactor consists of a horizontally mounted water cooled silica envelope, inside which the substrate is mounted on a SiC coated graphite susceptor. The susceptor rests in a quartz lining boat which inclines it at an angle to the incoming gas flow and is heated by an external radio frequency coil, the temperature being monitored by a thermocouple and controlled thermostatically. The susceptor can be baked out at high temperatures (>1000 ^{o}C) to outgas and remove any residue remaining from previous growths. The tilting of the susceptor produces more uniform growth. Without the tilt the reaction would proceed most rapidly at the front of the boat producing a non uniform thickness along the direction of flow.

The gases enter the reaction vessel through a mixer nozzle. Experiments were conducted with two types of nozzle. The first was simply a silica glass tube; the second was of the type used for III-V growth and consisted of a blanked off stainless steel tube with fine holes drilled at symmetrical positions in the sides. It was reported previously [10] that careful positioning of the silica tube nozzle was necessary to produce uniform growth. Using the III-V nozzle the growth was found to be less sensitive to the nozzle position and subsequently this nozzle was used for all growth.

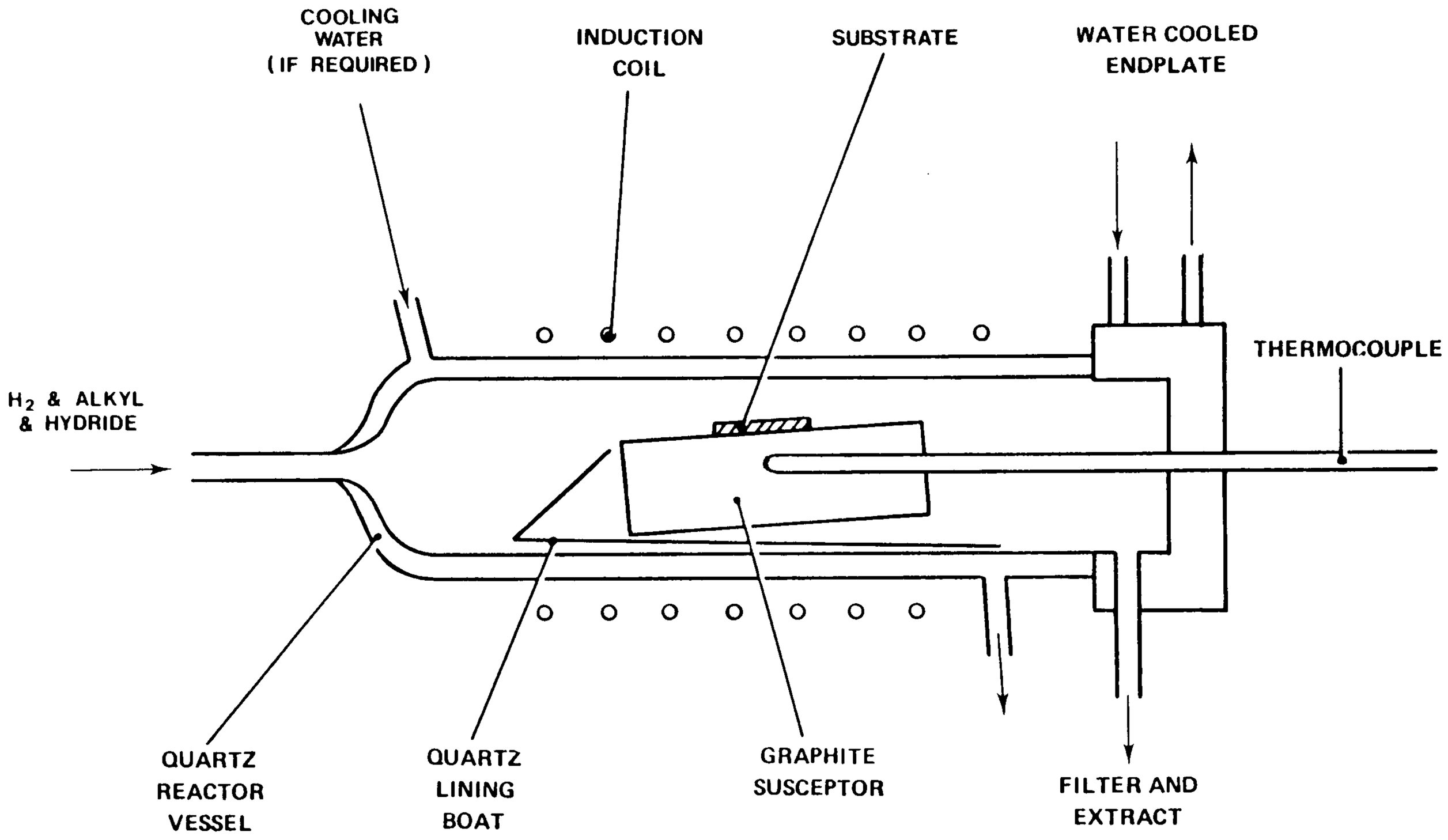

Figure 2.3. Schematic diagram of reactor vessel used for the growth of CdS and CdSe by MOCVD.

2.1.3 Gas flow system

The gas-flow system used to control the flow of reagents into the reactor is shown schematically in figure 2.4. It essentially the same as used for the growth of ZnS and ZnSe by P.J.Wright et al [10]. The reagents were conveyed along stainless steel pipes with mass flow controllers used to control the flow rate of the gases. The hydrides were passed into a manifold with the carrier gas; the alkyl was introduced just before the gases enter the nozzle. Mixing of reagents within the pipework was kept to a minimum to prevent prereaction within the tubing. The carrier gas was high purity hydrogen, diffused through palladium. For the growth of epilayers the carrier gas flow rate was 0.5 litre/min; for the growth of superlattices this was increased to reduce reagent clear time (see section 2.3.2).

2.2 Substrates

2.2.1 Substrate choice

The choice of substrate for the growth of CdS and CdSe was found to be critical to the quality of the produced layers. The structure of CdS and CdSe are normally wurtzite, but they both exhibit unstable cubic sphalerite phases [11]. It was expected that the most defect-free growth would proceed in the wurtzite phase. Previously CdS has been grown by VPE on a variety of substrates including GaAs, Ga, InP, CdTe, CaF_2, ZnTe, SrF_2 and CdS itself [12,12,13,14,15,16,17,17 respectively]. In these previous studies it was found that the substrate orientation influenced the structure of the CdS layer. It was also suggested that the 111 face of cubic compounds provided a good surface for hexagonal growth [18]. Although there are no related studies for the growth of

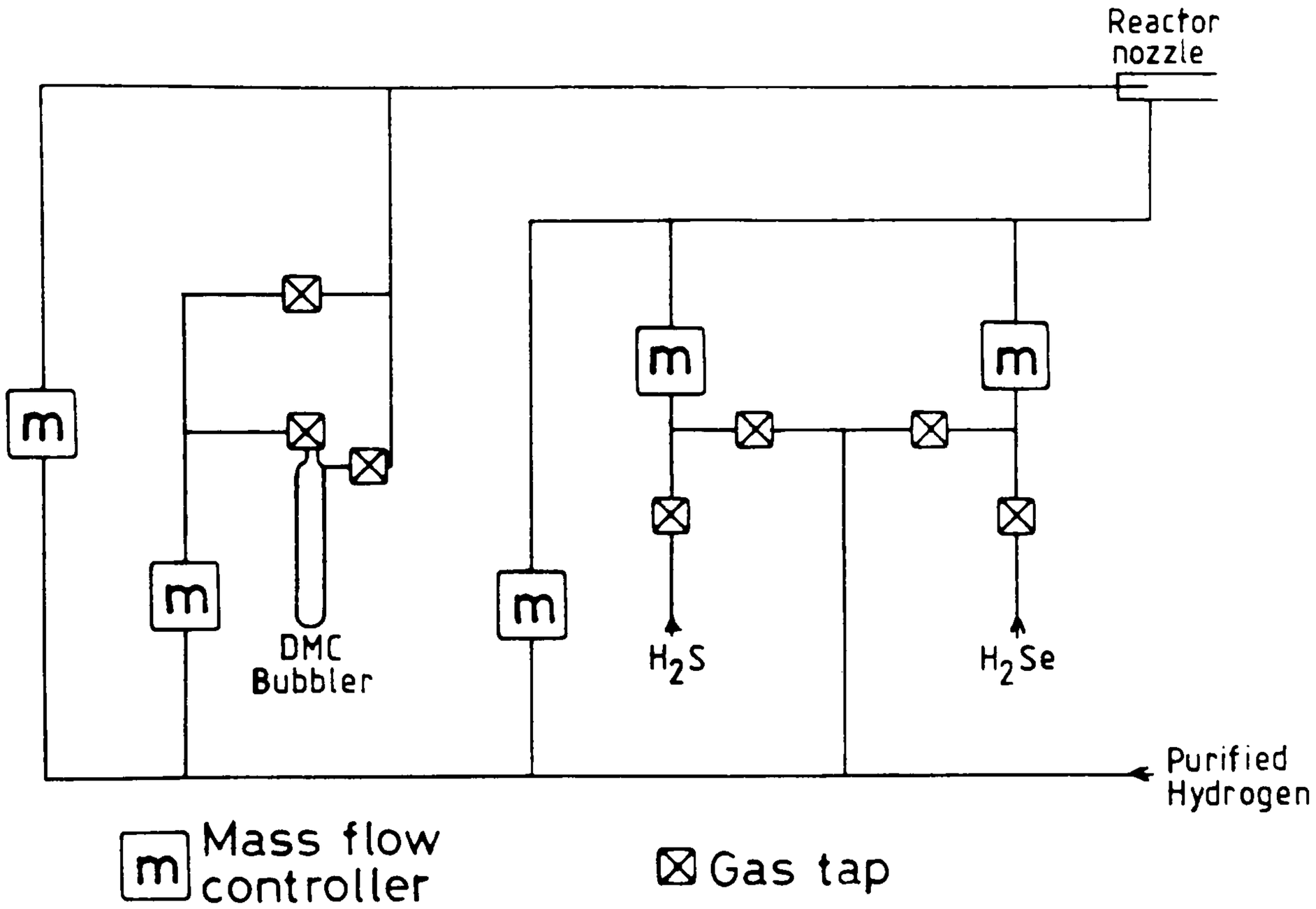

Figure 2.4. Schematic diagram of gas flow system used to control the growth of CdS and CdSe by MOCVD.

CdSe, one would expect a similar dependence on substrate orientation due to the wurtzite structure.

Initially, a range of substrates was investigated to ascertain the best substrate and orientation for wurtzite growth. Figure 2.5 shows the band-gaps and lattice constants of a number of II-VI and III-V compounds. It can be seen that the lattice constants of several of the III-V compounds lie between that of CdS and CdSe. The easy availability and ease of preparation of the III-V substrates made them attractive choices for CdS and CdSe epitaxial growth. The substrates available for this work are listed in table 2.2, along with their band-gaps and the mismatch of the (111) cubic face to that of the (0001) wurtzite face of CdS and of CdSe. Growth was attempted on all these substrates to determine the best surface for CdS and CdSe epitaxy.

2.2.2 Substrate preparation

All the crystalline substrates used were cut from single crystals grown at R.S.R.E by the Czochralski method. The (111) orientations were cut 3^{o} off orientation as is common practice in III-V epitaxial growth to prevent the faceting of the epilayers [13]. The GaAs and InAs were mechanically polished to a mirror finish using standard Syton techniques, so avoiding the pitting that can occur with chemical etches. The InP was chemically and mechanically polished on the (111)B face to a mirror finish. Unfortunately Syton polished InP was not available: this prevented growth on the (111)A face, which pits badly under chemical polishing.

Before loading into the reactor the substrates were cleaned and etched to remove work damage on the surface. For GaAs the approach by Stutius [19] was employed, although a shorter three stage method was

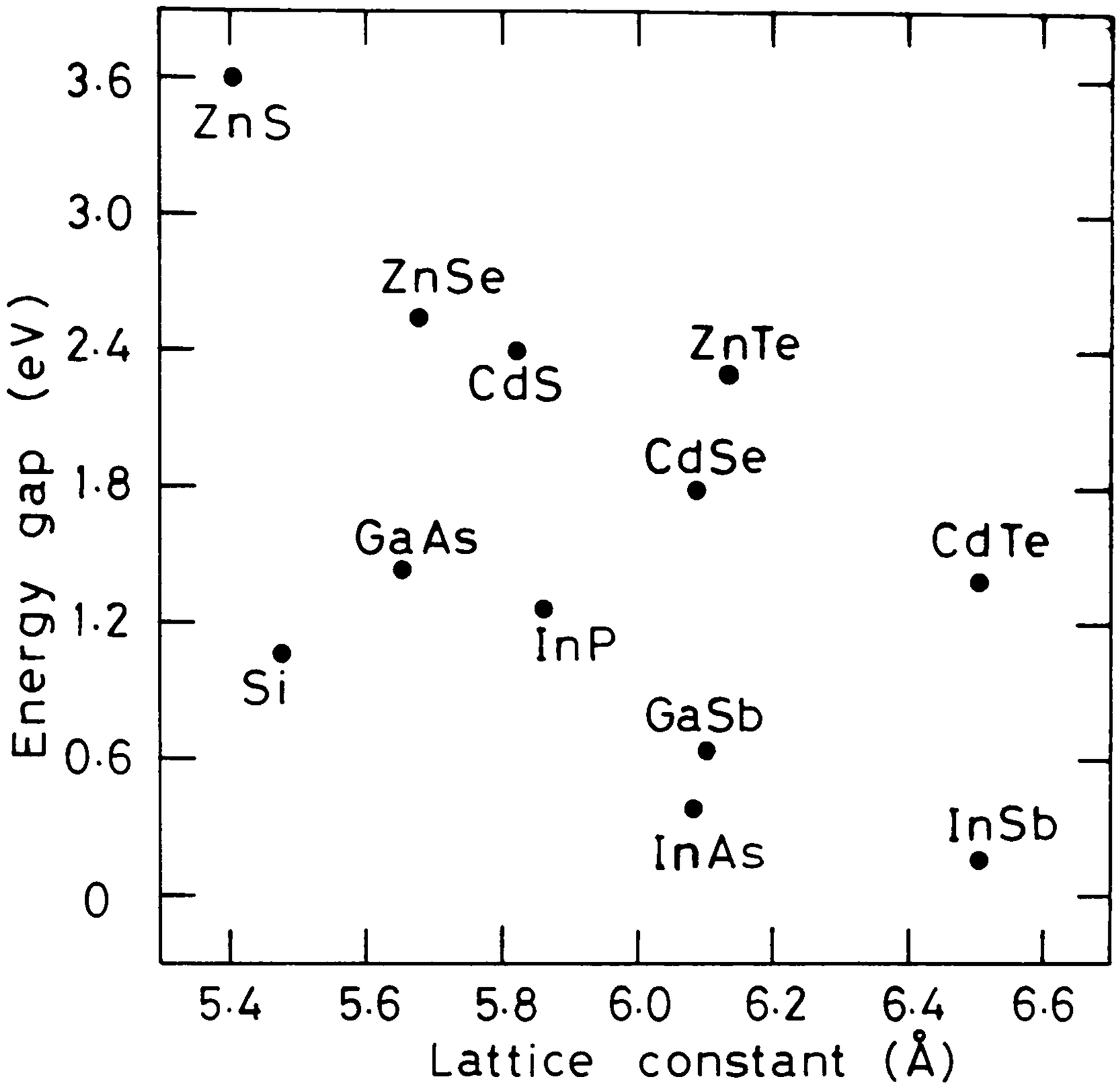

Figure 2.5. Energy gaps and lattice constants of a range of II-VI and III-V semiconducting compounds.

Compound	Orientation	mismatch to 0001 face (in percent)	
		CdS	CdSe
GaAs			
	100		
	110		
	111(B)	3.43	7.09
	111(A)	3.43	7.09
InP			
	111(B)	0.33	3.47
InAs			
	111(B)	-3.75	0.35
	111(A)	-3.75	0.35
Glass			

Table 2.2. Substrates used in this work. The mismatches are given for CdS and CdSe between the 111 cubic faces and the 0001 hexagonal face, a negative sign indicates the substrate has a larger lattice parameter than the epilayer.

used. Initially the substrate was degreased in boiling propan-2-ol and blown dry. It was then etched in a 5:1:1 solution of H_2SO_4:H_2O_2:H_2O at 40 ^{o}C for 5 minutes and washed thoroughly in deionised water. Finally, the substrate was again washed in boiling propan-2-ol, blown dry and loaded into the reactor.

This process was found to be adequate for the (100),(110) and (111)B orientations. However, the (111)A orientation was found to pit under these etching conditions. It was suggested that a faster, hotter etch would be more uniform. As a result the etching condition was altered to 1 min in boiling 5:1:1 solution which successfully stopped the pitting without any apparent reduction in the epilayer quality.

The InP and InAs were prepared in a similar fashion, but were etched in 5% bromo-methanol solution at 40 ^{o}C for 2 minutes. The glass was simply washed in boiling propan-2-ol. The appropriate substrate preparations were found to be satisfactory for all growths.

2.3 Crystal growth

2.3.1 Epilayer growth

The following procedure was adopted for a typical epilayer growth: the substrate was prepared as described above and placed at the centre of the susceptor inside the reaction vessel, which was then clamped in position in the system. The system was sealed and the carrier gas flow increased to approximately 0.5 litres/min as monitored on the exhaust line. The cooling water was switched on to both the vessel and the endplate. After the vessel had been flushed through with the carrier gas the R.F coil was switched on and any bakeout of the substrate performed. The GaAs was baked out at 500-550 ^{o}C for 5 mins in hydrogen.

The InAs was not baked out as the decomposition temperature is too low. The InP also decomposes at low temperature; however a bakeout at 400 ^{o}C under hydrogen sulphide was attempted with some growths, as suggested by Bettini at al [20]. After bakeout, the temperature was reduced to the growth temperature (T_g) and the hydride flushed through the vessel before the alkyl was introduced to start the growth.

All growth was conducted with the hydride in excess. In this way the growth can be controlled accurately by the alkyl flow and no deposition of elemental cadmium from DMC pyrolysis should occur. Typical flow rates were 50 cc/m hydride and 10 cc/m through the DMC bubbler.

After growth the reagents were flushed from the vessel and the epilayer was removed. The vessel was demounted and etched in aqua regia. Periodically the susceptor was heated to high temperature (1000 ^{o}C) to prevent the build up of reaction deposits.

2.3.2 Superlattice growth

The properties of the CdS/CdSe superlattices, and the structures grown, are discussed in chapter 4. Here only the modifications to the growth system required for their growth are described. Superlattices were grown by simple switching of the flows, growing a layer of CdS followed by a pause to allow the reagents to clear and then a layer of CdSe. It is required that this be repeated a large number of times, both to increase the signal obtained by assessment techniques such as photoluminescence and to assist theoretical work to interpret the electronic states. To allow this, the principal requirement is a fast gas flow through the reactor vessel with computer control of the switching system to provide consistent and precise growth period

control in the structures.

The gas flow system was adapted to allow 7 litres/min flow through the vessel and up to 0.5 litres/min along the hydride line alone. This was achieved by use of a fast gas manifold system [21]. In this system the gases can be switched either to vent or into the reactor by valves mounted on the manifold, providing the fastest possible switching of the reagent gases. The capacity of the reaction vessel is approx 1 litre. Thus, with 7 litres/min of carrier gas flowing through, a clear time of 10-30 seconds should be adequate. Experimentally a clear time of 30 seconds was found to produce good quality interfaces. A computer control system was used to control the gas flow system as described in reference 21.

2.4 Microscopy

2.4.1 CdS epilayers

The morphology of the all the epilayers grown was examined by optical microscopy. For this study the primary concern was to produce the smooth surfaces necessary for superlattice growth. Initially a series of CdS layers were grown at 300 ^{o}C on the three orientations of GaAs (100),(110) and (111)A. A relatively high growth rate of 5.1μm/hr was used allowing thick layers to be produced for cross sectional viewing of the epilayers. In the event it was found that the CdS grew polycrystalline on all these substrate orientations other than on the (111)A orientation of GaAs. Figure 2.6 shows two cross sectional views of MH3c and MH3a, two 8 μm CdS epilayers; the upper view is on GaAs (111)A the lower view on (100) GaAs. The polycrystalline nature of the latter is obvious. The surface of the layer grown on GaAs (111)A was of matt appearance and under the microscope showed a very rough surface. After this initial series, a second series was grown with one third of the growth rate. The substrates used this time were only (100) and GaAs (111)A. These samples showed excellent smooth surfaces on the (111)A surface but were still polycrystalline on the (100) surface. These observations are consistent with the findings of Kuznetsov et al [6] who reported 'mirror-like surfaces' of CdS grown by MOCVD on the (111)A face of GaAs. It is also in agreement with the observations of CVD growth studies for CdS where good epitaxy is observed on this face [18]. Subsequently, CdS layers were also grown on the (111)B face of GaAs and InP; these also showed apparently smooth surfaces.

Previously reported studies of the morphology of CdS epitaxial films centred on the appearance of hexagonal and 'star-like' growth structures [18]. Hexagonal 'flat-top' structures were occasionally

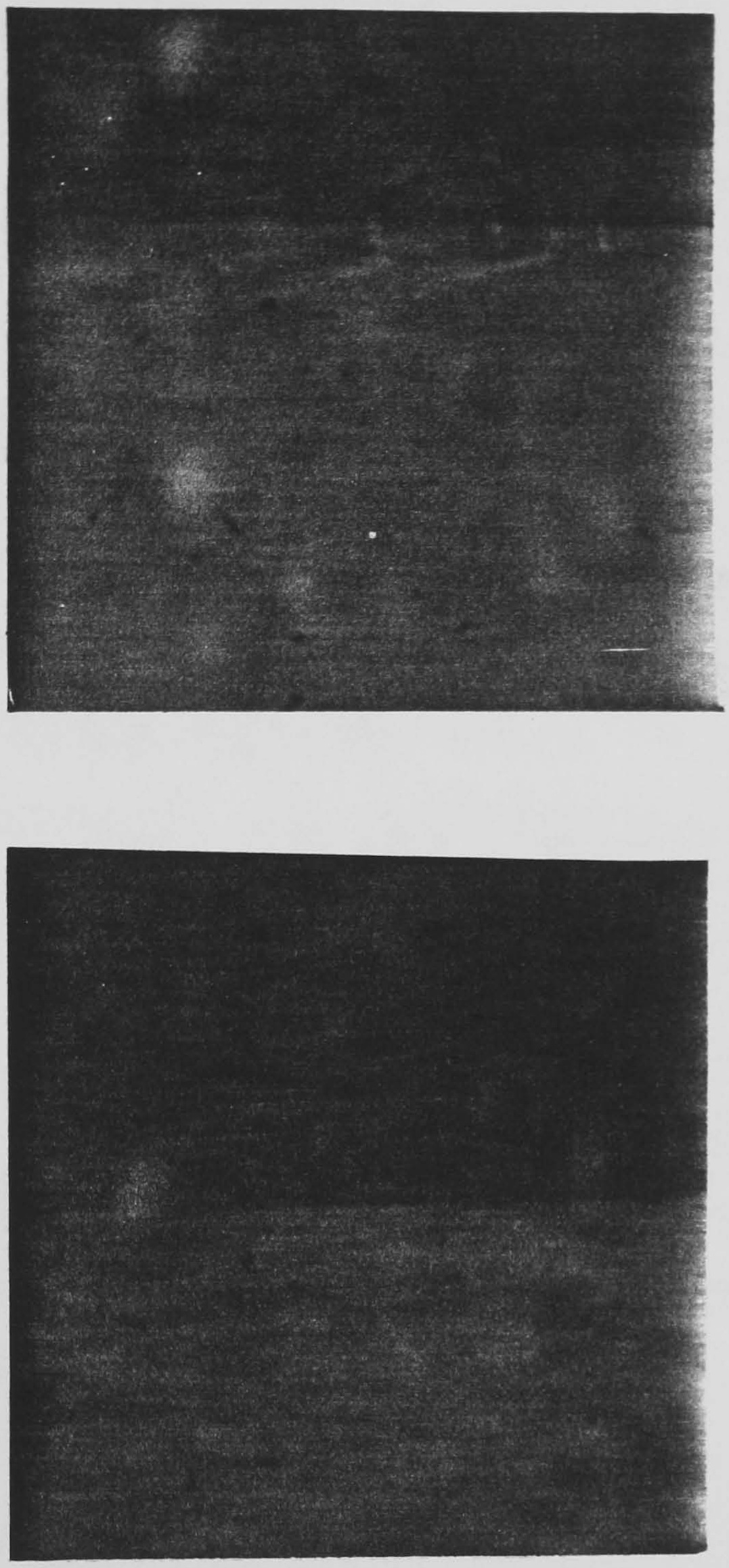

Figure 2.6. Edge on microscope images of CdS grown on GaAs at 300 ^{o}C. The upper image shows an 8μm layer grown on GaAs (100). The lower image shows a layer grown simultaneously on GaAs (111)A.

observed on CdS epilayers and became more frequent for increasing growth rate. Figure 2.7 shows the surfaces of three CdS epilayers grown with growth rates of 3.5μm/hr,2.6μm/hr and 1.3 μm/hr. The growth temperature was 450 ^{o}C (Samples MH134, MH138 and MH86 respectively). It can be seen that the surface is smooth at the lower rate but as the growth rate increases flat topped hexagonal growth features develop. It seems likely that the production of a very large number of such structures results in the matt appearance of the layers grown with very high growth rates. This supports the view of Strehlow [17] that they are the result of the high supersaturation of the vapour over the substrate (see section 2.4.4). The growth temperature had little other effect on the morpology. The surface roughness was found to increase slightly with increasing growth temperature. As T_g is lowered to below 300 ^{o}C the surface starts to show a milky appearence irrespective of the growth rate. The appearance of the hexagonal 'flat tops' seemed relatively independent of T_g. In general, the CdS grown on GaAs (111)A showed smooth surfaces with any growth structures being reduced by the use of a low enough growth rate.

2.4.2 CdSe epilayers

Cadmium selenide was grown on the three GaAs orientations (100),(110) and (111)A initially at 300 ^{o}C at a growth rate of 3.4 μm/hr. As observed in CdS, these epilayers were clearly polycrystalline on orientations other than on the (111)A face. However, unlike the CdS, when the growth rate was reduced the epilayer surface on the GaAs (111)A was not smooth but still showed a high density of hexagonal pyramid structures. Figure 2.8 shows a typical area of sample MH40 showing many pyramid features. There are also a few 'flat top' features

Figure 2.7 (Overleaf). Three microscope images showing the effect of growth rate on the surface morphology of the CdS epilayers grown on GaAs (111)A. The growth rates for each sample are indicated, also given are the image magnifications.

3.5 μm/hr
x530

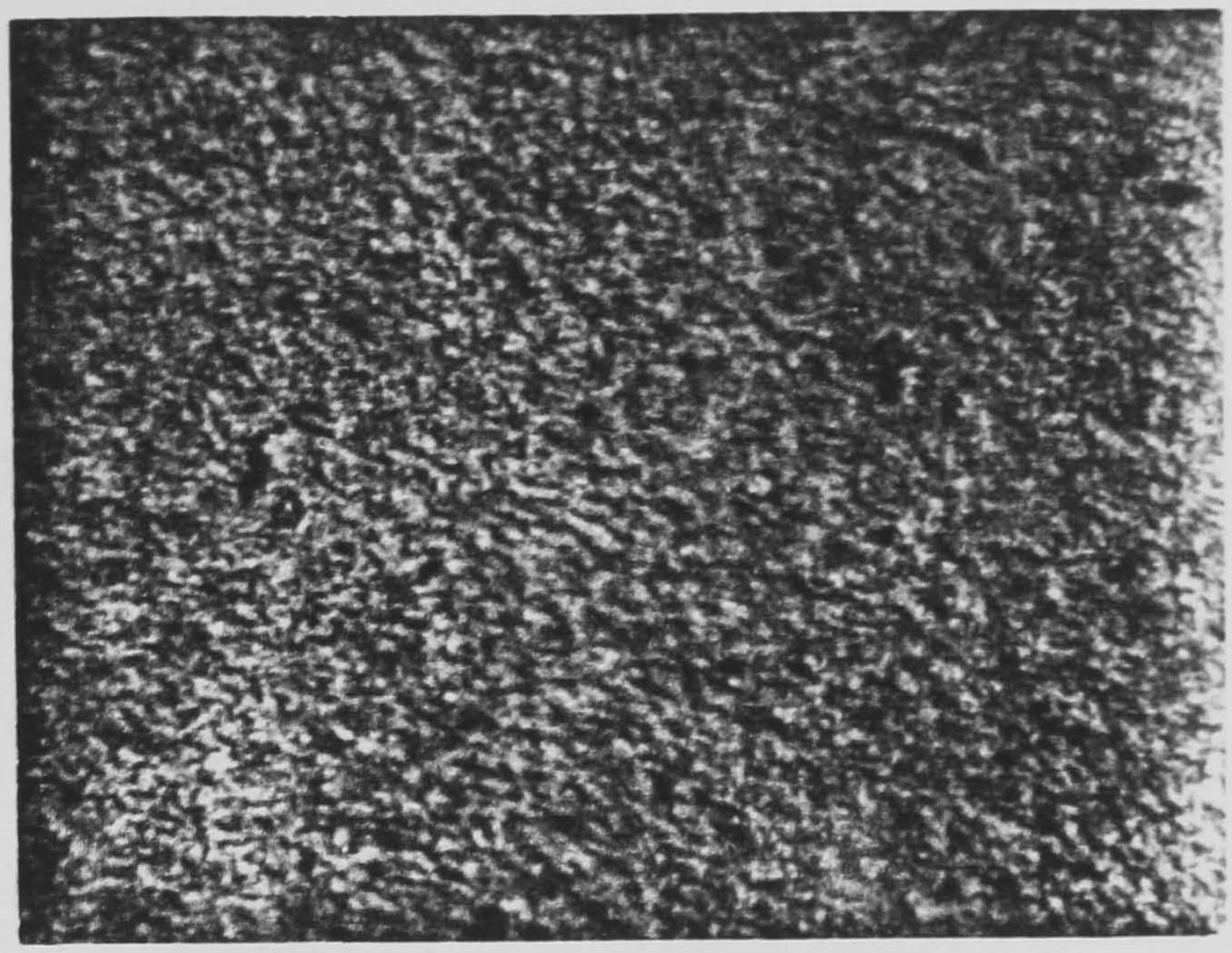

2.6 μm/hr
x530

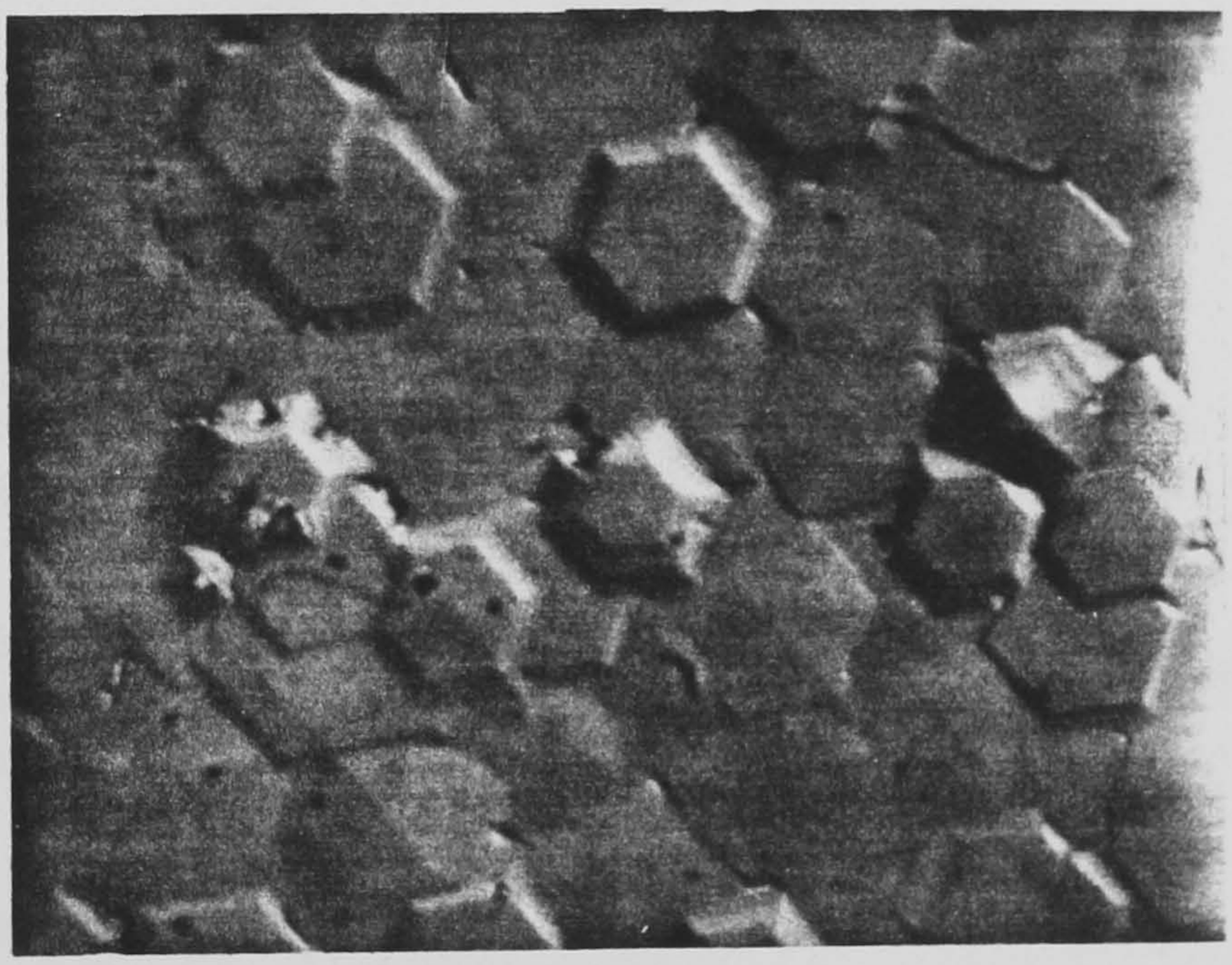

1.3 μm/hr
x 240

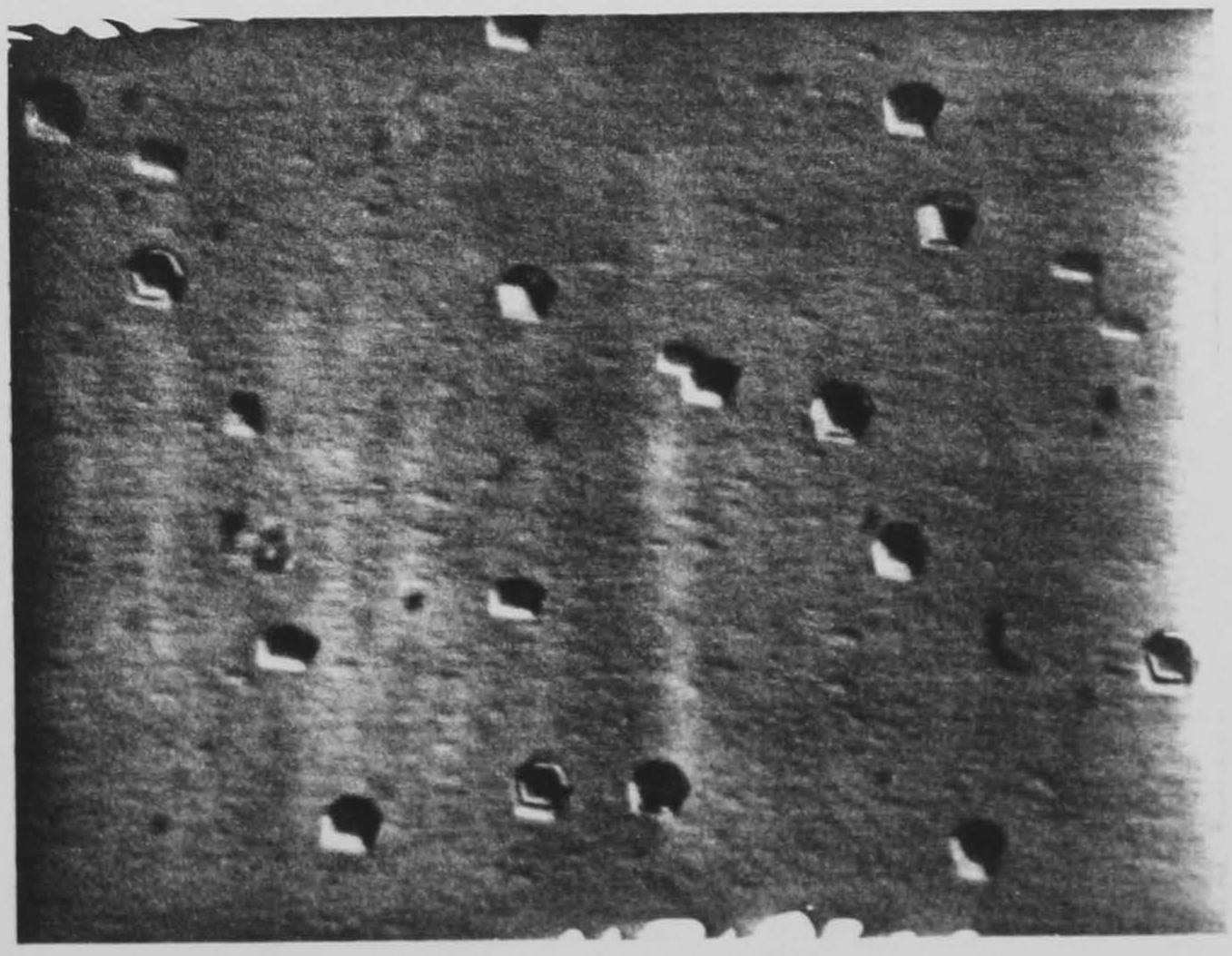

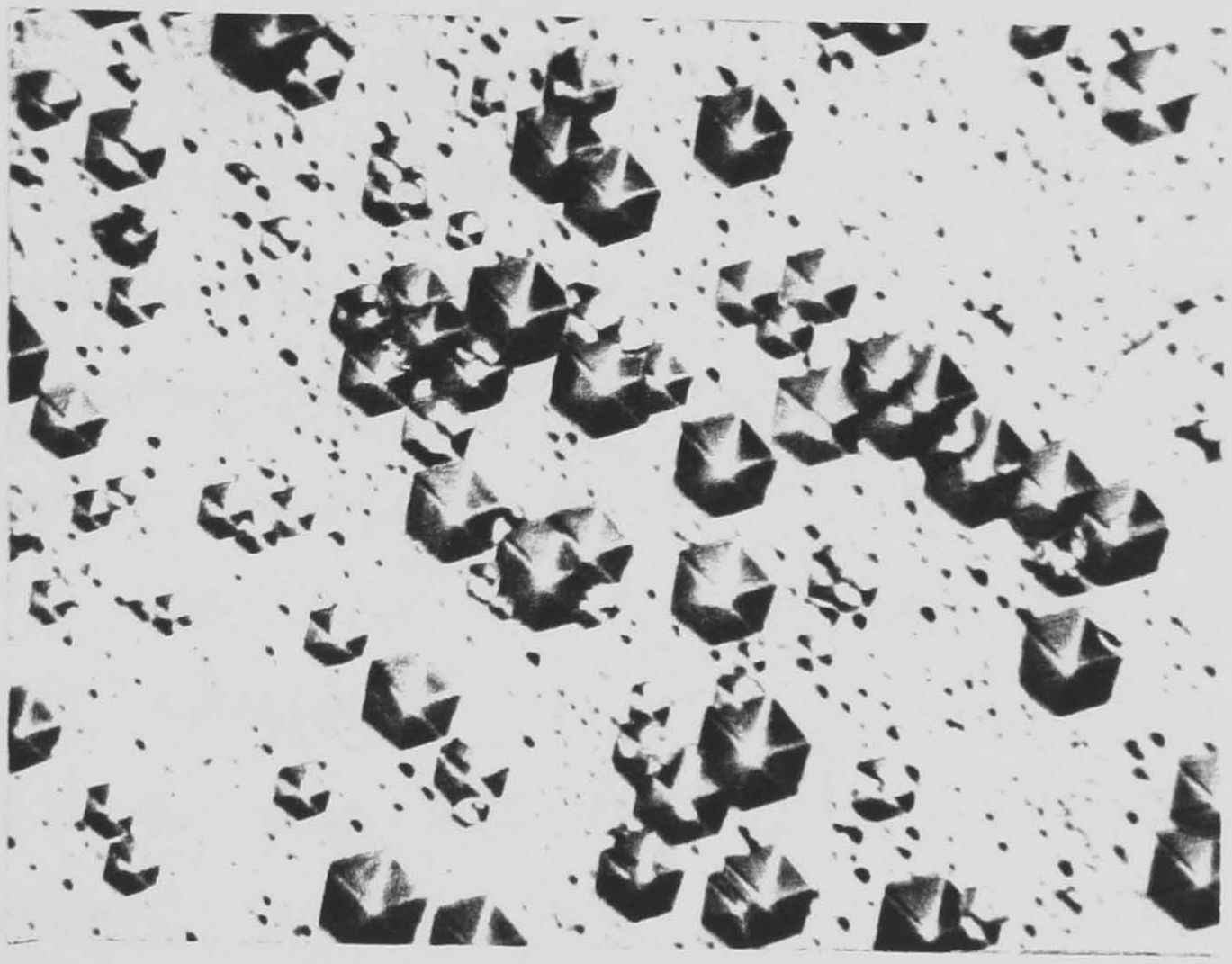

Figure 2.8. Region of CdSe epilayer grown on GaAs (111)A at 350 ^{o}C. The surface displays many hexagonal pyramid features as discussed in the text. The magnification is x530.

as described for CdS. The surface between these features appears very smooth. Moreover these features were always present irrespective of growth rate, although at high growth rates the granular nature of the surface eventually disguised them. In particular they were present at as low a growth rate as was practicable. To try and eliminate these features T_g was increased progressively. Figure 2.9 shows areas of three samples grown at 350,400 and 450 ^{o}C (MH40, MH42 and MH43 respectively). As can be seen the concentration of pyramids decreases with increasing temperature. However, it can be seen that the surface roughness increases considerably at 450 ^{o}C. InAs (111)A and a CdS buffer layer on GaAs (111)A were tried as alternative substrates for CdSe growth. The epilayer on InAs showed an apparently smooth layer with a slight milky appearance; that on the CdS buffer layer still showed the hexagonal pyramids. The possible origin of the growth spirals is discussed in section 2.4.4.

2.4.3 Superlattices

The superlattices were all grown on CdS buffer layers grown on GaAs 111(A). The surface morphology of these structures was similar to that of the CdS epilayers grown at the same temperature. However, for the structures with large total thicknesses the number of hexagonal flat tops increased. It is possible that the flat tops always form in the superlattice but only when there is sufficent total thickness does it become apparent. A small number of superlattices were grown at lower temperatures (350-400 ^{o}C) before T_g was raised for the reasons given in chapter 4. The low T_g superlattices showed interesting linear features on their surfaces, as shown for MH84 in figure 2.10. These lines occur at an angle to each other of 60^{o}, which suggests cracks along the

Figure 2.9 (Overleaf). Effect of growth temperature on the surface morphology of the CdSe epilayers grown on GaAs (111)A. The growth temperatures are as indicated, also shown are the sample numbers. The magnification is X530.

MH40

350°C

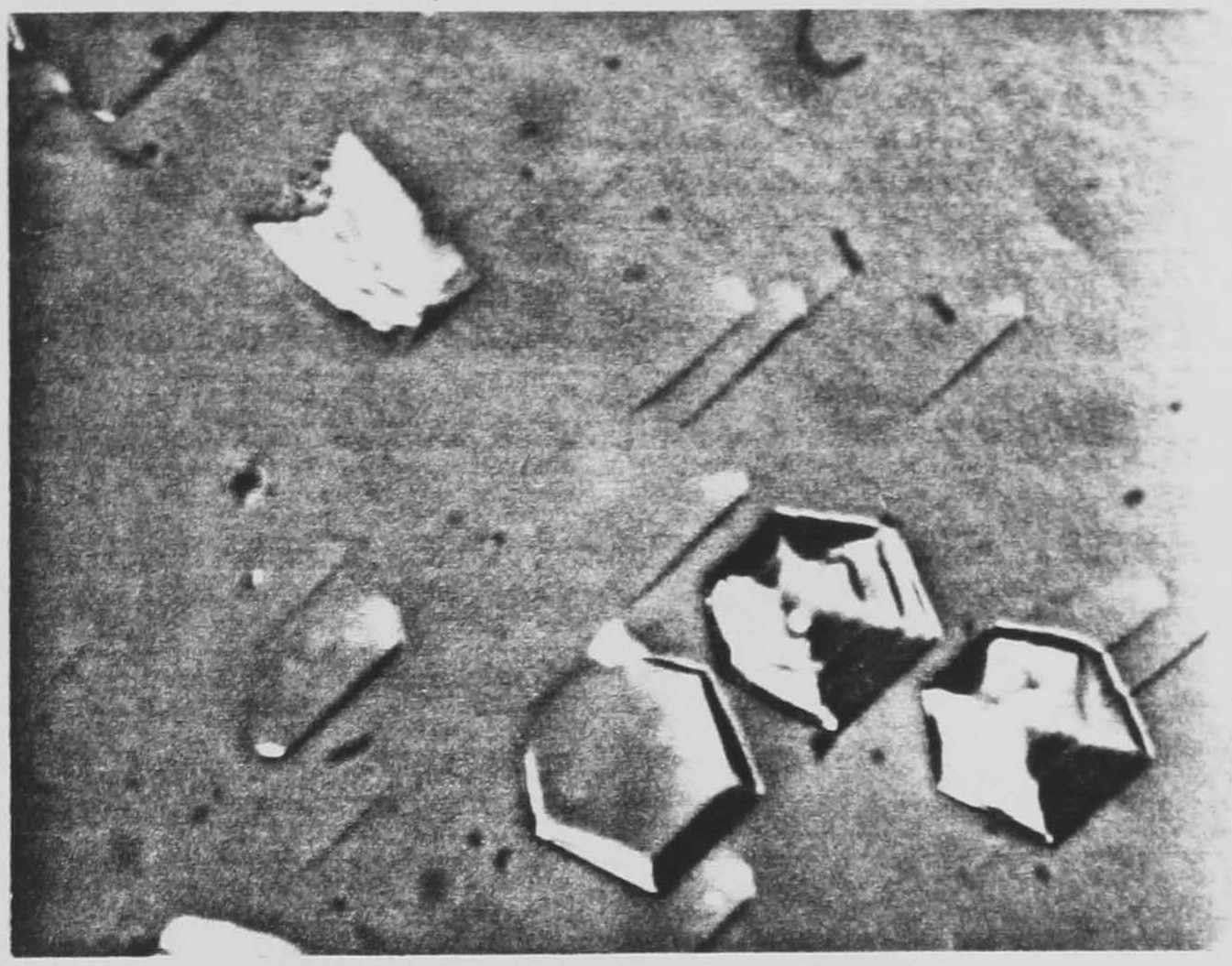

MH42

400°C

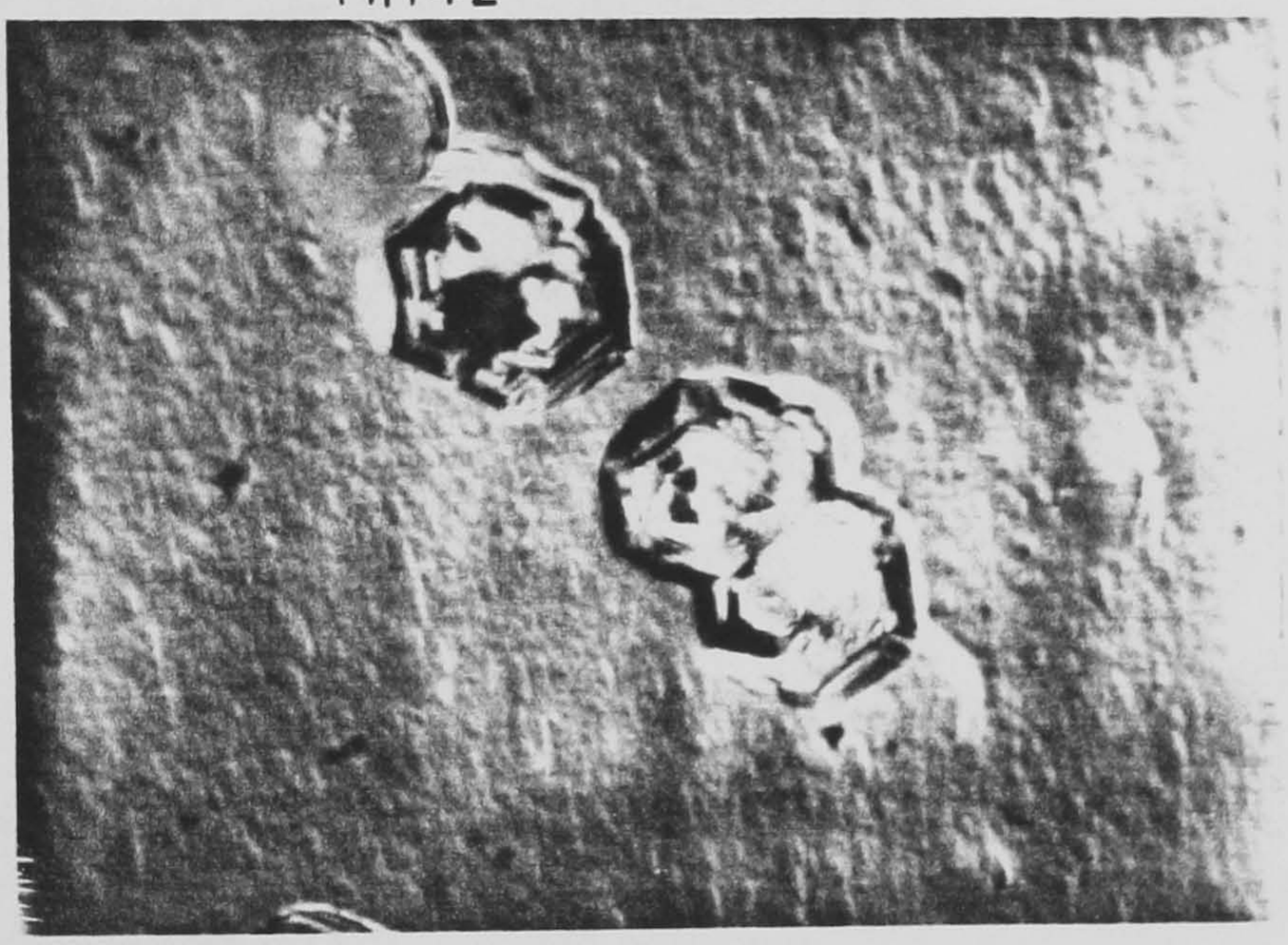

MH43

450°C

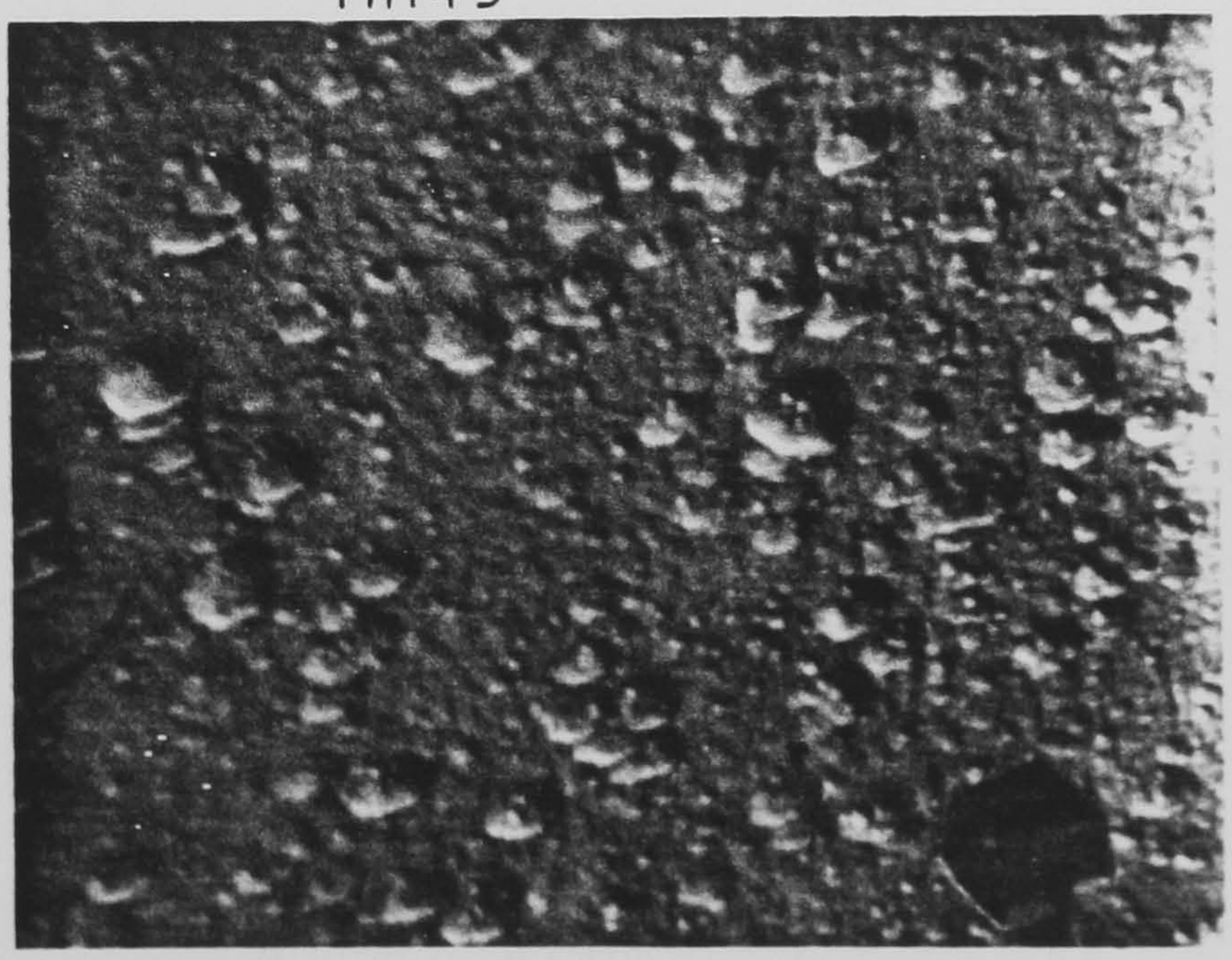

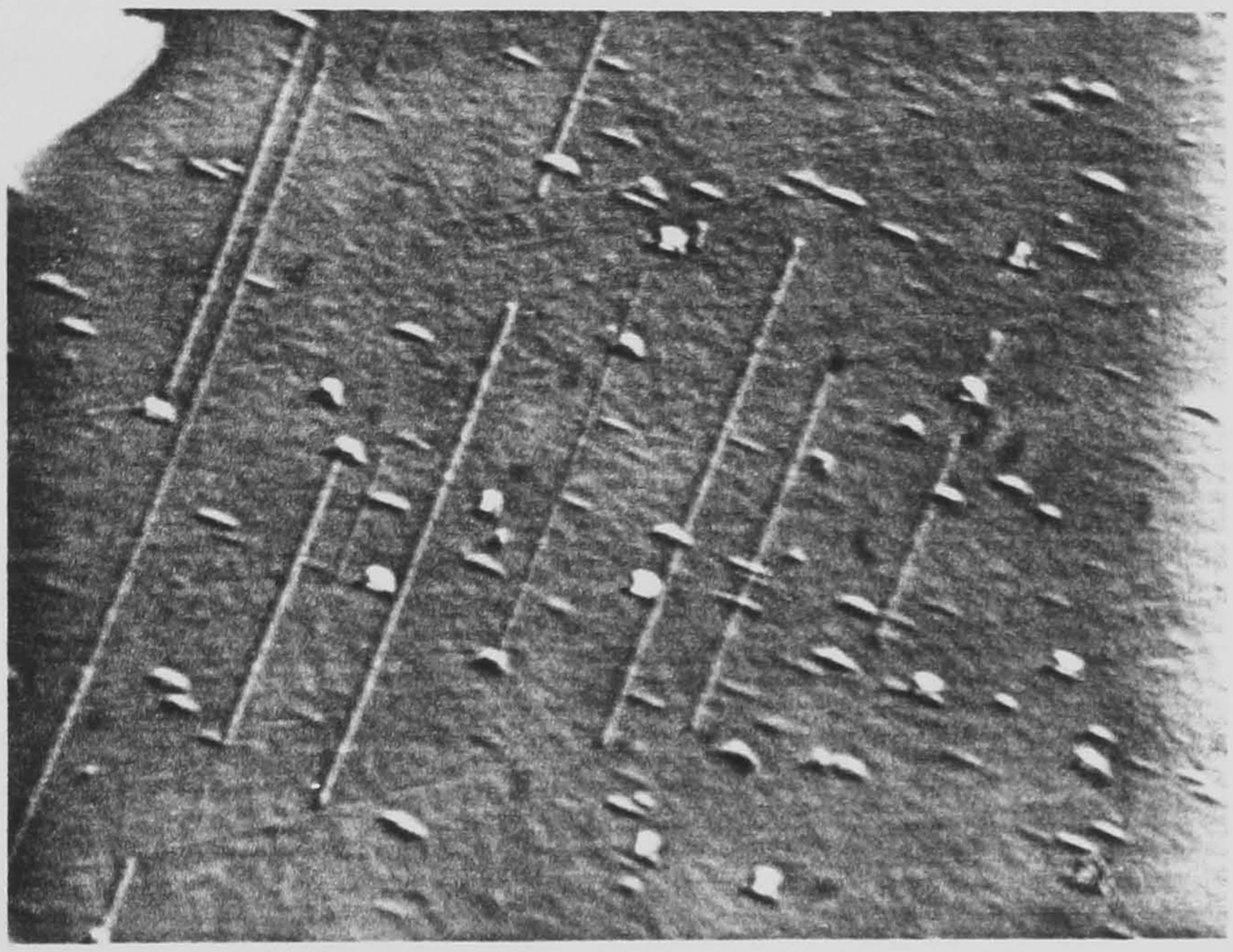

Figure 2.10. Surface of superlattice MH84. The surface shows linear features which occur at 60° to each other. The magnification is x530.

principal axes of the hexagonal structure. Similar cracks have been seen on CdS grown by CVD [22] on GaAs (111)B; there they were attributed to thermal stresses on cooling. The origin of these lines is almost certainly the misfit strain between the superlattice and the buffer layer. Indeed the lines may represent dislocations lying parallel to the interface (see section 3.1). It is interesting to note that these lines were not seen on superlattices grown at temperatures above 400 ^{o}C. The higher growth temperature will reduce the growth rate and this might prevent surface cracks from forming. A simpler explanation for the disappearance of the lines is the much higher quality of the material grown at 450 ^{o}C.

2.4.4 Origin of surface features

The surface morphology of epitaxial CdS has been the subject of several previous studies [18,19,20,21,22,23]. Although there are no similar studies of epitaxial CdSe, the nucleation processes involved have been linked to the wurtzite structure of CdS and as such will probably be common to both CdS and CdSe. Here the surface appearance is discussed with respect to the possible formation of defects in the layer.

All CdSe layers grown on GaAs (111)A displayed surface hillocks. In order to observe these features in more detail, sample MH40 was examined in a scanning electron microscope. MH40 is a 1μm layer of CdSe on GaAs (111)A grown at 350 ^{o}C at a rate of 1μm/hr. Visible light microscopy had shown that this sample displayed particularly well formed surface features. Figure 2.11 shows three views of the sample. The arrows indicate the principle type of features seen (a-d).

Feature (a) is a simple hexagonal 'flat top' structure. These

Figure 2.11 (Overleaf). Three scanning electron micrographs of the surface of MH40 (CdSe grown on GaAs (111)A at 350 ^{o}C). The surface show several different types of growth structure. The reference letters are referred to in the text. The scales are indicated on the images.

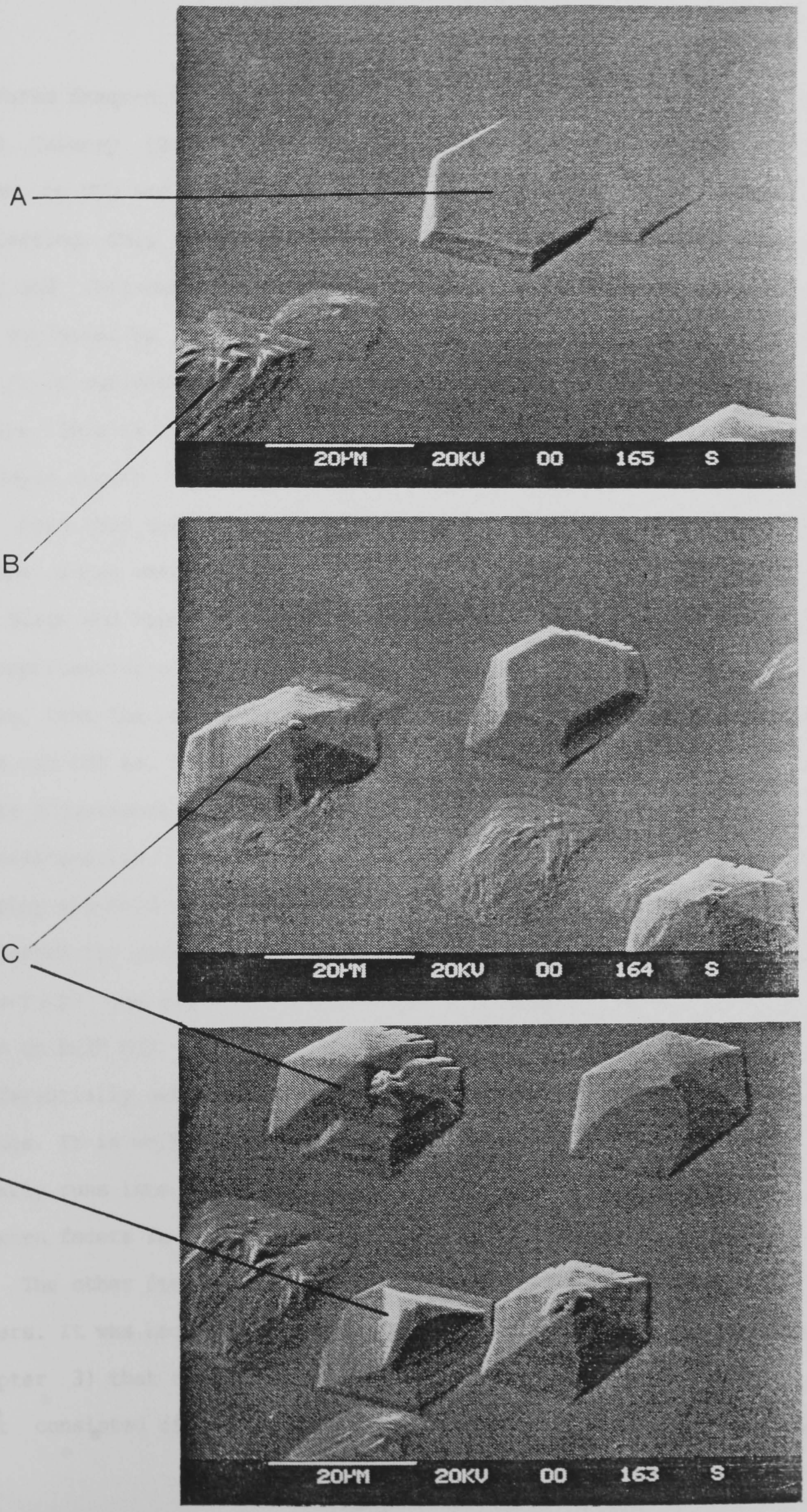
A
B
C
D
20µM 20KV 00 165 S
20µM 20KV 00 164 S
20µM 20KV 00 163 S

features frequently appeared on the CdS epilayers and invariably on the CdSe. Caveney [24] observed similar structures on the surface of CdS grown by CVD and identified them as a natural result of wurtzite 2D nucleation. This analysis was supported by the work of both Strehlow [17] and Christmann et al [25]. The formation of these structures can be explained by considering two possible forms of nucleation, 2D and 3D. In 2D nucleation the monolayers are deposited a single monolayer at a time. This is clearly the growth mechanism which is required for good epilayer growth. In 3D nucleation islands occur on the surface which are more than one monolayer thick and may subsequently develop facets at the edges which produce the observed structures. It has been shown by Hirth and Pound [26] that the 3D mechanism requires a higher degree of supersaturation than 2D nucleation. In this study it was noted (see above) that the concentration of these features reduced in both the CdSe and CdS as the growth rate was reduced or T_g was raised. Both these adjustments will have the effect of reducing the degree of vapour supersaturation, which supports the above analysis. The facets clearly display six-fold symmetry and the shape can only be explained if the epilayers are growing in the wurtzite [0001] direction for these structures (as confirmed by RHEED see section 3.2). Similar shapes are seen on bulk CdS crystal [27], where it is observed that nucleation preferentially occurs on the $(11\bar{2}0)$,(0001),$(10\bar{1}0)$,$(1\bar{1}00)$ and equivalent planes. It is worth noting that the 'flat top' in figure 2.11(i) clearly runs into the smooth layer, and consequently the layer in between facets is likely to be wurtzite as well.

The other features b–d were in general only seen on the CdSe layers. It was known from RHEED measurements and photoluminescence (see chapter 3) that the CdSe (including MH40) was of poor quality and in fact consisted of a mixture of the cubic and hexagonal phases as well

as polycrystalline material. In the light of this evidence the origins of features b–d were expected to be crystalline defects; their absence from CdS epilayers supports this view.

Feature b was common on the CdSe at all growth temperatures. It consists of a raised square or rectangular region of increased surface roughness. There is some indication on the top of these structures of three-fold symmetric 'star-like' hillocks (best seen on figure 2.11(iii)). Igarashi [22] observed similar hillocks (although larger and more clearly defined) on CdS grown on GaAs (111)B by evaporation, and attributed them to cubic CdS epitaxy. Such features are often seen on cubic materials grown on (111) orientated cubic substrates and these features bear a similarity to hillocks seen on CdTe grown homoepitaxially along the [111] axis [14]. In this case the roughness of the surface and the lack of any clear structure suggests these features may be regions of polycrystalline cubic growth. The obvious crystalline nature of the rest of the layer makes this explanation the most satisfactory.

Feature c is a hexagonal pyramid feature with an irregular peak. This structure was also observed in references [22] and [23] on epitaxial CdS. Christmann et al showed that these structures have a different crystallographic orientation to the rest of the epilayer (in contrast to the flat top structures) and suggested that hexagonal twins formed around cadmium droplets as their cause. The presence of the droplets induces stacking faults which, due to their high energy of formation in CdSe, produce twins. It was noted throughout growth that the selenide exhibited a much higher degree of prereaction than the sulphide, as shown by thick deposits of material on the reactor walls. It was stated in section 2.1.1 that hydrides could catalyse the pyrolysis of the DMC and this would lead to prereaction. If this is the

case then, during growth of the selenide, the production of cadmium droplets at the surface is possible. The droplets could thus lead to stacking faults and a series of different crystal defects including twins. In support of this assertion, it has been shown that the triangular growth pyramids observed in some III-V homeoepitaxy on the (111) face are cation-rich twins and probably form around cation droplets. The most notable cases are GaAs and GaP [28,29]. The present study could not confirm this identification. However, it was noted that the concentration of the pyramids reduced as the temperature increased. At higher T_g the cadmium atoms will have more energy to move about on the surface and locate at cation sites, reducing the formation of droplets.

Feature d was a rare feature on this sample but is relatively interesting. It appears as a hexagonal pyramid but at the top evolves clearly into a star-like feature. As mentioned above the formation of such three-fold symmetric structures is characteristic of cubic growth. This suggests that the top of this pyramid has changed phase during growth to produce a cubic top. This could be achieved by a twin-like cubic-hexagonal interface (see 3.2.2). This is supported by the observation of Igarashi that, for CVD growth of CdS on GaAs (111)B, the initial growth of CdS was hexagonal but as growth proceeded the cubic phase dominated.

The poor quality of the CdSe surface relative to the CdS is obvious. The cause of this must lie in the growth process. Although there is a greater mismatch for CdSe to GaAs compared with CdS (7% compared to 3.5%) good epitaxy on GaAs has been demonstrated for systems with very large mismatches (for example CdTe [30] with 17%). Moreover, the surface did not improve when the CdSe was grown on a CdS buffer layer on GaAs (111)A. As stated above there is a large degree of

prereaction for growth of the selenide and production of cadmium droplets at the surface is possible. This may cause a large number of stacking defects. Alternatively the cubic phase of CdSe may be more stable, producing growth in a mixture of phases. These possibilities are discussed further in chapter 3.

2.5 Summary

CdS and CdSe epilayers have been grown by MOCVD on a variety of substrates and crystallographic orientations. The reagents used were dimethyl cadmium as the cadmium source and hydrogen sulphide and hydrogen selenide as the sulphur and selenium sources respectively. It was demonstrated that CdS and CdSe could be grown epitaxially on the (111) face of the cubic sphalerite compounds of table 2.1 using the reagents described. It was found that the surface morphology of the layers grown depended on the growth conditions. For CdS it was possible to produce smooth layers on the (111)A face of GaAs. The surface roughness decreases as the growth rate is reduced. The optimum growth rate for CdS as judged by the morphology was approximately 1μm/hr at 350 ^{o}C. In contrast, the surface of the CdSe was always rougher and displayed a series of different growth structures. It was found that the concentration of these structures reduced as the temperature was raised but that the surface roughness also increased. It is suggested that the origin of these structures lies in formation of the cubic form of CdSe accompanied by the possible formation of Cd droplets on the substrate surface. These results are compared with the findings of other workers and are found to be in broad agreement. The growth of CdS/CdSe superlattices by MOCVD was described. The surface morphology

of the superlattices was found to be similar to that of the CdS epilayers.

2.6 Conclusions

From the results in this chapter it can be concluded that it is possible to produce mirror-like epitaxial layers of CdS on GaAs (111)A by MOCVD. The CdSe epitaxial layers grown under similar conditions on GaAs (111)A also exhibit a smooth surface between growth hillocks. The growth hillocks indicate the possible presence of a number of lattice defects in the CdSe epilayers. The CdS and CdSe layers grown on the other substrates do not exhibit the same mirror surfaces, but we cannot conclude that the layers are of poor quality by the morphology alone. In order to determine the exact structure, purity and crystalline quality of the layers more detailed information concerning the structural and optical properties of the layers is required. These properties are studied in chapter 3.

REFERENCES FOR CHAPTER 2

[1] B.Cockayne and P.J.Wright J. Cryst. Growth 68 223 (1984)

[2] H.M.Manasevit and W.I.Simpson, J.Electrochem. Soc 118 (1971) 644

[3] P.I.Kutsnetsov, V.V. Shemet, I.N.Odin, A.V.Novoselova, Dokl. Akad. Nauk SSSR 248 (1979) 248.

[4] A.N.Menster, B.G.Gribov, A.S.Pashinkin and K.V.Zinoviev, Dokl. Akad. Nauk SSSR 204 (1972) 881

[5] see for example J.B.Mullin, S.J.C.Irvine and J.Tunnicliffe J. Cryst. Growth 68 (1984) 214

[6] P.I.Kutsnetsov, V.H.Dvoryankin, V.V. Shemet, I.N.Odin, A.P.Porotikov and A.V.Novoselova, Dokl. Akad. Nauk SSSR 252 (1980) 155.

[7] J.B.Mullin, S.J.C.Irvine and D.J.Ashen, J. Crystal Growth 55 (1981) 92

[8] S.J.W.Price, Comprehensive Chemical Kinetics Vol.4, (Elsevier Amsterdam, 1972) p. 197.

[9] S.J.Bass J. Crystal Growth 31 (1975) 172

[10] P.J.Wright and B.Cockayne J. Crystal Growth 59 (1982) 148

[11] H.Holloway and E.Wilkes J. Appl. Phys. 39 (1968) 5807

[12] W.M.Yim and E.J.Stofko J.Electrochem. Soc 119 (1972) 381

[13] J.L.Shay, S.Wagner, K.L.Bachmann and E.Buehler J. Appl. Phys 47 (1976) 614

[14] G.R.Awan, A.W.Brinkmann, G.J.Russell and J.Woods J. Crystal Growth 85 (1987) 477

[15] J.C.Heyrand and L.Capella J. Crystal Growth 2 405 (1986)

[16] M.Aven and D.M.Cook J. Appl. Phys. 32 (1961) 960

[17] W.H.Strehlow J.Appl.Phys 41 (1969) 1810

[18] M.Weinstein and G.A.Wolff, Crystal Growth (Pergamon, Oxford 1967) p 537.

[19] W.Stutius, Appl. Phys. Letters 33 (1978) 656.

[20] M.Bettini, K.J.Bachmann and J.L.Shay J. Appl. Phys 49 (1978) 865

[21] R.J.M.Griffiths, N.G.Chew, A.G.Cullis and G.C.Joyce Electron Lett. 19 (1983) 988

[22] O.Igarashi Jap. J. Appl. Phys 8 (1969) 642

[23] A.Yoshikawa and Y.Sakai J.Appl.Phys 45 (1974) 3521

[24] R.J.Caveney J.Crystal Growth 2 (1968) 85

[25] M.H.Christmann, K.A.Jones, and K.H.Olsen J.Appl.Phys 45 (1974) 4295

[26] J.P.Hirth and G.M.Pound, Progr.Material.Sci 11 (1963)

[27] J.Woods Br.J.Appl.Phys 10 (1959) 529

[28] B.A.Joyce J. Cryst. Growth 3 4 43 (1968)

[29] A.Y.Cho J. Appl. Phys. 41 782 (1970)

[30] R.N.Bicknell, R.Yanka, N.C.Giles-Taylor, D.K.Blanks, E.L.Buckland and J.F.Schetzina Appl. Phys. Lett. 45 (1984) 94

3. OPTICAL AND STRUCTURAL CHARACTERIZATION OF CdS AND CdSe EPITAXIAL LAYERS

Introduction

In general the goal of crystal growth is to produce material as free from crystal defects and impurities as is possible. In order to assess the effectiveness of an epitaxial growth technique it is therefore necessary to determine the quality of the material grown. There are two areas in which information is required to allow an assessment of the epilayer quality: the structural perfection of the crystal lattice and the presence of impurity atoms within that lattice. These considerations govern what is often referred to as the 'quality' of the material.

There are a large number of characterization techniques that can be applied to epitaxial layers. These techniques can provide a variety of information concerning the structural, optical and electrical properties of the material. For the purpose of optimizing the growth conditions it was desirable that the techniques used be easy to interpret and non-destructive. It was decided to assess the epilayers principally by luminescence techniques with electron diffraction being used to study the crystal structure of the layers.

In this chapter the characterization of the epilayers is divided into three sections. The first section lays the theoretical groundwork for wurtzite epitaxial layers. The relaxation of strain within epitaxial layers is discussed and the effects of that strain on the band structure of CdS and CdSe calculated. The second section describes the structural assessment of the layers using Reflection High Energy Electron Diffraction (RHEED). In the third section the use of optical

techniques is described. The low temperature photoluminescence spectra of all the epilayers were recorded. The spectra are intepreted and conclusions are drawn as to the most suitable substrate and growth conditions for the two compounds. Also in this section, the growth of the ternary alloy $CdS_{1-x}Se_x$ is described and reflection spectroscopy and photoluminescence are used to obtain the values of x for a series of such alloys.

3.1 Theory of strained epilayers

3.1.1 Introduction: critical thickness

When an epitaxial layer of one crystalline solid is grown on to a substrate of another which possesses a different lattice constant there is said to exist between the layer and substrate a 'lattice mismatch'. It has been found that, provided the mismatch is small enough, the initial atomic monolayers will grow commensurately to the substrate, the layer being strained to the substrate lattice constant. As the layer grows thicker, dislocations will form to relieve the strain, until the layer material has the same lattice constant as that of its bulk value.

It was shown by Van der Merwe [1], by strain energy considerations, that the relaxation of the strain occurs after some critical thickness has been reached. Subsequently the existence of such a critical thickness was verified for a number of strained systems (for example ZnSe/GaAs and Ge/Si [2,3]). Below this thickness the strain in the layer will have important effects on its band structure. Moreover, this critical thickness will have special relevance in chapter 4 where the properties of CdS/CdSe superlattices are discussed. Hence, before

proceeding to study the epilayers, we consider here the theoretical value of this thickness for the system studied. Such a calculation allows us to obtain a feel for the magnitude of the critical thickness in our system and whether we might expect to observe strain effects or not. In addition, deformation theory is used to calculate the effects of biaxial strain on the band structure of the wurtzite epitaxial layer.

3.1.2 Calculation of critical thickness

The approach taken to calculate h_c (the critical thickness) is, in principle, simple. It is required to determine the layer thickness at which the tension along the dislocation line exactly balances the force exerted on the dislocation line by the stress generated in the layer by lattice mismatch. As the layer thickness increases so does the stress until the critical thickness is reached and dislocations form.

A number of authors attempted to solve the critical thickness problem by areal strain energy arguments, notably Van der Merwe [1],Matthews [4] and People and Bean [5]. The approach of Van der Merwe was derived from energy considerations and simply balanced the interfacial energy between epilayer and substrate by the strain energy stored in the strained epilayer. In contrast, the approach of Matthews was by mechanical equilibrium, considering different arrays of dislocations and the associated energy densities. When the rate of change of the total energy with thickness (where total energy is the sum of dislocation and strain energy densities) is zero then the critical thickness has been reached.

The approach of People and Bean is an energy balance one. It has been found to give excellent agreement with experiment and it is this

theory, modified slightly for the wurtzite case, that is discussed here. In this approach it is assumed that h_c can be determined by energy considerations alone. This implies that h_c can be derived by simply equating the areal strain energy to the areal energy associated with the formation of a dislocation. For the wurtzite structure the dislocation with the lowest formation energy is the screw dislocation [6]. The energy per unit area associated with an isolated screw dislocation a distance h from a free surface in a compound is given by

$$\varepsilon_D = (Gb^2/8\pi\sqrt{2}a)\ln(h/b) \qquad \text{(i)}$$

where G is the shear modulus, b is the magnitude of the burgers vector and a is the lattice constant. The strain energy per unit area contained within a strained epilayer of thickness h is given by [7].

$$\varepsilon_h = 2G(1+v)/(1-v)hf^2 \qquad \text{(ii)}$$

Where v is Poisson's ratio and f is the mismatch. To obtain the critical thickness h_c in the People and Bean approach equations (i) and (ii) are simply equated to give

$$h_c = (1-v)(b^2/a)/[(1+v)(16\pi\sqrt{2})f^2]\ln(h_c/b) \qquad \text{(iii)}$$

The values of the constants v,G and a can be obtained in the literature [8]. In a wurtzite epilayer growing with the c-axis vertical the simplest screw dislocation lying parallel to the interface will be orientated along the $[1\bar{2}10]$ direction, with a burgers vector $[\bar{2}110]$ [6]. This gives us a value for the magnitude of the burgers vector b given by

$$b = a\sqrt{3} \qquad \text{(iv)}$$

This takes the value of 7.1 and 7.4 angstroms for CdS and CdSe respectively. Equation (iii) was solved numerically to provide a theoretical estimate for the value of h_c. The values of Possion's ratio used were 0.259 and 0.236 for CdS and CdSe respectively. Figures 3.1 and 3.2 show the calculated critical thicknesses for CdS and CdSe respectively, as a function of mismatch to substrate. It can be seen that h_c is a very strong function of the mismatch. Included on the diagram are dotted lines indicating the mismatches to the principle substrates. Most of the epitaxial layers were grown on GaAs, for this substrate CdS has an estimated critical thickness of 220Å. If this is the case then we would not expect to see large strain effects for epilayers more than a few tens of monolayers thick.

3.1.3 Strain components in an epilayer

In order to investigate the effects of the biaxial strain on the band structure of the epitaxial layer we need to determine the components of the biaxial strain. This is an elementary problem in strain theory and is best solved by use of the wurtzite strain tensor [9] :-

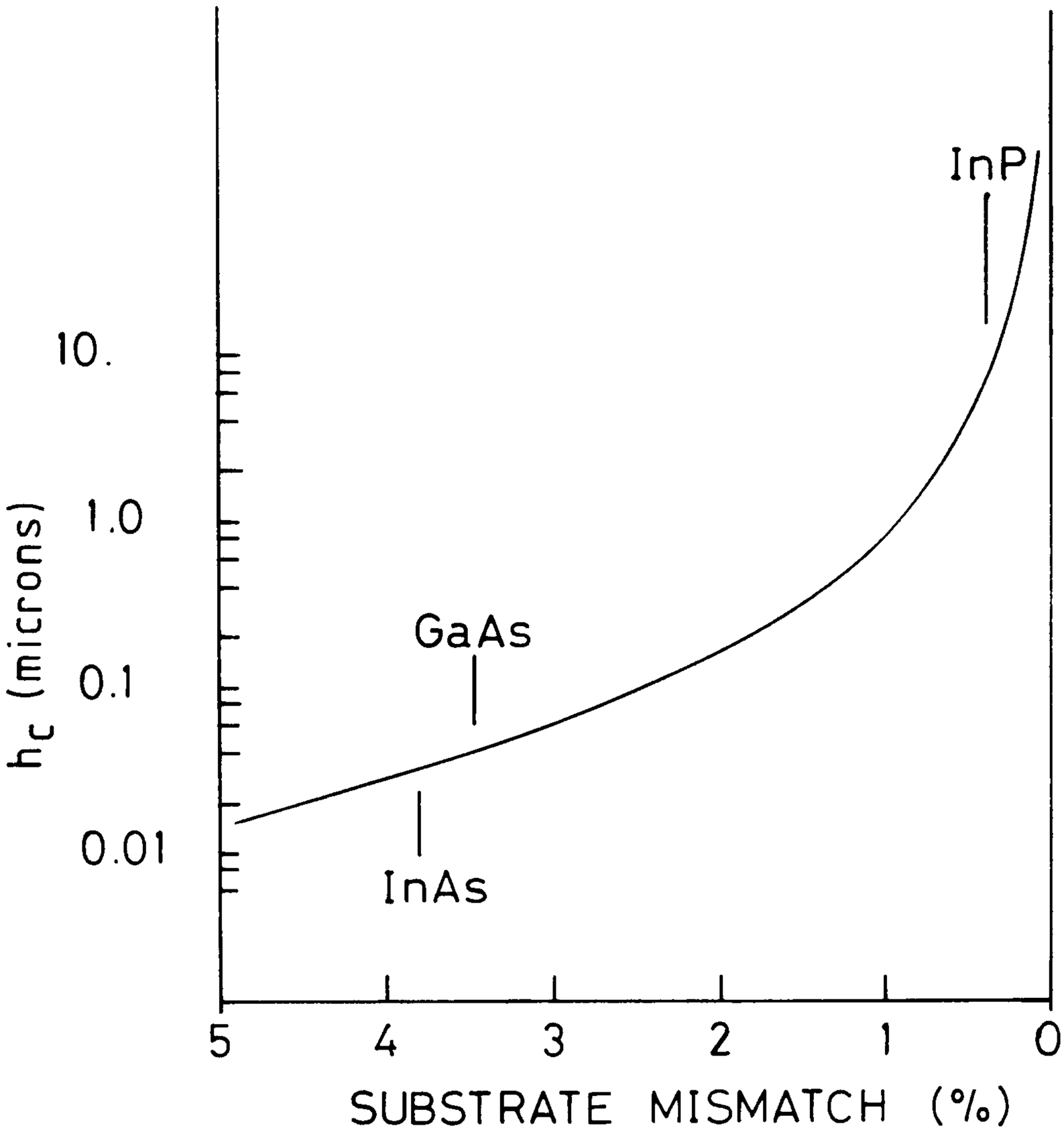

Figure 3.1. Critical thickness of CdS epilayer as a function of mismatch to substrate, as calculated in section 3.1.2. The dotted lines indicate the mismatch between the (111) faces of the named compounds and the CdSe (0001) face.

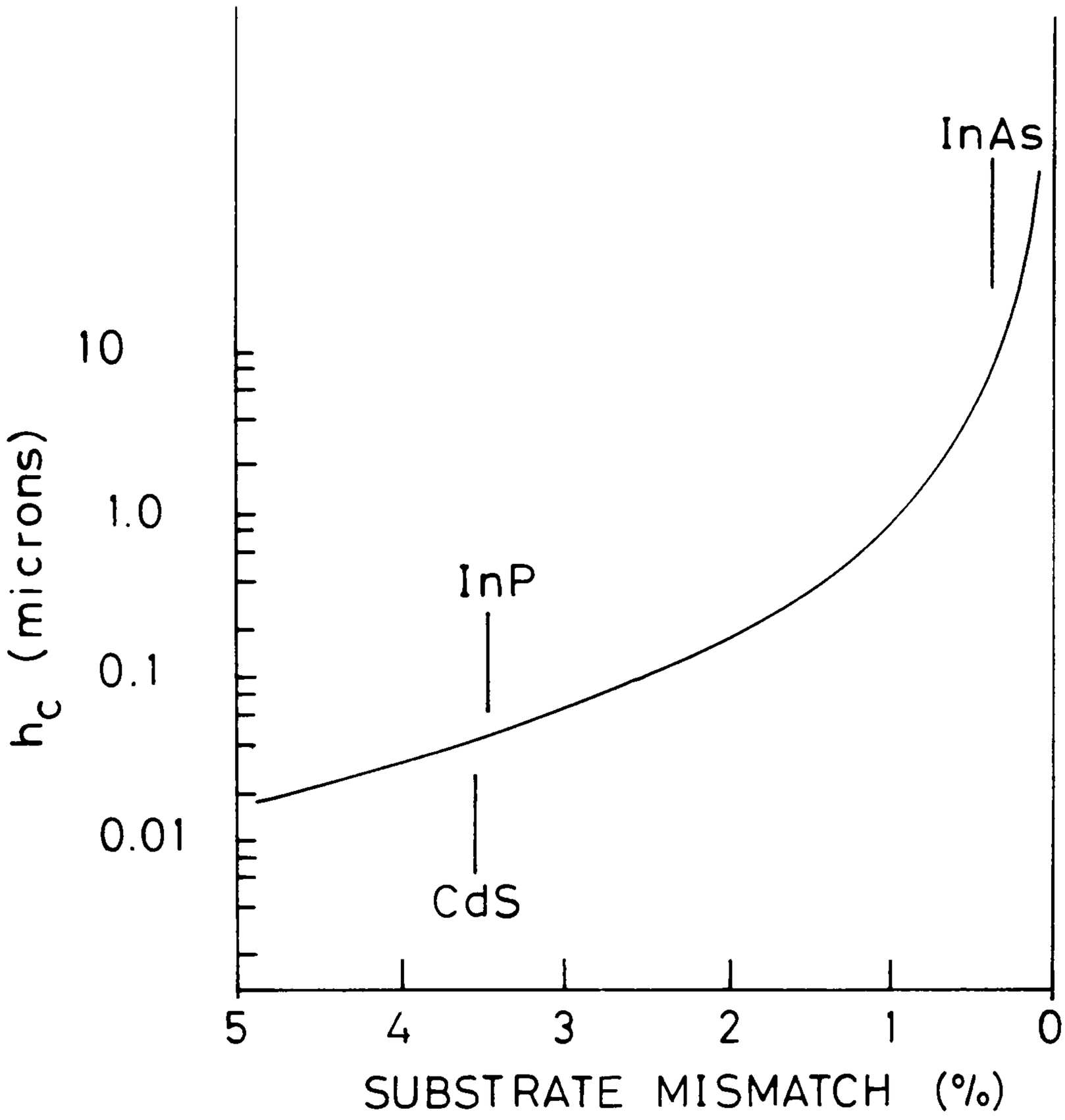

Figure 3.2. Critical thickness of CdSe epilayer as a function of mismatch to substrate. The dotted lines indicate the substrate mismatches between the CdS (0001) face and the (111) face of the compounds named.

	E_{xx}	E_{yy}	E_{zz}	E_{xy}	E_{yz}	E_{zx}	
X_x	c_{11}	c_{12}	c_{13}	0	0	0	
Y_y	c_{12}	c_{11}	c_{13}	0	0	0	
Z_z	c_{13}	c_{13}	c_{33}	0	0	0	
X_y	0	0	0	c_{44}	0	0	(v)
Y_z	0	0	0	0	c_{44}	0	
Z_x	0	0	0	0	0	c_{66}	

where the c_{ij} are referred to as strain moduli. The tensor is arranged so that the columns represent the strain components and the rows the stresses giving rise to those strains. The terms along the left edge are stresses on those faces in the subscripted direction e.g. X_x is the stress on the x face along the x-axis. The E's are strains with similar notation. The first letter is the face and the second the direction e.g Exx is the fractional displacement of the x face along the x-axis. Hookes law in this system is now given by

$$S_j = \sum_{i=1}^{6} E_i c_{ij} \qquad \text{(vi)}$$

Where i is the column, j the row and S is the strain. For a biaxially strained epilayer (c-axis normal to the substrate) we use the convention that the z-direction is along the c-axis and the two components of the strain lie in the x and y directions, which are symmetrically equivalent. Putting $E_{xx}=E_{yy}=-E$ (using the convention of negative for compressive strain) into (vi) we get the equation in Z_z:-

$$Z_z = -2Ec_{13} + E_{zz}c_{33} \qquad \text{(vii)}$$

As the epilayer is free to expand in the z direction we can put $Z_z=0$ and equate to obtain the three strain components.

$$E_{xx} = -E$$

$$E_{yy} = -E \qquad \text{(viii)}$$

$$E_{zz} = 2E \times C_{13}/C_{33}$$

Note that the off-axis components of the strain E_{xy}, E_{yz} and E_{xz} are all zero.

3.1.4 Deformation theory

When a crystal of semiconductor is strained there will in general be a change in that compound's band structure. In the case considered above, this change can be considered to originate from two components of the strain, the hydrostatic component and trigonal distortion component. The hydrostatic component acts so as to reduce the lattice constants of the compound, the essential symmetries of the crystal lattice being preserved. The trigonal distortion, however, will produce directionally-dependent strain, consequently altering (usually lowering) the lattice symmetry. The effects of these two components on the band structure depend on the symmetries of the conduction and valence bands.

The band structure of wurtzite CdS and CdSe was described in

chapter 1. Figure 1.3 showed the origin of the bands at the Γ point in CdS [10]. At the Γ point in CdS and CdSe the conduction band consists of a doubly degenerate s-like band having the symmetry Γ_1. The valence band is p-like and consists of a fourfold degenerate Γ_5 band which is split by the spin orbit interaction into doubly degenerate Γ_7 and Γ_9 bands with angular momenta of $J=\pm 1/2$ and $J=\pm 3/2$ respectively. There is also a Γ_7 band split off by the trigonal crystal field at somewhat lower energy than the other two.

The hydrostatic component of the strain will move the conduction and valence bands relative to each other without altering the valence band structure. The trigonal component will affect the valence bands by altering the energy separation of the the three bands relative to each other and the conduction band. To calculate the movement of the bands under stress we use the linear approximation for the effect of stress on the wurtzite band structure obtained by Pikus and Sandomirskii [11,12].

$$E_A = E_A + \delta_1 + \delta_2 \qquad \text{(ix)}$$

$$E_B = E_B + \delta_1 + \frac{\delta_2}{2}\left(1 + \frac{\Delta_1 - \Delta_2}{[(\Delta_1 - \Delta_2)^2 + 8\Delta_3^2]^{1/2}}\right) \qquad \text{(x)}$$

$$E_C = E_C + \delta_1 + \frac{\delta_2}{2}\left(1 - \frac{\Delta_1 - \Delta_2}{[(\Delta_1 - \Delta_2)^2 + 8\Delta_3^2]^{1/2}}\right) \qquad \text{(xi)}$$

Where:- $\delta_1 = C_1 E_{zz} + C_2 E_\perp$ & $\delta_2 = C_3 E_{zz} + C_4 E_\perp$

The Δ's are the k.p band parameters, C_1, C_2, C_3 and C_4 are deformation potentials and the $E_{A,B,C}$ are the undeformed respective bandgaps.

These expressions can now be evaluated by using equation (viii).

We find a simple linear (for biaxial strain perpendicular to the c-axis) relationship exists between the strain and the energy gap for the three valence bands. The values for the deformation potentials have been determined from uniaxial pressure measurements by other workers [13,14]. The potentials, band parameters and elastic moduli used in this study for CdS and CdSe are given in Table 3.1. The change in band gaps with strain E for CdS and CdSe are thus given by

	CdS	CdSe	
$E_A=E_A$	-0.82E	-1.379E	(xii)
$E_B=E_B$	+2.27E	+3.3E	(xiii)
$E_C=E_C$	+3.17E	+2.01E	(xiv)

Where the potentials are in electron volts. The relative intensity of the recombination emission for the three bands as a function of strain can also be calculated [13]. However, this proved to be unnecessary for this study as no such intensity variations were observed in single epilayers. The above theory, however, is used in chapter 4 to calculate the band structure for the CdS/CdSe superlattices, and to interpret the observed recombination emission from CdSe in the multilayer structures.

	CdS	CdSe
Δ_1	28.4	68.8
Δ_2	20.9	138.0
Δ_3	20.7	150.7
C_1	-2.8	-0.76
C_2	-4.5	-3.7
C_3	-1.3	-4.0
C_4	2.9	2.2
C_{13}	4.6	3.9
C_{33}	9.4	8.45

Table 3.1. Band parameters, deformation potentials and elastic moduli of wurtzite CdS and CdSe. The units of the Δ's are meV, the units of the C's are eV and the elastic moduli are in N/m^2. Data taken from reference [13].

3.2 RHEED studies

In chapter 1 the properties of cadmium sulphide and cadmium selenide were reviewed. It was noted that both compounds can have either cubic sphalerite or hexagonal wurtzite crystal structures depending on the growth conditions. Although the wurtzite phase is usually the most stable, it was clearly of great interest to this study that the lattice structure of our epilayers should be known.

It is possible to determine the crystal structure of CdS and CdSe from spectroscopic studies. This relies on observing the splitting of the valence band in unstrained crystals, as this only occurs for the wurtzite structure. However, as strain can have this effect as well, it was decided that more unequivocal structural information was required to judge the best substrate for the growth of purely wurtzite CdS and CdSe by MOCVD. In particular we wanted to be able to detect the possible presence of both phases in the same epilayer.

Reflection high energy electron diffraction (RHEED) is a well established epitaxial layer assessment technique. It provides a convenient way to assess the single crystalline nature of an epilayer as well as giving information on layer smoothness and the presence of defects such as twins within the layer. The RHEED patterns of a selection of CdS and CdSe epilayers were studied.

3.2.1 Experimental technique and theory

In RHEED a beam of high energy electron is projected on to a crystalline surface at a very oblique angle (see figure 3.3).

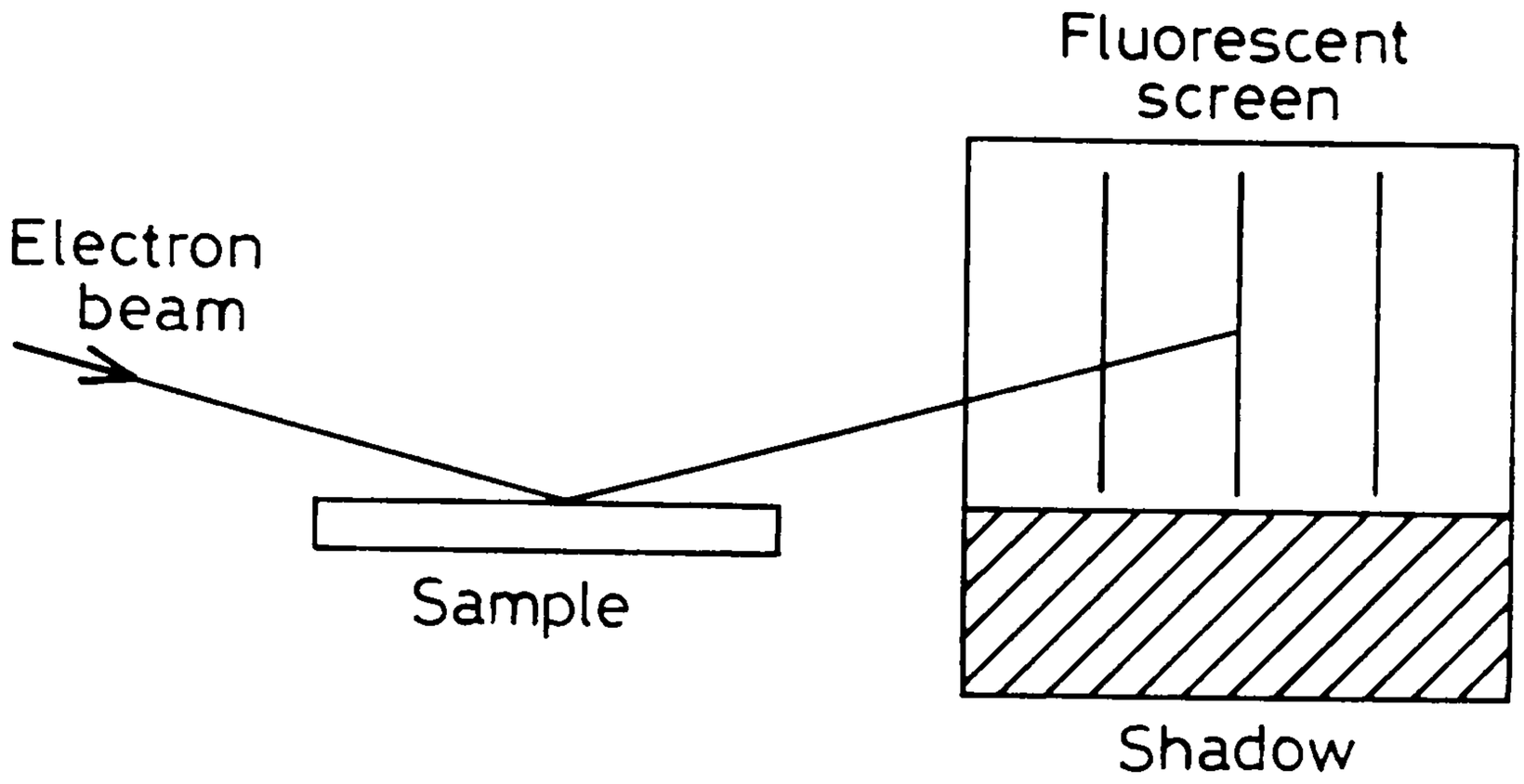

Figure 3.3. Experimental arrangment for RHEED.

The resulting RHEED diffraction pattern formed is characteristic of the arrangment of the surface atoms. The incident electrons are primarily reflected by the initial monolayer of atoms; as a result RHEED is essentially a surface assessment technique. The interpretation of RHEED patterns has been covered in detail by other authors and here only the basic principles are described.

Any surface of a crystalline solid will possess a two dimensional arrangment of atoms which must belong to one of five possible surface nets. These nets are the two dimensional equivalent of the three dimensional Bravais lattices [15]. The exact nature of the net will depend on the structure of the solid and the orientation of the surface normal. In the ideal case of a perfectly smooth epilayer surface the RHEED pattern shows the interference pattern of electrons scattered by

the initial monolayer of the crystal face. It can be shown that, for high enough energy electrons, such a pattern will consist of a series of streaks lying parallel to the plane normal [16]. The separation of the streaks depends on the lattice constant of the compound and the orientation of the sample's crystallographic axes relative to the electron beam.

Some epitaxial material does indeed demonstrate only diffraction streaks (for example high quality MBE grown material [17]). However, for the purpose of determining the structure of the layer, these patterns have limitations. In particular, the pattern of streaks cannot be used to distinguish between the wurtzite (0001) and sphalerite (111) faces. This can be seen from (as noted in chapter 1) the close similarity of wurtzite and sphalerite structures along the [111] and [0001] directions respectively. The surface atoms of the (111) cubic and (0001) hexagonal faces possess the same (hexagonal) surface net.

In practice the ideal case of a totally smooth epilayer is difficult to achieve and some parts of an epilayer surface will inevitably be raised above other areas. This will cause the electron beam penetrating into the compound to be diffracted by the three dimensional lattice structure. The degree to which this occurs depends on the surface roughness. Consequently, as we move from the case of a perfectly smooth surface to a very rough one the pattern will change from streaks to streaked spots to spots only. Hence, streaking of the diffracted spots from a surface can indicate smoothness [17]. For rough surfaces, the diffraction pattern will simply correspond to the well studied electron diffraction pattern for the beam lying along the appropriate crystal axis. In this manner, with a knowledge of the expected patterns, the difference in crystal structures can be resolved.

Figure 3.4 shows the surface net for the (111)/(0001) plane, the notations refering to the cubic and hexagonal crystallographic systems respectively.

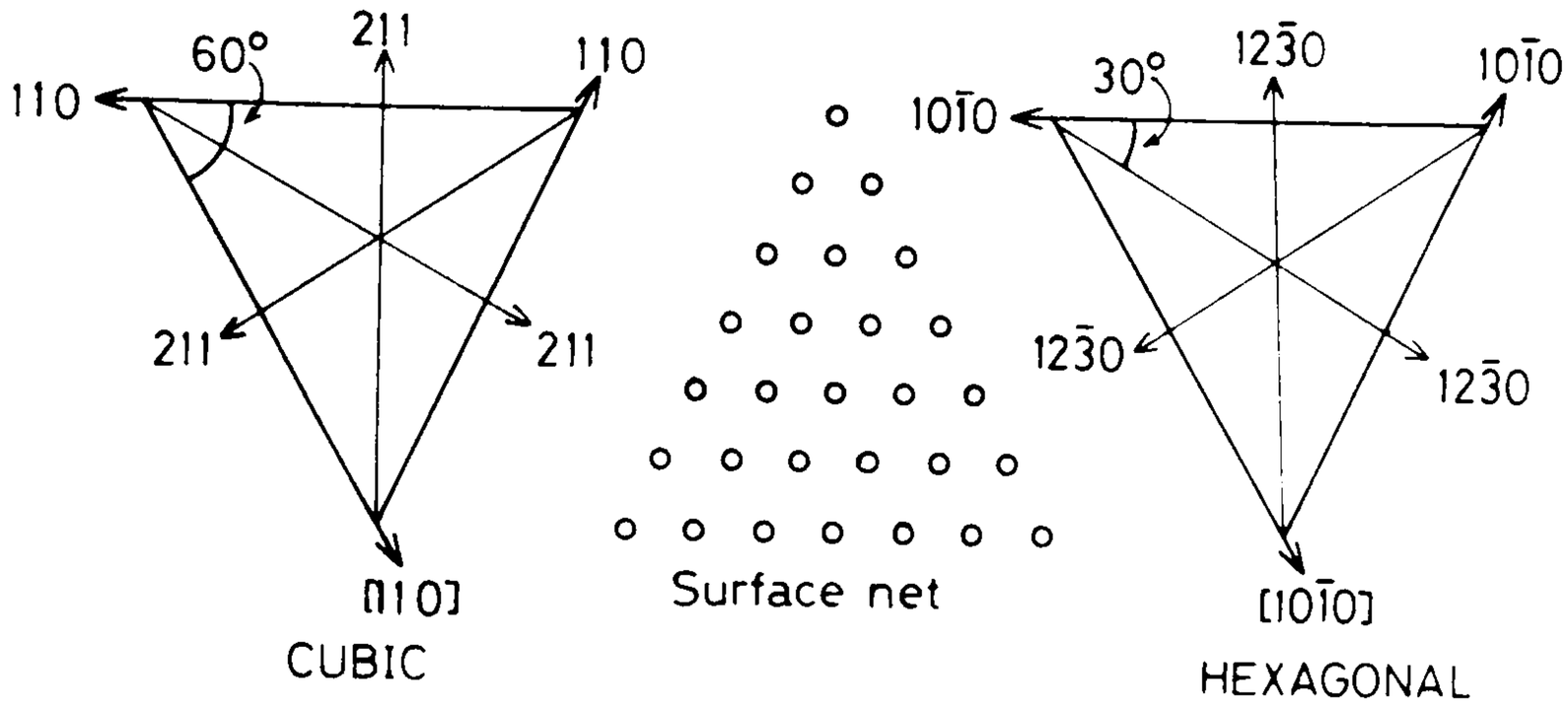

Figure 3.4. Surface net for wurtzite (0001) or zincblende (111) surface. The figures indicate the main axes in the plane, although in practice these would be cyclic permutations of the Miller indices indicated, they are symmetrically equivalent.

The main high symmetry axes are indicated on the figure for both systems. The [110] axis lies in the plane for both (111) and (100) orientations. The electron diffraction patterns for an electron beam lying along the cubic [110] and equivalent hexagonal [10$\bar{1}$0] axes (referred to as the "[10$\bar{1}$0] zone axis") are shown in figure 3.5 [18,19]. It can be seen that the wurtzite pattern is easily distinguishable from the cubic pattern. In addition, cubic twinning can be observed in this orientation by the presence of additional diffraction spots [19]. The pattern corresponding to the [211]/[12$\bar{3}$0] zone axis is also shown in figure 3.5, the pattern is the same for both phases.

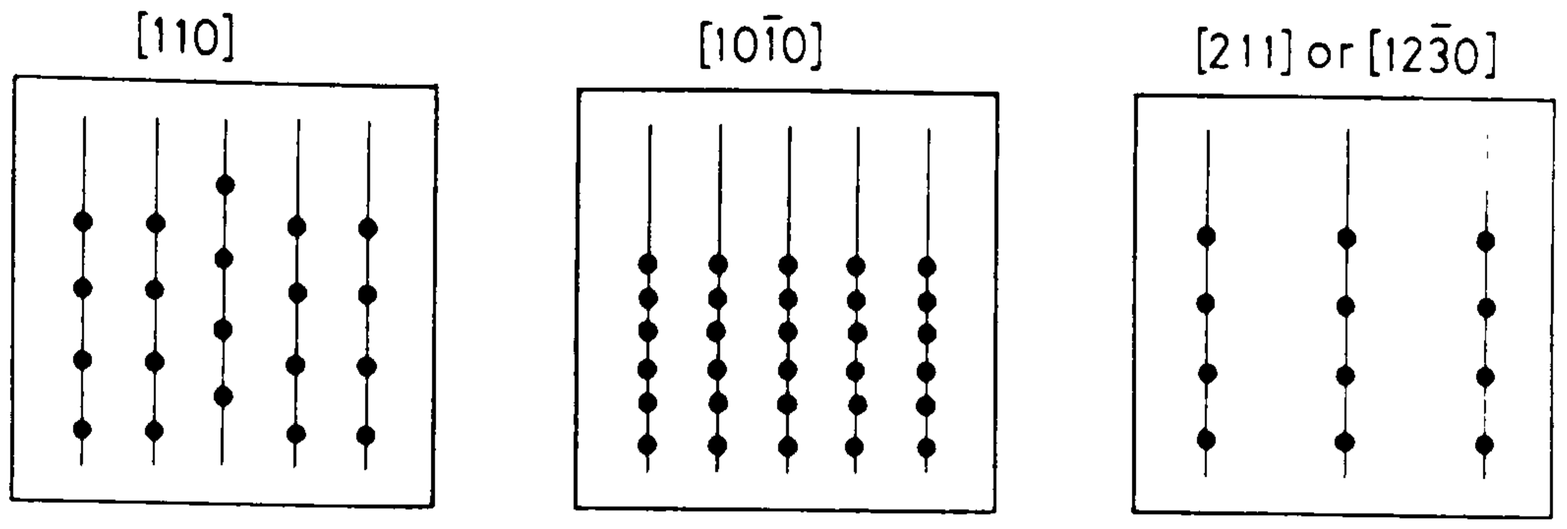

Figure 3.5. Electron diffraction patterns for beams lying along the indicated crystallographic axes. The dots correspond to diffraction maxima.

The RHEED measurments were conducted at Durham university under the supervision of G.J.Russell. The samples studied were mounted inside a modified JEOL 150 electron microscope and a 100KeV electron beam was reflected off the surface onto a luminescent screen to produce the desired patterns.

Results and discussion

3.2.2 Cadmium sulphide

Figure 3.6 shows the RHEED patterns obtained from sample MH8b a 1 μm CdS epilayer grown on (111)A GaAs at a growth temperature of 350^{o}C. The upper photograph shows the diffraction pattern from an electron beam lying along the [10$\bar{1}$0] axis of a wurtzite crystal. The epilayer has unequivocably the wurtzite crystal structure. To demonstrate the epitaxial relationship the epilayer was rotated by 30^{o} about the surface normal. It can be seen from figure 3.5 that this should obtain the pattern corresponding the the cubic [211] or hexagonal [12$\bar{3}$0] zone axis. The lower photograph in figure 3.6 shows this pattern for the previous sample. The pattern is the same for the two phases, but, its presence at 30^{o} to the [10$\bar{1}$0] pattern confirms the expected epitaxial relationship. The CdS epilayer is growing on the (111) cubic substrate orientated with axes aligned [0001] || [111] and [110] || [10$\bar{1}$0].

All the CdS epilayers on (111)A GaAs showed the same patterns. They also displayed the Kikuchi diffraction lines characteristic of high crystalline perfection. Figure 3.7 shows the [10$\bar{1}$0] zone axis from MH55, a 150 Å thick layer of CdS on (111)A GaAs. The pattern confirms that the epilayers grow as wurtzite from the interface. The patterns also shows a noticeable degree of spot streaking (clearer when viewed on the luminescent screen) indicating a degree of surface smoothness.

In addition to the layers grown on (111)A GaAs, CdS epilayers on GaAs (111)B and (100) surfaces were studied. The CdS epilayer MH10a was studied by RHEED. This sample consisted of a thin CdS layer grown on GaAs (100) at a growth temperature of 400 ^{o}C. For this orientation, if the layer is growing epitaxially, we expect the GaAs 110 axis to be aligned with either the cubic CdS [110] or hexagonal CdS [10$\bar{1}$0] axis,

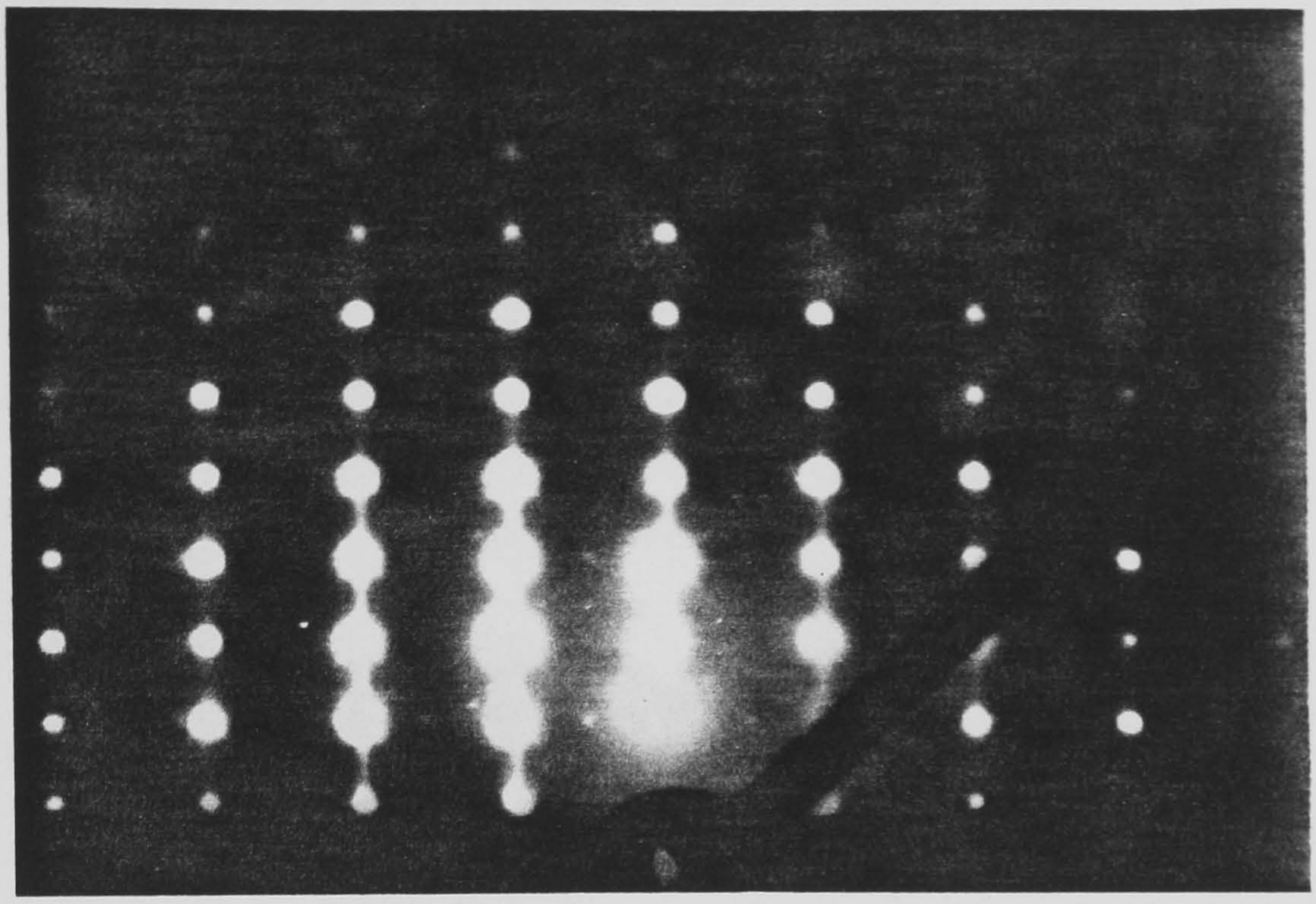

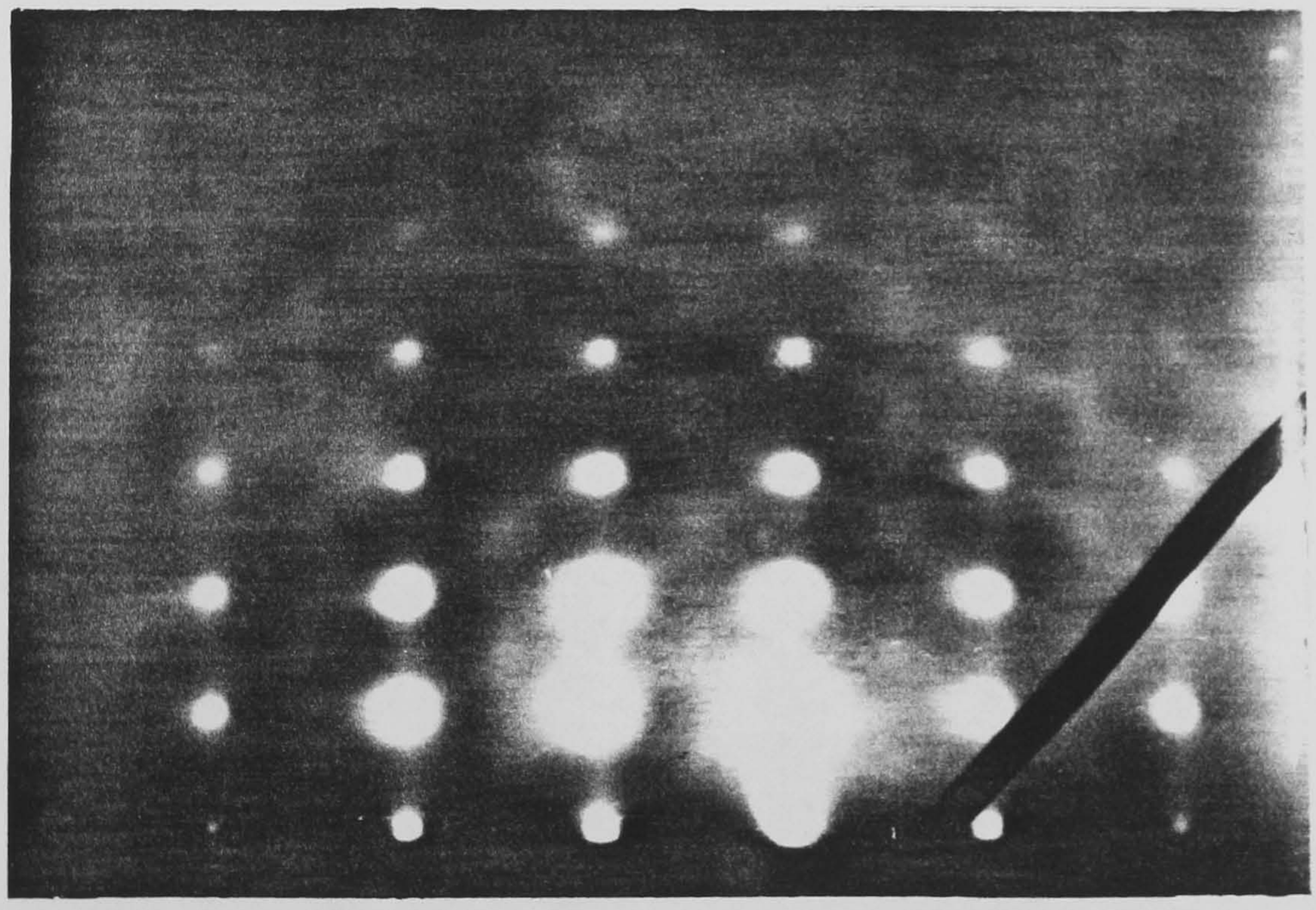

Figure 3.6. RHEED diffraction patterns taken from sample MH8 (see text). The upper image shows the hexagonal $[10\bar{1}0]$ zone axis, the lower shows the hexagonal $[12\bar{3}0]$ zone axis.

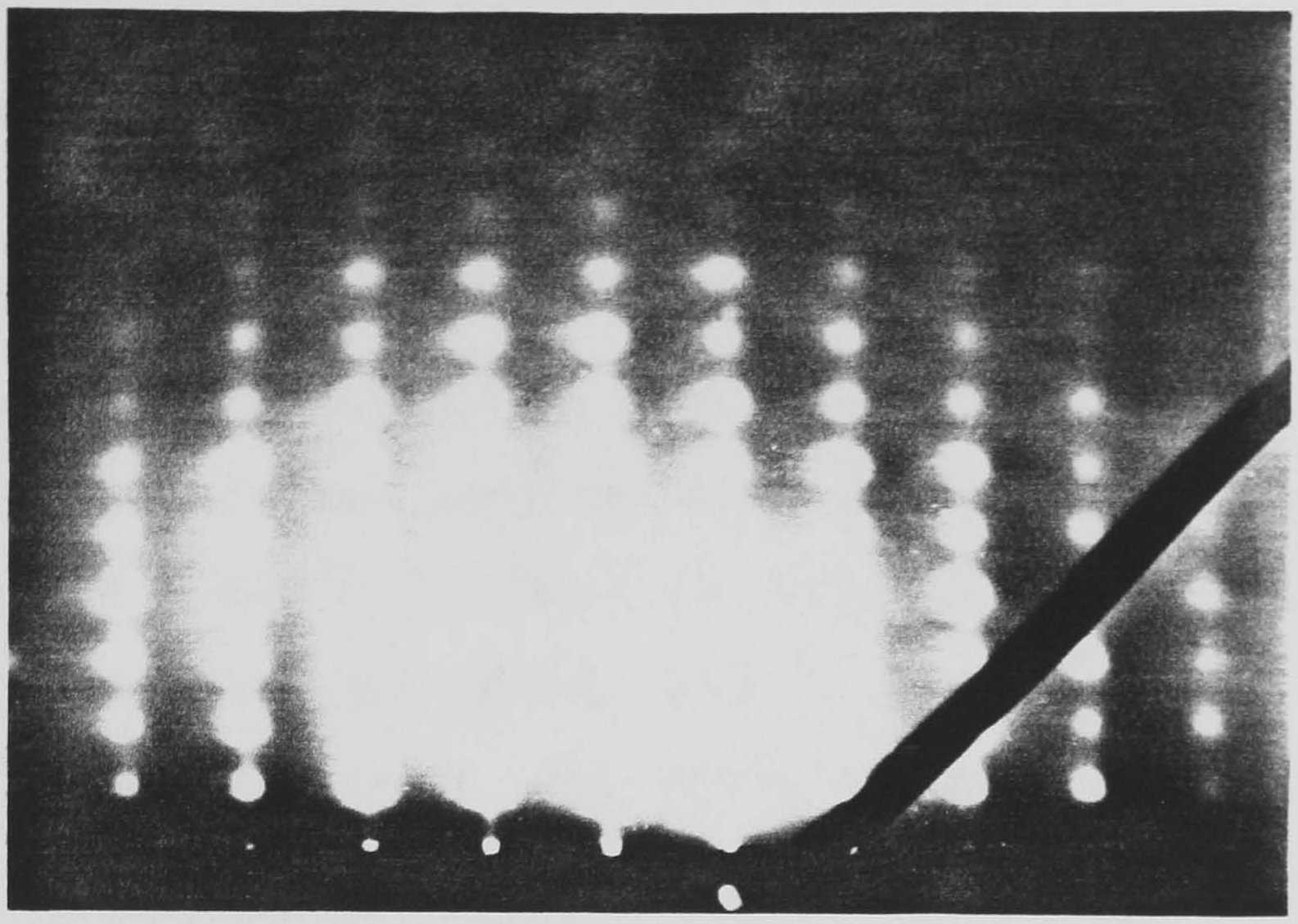

Figure 3.7. [10$\bar{1}$0] zone axis from sample MH55.

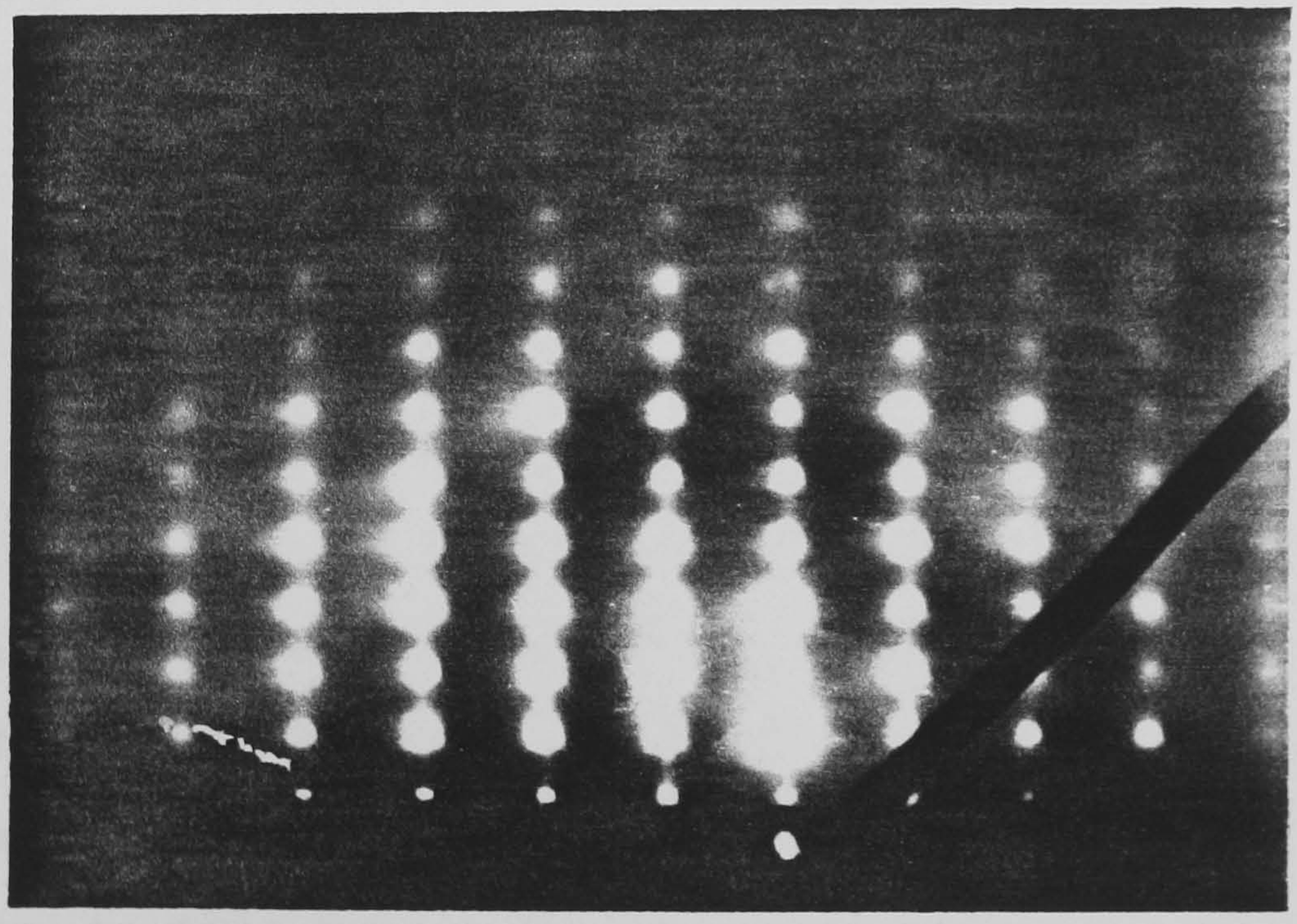

Figure 3.8. [10$\bar{1}$0] zone axis diffraction pattern from sample MH10. Two such patterns were observed with a 180^{o} rotation of the substrate and epilayer between them.

depending on the phase of the CdS epilayer. The diffraction pattern obtained is shown in figure 3.8: it demonstrates clear hexagonal structure. Two such patterns were found with a 180^{o} rotation between them, showing that one $[10\bar{1}0]$ hexagonal axis lies in the plane for this growth orientation. It was reported in chapter 2 that thick CdS epilayers grown at 350 ^{o}C on GaAs [100] were clearly polycrystalline. This sample grown hotter and slower than 3 μm/hr showed a smooth surface and appeared epitaxial. The RHEED results indicate hexagonal CdS epitaxy on this surface and under these growth conditions. In section 3.3.3.2 it is found that the CdS epilayers grown on the (100) GaAs face produced poor luminescence. This can be understood if the epilayers contain a high density of lattice defects, which cannot be detected in the RHEED patterns. Figure 3.9 shows the $[10\bar{1}0]$ diffraction pattern from MH14 a 0.4μm layer grown on (111)B GaAs at 350^{o}C. The initial pattern obtained is shown in the upper photograph of figure 3.9. It can be seen that the spots are drawn out into streaks, the layer demonstrating a typical diffraction pattern from a very smooth surface. Although this is initially encouraging, it is not possible to resolve clearly the spots and the phase of the epilayer cannnot be deduced. To observe the diffraction spot pattern the epilayer was etched for ten seconds in hydrochloric acid, roughening the surface, a similar procedure having been used previously for CdTe [19]. Subsequently the required pattern was recorded and is shown in the lower photograph of figure 3.9. The pattern is that of the cubic [110] zone axis accompanied by diffraction spots at intermediate positions corresponding to cubic twinning of the layer. This provides direct evidence for CdS having a cubic structure when grown on this face of GaAs. The pattern also clearly shows that the layer is of poor structural quality despite possessing a very smooth surface. Similar

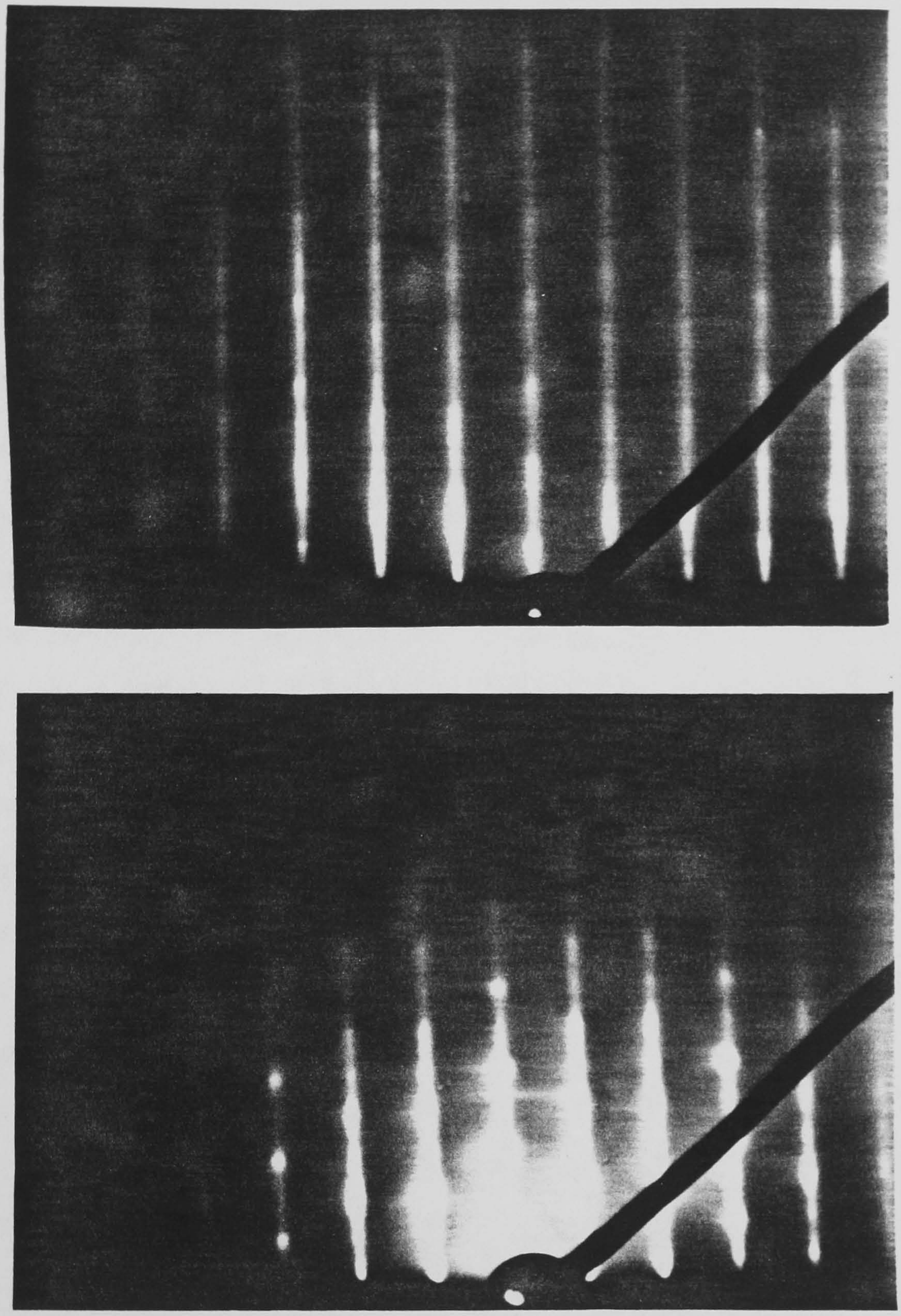

Figure 3.9. [110] zone axis patterns from sample MH14, a CdS epilayer grown on GaAs (111)B. The upper image (3.9a) shows the pattern obtained from the 'as grown' sample. The lower image (3.9b) was taken from the sample after etching as described in the text. The streaks in the lower image show extra spots in addition to those expected for the hexagonal [12$\bar{3}$0] zone axis (figure 3.5) indicating twinning.

electron diffraction patterns were reported in reference [20] for CdS evaporated on an InSb (111) surfaces. These results are consistent with the findings of other workers (e.g. Igarashi [21]) who found that CdS grown by VPE on GaAs (111)B had the sphalerite structure.

3.2.3 Cadmium selenide

The RHEED patterns from the CdSe epilayers grown on (111)A GaAs were studied. Figure 3.10 shows the [10$\bar{1}$0] pattern for a layer of CdSe (MH40) grown on GaAs (111)A at 350 ^{o}C. The pattern shows many features, the most striking being the polycrystalline rings. In addition to the rings there are intense spots at the cubic positions and many spots at intermediate positions corresponding to cubic twins. We can conclude that the layer is largely cubic and contains many cubic twins.

It was noted in section 2.4 that this epilayer showed a very smooth surface with prominent surface hillocks at some positions. It is not possible directly to determine which surface feature could be responsible for the observed RHEED effects. However, it was observed that the surface contained regions of apparently polycrystalline growth. If the polycrystalline diffraction rings originate in these features then the rest of the layer must be epitaxial cubic growth. It was also noted in section 2.4 that some of the hexagonal growth features showed evidence of cubic twinning.

Electron diffraction patterns similar to that shown in figure 3.10 were observed from cubic CdS epilayers grown by evaporation on InSb [20]. In this case, the diffraction spots were identified as being due to the (222) reflection from twinning about the [111] axis, the cubic twins being derived from a change in the tetrahydral layer

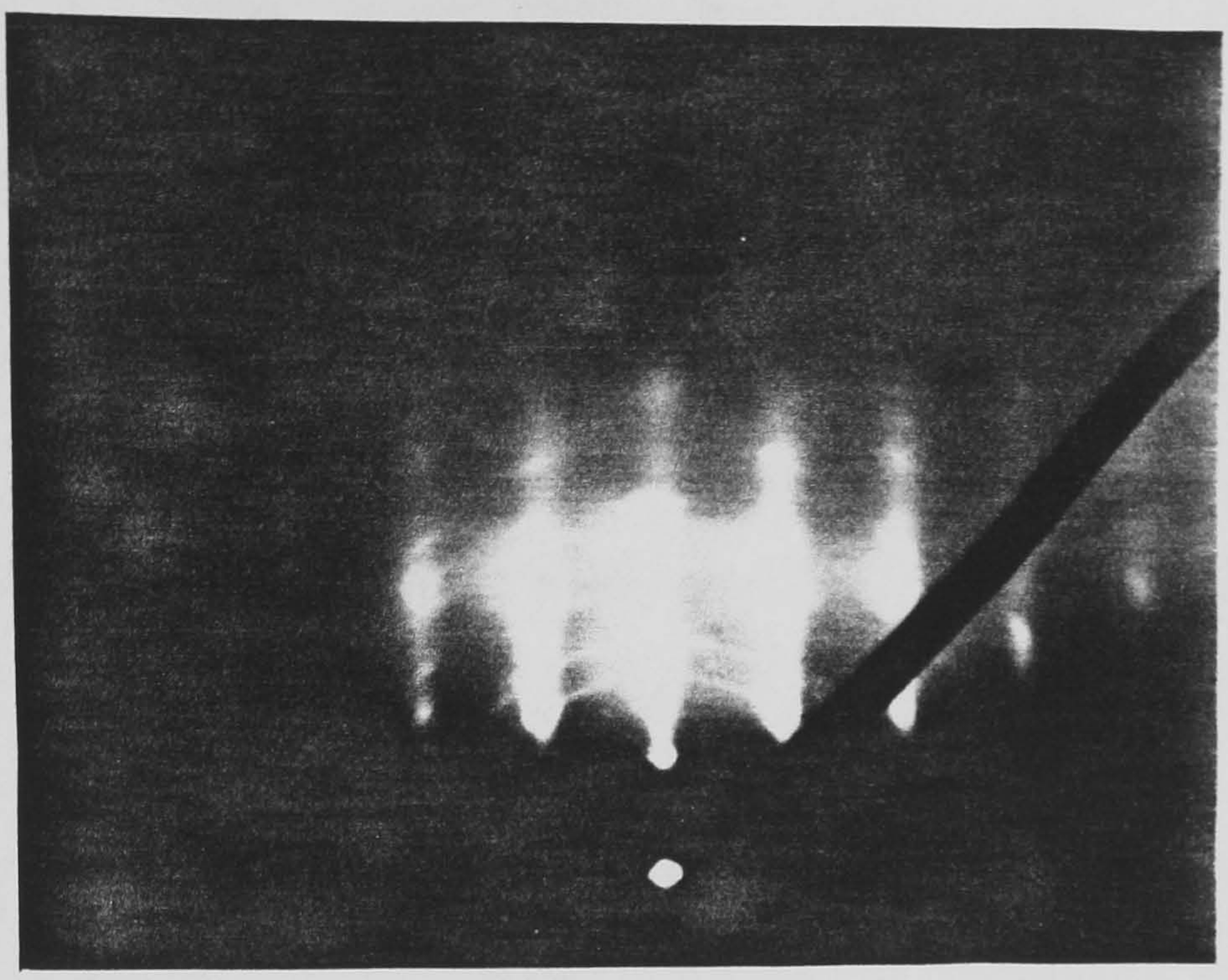

Figure 3.10. RHEED pattern from CdSe epilayer grown on GaAs. The image shows the [10$\bar{1}$0] zone axis, the material is clearly polycrystalline (diffraction rings) and twinned (double spots).

stacking sequence along the [111] growth direction. It is clear that the CdSe epilayers grown at low temperature are of poor quality and contain many twins.

A similar degree of cubic twinning is observed in other II-VI epitaxial layers grown along the [111] direction of the sphalerite structure, for example CdTe [19]. In section 1.2.4 the production of these so called 'lamella twins' from the tetrahedral orientated layers was described. Since one result of such twinning is the production of a wurtzite nearest neighbour environment for the stacked layers, heavy twinning of cubic CdSe (and CdS) might, qualitatively, be expected. This situation is similar to that of other II-VI compounds such as ZnS which demonstrate two stable phases. The energy of formation of the lamella twins is small so that the continuity of the stacking sequence along the [111] axis varies according to growth conditions. It is observed in ZnS bulk growth that such twinning is frequent and unavoidable (see section 1.2). Possible reasons for the poor quality of the CdSe epilayers relative the CdS were discussed in section 2.4.4.

In section 3.3.5 the preparation of the ternary alloy $CdS_{1-x}Se_x$ is discussed. The RHEED patterns from an alloy $CdS_{0.02}Se_{0.98}$ grown at 350^{o}C on GaAs (111)A were studied visually to investigate the effect of the addition of small quantities of sulphur to the CdSe. It was found that the layer showed purely hexagonal growth with no apparent cubic twinning or polycrystallinity. The effect of hydride mixing on the structure and quality of the epilayers was studied further in section 3.3.4.2.

3.3 Photoluminescence studies

3.3.1 Introduction

Photoluminescence spectroscopy is an established technique for the characterization of semiconductors. It provides a convenient non-destrucive method for determining the relative purity and perfection of the crystal lattice. This allows the study of growth aspects such as the effect of misfit dislocations in the layer and the diffusion of impurities from the substrate. In this way the growth parameters can be optimised with respect to these quantities. CdS and CdSe are luminescing materials and their photoluminesence spectra have been studied extensively. The wealth of literature relating to both bulk and epitaxial CdS and CdSe provided a convenient source with which to compare the luminescence from the MOCVD material. The low temperature photoluminescence spectra of all samples grown were recorded. Reflection spectroscopy was also used to measure free exciton energies in order to determine the sulphur content of alloy samples.

3.3.2 Experimental technique

The experimental arrangement for photoluminescence is shown schematically in figure 3.11. The samples were mounted on the copper sample rod using low temperature varnish. To avoid thermal stressing care was taken to insure that the samples were fixed only at one corner. The sample rod was lowered into a liquid helium immersion cryostat. The helium reservoir was then overpumped to below the helium lambda point achieving a final sample temperature in the range 1.6-2 K. The luminescence was excited with the light from a Spectra-Physics series 2020 Argon-ion laser. The laser lines used were the 458nm line

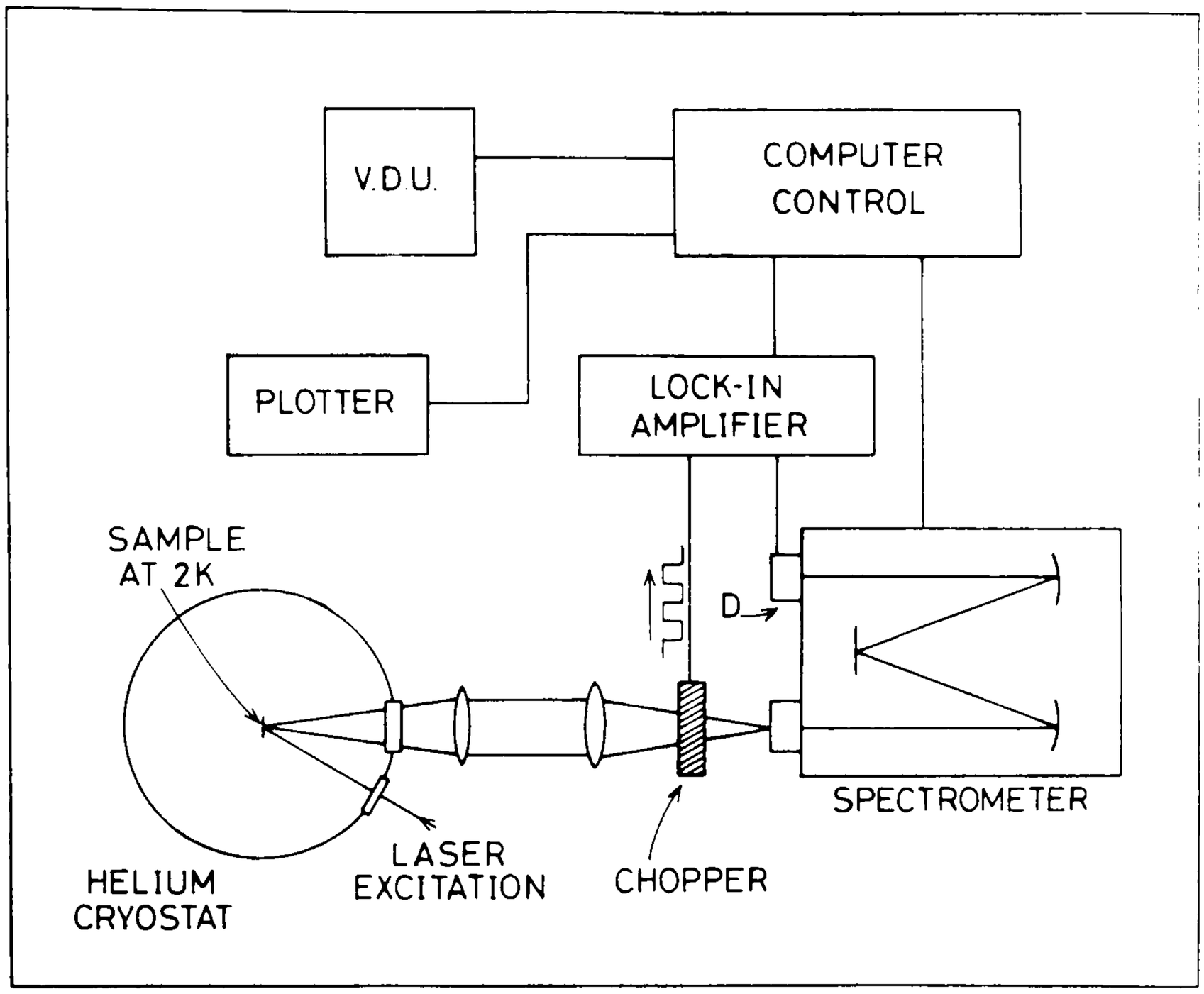

Figure 3.11. Experimental arrangment for Photoluminescence. D is the photodetector (see text).

for CdS and the alloys, and the 488nm line for the CdSe samples. Laser light was passed through an interference filter which greatly attenuated the plasma lines at frequencies other than the principal line. The monochromatic beam was then focussed on to the sample surface and the resulting luminescence collected at an angle of 33^{o} to the incident light. A Wratten filter was used to remove the unwanted laser light and plasma lines at wavelengths shorter than the luminescence (filters used were W8 for the 458nm line and W16 for the 488nm line). A 1m focal length Spex was used to disperse the luminescence using a 500nm blazed grating with 1200 lines/mm. The light was then detected with a Hamamatsu trialkali photomultiplier tube for the wavelength region 4000-8000Å and a North Coast Scientific cooled germanium detector for the region 8000-14000Å. The luminescence was chopped and recorded using standard lock-in techniques (see figure 3.11). The resolution of the spectrometer was limited by the slit width and was in the range 0.2-30 Å. Allowance was always made for the delay effect of the PSD time constant and spectrometer scan rate. The spectrometer was calibrated by passing the (greatly attenuated) laser line through the system and was found to be accurate to 0.2 Å over the region of the CdS and CdSe edge emissions.

The spectrometer was controlled by a Victor VPC II microcomputer. An analoque to digital conversion system allowed the computer to collect and display the data. The data were then corrected for system response by the computer using a correction curve. It was possible to store the data on floppy disc for subsequent recall and processing.

The temperature dependence of the luminescence was also investigated using an Oxford Instruments CF1204 continuous flow cryostat. The sample was mounted on a cold finger which was cooled by pumping cold helium gas into the surrounding space. The temperature

could be controlled thermostatically via a heating element attached to the cold finger. The minimum temperature obtainable in this system was found experimentally to be 4 K. The luminescence was detected in the same way as above.

Reflection spectroscopy was conducted using the same apparatus as for the photoluminescence. Light from the white light source was dispersed by the 1m Spex, chopped and passed into the cryostat. The reflected light was then detected by a trialkali photomultiplier tube and the signal detected by standard lock-in techniques.

Results and discussion

3.3.3 Cadmium sulphide

The initial layers of CdS were grown on various substrates at a growth temperature of 300-350 ^{o}C. It was not known which substrate would prove the best for the growth of CdS and photoluminescence was used principally to identify the most promising CdS epilayers. A series of CdS epilayers were grown on GaAs (111)A,(111)B,(110),(100), InP (111)B and glass substrates, as described in chapter 2. The luminescence spectra of these layers were then studied.

Figures 3.12,3.13 and 3.14 show six spectra from layers grown under similar growth conditions on the substrates above. The sample numbers and substrates used are indicated on the diagrams. The spectra show the near-gap emission and consist of the well-known bound excitonic and green edge emissions of CdS. Without studying the luminescence in detail, it can be clearly seen that, unlike that grown on the other faces, the material grown on the (111)A face of GaAs shows very bright and narrow excitonic emission and faint green edge

Figures 3.12,3.13 and 3.14 (overleaf and on successive pages). Low temperature (2K) photoluminscence from CdS epilayers grown on various substrates at 300-350^{o}C. The substrates used and sample numbers are as indicated in the top right of each spectrum.

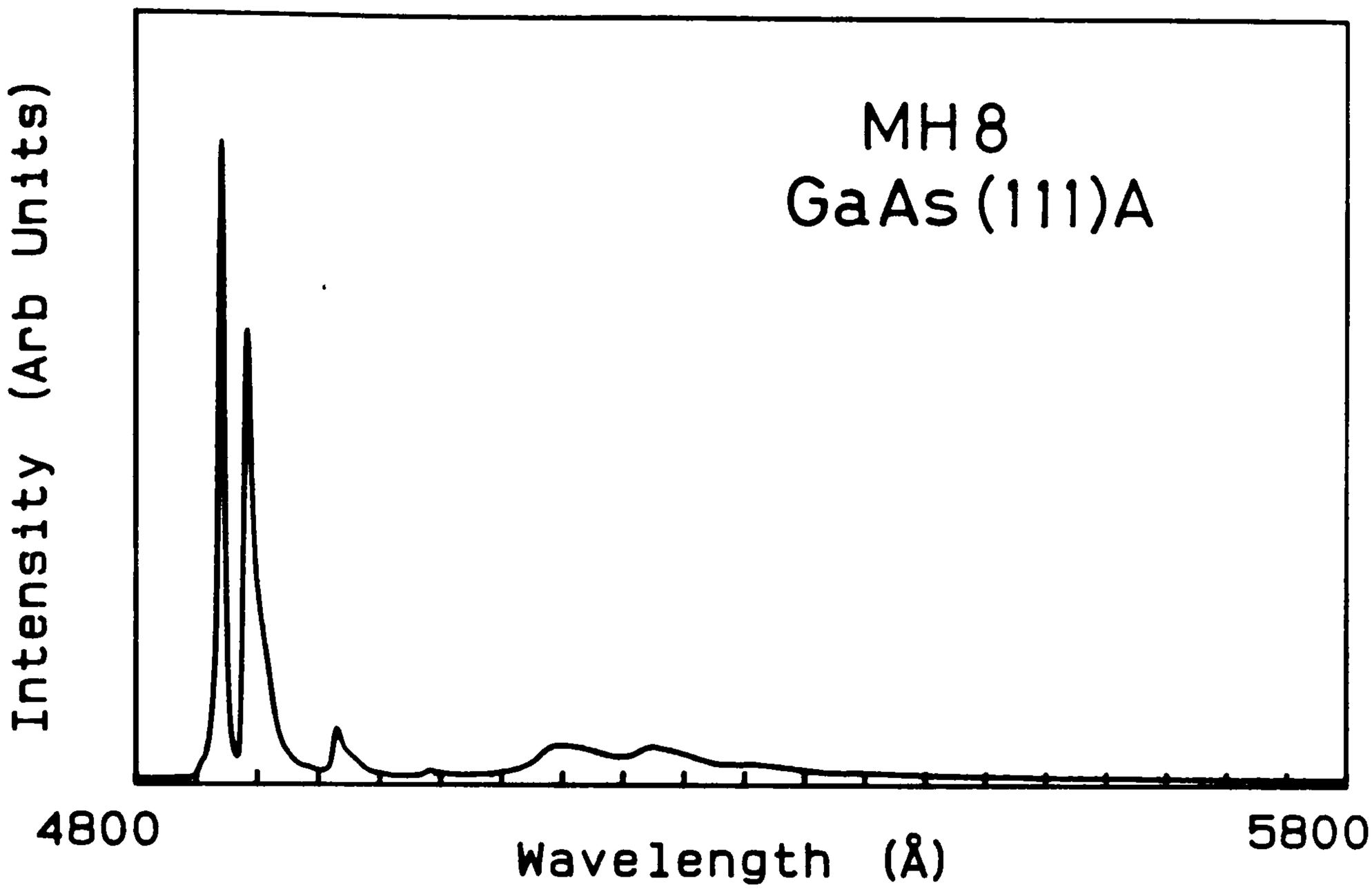
MH 8
GaAs (111)A
Intensity (Arb Units)
4800
5800
Wavelength (Å)

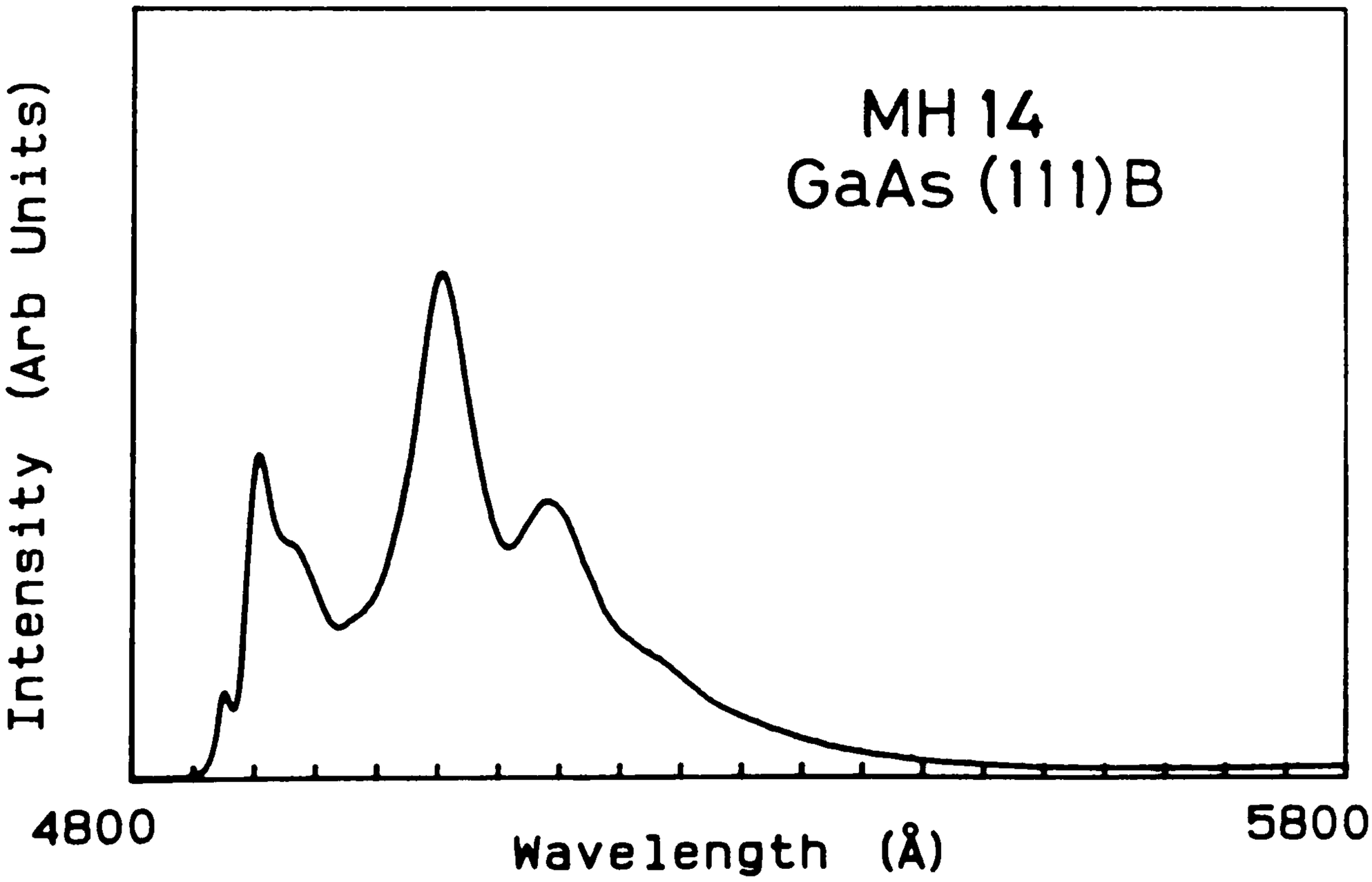
MH 14
GaAs (111)B
Intensity (Arb Units)
4800
5800
Wavelength (Å)

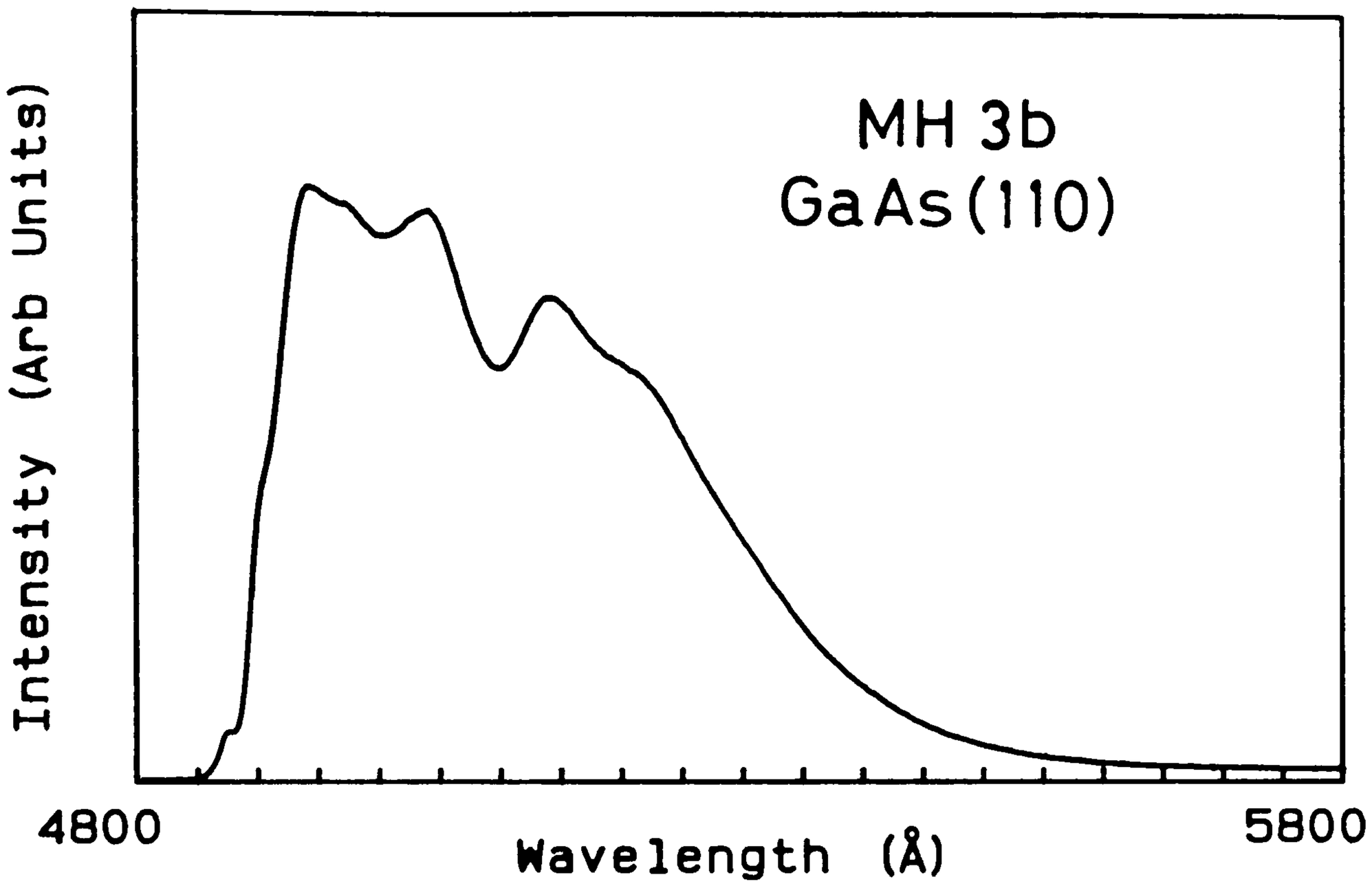
MH 3b
GaAs(110)
Intensity (Arb Units)
4800
5800
Wavelength (Å)

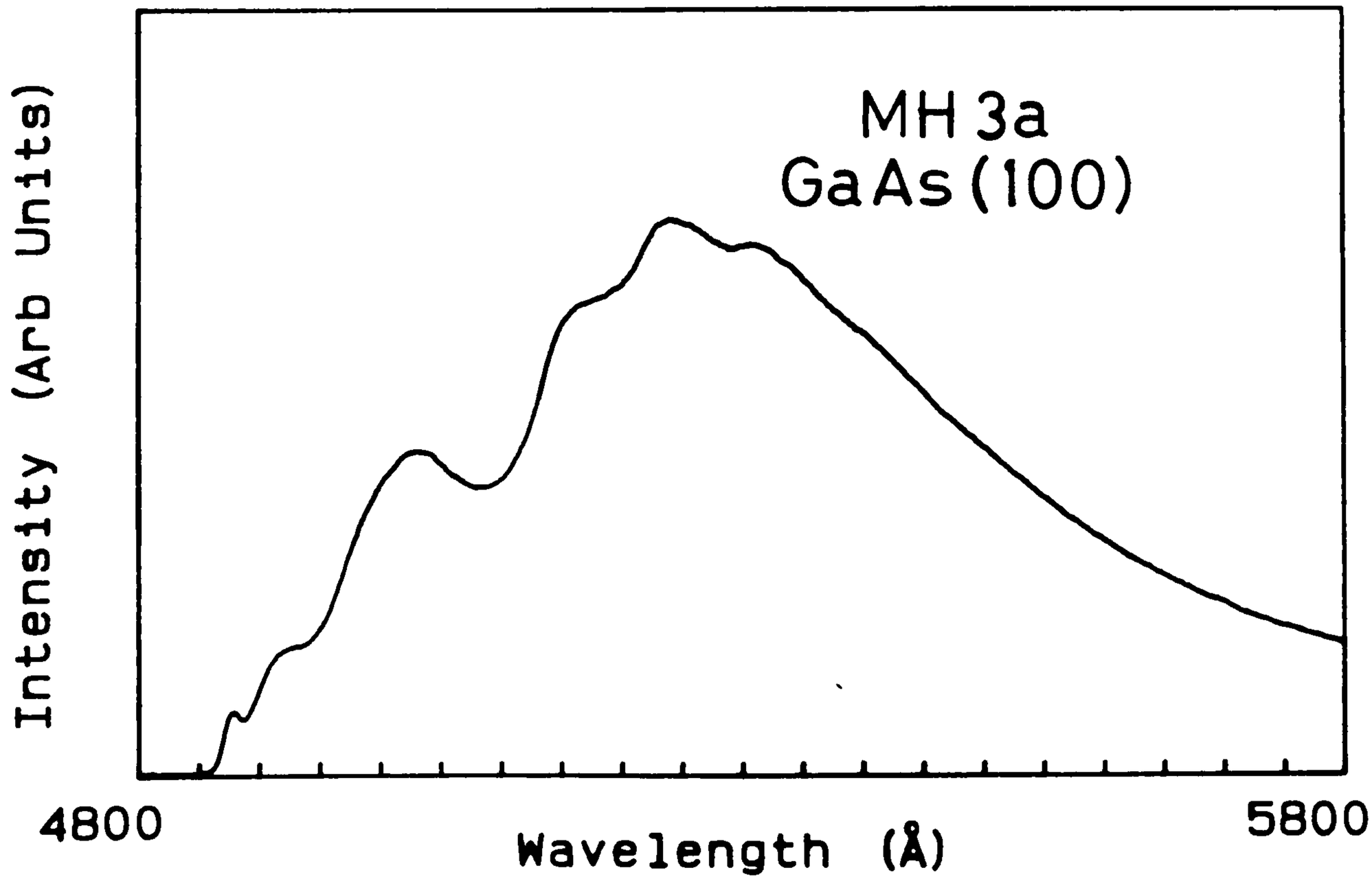
MH 3a
GaAs(100)
Intensity (Arb Units)
4800
5800
Wavelength (Å)

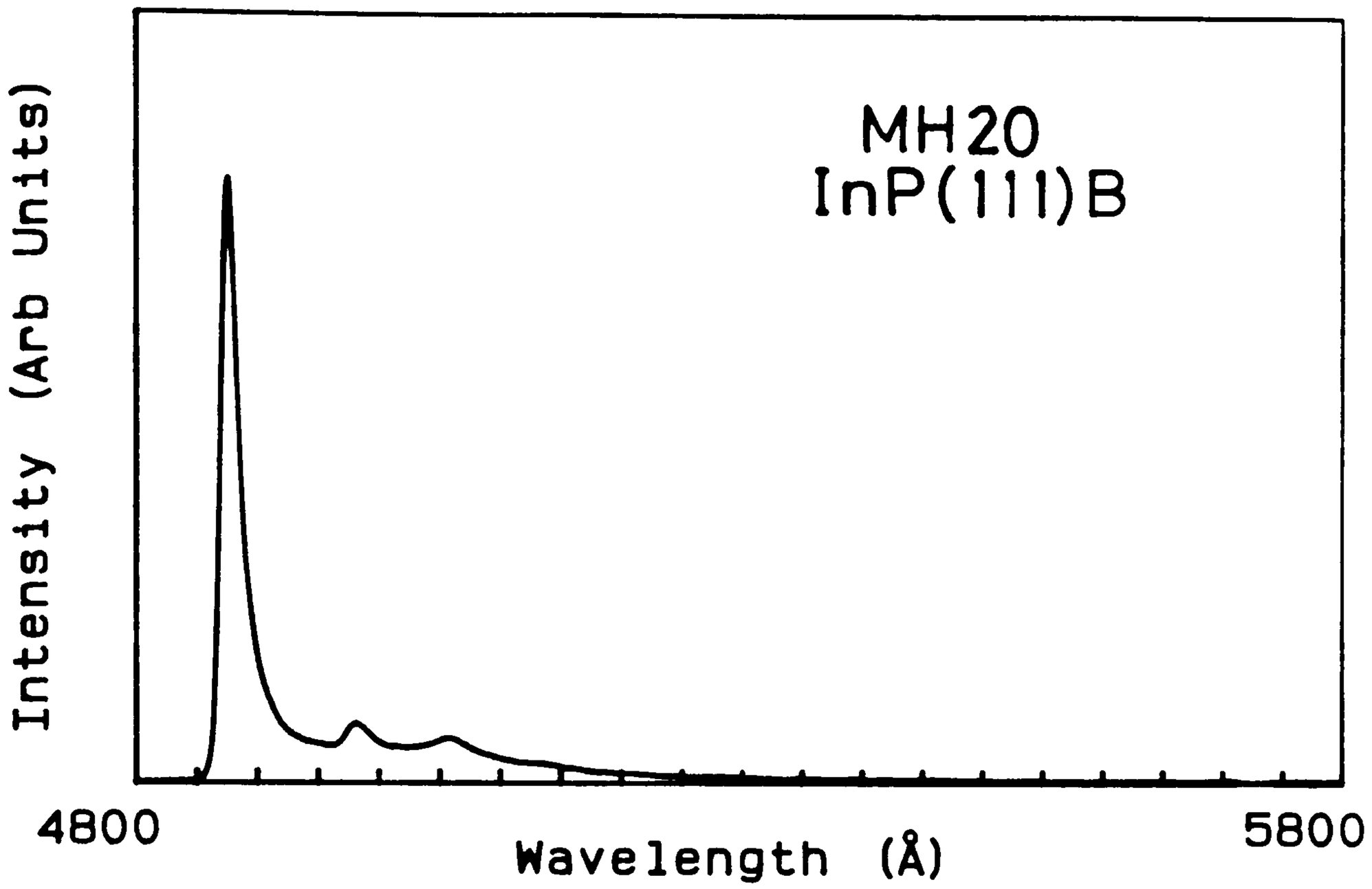
MH20
InP(111)B
Intensity (Arb Units)
4800
5800
Wavelength (Å)

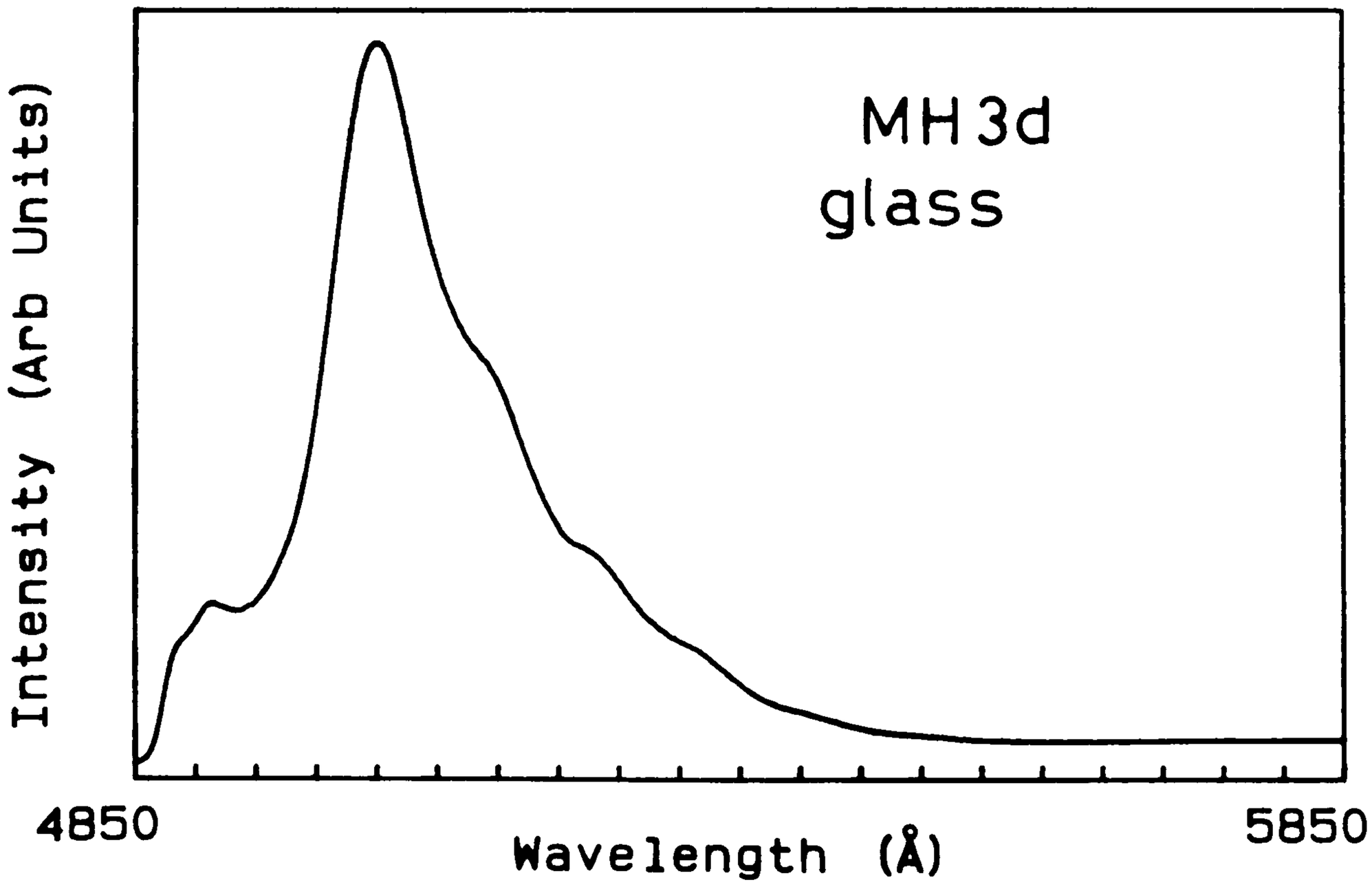
MH3d
glass
Intensity (Arb Units)
4850
5850
Wavelength (Å)

emission. The luminescence from CdS grown on the other substrates is broader and typically ten times fainter than that grown on GaAs (111)A.

In general broad excitonic emission can be due to either high impurity levels or a high concentration of lattice defects [22]. Both of these properties introduce central cell corrections to the recombination processes as described in section 1.5.2. In addition, the presence of extended lattice defects will strain the lattice, causing strain broadening [23]. Moreover, it has been observed previously for evaporated CdS that high levels of dislocations lead to such line broadening [24]. The RHEED studies showed that the CdS epilayer grown on GaAs (111)B contained large numbers of cubic twins. It was also found by microscopy that the layers grown on GaAs (100) and (110) at this temperature were polycrystalline (chapter 2). We conclude that, qualitatively, the photoluminescence results support the RHEED and morphology studies and are consistent with good epitaxy at this growth temperature on the GaAs (111)A face. The three principal substrates used for subsequent CdS epitaxy where GaAs (111)A, GaAs (100) and InP (111)B and the photoluminescence from the epilayers grown on these substrates is described below.

Effect of substrate on CdS photoluminescence

3.3.3.1 GaAs 111(A) substrates

The photoluminescence from the layers grown on GaAs 111(A) shows many clear emission features. Figures 3.15 and 3.16 show two luminescence spectra obtained from a 0.7 μm layer of CdS grown at 350^{o}C (MH26). The principle lines are identified using the notation of Thomas and Hopfield [25]. The two bright emission lines shown in figure 3.15

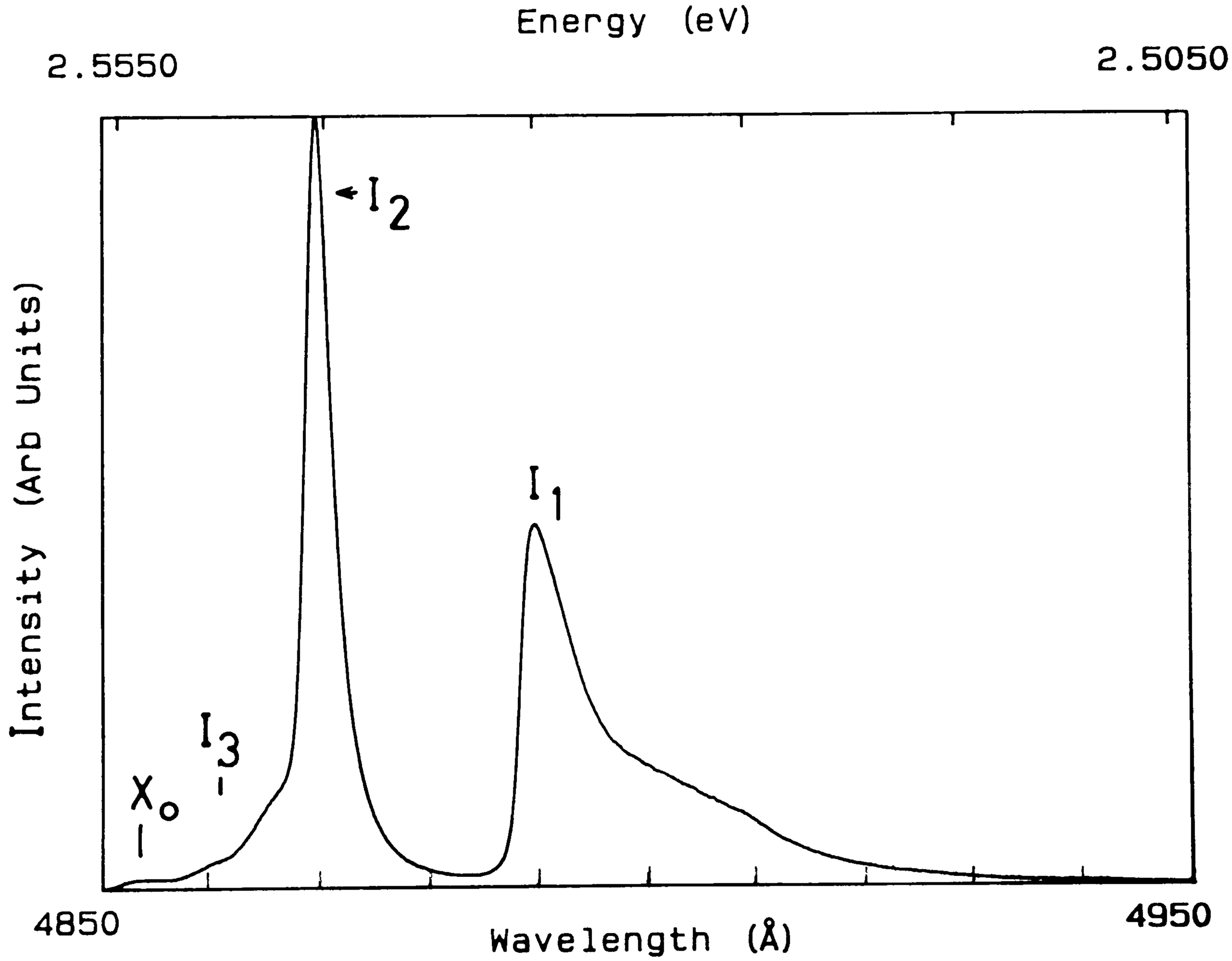

Figure 3.15. High resolution spectrum from MH26. The spectrum shows the excitonic emission region of CdS, the notation is referred to in the text.

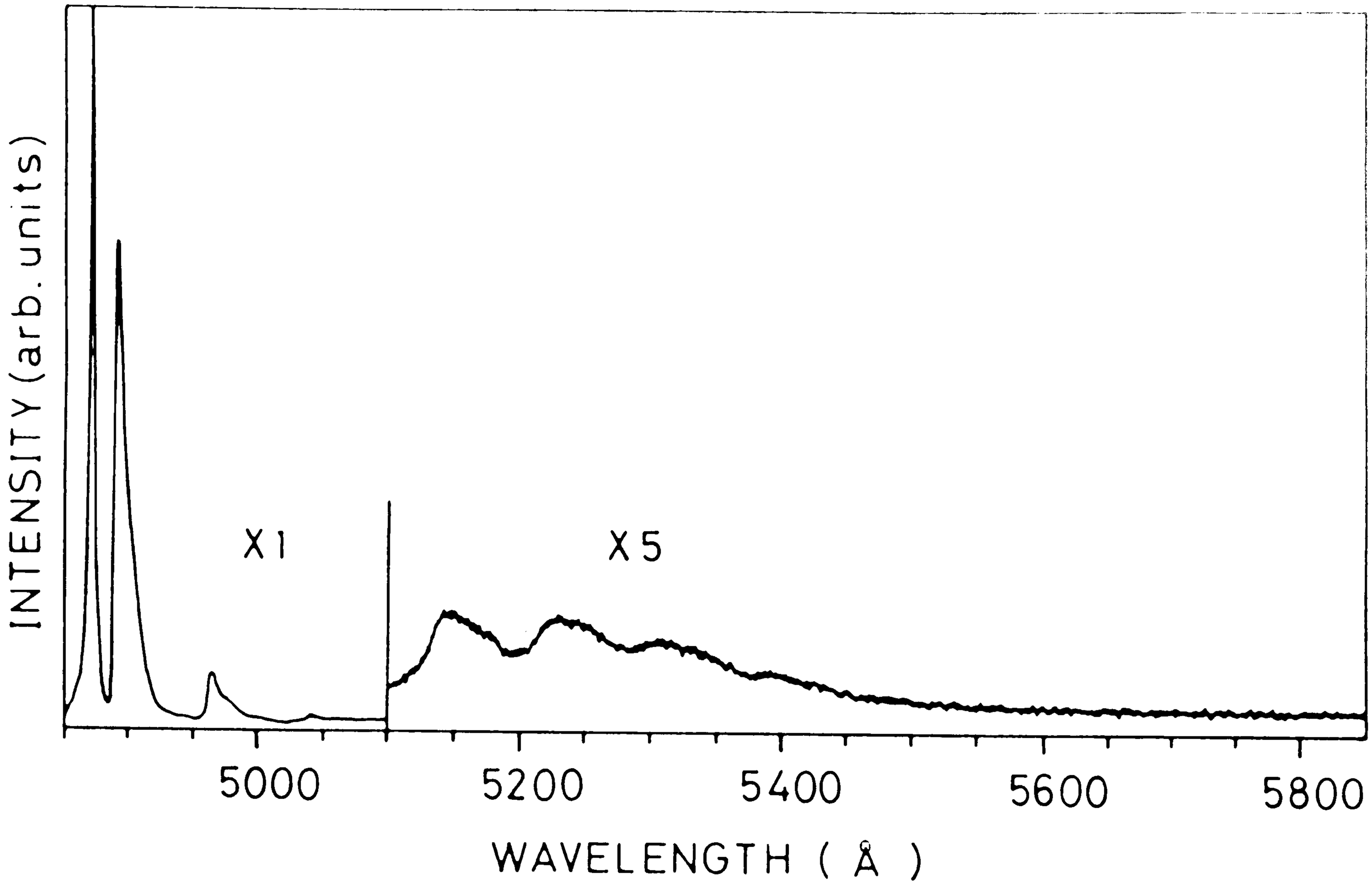

Figure 3.16. Low temperature CdS edge emission as displayed by MH26, the lines are identified in the text.

occur at 4888.4 Å and 4869.9 Å respectively; these correspond to the well known I_1 and I_2 bound exciton emissions. The origin of these lines was shown by Thomas and Hopfield [25] to be excitons bound to neutral acceptors and neutral donors respectively. There is also further structure in this spectrum including a high energy shoulder on the I_2 line possibly due to the I_3 emission from excitons bound to ionised donors and the free exciton emission X_o at 4853Å (indicated on the figure). The low energy tail on the I_1 line is due to acoustic phonon interaction, although other authors reported emission lines in this region these lines maybe obscured in our spectra by this tail.

A frequently used measure of crystal quality is the full width at half maxima (FWHM) of the bound excitonic emission, measured as the width of the emission line at one half of the maximum luminescence intensity. In the best layers this was typically 1 meV, compared to 0.1 meV reported by Thomas and Hopfield [25] for selected vapour phase platelets. However, our value compares favourably to that reported for other II-VI compounds grown by MOVPE (e.g 0.8 meV for ZnSe on GaAs [26]).

It is, in principle, possible to identify the impurity species responsible for an emission line by photoluminescence. This relies on the binding energy of the donor and acceptor impurities being different for each atomic species. These different binding energies will alter the line positions. There are only two common shallow acceptor impurities in CdS, lithium and sodium. The I_1 positions ascribed to these impurities are 4888.2 Å and 4888.57 Å for Li and Na respectively [27]. The I_1 position in our material was 4888.4+_0.2 Å. Although our data are consistent with the presence of either (or both) of these impurities, it is impossible to resolve which is present. However the precision of this measurement does confirm that, at this thickness at

least, there is no residual compressive strain from the interface region. Such strain would alter the band gap and shift the peak position, using the relationships calculated in section 3.1.4 we can estimate that the epilayer is less than 0.01% strained.

There are a large number of possible donors in CdS and the position of the I_2 line is relatively insensitive to their identity. The measured position of the I_2 line in our MOCVD material was 4869.9 Å, which is consistent with the findings of other workers and corresponds to a whole series of possible donors including Li,F,Cl,Ga and Al [28]. The possible autodoping of the layers by gallium is discussed below.

Figure 3.17 shows the CdS green edge emission of the same sample. The emission is approximately one thirtieth of the intensity of the excitonic emission. The spectrum shows a band peaking at 5145Å followed by a series of phonon replicas. There are also some phonon replicas of the excitonic emission which are identified on the figure. The green edge emission can originate from either of two processes, the so called high energy series (HES) and low energy series (LES) [29]. The LES originates from donor-acceptor pair recombination in which an electron bound to a donor impurity recombines directly with a hole bound to an acceptor impurity. The HES is caused when a free electron recombines with a hole at an acceptor site. Both these emissions can display extra bands due to recmbination with the 2s state of the acceptor [30]. The expressions for the recombination energy for the donor-acceptor pair and free to bound recombination processes was given in section 1.5.3 [27,31]. We can use the free to bound expression (equation (x) section 1.5.3) to estimate the depth of the acceptor involved. We note that the kT_e term in expression (x) in section 1.5.3 involves an unknown quantity T_e the electron temperature. We ignore this term here as it is

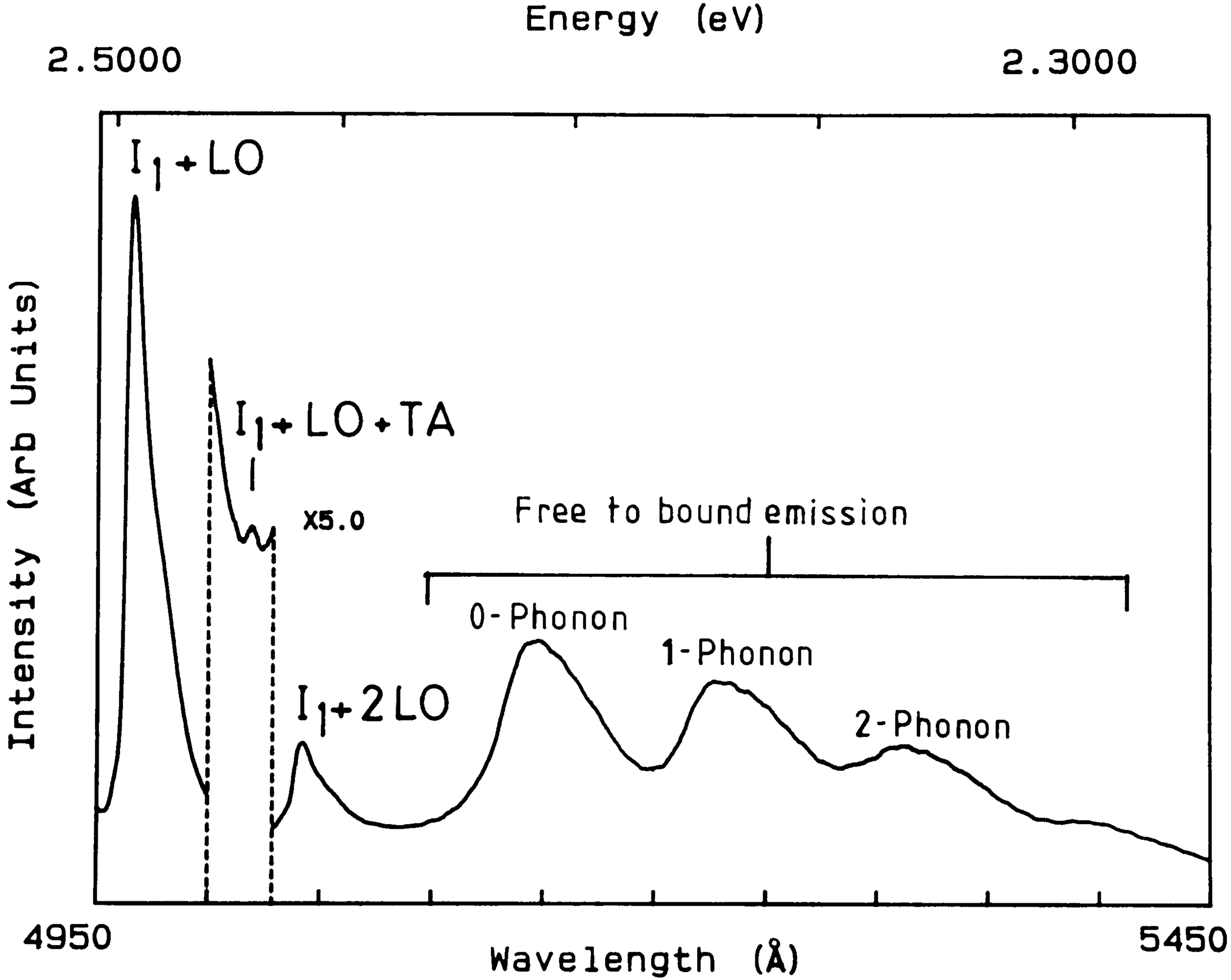

Figure 3.17. CdS green edge emission spectrum from sample MH26. This spectrum also shows several phonon replicas of the bound exciton lines, they are identified using the notation of reference [27].

usually small, however, we note that as a result the estimates of the acceptor depths are lower limits.

The recombination energy in all the best CdS samples has a zero-phonon peak at 5145+_5 Å. This represents a recombination energy of 2.4095+_.003 eV. This is more than the energy observed by Henry et al [27] for distant D-A pairs in CdS (2.391-2.397eV) is consistent with free to bound recombination. The calculated acceptor depth for this transition (in the free to bound case) is 170+_3 meV, which agrees well with the depth of Na or Li acceptors of 169+_6 meV and 165+_6 meV respectively [27]. The temperature dependance of this emission is shown in figure 3.18. It can be seen that the emission intensity remains approximately constant up to 120 K; after this the luminescence is quenched with an activation energy of 54 meV. This dependence is consistant with CdS free to bound recombination as studied by other workers [29]. Bound to bound recombination in CdS has not been observed above 77k (it was historically referred to as the low temperature series [26]). Moreover, d-a pair emission generally quenches with the activation energy of the donor, no known donor exists at a depth of 54 meV below the CdS conduction band. If such a donor did exist than the depth of acceptor this implies is 100 meV, again no known acceptor lies at this depth in CdS. No shift in the peak position with increasing laser intensity was observed for the green emission, d-a pair recombination will usually show a shift lower energy due to the saturation of the close pairs. We conclude that the series starting at 5145A is almost certainly free to bound recombination.

In order to optimize the growth conditions the effect of growth temperature on the photoluminescence was investigated. Figure 3.19 shows a series of three spectra demonstrating the effect of growth temperature (T_g) on the bound exciton emission from the CdS. For

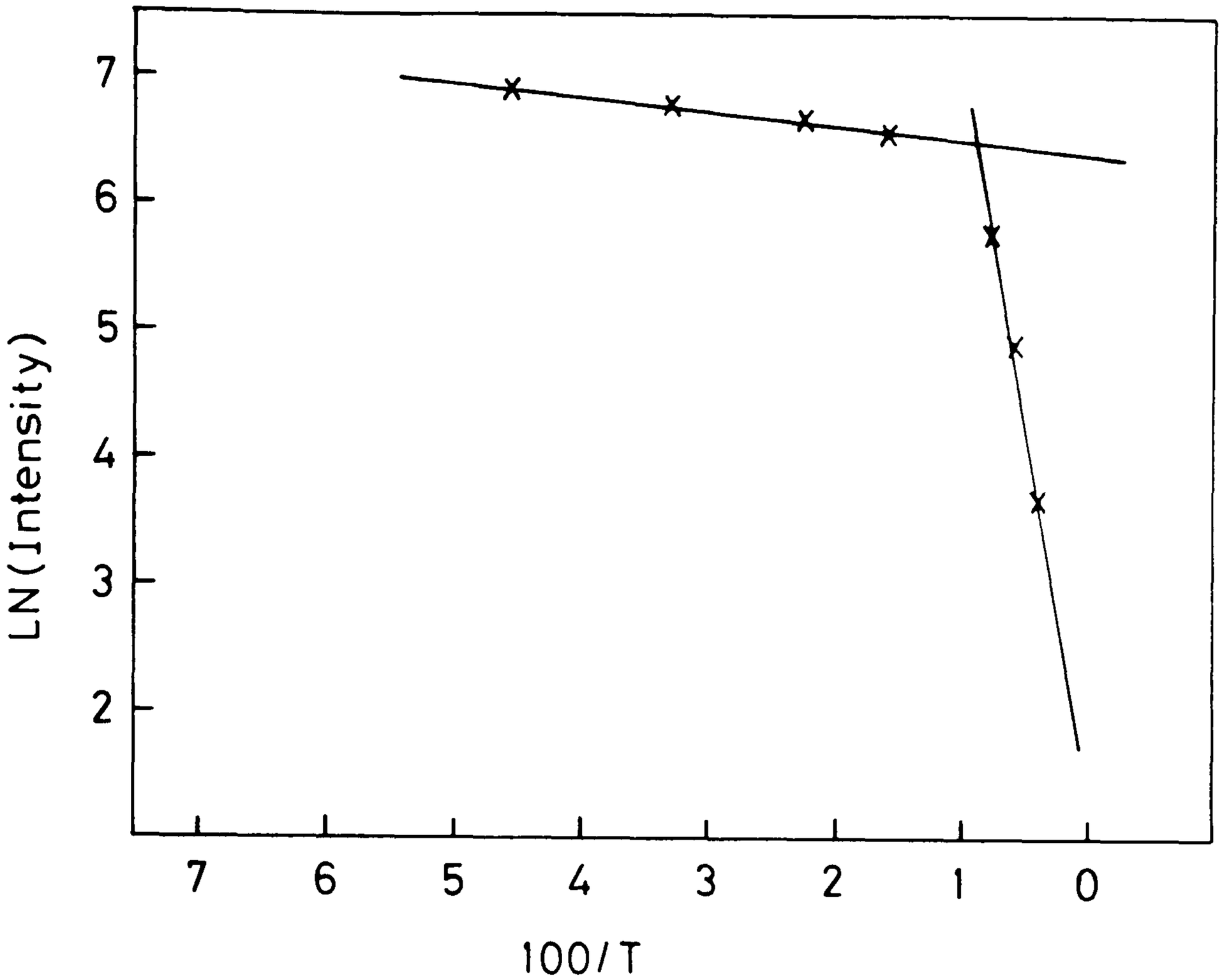

Figure 3.18. Arrhenius plot of the temperature dependance of the green edge emission from MH26. The intensity is measured at the peak of the zero-phonon line and is in arbitary units. The straight line drawn on the right represents an activation energy of 54 meV.

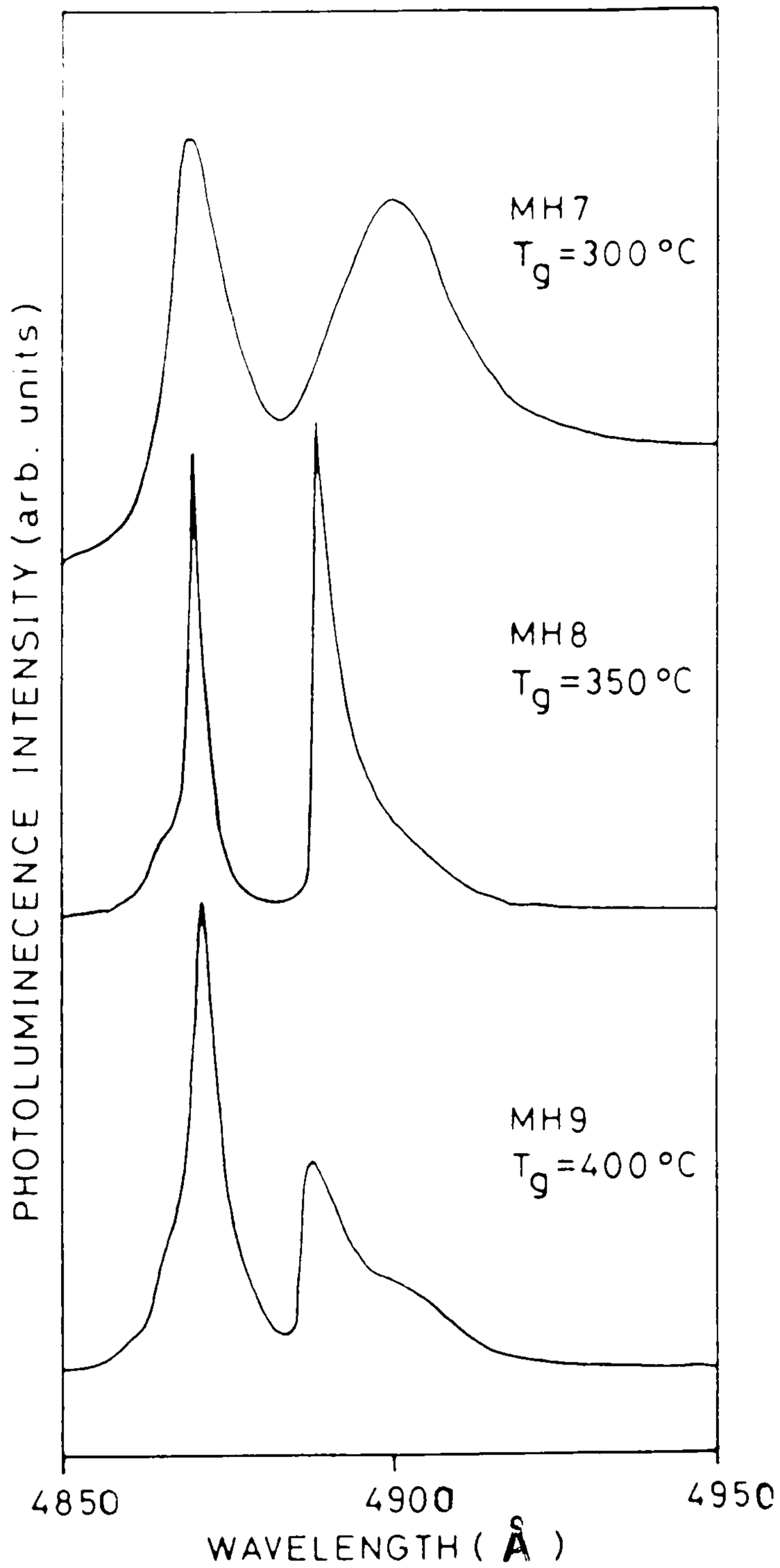

Figure 3.19. Three spectra showing the effects of growth temperature on the bound excitonic luminescence from the CdS epilayers grown on GaAs (111)A.

samples with T_g smaller than 350 ^oC the emission is broad and faint, characteristic of poor material. As T_g was raised above 350 ^oC the luminescence from the epilayers sharpened and brightened rapidly until some broadening was evident again above 400 ^oC. The poor quality of the low T_g material's luminescence is almost certainly due to a high level of crystalline defects. At this low temperature the atoms do not have sufficent kinetic energy to move on the surface and find their correct sites. Such effects are seen for all epitaxial techniques when the substrate temperature is too low. The broadening for high T_g samples may be due to a higher level of impurities in the layer (see section 3.3.3.4).

The green edge emission also showed changes as the growth temperature was raised. Figure 3.20 shows the luminescence from a sample grown at 450 ^oC. It can be seen that the green edge emission is considerably more intense than the excitonic emission, unlike the spectra in figure 3.15 where it is approximately 30 times fainter. The intensity of the green edge emission relative to the excitonic emission is very sensitive to the level of impurities within the layer [28]. The intensity of either the HES or LES series increasing rapidly as the impurity concentration increases. Consequently, the intensity change is consistent with higher impurity incorporation at higher growth temperatures.

Reflection spectroscopy was also applied to the CdS epilayers. The imaginary parts of the refractive index of semiconductors show large anomalies below the band edge corresponding to the free exciton resonances, the reflection minima are taken as occuring at the free exciton energies [32]. Figure 3.21 shows two spectra for layers grown at 350^oC and 450 ^oC. The spectra clearly show the three valence bands (indicated on the figure) characteristic of the wurtzite valence band.

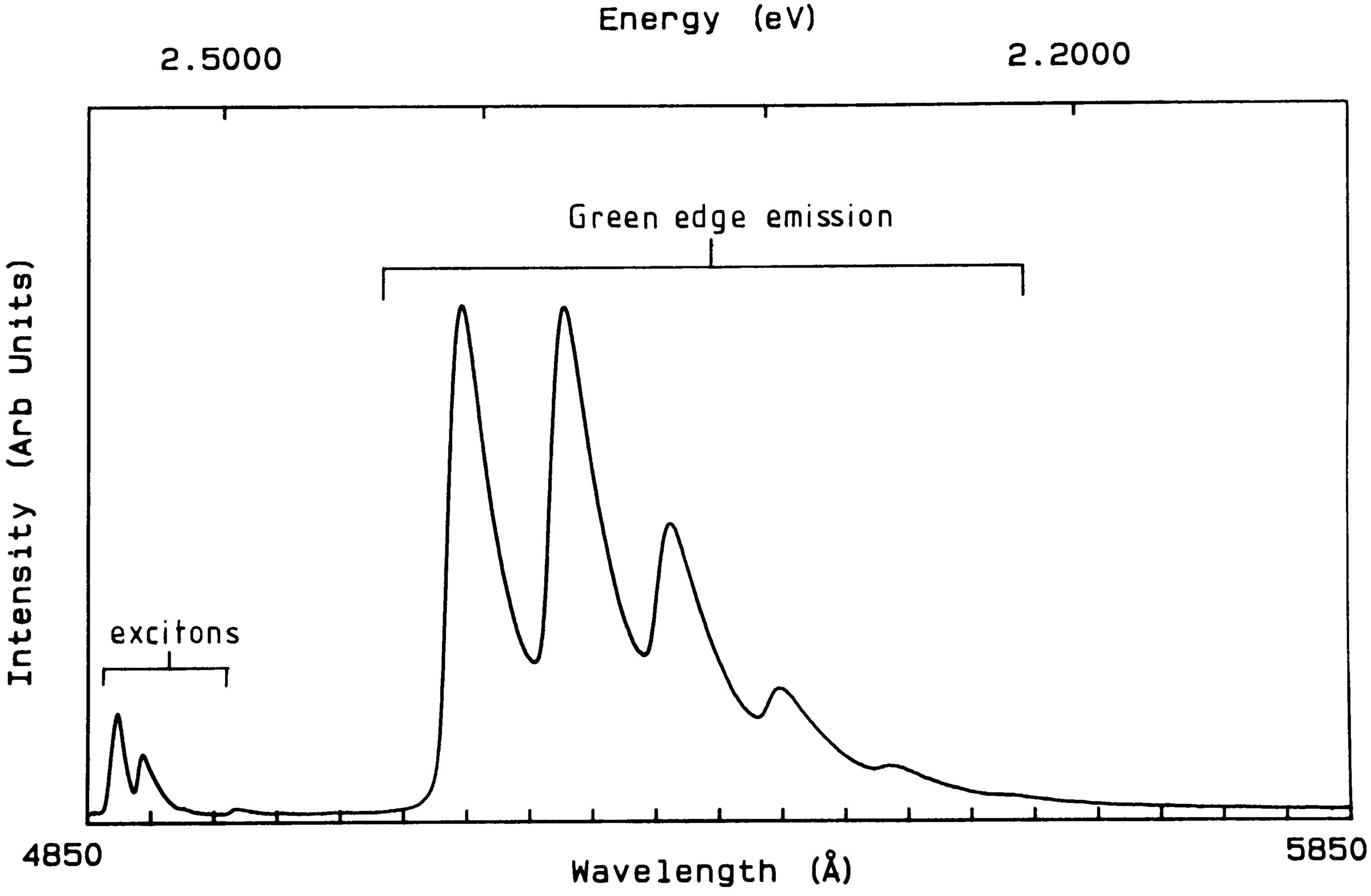

Figure 3.20. Spectrum of edge emission from CdS epilayer grown on GaAs (111)A at 450 ^{o}C (MH102).

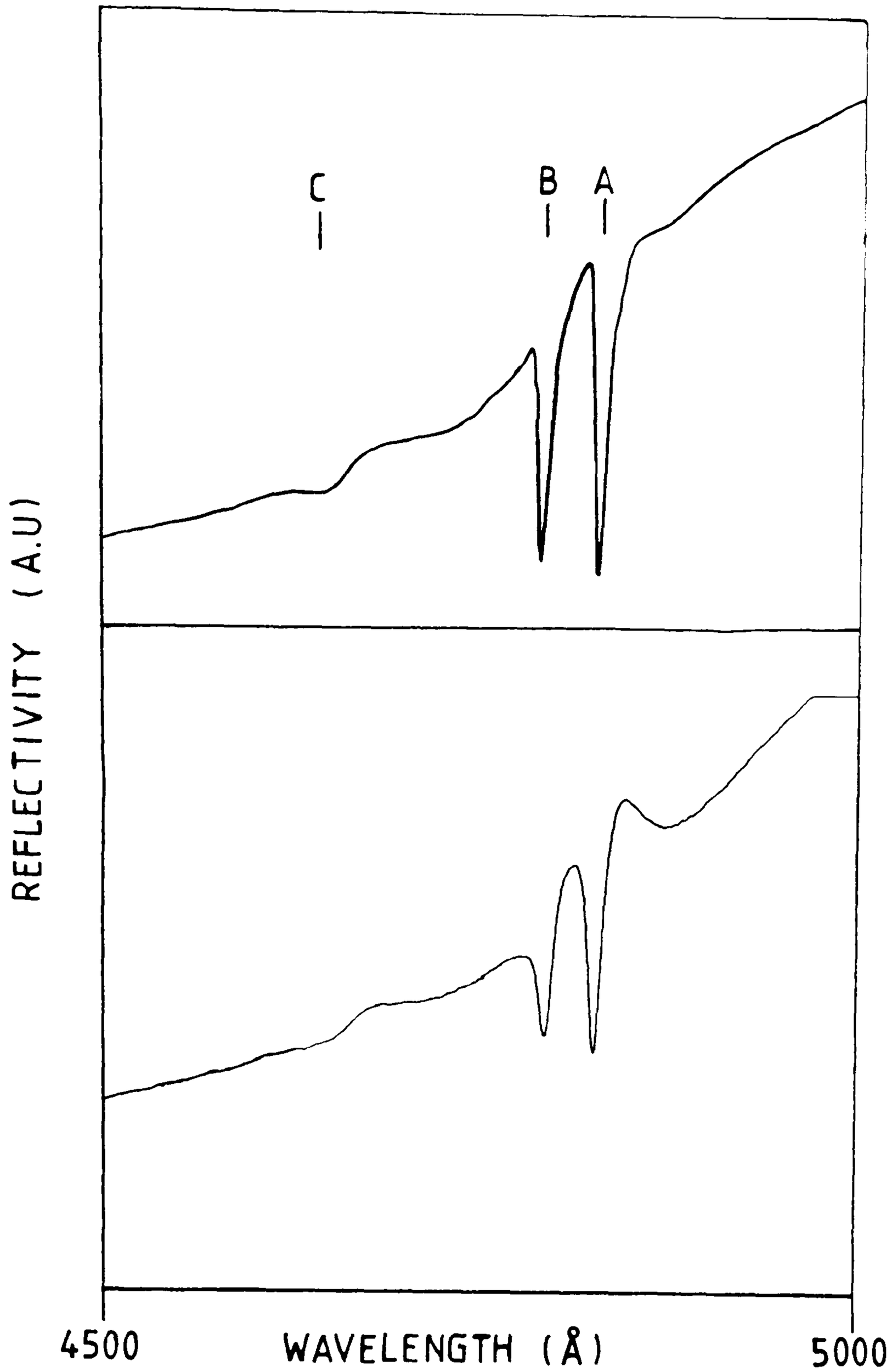

Figure 3.21. Two reflection spectra from CdS epilayers grown on GaAs (111)A showing the three reflection minima corresponding to the three valence bands of the wurtzite band structure. The upper spectrum was obtained from a sample grown at 450°C the lower 350°C.

The reflection minima occuring at 2.551,2.566 and 2.632 eV. These energies correspond exactly to the reflection minima of the A,B and C excitons as reported by Thomas and Hopfield [32]. There is no evidence of strain-induced shifts for these thicknesses (approx 1 μm), indicating that the layers are thicker than the critical thickness. There is a noticeable improvement in the spectra for the higher T_g sample, the resonances become more clearly defined and the C resonance is much more easily seen.

3.3.3.2 GaAs 100 substrates

Figure 3.22 shows the near gap emission from a layer of CdS grown at 400^{o}C on GaAs(100) (sample MH10a). The emission shows clearly both excitonic emission and green edge emission. It was observed in the RHEED section that this sample demonstrated wurtzite epitaxy on the sphalerite (100) face. However, the photoluminescence indicates poor quality on this face relative to the CdS grown on the (111)A face (see previous section) with an exciton line FWHM of 15 meV (cf 1.5 meV above). The green edge emission is not well resolved and is of comparable intensity to the excitonic emission. The green edge emission seems to contain luminescence bands from several different defect centres.

In the light of the purity of the layers grown on GaAs (111)A, we attribute the breadth of the excitonic emission to high levels of dislocations causing strain broadening. It is obvious that the CdS grown on the (111)A face is of superior quality. Moreover, the CdS grown on the (111)A face was grown at the lower temperature of 350 ^{o}C. CdS grown on 100 GaAs at this temperature was polycrystalline and showed only broad band luminescence. We conclude that the CdS grown on

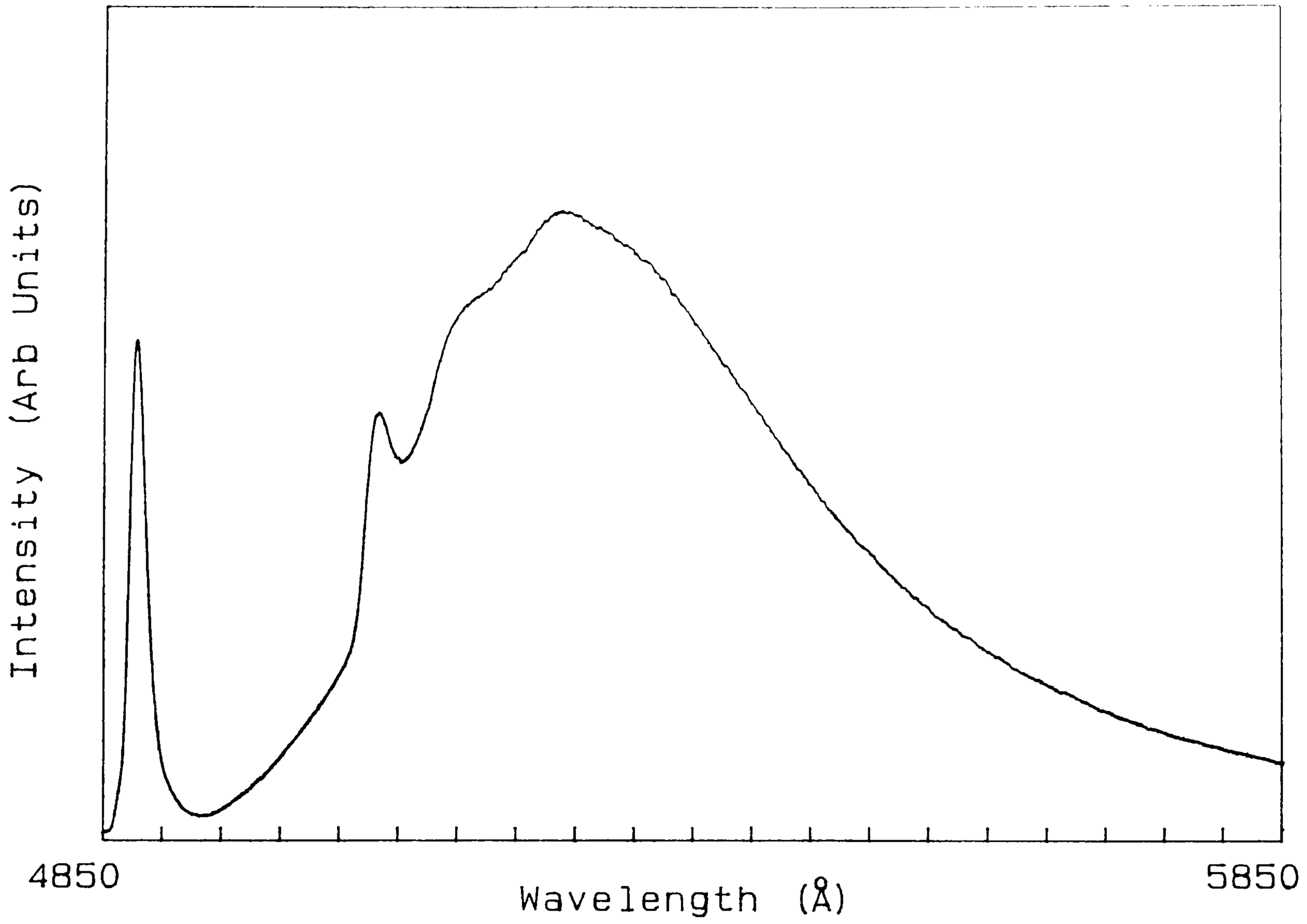

Figure 3.22. Photoluminescence spectrum showing the edge emission from a CdS epilayer grown on GaAs (100) at 400°C (MH10b).

(100) GaAs, although epitaxial, contains more lattice defects than that grown on (111)A GaAs at the same temperature. We note, however, that the CdS epitaxy on this face at higher growth temperatures is of surprisingly good quality and represents the first reported wurtzite epitaxy on a sphalerite (100) face.

3.3.3.3 InP (111)B substrates

The other principal substrate experimented with for CdS growth was InP (111)B. The mismatch between the (111) InP face and the CdS (0001) face is 0.27% compared to a figure of 3.5% for GaAs. It was hoped that the close lattice matching would reduce the level of dislocations in the epilayer and restrict impurity diffusion. Figures 3.23 and 3.24 show two spectra of the luminescence from sample MH20, a 1 μm CdS epilayer grown on InP 111(B) at 350 ^{o}C. The emission is dominated by the I_2 donor bound exciton emission at 4868.6Å (2.545 eV). This line is twenty times broader than for CdS grown under similar conditions on GaAs (111)A. There is no evidence of the usual CdS green edge emission, only a weak peak at 4985 Å accompanied by what appear to be phonon replicas. The breadth of the I_2 line indicates a high concentration of donor impurities. The material grown on GaAs under the same conditions does not show such a broad I_2 line and we can conclude that the donors responsible are either intrinsic or originate from the InP substrate. We can estimate the depth of the donor responsible for the I_2 line by using Haynes rule as outlined in section 1.5.2, equation (ix) [33]. Using the value for k_d in CdS of 0.22 [27], we find a donor depth of 33.2+_1 meV. This is consistant with the presence of several possible donors including Indium, which forms a shallow donor in CdS with a depth of 33.8 meV [28].

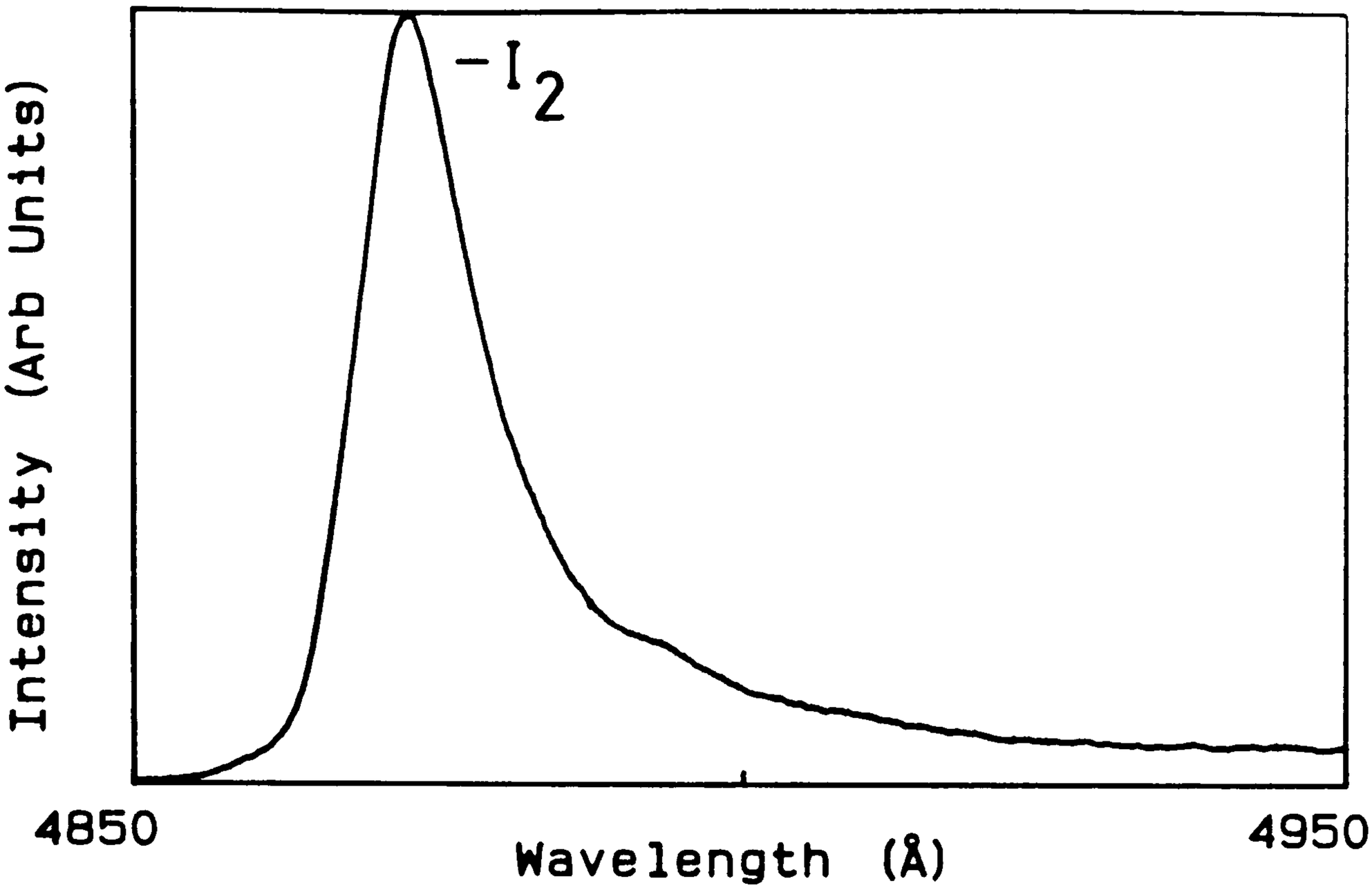

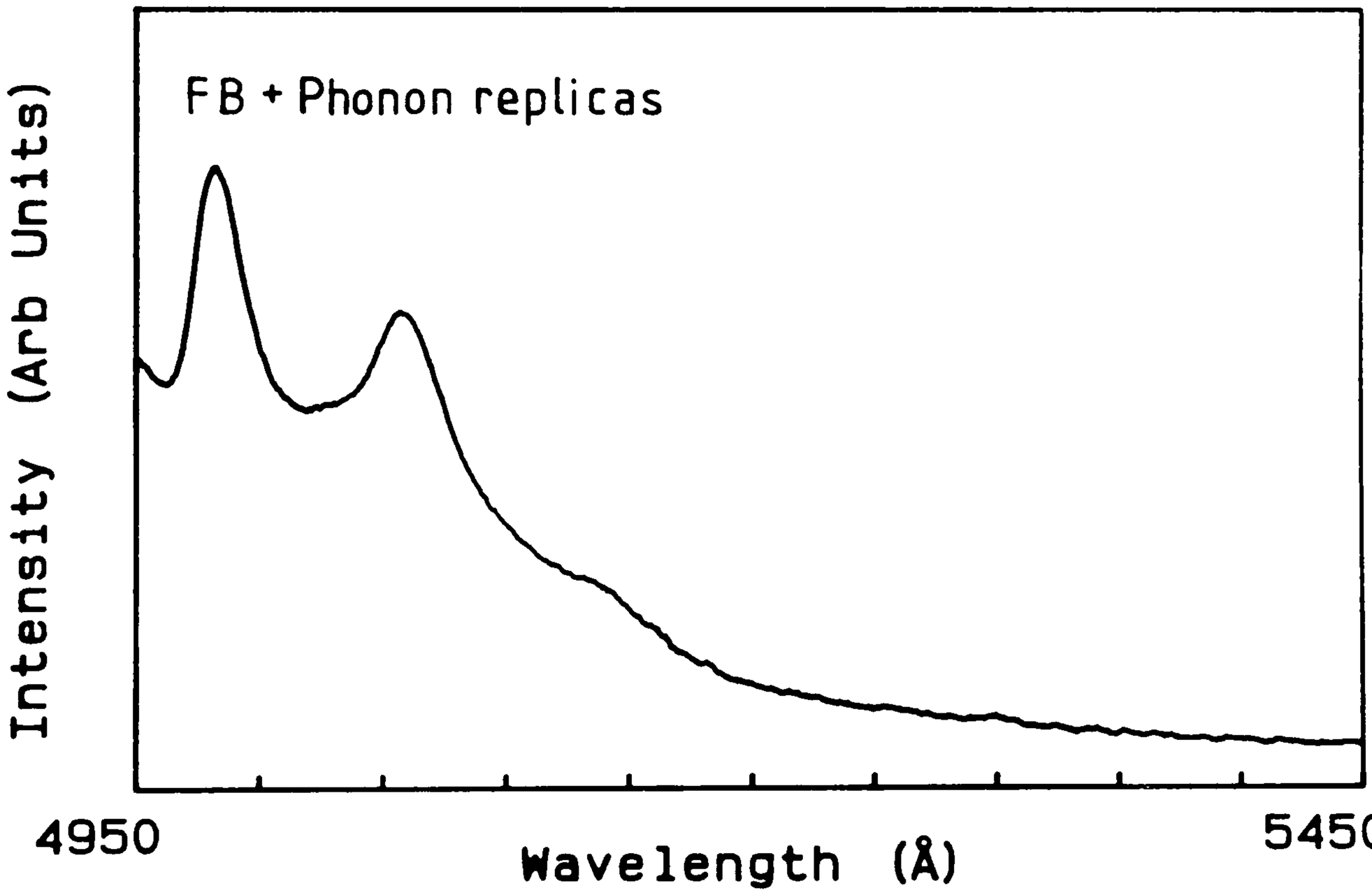

Figures 3.23 (upper spectrum). Photoluminescence spectrum showing excitonic emission from a CdS epilayer grown on InP (111)B at 350°C.

Figure 3.24 (lower spectrum). Spectrum from same sample showing green edge emission.

Figure 3.24 shows the green edge emission from the sample. The emission appears to show a zero-phonon peak at 4985 Å accompanied by a series of phonon replicas with the right energy spacing for the CdS LO-phonon. Figure 3.25 shows the temperature dependence of this emission. It can be seen that the emission intensity remains constant until approximately 50 K. Above 50K the peak intensity is quenched with an activation energy of 35 meV. This behaviour is consistent with free to bound recombination [29]. Also, the emission is much shallower than any previously reported bound to bound process in CdS. Assuming a free to bound recombination process we calculate from equation (xviii) an acceptor depth of 106+_3 meV. It is known that phosphorus forms an acceptor complex centre approximately 120 meV above the valence band in CdS [34]. The discrepancy in these two values could be accounted for by the kinetic energy term in equation (x), section 1.5.3. Moreover, there are no other reported acceptors close to this depth in CdS. A similar band was observed in CdS grown at high temperatures on GaAs, this band was ascribed to free to bound recombination at arsenic complexes lying 94 meV above the valence band (see section 3.3.3.4). We therefore ascribe the emission at 4985Å to free to bound recombination at phosphorus complex acceptor sites.

The conclusion is clear: large scale indiffusion of In and P occurs when CdS is grown on InP at this temperature. The diffusion must be the result of the greater reactivity of the InP relative to GaAs. The CdS epilayers grown on this face are of reasonable structural quality but, even when grown at 350^{o}C, autodoping by both indium and phosphorus is dominating the optical properties of the resulting layers. Because of the close lattice match to InP many CdS layers were grown on it under different conditions and with varying substrate preparations (see appendix 1). The luminescence shown in figures 3.23

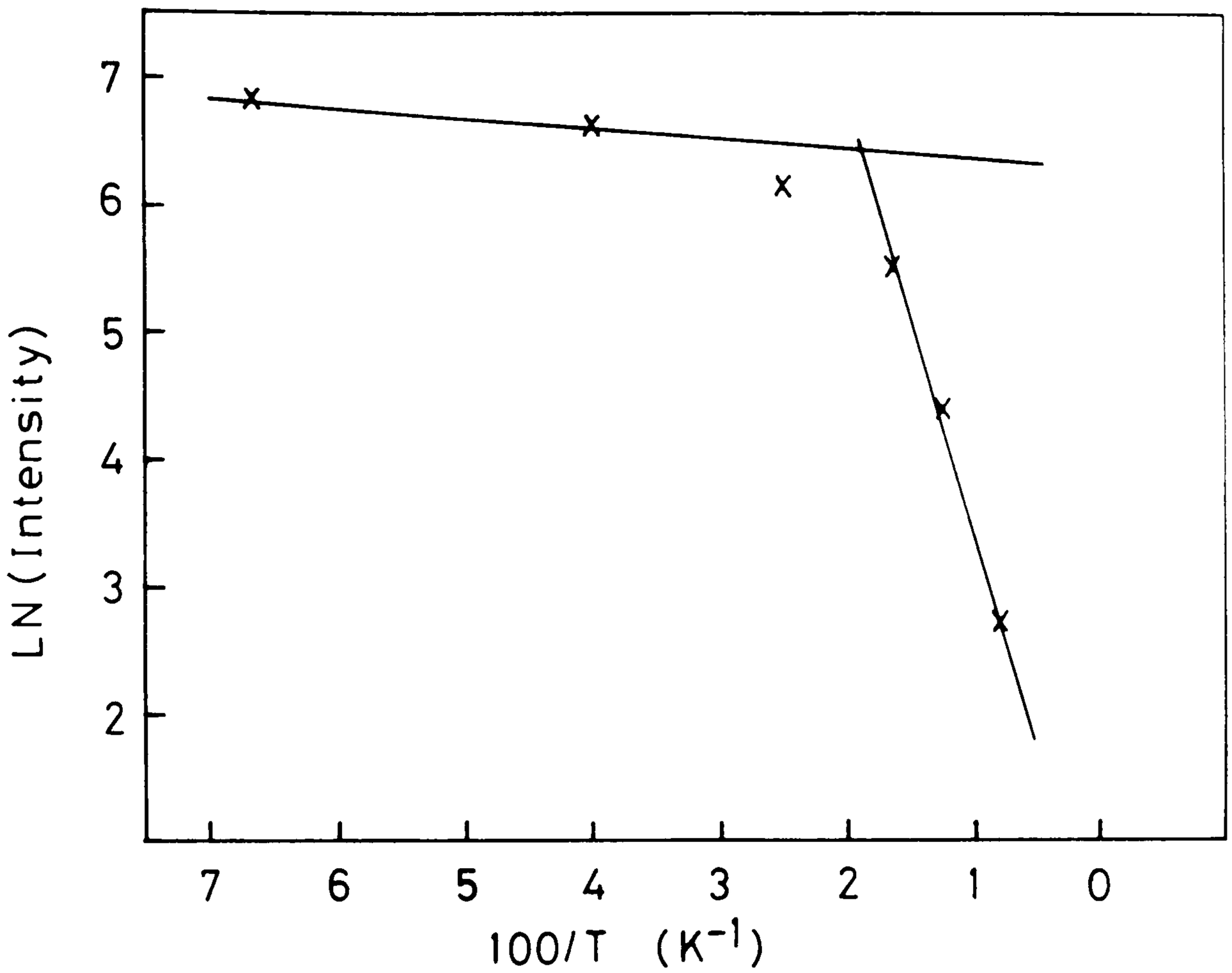

Figure 3.25. Arrhenius plot of the temperature dependence of the green edge luminescence from a CdS sample grown on InP (111)B (MH34). The straight line drawn on the right represents an activation energy of 35 meV.

and 3.24 was the best obtained from any such epilayer. It was apparent that the problem of massive autodoping was not easily solved. For this reason InP is an unattractive substrate for the growth of CdS by MOCVD. However, such evidence of diffusion was not found for CdS grown on GaAs, where the lattice mismatch is greater. It is clearly of interest to study whether autodoping occurs in this case.

3.3.3.4 Autodoping on GaAs

Table 3.2 shows the spectral and energy positions of all the major emissions observed in the epitaxial CdS along with our identifications and the sources used for comparison. It is interesting to compare the luminescence from the MOCVD grown material with that grown by other epitaxial methods. Christmann et al [35] studied CdS grown by VPE on GaAs (111)A at high temperature (650-750 ^{o}C). They observed a spectrum similar to that from the MOCVD material but the green edge emission was much more intense than the excitonic emission. In addition they observed the I_{8p} and I_5 lines [36]. These they ascribed to cadmium interstitials resulting from the large cadmium over-pressure present in their growth process. Yoshikawa and Sakai [37] studied the luminescence from CdS layers grown by the close-space technique on GaAs (111)A. These samples differ from the MOCVD material mainly in their growth temperature being much higher (>500^{o}C). These authors conducted their experiments at 77K and observed the I_2 and free to bound emissions; in addition they observed two extra emissions at 500nm and 510nm and called them the X and HT2 bands. These were ascribed to pair recombination involving two acceptor complexes at 94meV and 143meV. They postulated that these complexes were due to arsenic and GaV_{cd} complexes respectively, hence assuming a large degree of gallium and

Wavelength(Å)	energy(eV)	name	origin
4853	2.554	X_o	free exciton
4859	2.550	I_3	exciton bound to D^+
4869.9	2.5447	I_2	Donor bound exciton
4888.4	2.5356	I_1	Acceptor bound exciton
4958	2.500	I_1-LO	phonon replica
5045	2.456	I_1-2LO	phonon replica
5145	2.409	FB	free to bound emission

Table 3.2. Emissions observed from CdS grown on GaAs. The identifications are based on the peak positions given in [27]. The identification of the free to bound emission is described in the text.

arsenic indiffusion. We observed no such features at 1.6K or at 80K for any of our CdS epilayers. Indeed there was no clear evidence of a large impurity presence. The low growth temperature of MOCVD evidently reduces the indiffusion greatly. It is also possible that the superior quality of the MOCVD grown CdS prevents the formation of the complexes involved by restricting the formation of intrinsic defects. The width of the I_2 line increases for the high T_g samples suggesting greater concentrations of donors for these samples.

Autodoping of epitaxial layers by impurities from the substrate is a well studied problem in epitaxial growth. It has been shown that even at 300^{o}C there is significant diffusion of gallium into epitaxial ZnSe [38]. Of the two substrate elements Ga and As we would expect the smaller atom (gallium) to diffuse the most rapidly. Gallium forms a shallow donor in CdS at 33.1 meV below the conduction band [28]. It was noted above that the position of the I_2 line in the spectra is consistent with the presence of gallium or a number of other possible donors. We are therefore unable to state whether Ga is the major impurity in the layers grown at 350 ^{o}C.

It is possible to gain an insight into the problem of autodoping by considering the diffusion of Ga into CdS. We will use epitaxial ZnSe as a comparison material as it is known to show the effects of Ga diffusion even at low temperatures. Unfortunately there are no measurements of the diffusion of Ga into CdS in the temperature range 350-450^{o}C. However, Jones and Mykura [39] did study this diffusion in the range 660-960 ^{o}C and for this range. By studying experimental data they proposed the following form for the diffusion constants of Ga along the c-axis of CdS.

$$D_{\perp} = 4.7 \times 10^{-4} \exp\left(\frac{-2.35}{KT}\right) \quad m^2 s^{-1} \text{ at.}\%^{-1} \qquad \text{(xv)}$$

Notice that the constant is inversely proportional to the Ga concentration. Jones and Mykura suggested that in the limit of low concentration D becomes independent of the concentration below 0.1 At%. The same relation was studied for the diffusion of Ga in ZnSe in the temperature range 500-700^{o}C by Takenoshita et al [40]. They found that the diffusion constant was independent of concentration and could be expressed as

$$D_{znse} = 6.76 \times 10^{-2} \exp(-1.8/KT)\ m^2 s^{-1} \qquad \text{(xvi)}$$

We can now simply extrapolate backwards to achieve an estimate of the relative diffusion of Ga in the two compounds, neglecting the effects of misfit dislocations in epitaxial material. The curves resulting for these equations are shown in figure 3.26. It is evident that the diffusion rate of Ga is somewhat higher in ZnSe than in CdS over this temperature range, in particular at 450 ^{o}C the rate is 10 times greater in ZnSe than in CdS. Thus the observation of the purity of the layers, relative to other II-VI compounds grown on GaAs, even when grown at higher temperature, is partially supported by the Ga diffusion rates. Although some Ga diffusion must occur and there is evidence for this in the luminescence. It is worth noting that the Ga diffusion rate in CdS is inversely proportional to the Ga concentration. Therefore, qualitatively, the diffusion rate at any particular distance from the interface will fall with time. This effect may restrict the diffusion of gallium into CdS below that in a similar ZnSe epilayer. This calculation, however, is governed only by the rate of diffusion of Ga into the two compounds. In practice other effects may be more important such as chemical reactions between the GaAs surface and the growing layer. Such effects will be strongly dependent

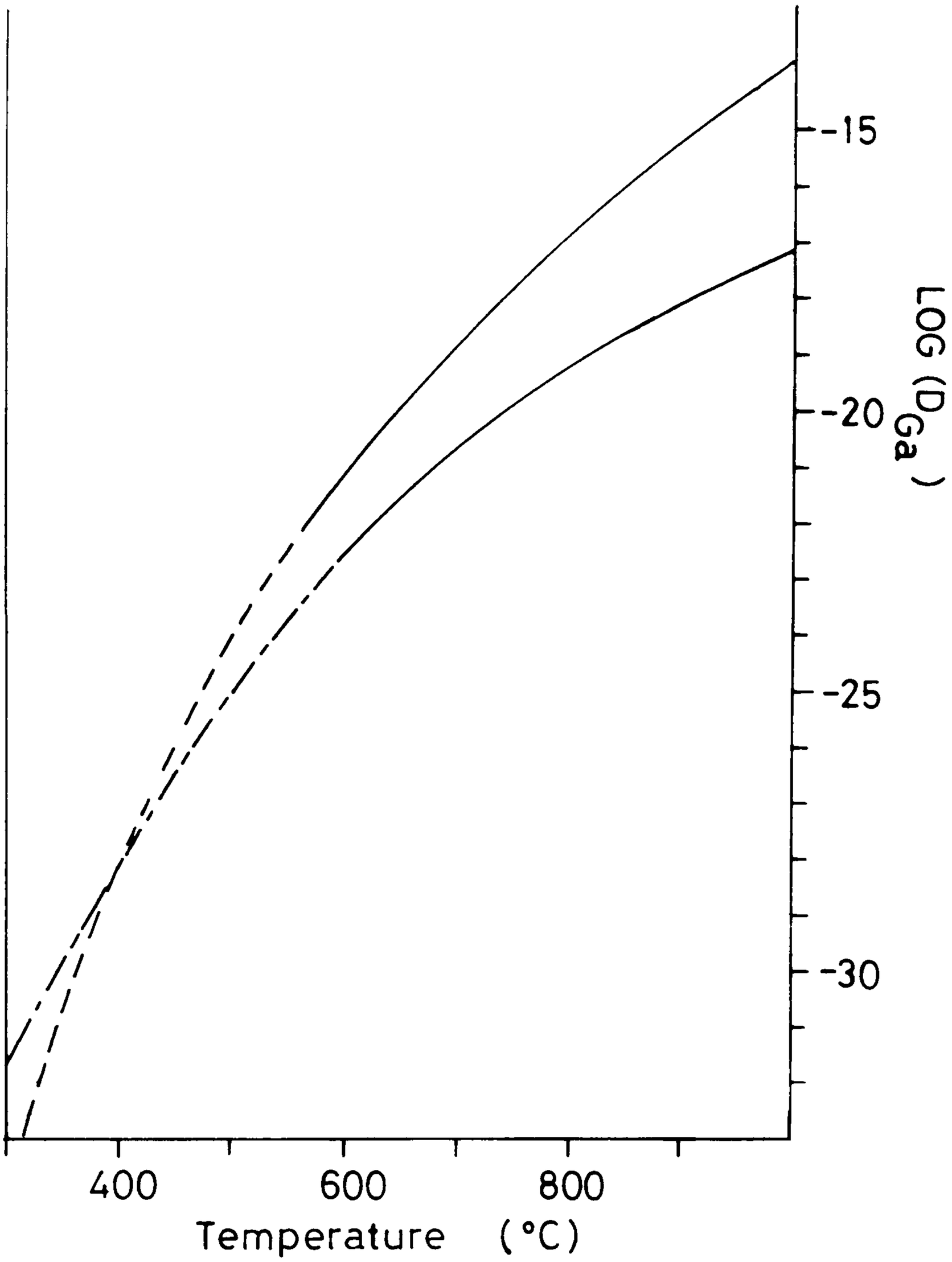

Figure 3.26. Diffusion rates of Ga in CdS and ZnSe calculated using equations (xix) and (xx) in section 3.2.2.4 respectively. The upper curve is that of CdS.

on the surface grown on and the reagent used, these aspects are too complex to be discussed here.

3.3.4 Cadmium Selenide

3.3.4.1 Epilayer quality

In the same manner as for the CdS samples, the CdSe epilayers were initially grown on a series of substrates. Photoluminescence was then used to assess the suitability of these substrates for the growth of good quality material. Figures 3.27,3.28 and 3.29 show a series of spectra of the near gap emission obtained from CdSe layers grown at 350 ^{o}C on InAs (111)A, GaAs (100),(110), InP (111)B and a buffer layer of CdS on GaAs (111)A: figure 3.30 shows similar spectra from CdSe grown on GaAs (111)A. The sample numbers and substrates used are indicated on the diagrams. These spectra from layers grown under similar growth conditions do not show the large differences as do photoluminescence from CdS epilayers grown on the same substrates. The luminescence from the layer grown on the GaAs 111(A) shows resolved exciton lines, unlike those grown on the other substrates. The problems associated with the reactivity of the InAs and InP substrates made these less attractive choices than GaAs although the mismatch is less for these compounds. It was decided as a result of the photoluminescence results, and in the light of the quality of the CdS grown on this surface, to concentrate attempts at CdSe growth on GaAs 111(A) substrates.

The poor quality of the CdSe epilayers relative to the CdS was discussed in sections 3.2.3 and 2.4. It was suggested there that the higher stability of the CdSe cubic phase and reagent prereaction were responsible for the observed differences. It was reported in section

Figures 3.27,3.28 and 3.29 (overleaf and on successive pages) Series of photoluminescence spectra showing edge emission from CdSe epilayers grown on various substrates at 300-350 C. The substrate used and sample number are indicated in the top right of each spectrum.

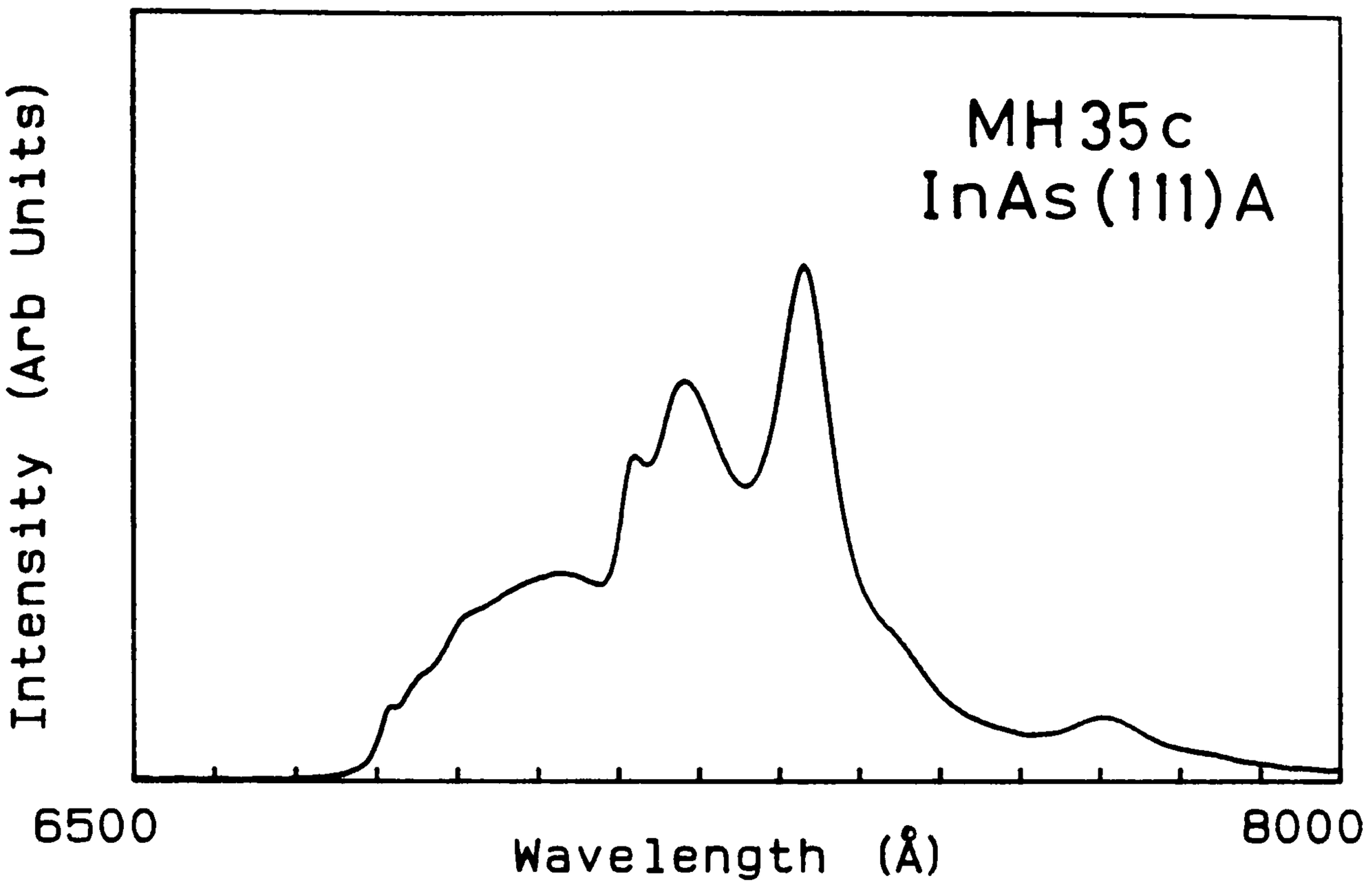
MH35c
InAs(111)A
Intensity (Arb Units)
6500
8000
Wavelength (Å)

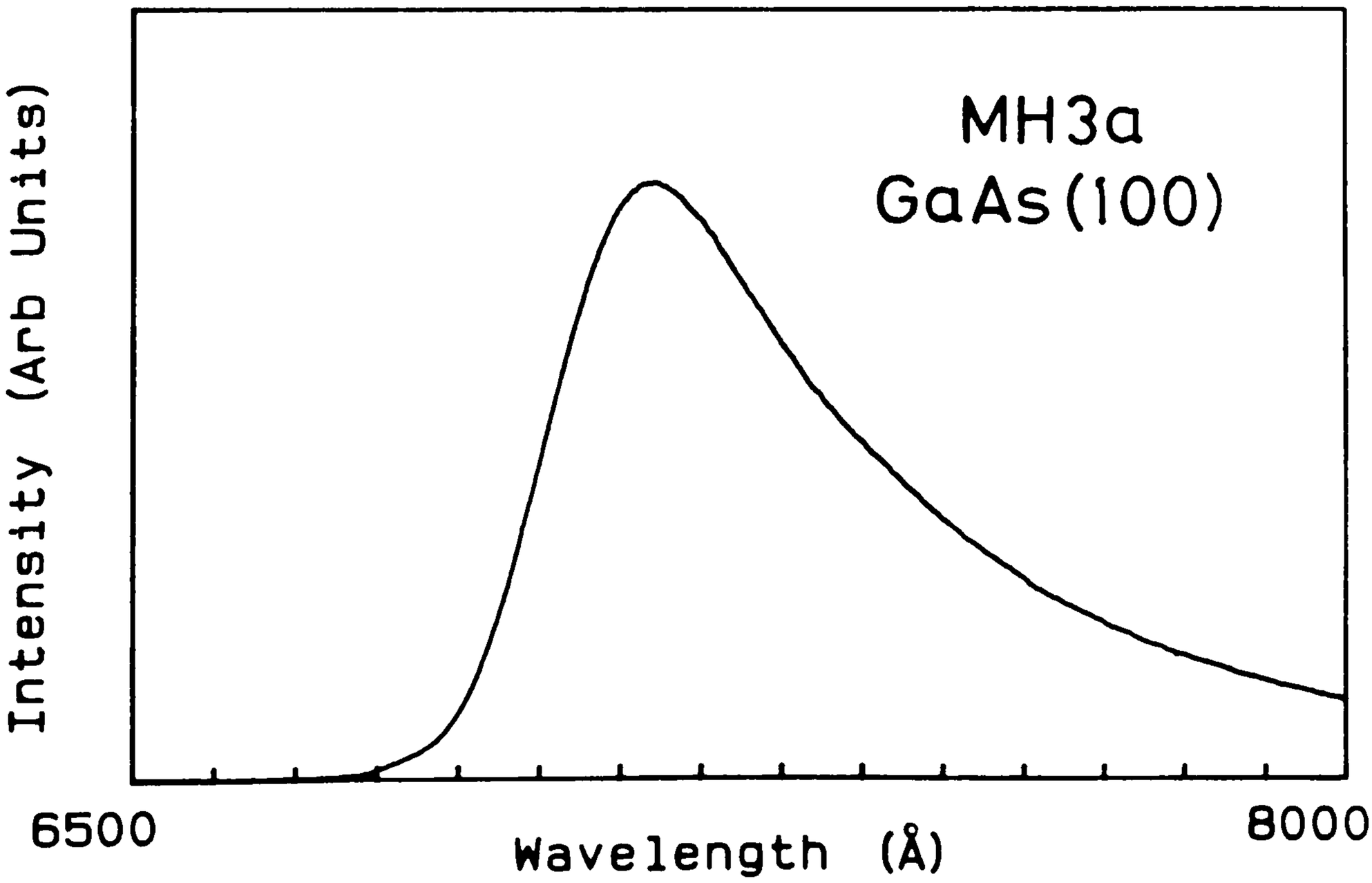
MH3a
GaAs(100)
Intensity (Arb Units)
6500
8000
Wavelength (Å)

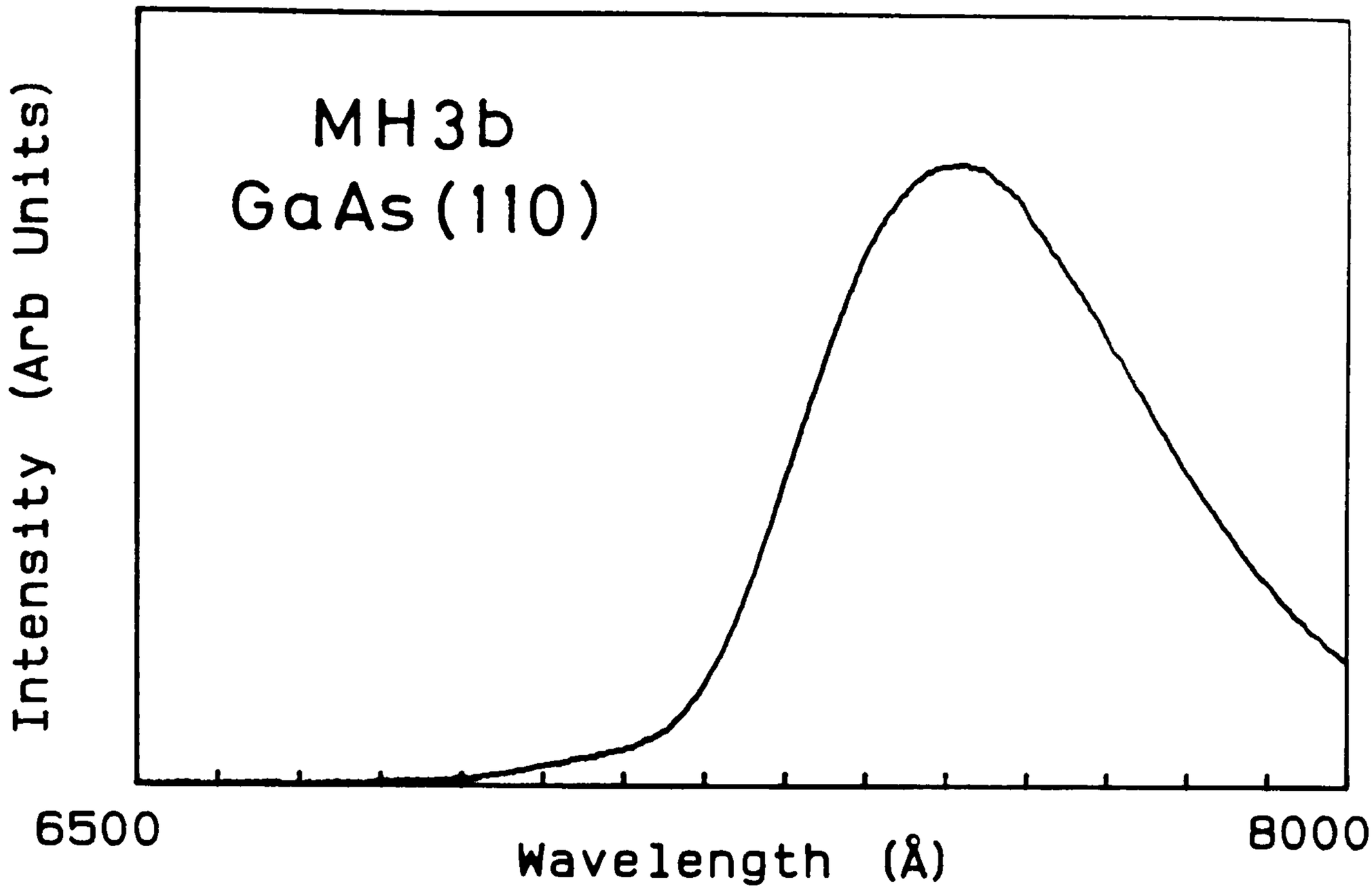
MH3b
GaAs(110)
Intensity (Arb Units)
6500
8000
Wavelength (Å)

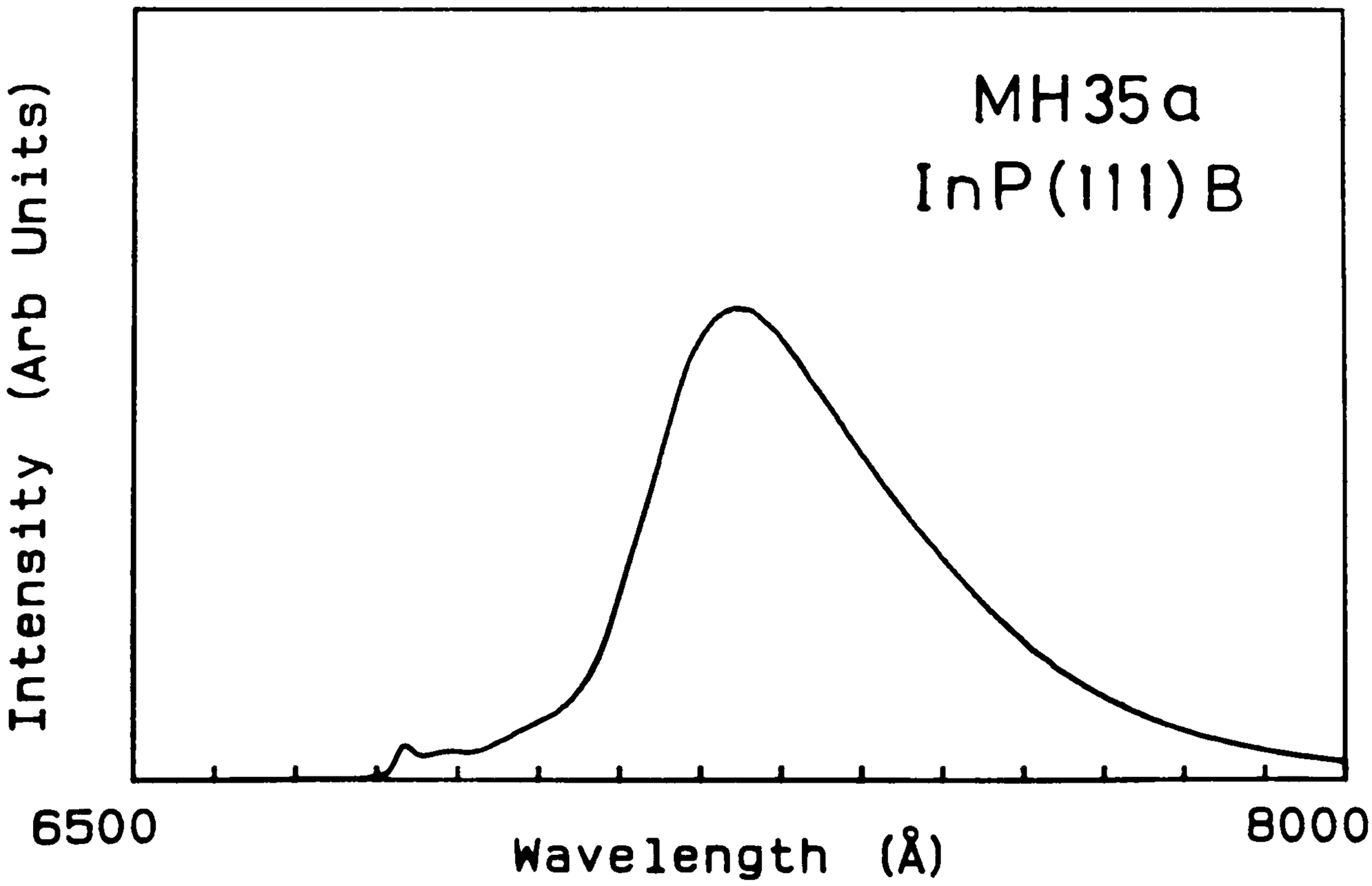
MH35a
InP(111)B
(Arb Units)
Intensity
6500
8000
Wavelength (Å)

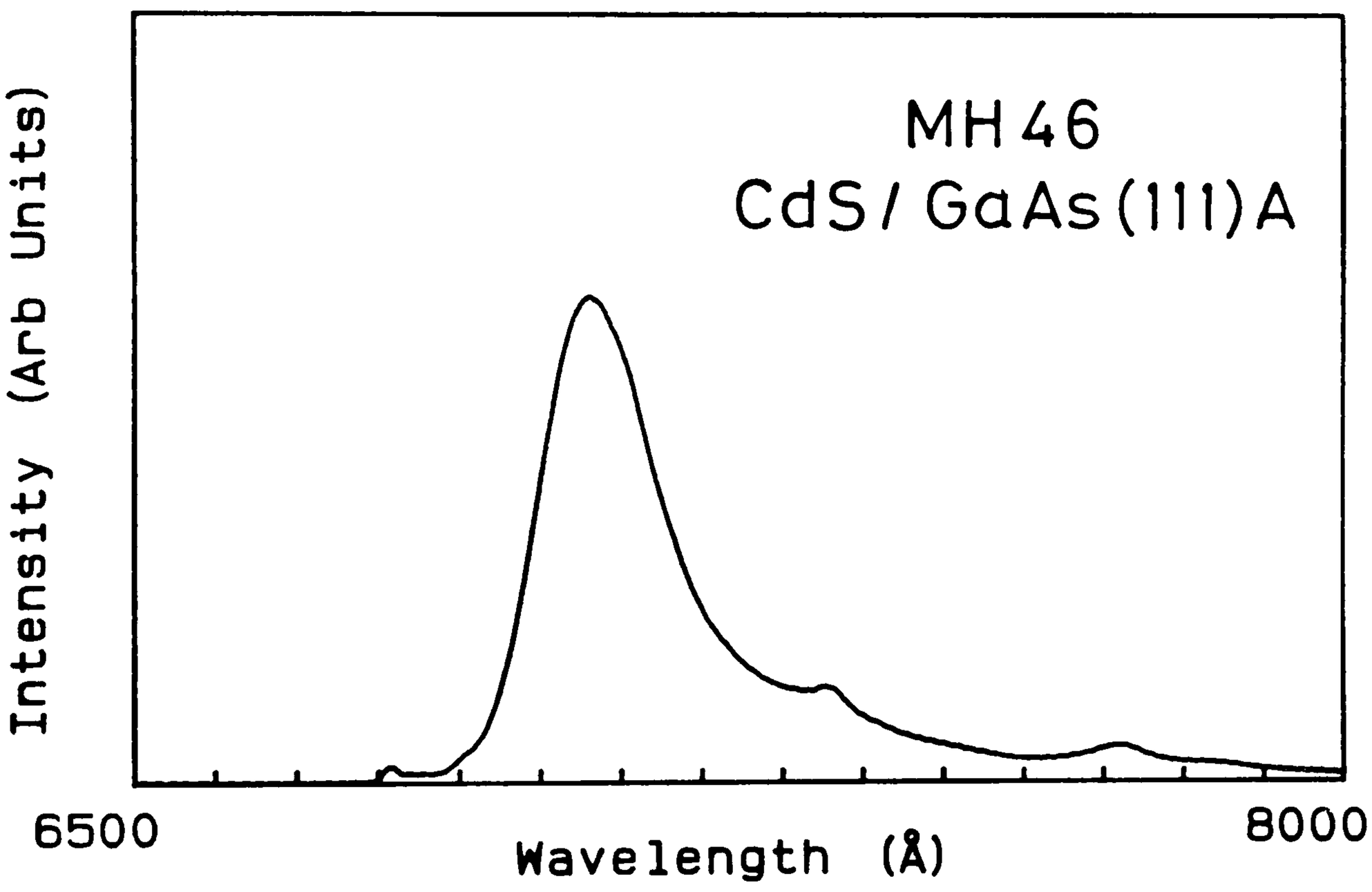
MH 46
CdS / GaAs (111) A
Intensity (Arb Units)
6500
8000
Wavelength (Å)

2.4 that raising the temperature reduced the formation of the hexagonal growth structures and this could be a result of lower vapour saturation and/or a decrease in the stability of the cubic phase. In order to investigate the effect of growth temperature, a series of CdSe epilayers was grown on GaAs (111)A with increasing T_gs. The photoluminescence spectra of the series were then recorded.

Figures 3.30 and 3.31 show four spectra of the near-gap emission from CdSe epilayers grown on GaAs at 300,350,400 and 450^{o}C. The luminescence from the layer grown at 300^{o}C is interesting as at first appearances it shows excellent quality. In fact it demonstrates the limitations of photoluminescence as an assessment technique, since Laue X-ray plates of this sample clearly show that it is polycrystalline. To explain the luminescence we must propose that the individual crystals have grown so large as to produce good quality emission. Similar effects are seen for polycrystalline ZnSe when the particle size exceeds a few tens of microns [41]. It is clear that the layer is not growing epitaxially. However, the quality of the spectrum at least serves to demonstrate that large quantities of impurities are not being incorporated from the MOCVD sources. Indeed the crystalline quality of the individual crystals must be relatively high. The remaining spectra show a clear trend to higher quality epitaxial material as the temperature is raised.

The emission for the low T_g samples is dominated by a broad band peaking at 7015Å (1.765 eV labelled as Y in the diagram). As the growth temperature is raised the emission at 7015Å fades and a deeper emission at 7150 Å accompanied by phonon replicas dominates in the infra-red. This emission occurs at the spectral position of the free to bound recombination reported by Reynolds et al [42]. The corresponding acceptor depth being 110+_ 3 meV, consistent with either Li or Na

Figures 3.30 and 3.31. Four photoluminescence spectra showin the effect of growth temperature on CdSe epilayers grown o GaAs (111)A. The growth temperatures and samples numbers ar indicated in the top right of each spectra.

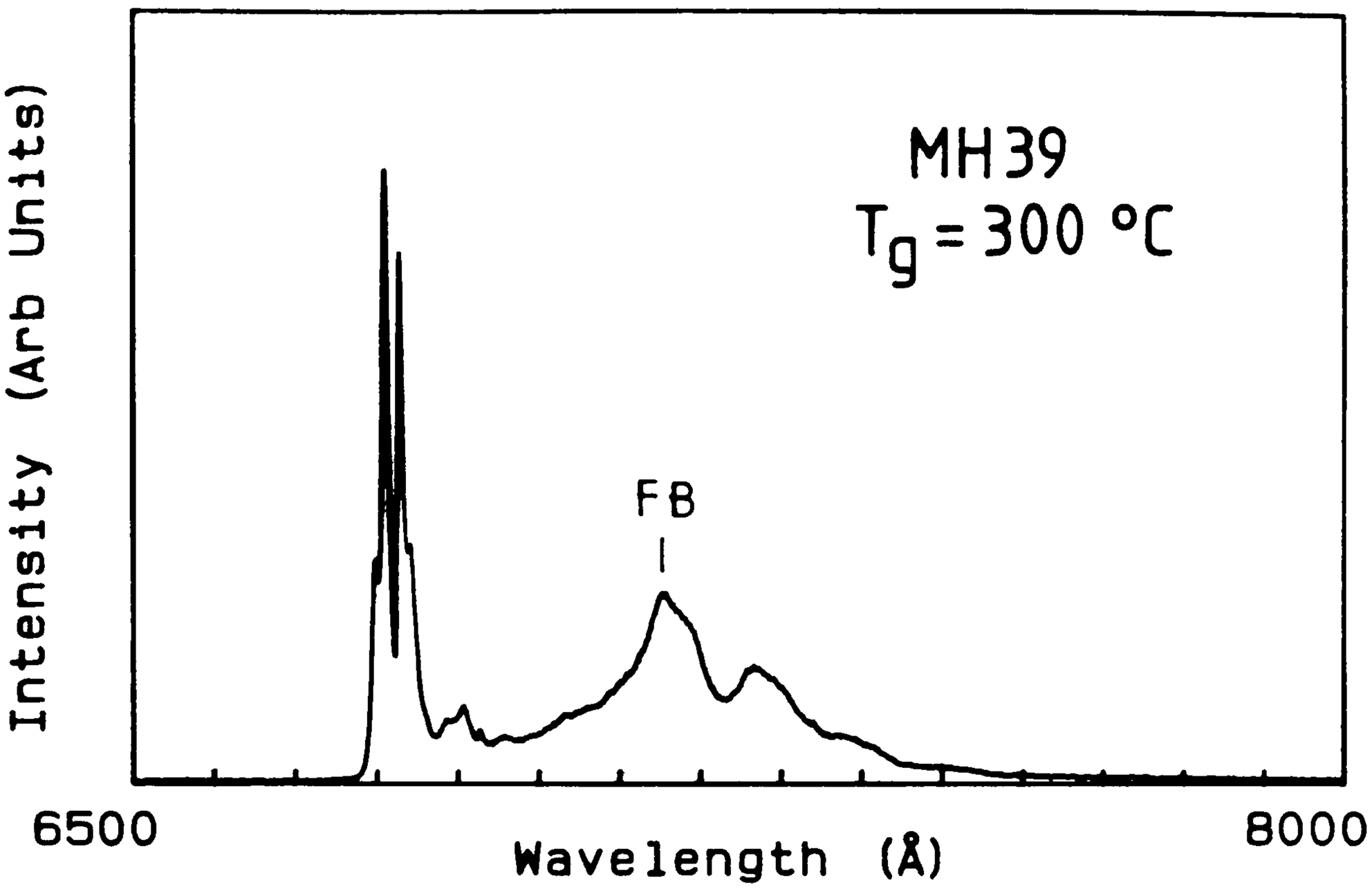
MH39
T_g = 300 °C
FB
Intensity (Arb Units)
6500
8000
Wavelength (Å)

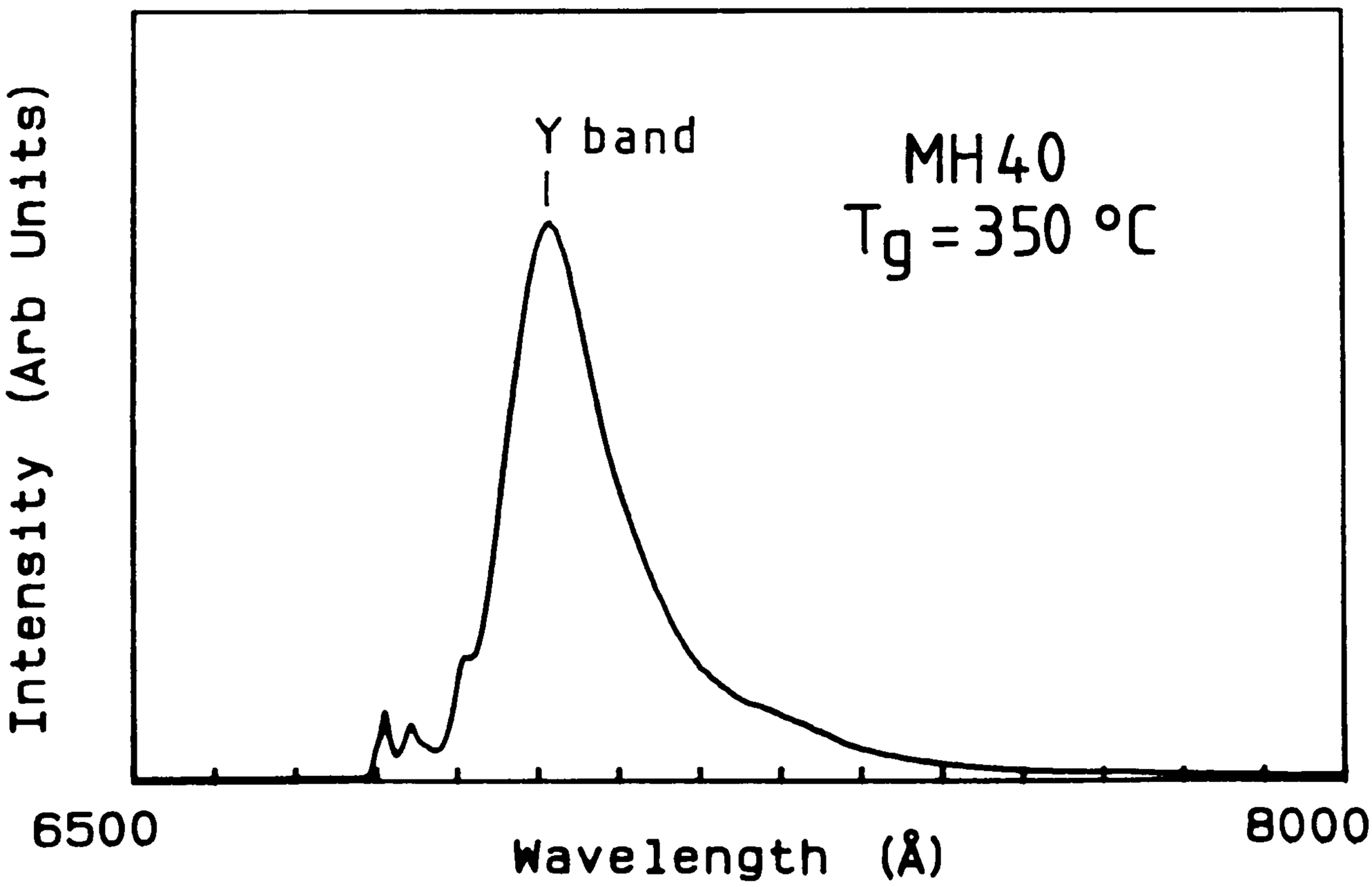
Y band
MH40
T_g = 350 °C
Intensity (Arb Units)
6500
8000
Wavelength (Å)

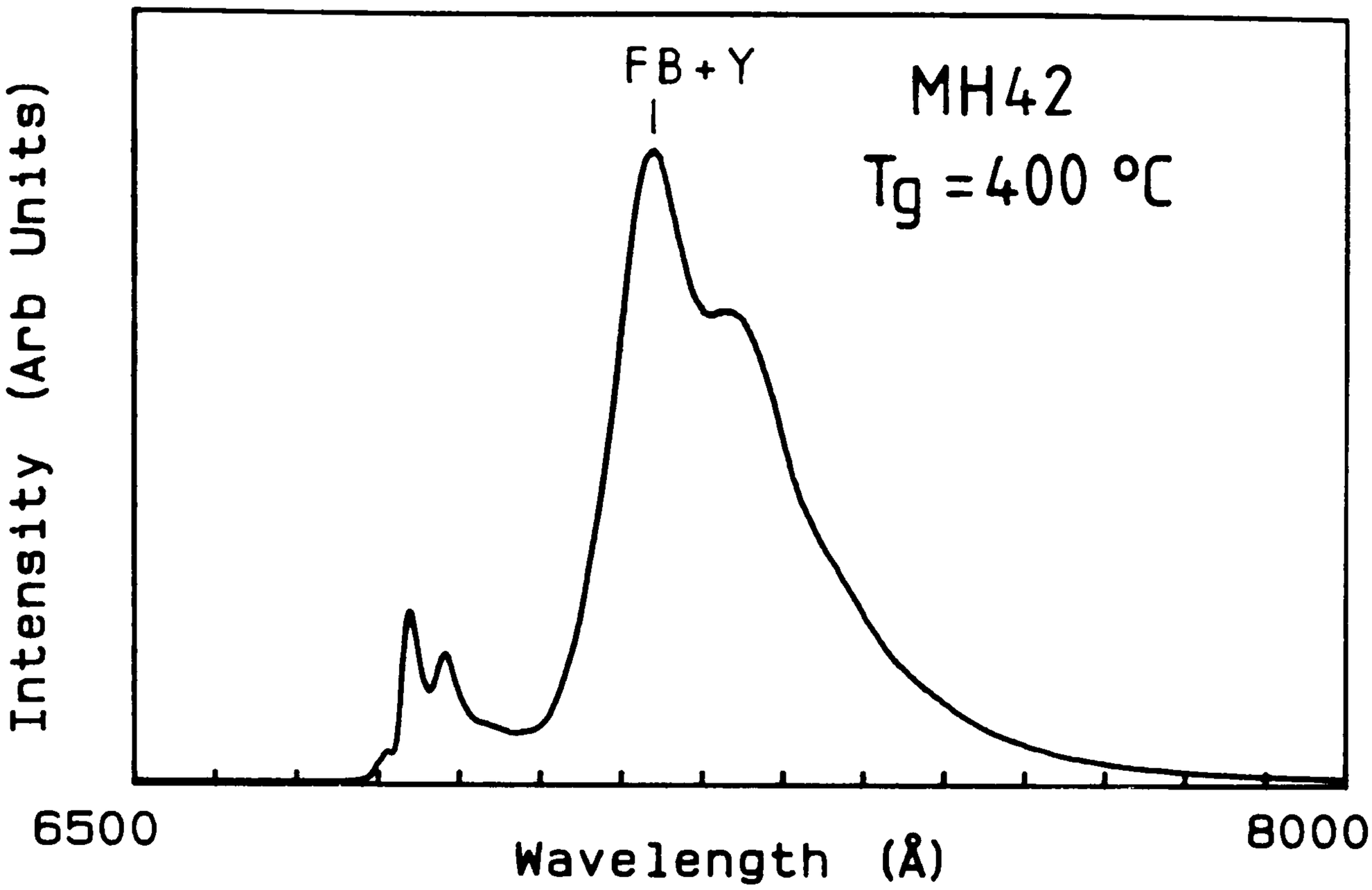
FB + Y
MH42
T_g = 400 °C
Intensity (Arb Units)
6500
8000
Wavelength (Å)

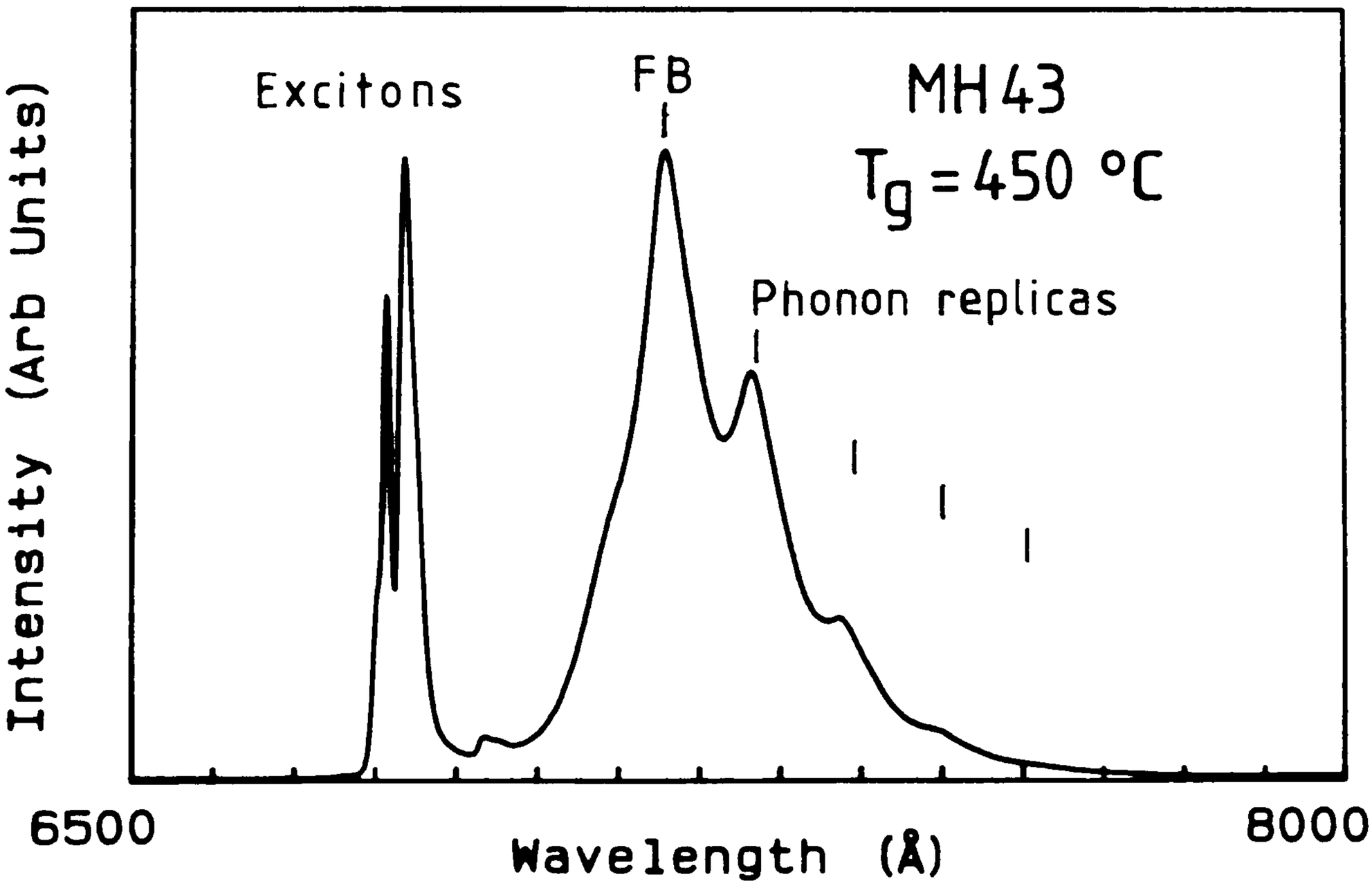
Excitons
FB
MH43
T_g = 450 °C
Phonon replicas
Intensity (Arb Units)
6500
8000
Wavelength (Å)

acceptors [43].

As T_g is raised the luminescence shows an increase in quality. The photoluminescence from the epilayers grown at high T_g show a number of characteristic CdSe spectral features. Figure 3.32 shows the excitonic emission from MH43 grown at 450°C. The principle emission lines occur at 6805 Å (1.821 eV) and 6824.5 Å (1.816 eV), which correspond to the I_1 and I_2 lines due to the neutral acceptor and donor bound excitons (observed in Na doped material) respectively [43]. The X_o line of the free exciton is also present at 6794.5 Å (1.824 eV). The FWHM of the I_2 line is 1.5meV in the best samples compared to typically 0.1 meV observed in bulk platelets [27]. The luminescence from the high T_g samples is therefore consistent with good quality material. In particular the emission still indicates relatively pure material.

3.3.4.2 Origin of defects: effect of growth under H_2S

In order to assess the reasons for the poor quality of the CdSe we need to determine the origin of the luminescence observed from these epilayers. In particular, the origin of the Y band is of interest, as this feature has also been observed in CdSe and $Zn_xCd_{1-x}Se$ grown by MBE on GaAs and ZnSe at low temperatures [45]. It is obvious both from the morphology studies and from photoluminescence studies that the structural quality of the CdSe improved as the growth temperature was raised. The Y emission is not present in the luminescence from CdSe layers grown above 400°C. Further, we know from the CdS luminescence that the epilayers become less pure as the temperature is raised. We therefore conclude that the centre involved in the Y emission is either intrinsic or is a complex involving an intrinsic defect. This requires that the concentration of intrinsic defects reduces as the growth

temperature is raised.

In order to try and identify the nature of the Y band the emission's dependence on temperature was studied. Figures 3.33 and 3.34 show this dependence for both the Y band and the free to bound zero phonon peak. It can be seen that both emissions remain fairly constant in intensity until they start to quench at 40K for the Y band and 60 K for the free to bound, decaying with activation energies of 18 and 54 meV respectively. The dependence of the 7150Å band is totally consistant with its identification with free to bound recombination [29]. However, the Y band dependence is inconclusive as the luminescence quenches at relatively low temperature. In fact the dependence is not particularly characteristic of free to bound or D-A pair emissions. The lack of clearly resolved phonon replicas for the band also makes these possibilities unlikely. Samarth pointed out that the Y emission disappears for the MBE samples after annealing in Se and suggested a Se vacancy complex may be involved [46]. The MBE samples were grown exclusively in the cubic phase. We note that the emission band was totally absent in the emission from the polycrystalline layer. It is apparent that the defect is associated with the epitaxial growth process.

Interesting evidence for the origin of the Y band came during the attempted growth of alloys (section 3.3.5). Figure 3.35 shows the near gap emission from an epilayer grown at 350^{o}C on GaAs (111)A with 10 cc/m H_2Se and 60 cc/m H_2S flowing (MH50 see appendix 1). This layer was assessed by reflectivity to contain 2% sulphur. It is obvious that the quality of the luminescence is superior to that from CdSe grown under the same conditions without H_2S flowing. In particular the emission at 7015Å is totally absent. Growing with an overpressure of H_2S prevents the formation of the defect involved in the Y band. Layers grown under

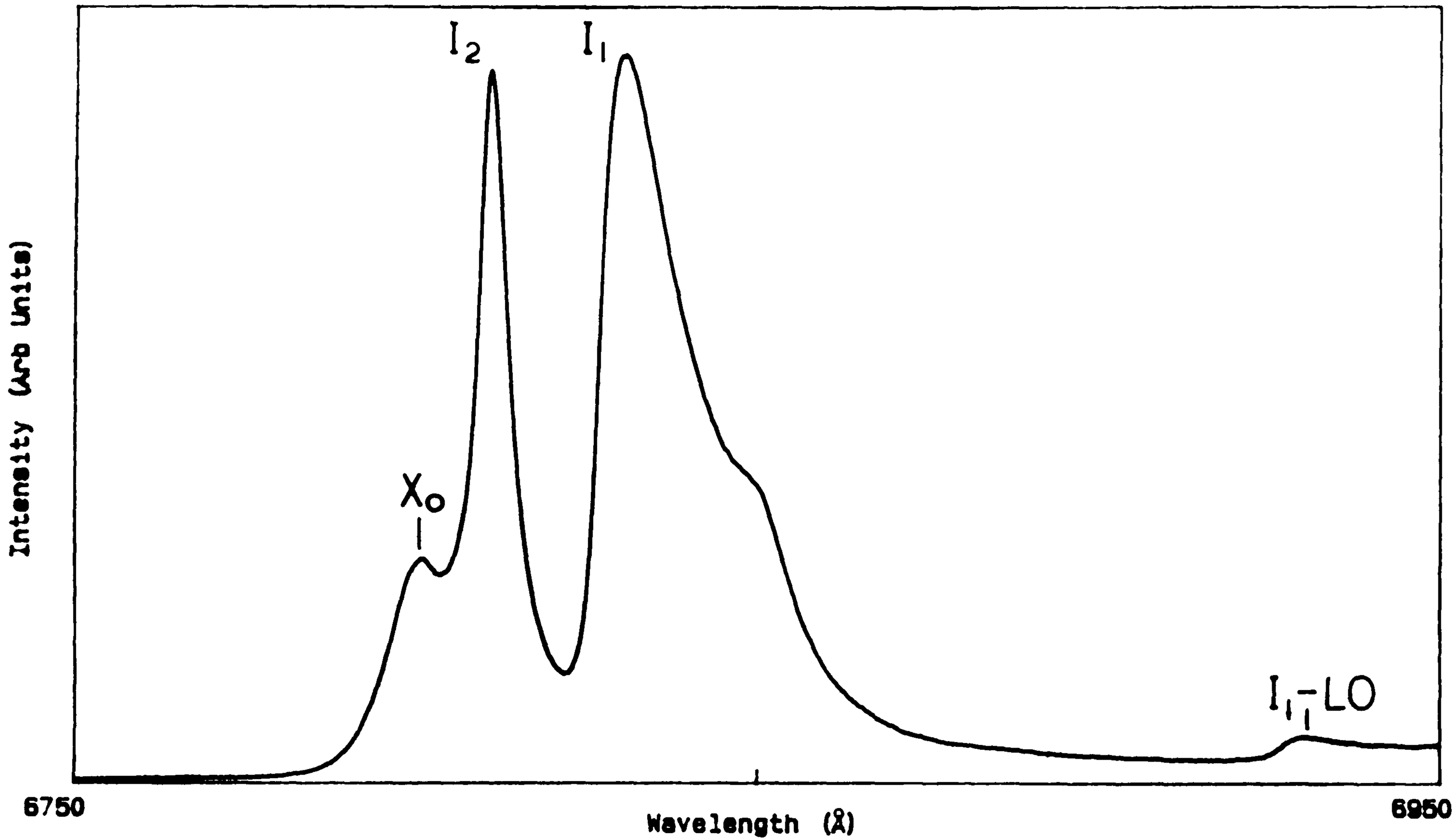

Figure 3.32. Photoluminescence spectrum showing the excitonic emission from a CdSe epilayer grown on GaAs (111)A at 450°C (MH43).

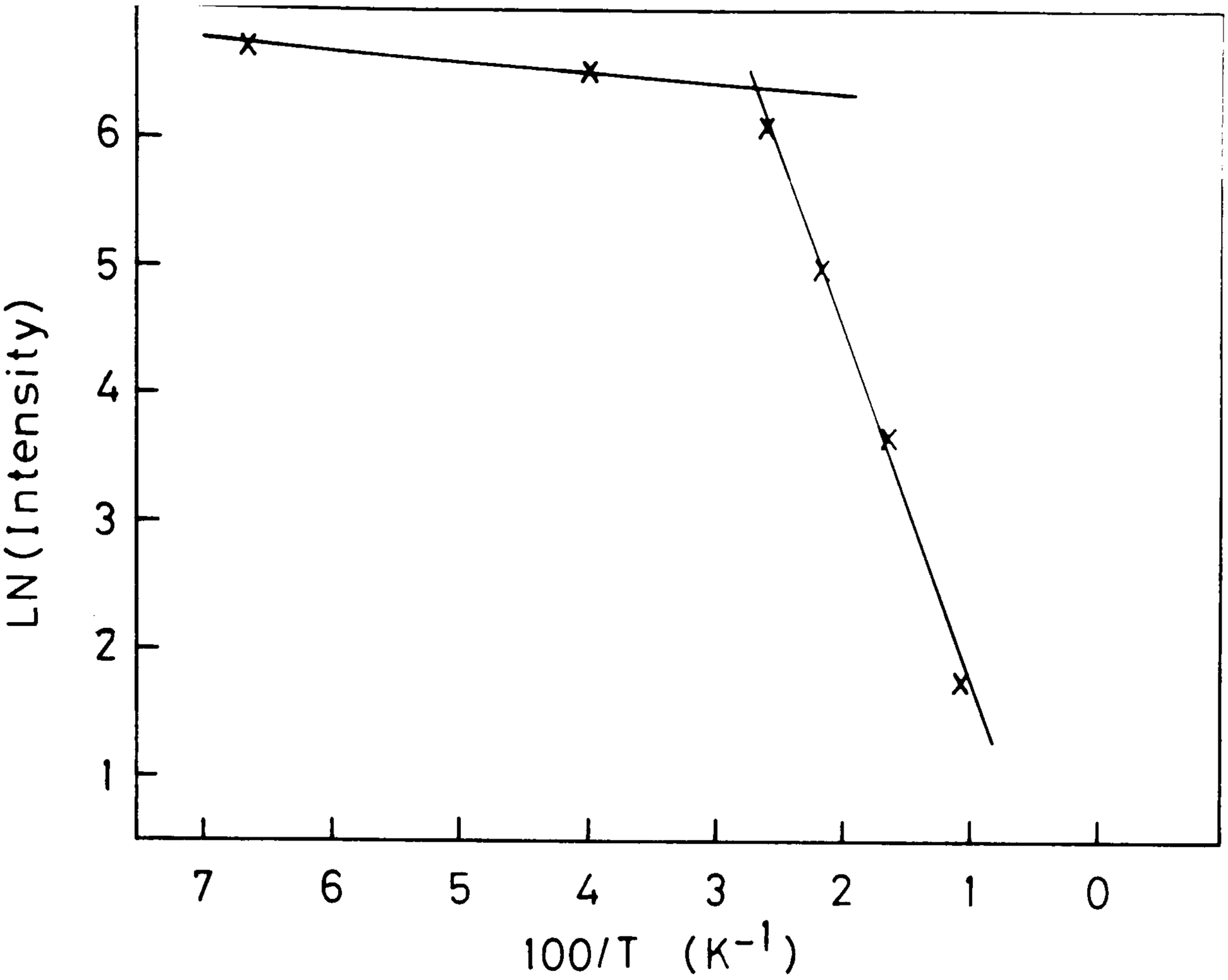

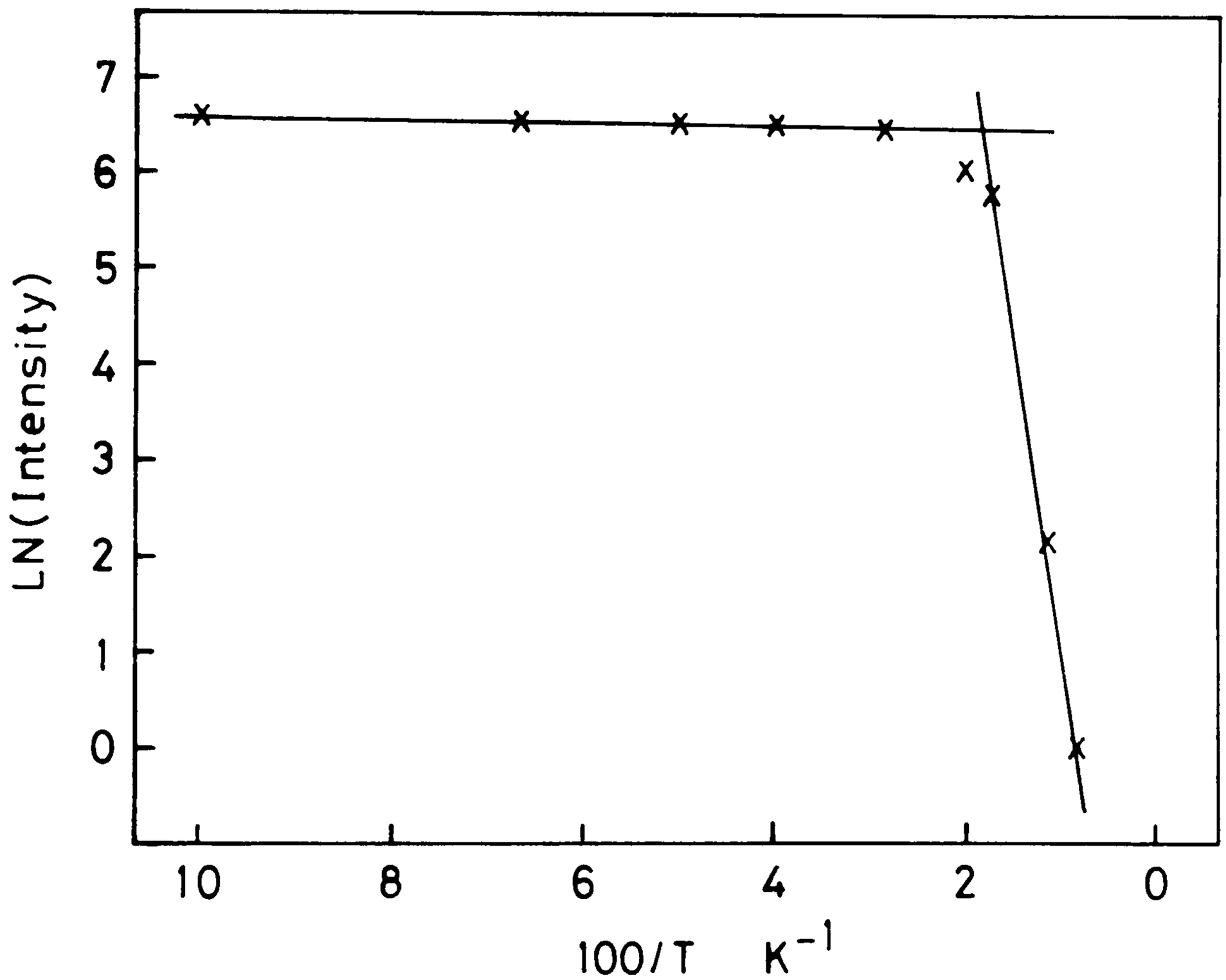

Figure 3.33 (upper figure). Arrhenius plot showing temperature dependance of the 'Y' band emission from the CdSe epilayers grown on GaAs (111)A at 350°C. The straight line drawn on the right hand side corresponds to an activation energy of 18 meV.

Figure 3.34 (lower figure). Same plot for the free to bound recombination observed from the CdSe epilayers grown on GaAs (111)A. The straight line on the right hand side corresponds to an activation energy of 54 meV.

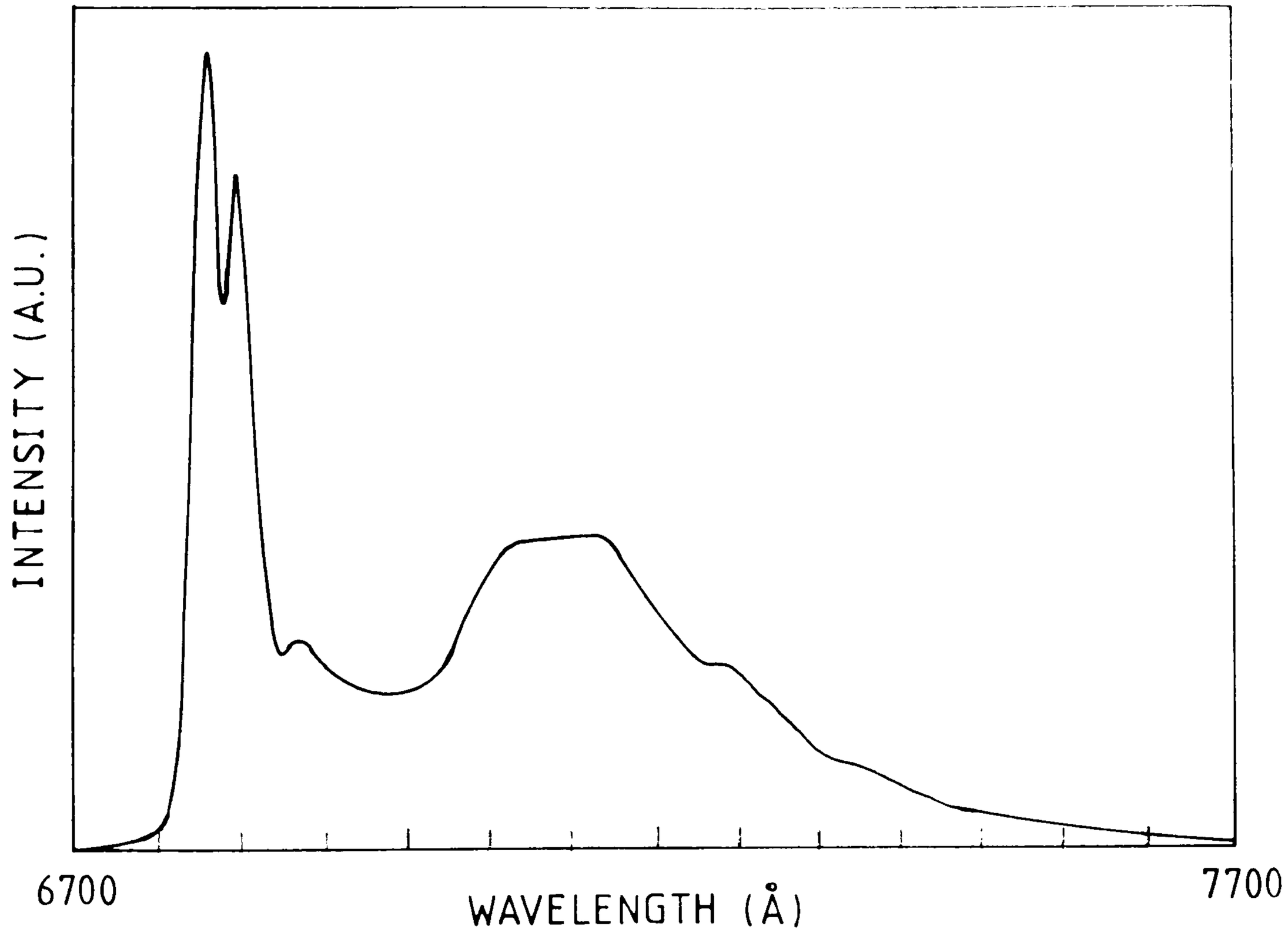

Figure 3.35. Photoluminescence spectrum from a $CdS_{0.02}Se_{0.98}$ alloy grown at 350°C.

insufficent H_2S to incorporate any sulphur proved to show similar luminescence to the pure CdSe samples. It was reported in the RHEED section that the same sample, MH50, grown on GaAs (111)A was purely wurtzite. It can be concluded that the incorporation of even small amounts of sulphur in the CdSe epilayers has a beneficial effect on the structural quality. The most likely reason for this change in phase is simply the lower stability of the cubic phase in CdS relative to CdSe when grown epitaxially.

The addition of small amounts of sulphur is unlikely to prevent the formation of point defects such as acceptor complexes although it could conceivably passivate them. A more likely explanation, therefore, is that the absence of the Y band from this sample is a result of the change of phase. This suggests that the Y band is associated with the cubic twinning in the pure CdSe layers grown at low temperature. The Y_o band observed in the luminescence from ZnSe is known to be associated with carrier trapping by twins [41], and occurs at a similar depth to the Y band in CdSe (allowing for the difference in band gaps). Although we cannot positively identify the Y band, we believe that the above analysis presents strong evidence for recombination at extended defects in the epilayers being responsible.

3.3.5 Ternary alloys

The growth of alloys by MOCVD is, in principle, possible by simple mixing of the appropriate reagent flows. In this manner other workers have been able to grow a number of ternary alloys, including ZnS_xSe_{1-x} and $Cd_xHg_{1-x}Te$ [38,47]. The values of x achieved will be a function of the gas phase ratios of the MOCVD reagents and the growth temperature. For our study the growth of the ternary alloy $CdS_{1-x}Se_x$ was attempted by mixing of the H_2S and H_2Se gas flows in the reaction vessel. The hydride flows were mixed so as to produce a gas partial pressure of H_2Se defined by

$$R = \frac{[H_2Se]}{[H_2Se] + [H_2S]} \qquad \text{(xvii)}$$

The alloy concentration x will be a function of R. The nature of the x-R relationship is governed by a number of factors relating to the reagent sources used. In general the x-R relationship will usually be a non-linear function. To determine the x-R curve for the $CdS_{1-x}Se_x$ a series of alloy samples was grown with varying H_2S partial pressures. The x values were determined from reflection spectroscopy and/or photoluminescence. The variation in the alloys A exciton band gap E_a with x is given by [48]

$$E_a(x) = E_a(0)+(E_a(1)-E_a(0))x-bx(1-x) \qquad \text{(xviii)}$$

Where b is the band bowing parameter. Figure 3.36 shows the variation of E_a with x assuming a value of 310meV for b as in [48].

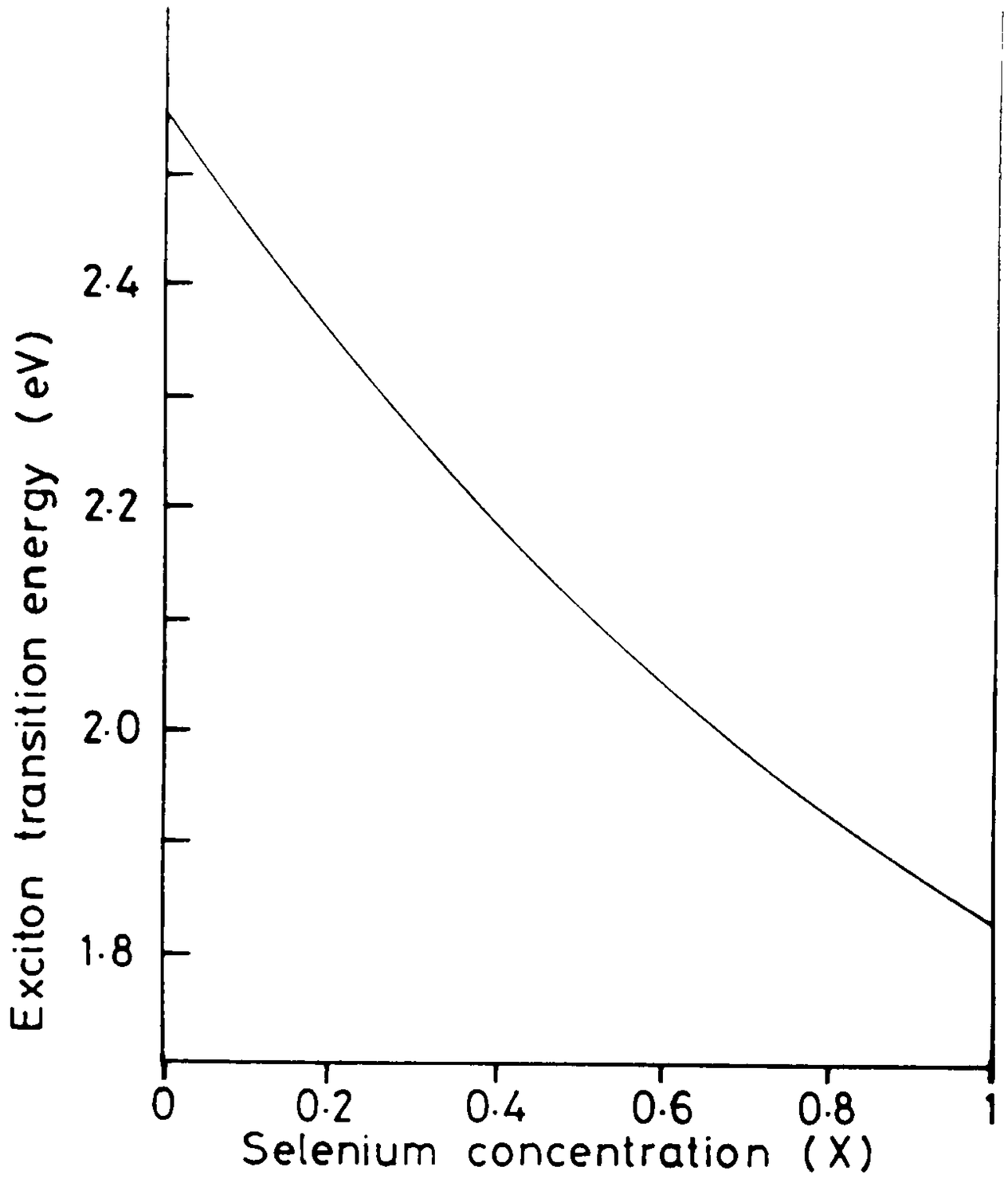

Figure 3.36. Variation of band gap with x for the alloy $CdS_{1-x}Se_x$.

Reflection spectroscopy is an established technique for determining alloy concentrations. The free exciton energy is taken as being at the reflection minimum [48] and the band gap calculated by adding the binding energy of the exciton. Photoluminescence allowed an assessment of the alloy's quality and consistency. In particular the small size of the focussed laser spot (approx 0.1mm diameter) allowed the variation in alloy concentrations across the sample to be assessed. A series of alloys was grown at 350°C and 400°C, all on GaAs (111)A. The flow rates of the reagents were 10 cc/m of DMC and a total of 100 cc/m hydride flow (i.e. the sum of the hydride flow rates was a constant 100cc/m).

Figures 3.37 and 3.38 show the variations of x with R for the two growth temperatures. The points are experimental and indicate the degree of variation of the alloy concentration across the samples (error bars). It can be seen that a considerable over-pressure of H_2S is necessary in order to achieve some sulphur incorporation in the layer. This is similar to the situation in the related ZnS_xSe_{1-x} system [49] where an over-pressure of H_2S is also necessary to incorporate sulphur.

The relationships shown render the growth of alloys in the x range 0.1-0.9 extremely difficult as fluctuations in the H_2Se flow rate are very significant. A change in the H_2Se flow rate will cause a variation in x whose magnitude will be proportional to the gradient of the x-R graph. Thus, in the range x=0.1-1 large variations in the alloy concentration with depth and laterally across the substrate can be expected.

The effect of this is illustrated in figure 3.39 which shows a luminescence spectrum from an alloy grown at 350 ^{o}C with an x value of 0.3. The very large breadth of the emission from the x=0.3 sample is obvious. In fact it is impossible to resolve any clear features in the reflection spectra and the concentration is estimated from the luminescence spectrum. Furthermore, the apparent concentration for this sample varied appreciably according to which part of the sample the laser spot illuminated. This breadth makes an assessment of the alloys structural quality and purity difficult. However, it was observed from all the alloys in this range that the total photoluminescence intensity was much higher than that observed from either the pure CdS or the pure CdSe epilayers.

Unfortunately the mass flow controllers fitted to the growth system could not control the flow of the H_2Se accurately enough to

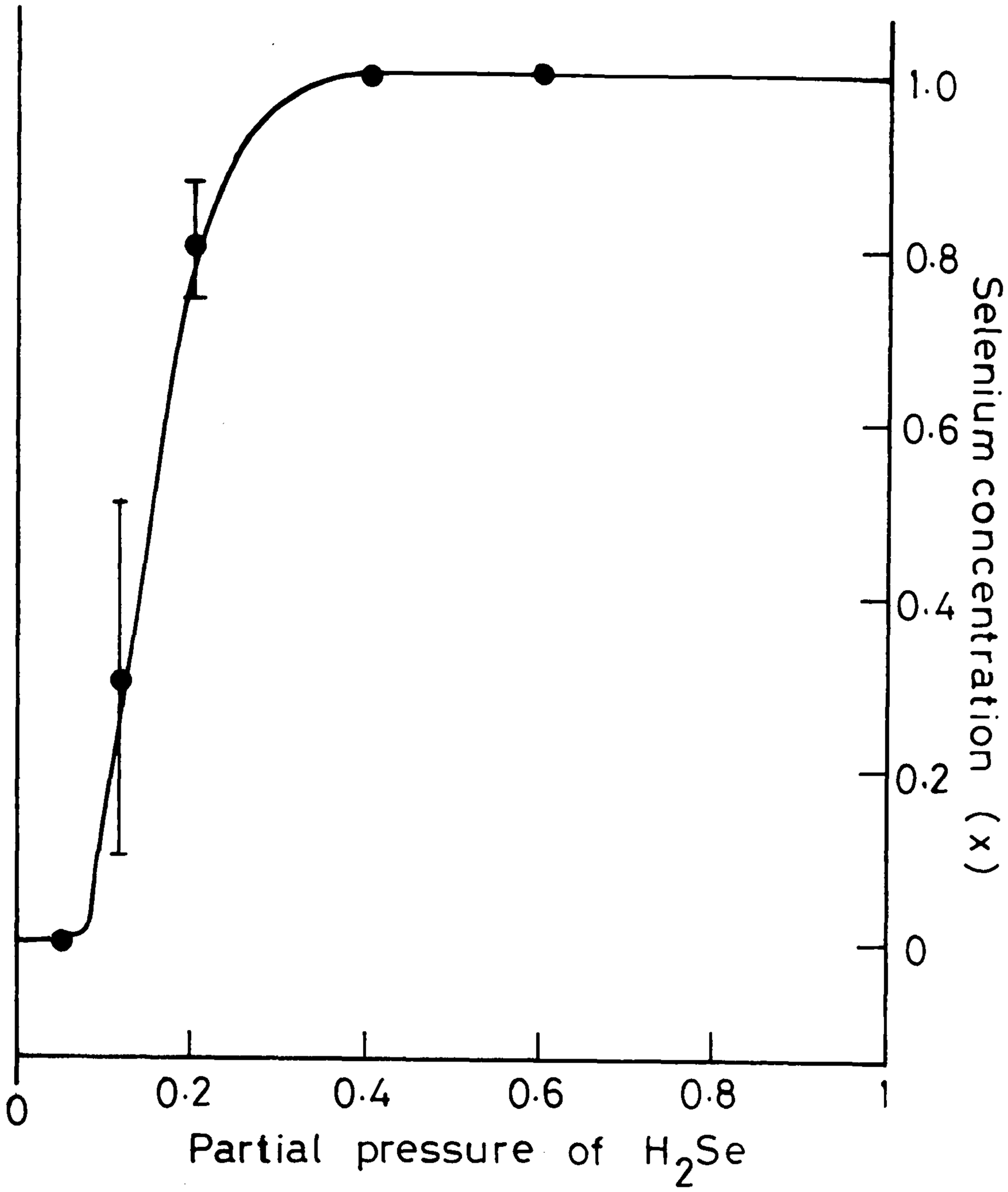

Figure 3.37. Dependance of x with partial pressure of H_2Se for $CdS_{1-x}Se_x$ grown in reaction vessel at 350°C. The points are experimentally determined from photoluminescence and/or reflection spectroscopy, the line is drawn to aid the eye.

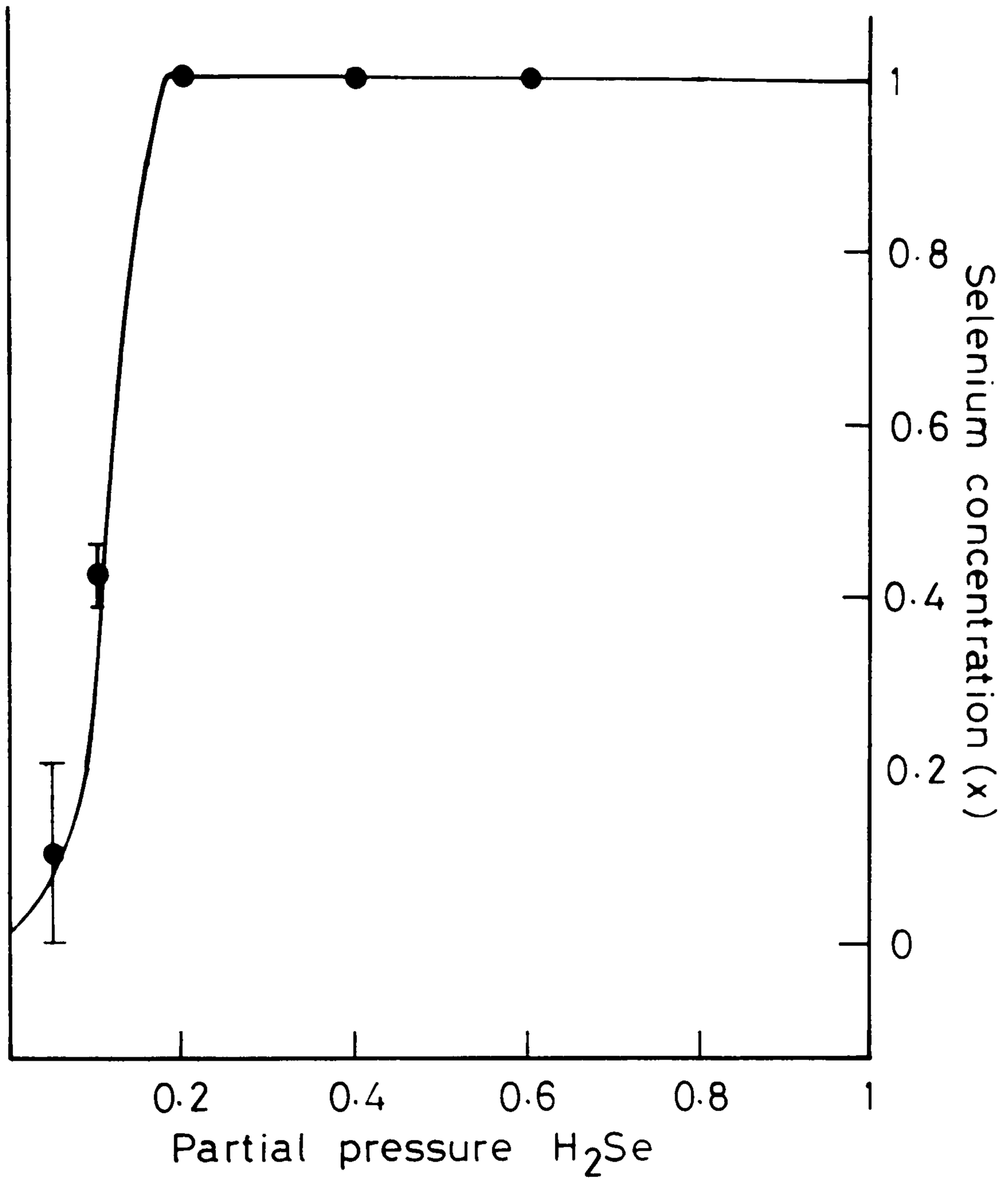

Figure 3.38. Dependance of x with partial pressure of H_2Se for $CdS_{1-x}Se_x$ grown in reaction vessel at 400°C. The points are experimentally determined from photoluminescence and/or reflection spectroscopy, the line is drawn to aid the eye.

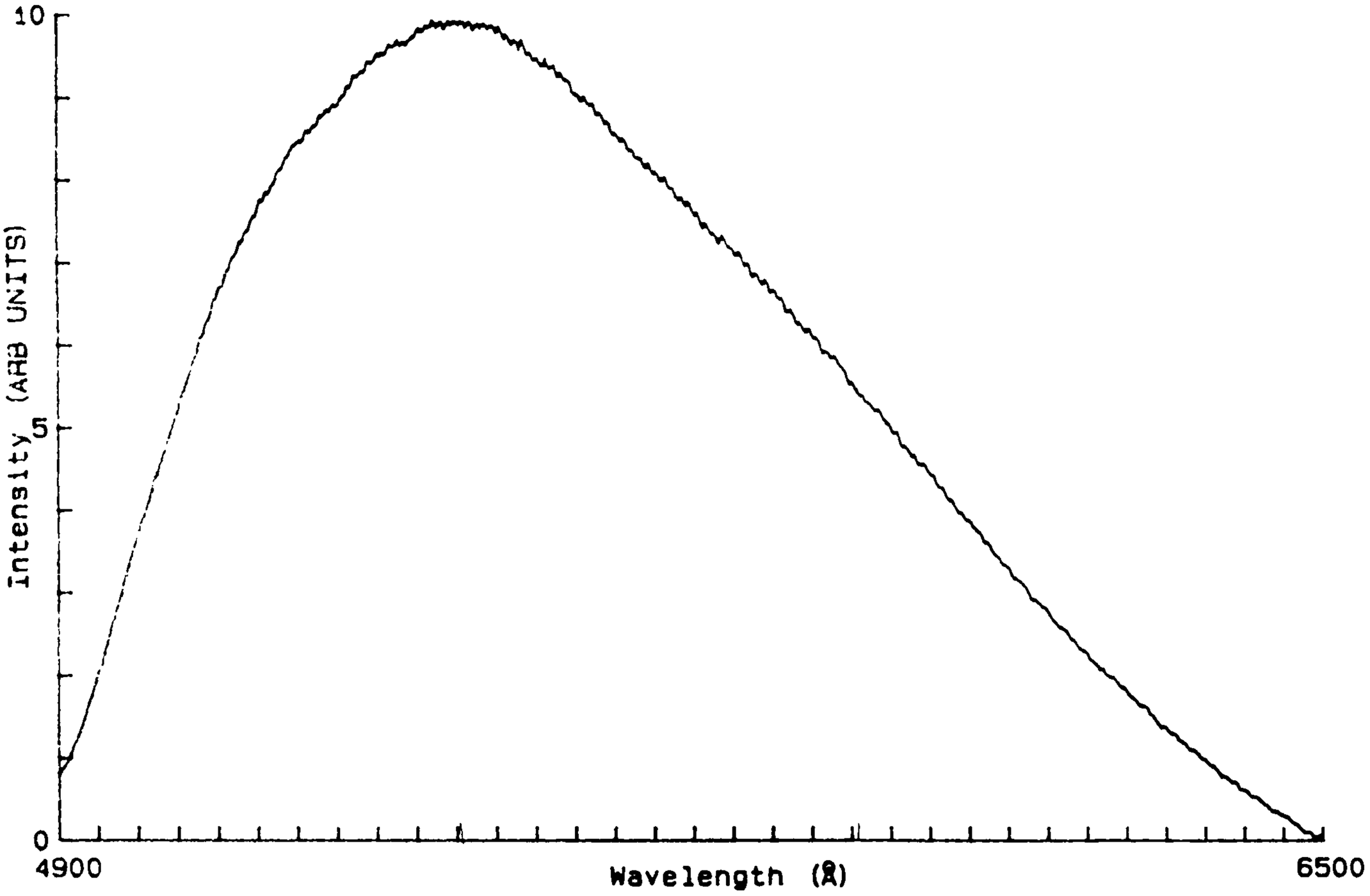

Figure 3.39. Photoluminescence spectrum obtained from an alloy grown on GaAs (111)A at 350 ^{o}C (MH70). The estimated x value for this sample is x=0.3 .

allow alloys of consistent composition to be grown in the range x=0.1-0.9. The luminescence from these alloys is investigated further in section 4.2.1, where the origin of the superlattice emission is studied.

3.4 DISCUSSION AND CONCLUSIONS

From the results in this chapter we can draw a number of conclusions concerning the growth of CdS, CdSe and the ternary alloy $CdS_{1-x}Se_x$ by MOCVD. The quality of the CdS epilayers was dominated by the substrate used. It was found that the production of high quality, smooth and purely wurtzite CdS epilayers by MOCVD is possible on the (111)A face of GaAs. That CdS should grow hexagonally on this face, despite the 3.5% lattice mismatch between GaAs and CdS, is understandable in terms of the similarity of the wurtzite (0001) and sphalerite (111) surfaces. In contrast, the CdS layers grown on GaAs (111)B consisted of heavily twinned cubic material. The structural difference between CdS grown epitaxially on GaAs (111)A and (111)B has been noted by other authors. The reasons for the cubic structure of the CdS grown on the arsenic face (the B face) unlike that grown on the gallium face are unclear. We only note that it must originate from different chemical natures of the two faces as they are structurally identical. The CdS was also wurtzite when grown on GaAs (100) at high growth temperatures. However, photoluminescence indicated a high density of lattice defects in the layers grown on GaAs (100).

CdS layers grown on InP (111)B were also studied. The photoluminescence showed clear evidence of indium and phosphorus diffusion into these epilayers, even for a low growth temperature of 350^{o}C. It was evident that the high reactivity of the InP surface was encouraging autodoping of the epilayers. We can conclude that InP is not suitable for the growth of high purity CdS at this temperature.

From the photoluminescence evidence we can conclude that the optimum growth temperature for CdS, as judged by the FWHM of the bound exciton emission, was 350 ^{o}C. There was no evidence in the

photoluminescnce spectra of large scale diffusion of Ga when grown at 350^{o}C. It was observed that the impurity level increased as the growth temperature was raised.

The growth of CdSe epitaxially was also studied and this was the first report of such a study. The photoluminescence from CdSe samples grown on a variety of substrates was investigated. RHEED studies proved that at low growth temperatures the CdSe grown on GaAs (111)A was largely cubic and was heavily twinned. The photoluminescence confirmed poor quality and was dominated by an emission band 79 meV below the band edge, referred to here as the Y band. The temperature dependence and shape of the emission was found to be inconsistent with either conventional free to bound or d-a pair recombination. It was suggested that the emission was associated with the presence of cubic twins within the layer.

The luminescence indicated considerable improvement in structural quality for higher T_g samples. It was found that CdSe grown on wurtzite CdS at 350^{o}C was of no better quality than when grown on the cubic GaAs (111)A face. We conclude from this that the poor quality of the CdSe epilayers is not a result of the use of a cubic substrate.

It is evident that the CdSe contains many more lattice defects than CdS grown at the same temperature. The reasons for the poor quality of the CdSe must lie in epitaxial growth process for this material. Similar results have been obtained from MBE-grown CdSe [45]. Moreover, the quality of the CdSe showed considerable improvement even when very small quantities of sulphur were incorporated in the layers, the presence of sulphur preventing the formation of the centre responsible for the Y band. In order to explain these results, we suggest that the incorporation of sulphur greatly enhances the stability of the wurtzite phase in the alloy. It was observed by RHEED

that the addition of sulphur to the layer prevented cubic or polycrystalline growth. The suppression of the Y emission in the alloys is probably linked to the change in phase. The suppression of the Y emission for higher T_g samples supports the view that these layers contain fewer twins. We conclude that the reagents used for our growth were not suitable for the growth of pure CdSe at low temperatures. At high growth temperatures, however, reasonable quality material can be grown on GaAs (111)A.

The ternary alloy CdS_xSe_{1-x} was studied. We concluded from the relationship between x and the gas phase ratio R that it is difficult using our gas system to grow uniform alloys in the x range 0.9 -0.1. This is a result of the preferential reaction of the dimethyl cadmium with the H_2Se. We can conclude, however, that the quality of the alloys grown can be high, RHEED showing that the layers grown on GaAs (111)A are purely wurtzite. In addition it was observed that the integrated photoluminescence intensity from the alloys was extremely high.

REFERENCES FOR CHAPTER 3

[1] J.H.Van der Merwe J. Appl. Phys. 34 (1962) 123

[2] T.Yao, Y.Okada, S.Matsui, K.Ishida and I.Fujimoto J. Cryst. Growth 86 (1986)

[3] J.C.Bean, L.C.Feldmann, A.T.Fiory, S.Nakahara and I.K.Robinson J. Vac. Sci. Technol A2 (1984) 436

[4] J.W.Matthews, S.Mader and T.B.Light J. Appl. Phys. 41 (1970) 3800

[5] R.People and J.C.Bean Appl. Phys. Lett. 47 (1985) 322

[6] B.N.Das and M.Weinstein Proceedings international conference II-VI compounds (1967) pg 147

[7] F.R.N.Nabarro, Theory of crystal dislocations (Clarendon, Oxford 1967), pg 75

[8] D.Berlincourt, H.Jaffe and L.R.Shiozawa, Phys. Rev. 129 (1963) 1009

[9] J.F.Nye, Physical properties of crystals (Clarendon, Oxford 1960). chpt VIII

[10] J.L.Birman, Phys. Rev. 114 (1959) 1490

[11] G.E.Pikus JETP 14 (1961) 1075

[12] V.B.Sandomirski Fizika Tver. Tela 6 (1963) 261

[13] D.W.Langer, R.N.Euwema, K.Era and T.Koda Phys. Rev. B 2 (1970) 4005

[14] O.Goede, M.Blaschke and K.H.Klohs Phys. Stat. Sol. 76 (1976) 267

[15] for a review see E.A.Wood, J. Appl. Phys. 35 (1964) 1306

[16] M.M.Woolfson 'An introduction to X-ray crystallography' (Cambridge university press 1970), Chpt 3.

[17] Andrew Zangwill 'Physics at surfaces' (Cambridge University press 1988), Chpt 16.

[18] G.R.Awan, A.W.Brinkman, G.J.Russell and J.Woods J. Cryst. Growth 85 (1987) 477

[19] J.E.Hails, G.J.Russell, P.D.Brown, A.W.Brinkman and J.Woods J. Cryst. Growth 86 (1988) 516

[20] H.Holloway and E.Wilkes J. Appl. Phys. 39 (1968) 5807

[21] O.Igarashi, Jap. J. Appl. Phys. 8 (1969) 642

[22] P.J.Dean and D.C.Herbert 'Bound excitons' in Excitons Edited by K.Cho Topics in modern physics (Springer, Berlin 1979) 14 Chpt 3

[23] D.M.Larsen Phys. Rev. B13 (1976) 1681

[24] C.Z. van Doorn, J. Phys. Chem. Solids 29 (1968) 599

[25] D.G.Thomas and J.J.Hopfield, Phys. Rev. 128 (1962) 2135

[26] T.Yodo, T.Koyama and K.Yamashita J. Cryst. Growth 86 (1988) 273

[27] C.H.Henry, K.Nassau and J.W.Shiever, Phys. Rev. 4 (1971) 2453

[28] K.Nassau, C.H.Henry and J.W.Shiever, Proceedings 10th Int Conf. Phys. Semicond. Cambridge, Mass. USA (1970) 629

[29] D.L.Kingston, L.C.Greene and L.W.Croft J. Appl. Phys 39 (1968) 5949

[30] J.Voight. F.Spiegelberg and M.Senoner Phys. Stat. Sol 91 (1979) 189

[31] J.M.Francou, K.Saminadayar, J.L.Pautrat, J.P.Gaillard, A.Million and C.Fontaine, J. Cryst. Growth 72 (1985) 220

[32] D.G.Thomas and J.J.Hopfield, Phys. Rev. 116 (1959) 573

[33] P.J.Dean, Luminescence of Crystals, Molecules and solutions, Edited by F.E.Williams (Plenum press, New York, 1973), p 538

[34] S.L.Hou and J.A.Marley, J. Appl. Phys. Letters 16 (1970) 467

[35] M.H.Christmann, K.A.Jones and K.H.Olsen J. Appl. Phys. 45 (1974) 4295

[36] C.W.Litton and D.C.Reynolds, II-VI semiconducting compounds (Benjamin, New York 1967). p 694

[37] A.Yoshikawa and Y.Sakai, Jap. J. Appl. Phys. 13 (1974) 1353

[38] N.Maung and J.O.Williams, J. Cryst. Growth 86 (1988) 629

[39] E.D.Jones and H.Mykura, J. Phys. Chem. Solids 41 (1980) 1261

[40] Takenoshita, K.Kido and K.Sawai, Jap. J. Appl Phys. 25 (1986) 1610

[41] P.J.Dean, Phys. Stat. Solidi (a) 81 (1984) 625

[42] D.C.Reynolds, C.W.Litton and T.C.Collins, Phys. Rev. 156 (1967) 881

[43] Y.S.Park and D.C.Reynolds, Phys. Rev. 132 (1963) 2450

[44] C.H.Henry, K.Nassau and J.W.Shiever, Phys. Rev. B4 (1971) 2409

[45] N.Samarth, H.Luo, J.K.Furdyna, S.B.Qadri, Y.R.Lee, R.Alonso E.L.Suh, A.K.Ramdas, and H.Otsuka. To be published in Surface science.

[46] Nitin Samarth, NotreDame Univ, USA private communication

[47] J.B.Mullin, S.J.C.Irvine and J.Tunnicliffe J. Cryst. Growth 68 (1984) 214

[48] O.Goede, L.John and D.Hennig, Phys. Stat. Sol (b) 89 (1978) K183

[49] P.J.Wright and B.Cockayne, J. Cryst. Growth 59 (1982) 148

4. CdS/CdSe SUPERLATTICES AND MULTILAYER STRUCTURES

4.1 Introduction

With the advent of precision epitaxial growth techniques it has proved possible to construct semiconductor structures with a precision on the atomic scale. In particular, the growth of modulated epitaxial structures has been studied intensively for a wide variety of material systems. In chapter 1 the field of II-VI superlattices was reviewed. It was noted that, to date, there has been no reported growth of superlattices using either CdS or CdSe. The reasons for this lie in the difficulties associated with the two stable phases of these compounds [1]. We showed in the previous chapter, and reported in [2], that high quality and smooth wurtzite CdS epilayers can be grown on GaAs (111)A substrates by MOCVD. We also found that good quality CdSe epilayers could be grown on either the CdS epilayers or GaAs (111)A at high growth temperatures. It was now clearly of great interest to determine if it was possible, using MOCVD, to grow a wurtzite superlattice using these two compounds.

In this chapter the assessment of all the CdS/CdSe multilayer structures grown is presented. The chapter is divided into five sections. In the first section the structures grown are described. Transmission electron microscopy (TEM) images were used to study the structural quality of the layers. The second section discusses the results of optical assessment of the multilayers. The third section considers the theoretical background of the CdS/CdSe system. The fourth section uses theory to interpret the observed properties of the superlattice luminescence; in this section a measurement of the band offsets is made. A final section gives the summary and

conclusions to the chapter.

4.2. Transmission electron microscopy measurements

4.2.1 Samples grown

Following the successful growth of wurtzite CdS on GaAs (111)A the MOCVD growth apparatus was modified as described in section 2.3.2. This allowed the growth of multilayer structures with a thickness precision of a few atomic monolayers. It was decided that to minimise the effect of the substrate mismatch and autodoping the superlattices would principally be grown on a CdS buffer layer on GaAs (111)A. Moreover, it was known that the CdS grown on this face produced a good quality smooth wurtzite surface suitable for superlattice growth. A series of superlattices were then grown at temperatures of 350,400 and 450^{o}C. A typical structure is shown schematically in figure 4.1.

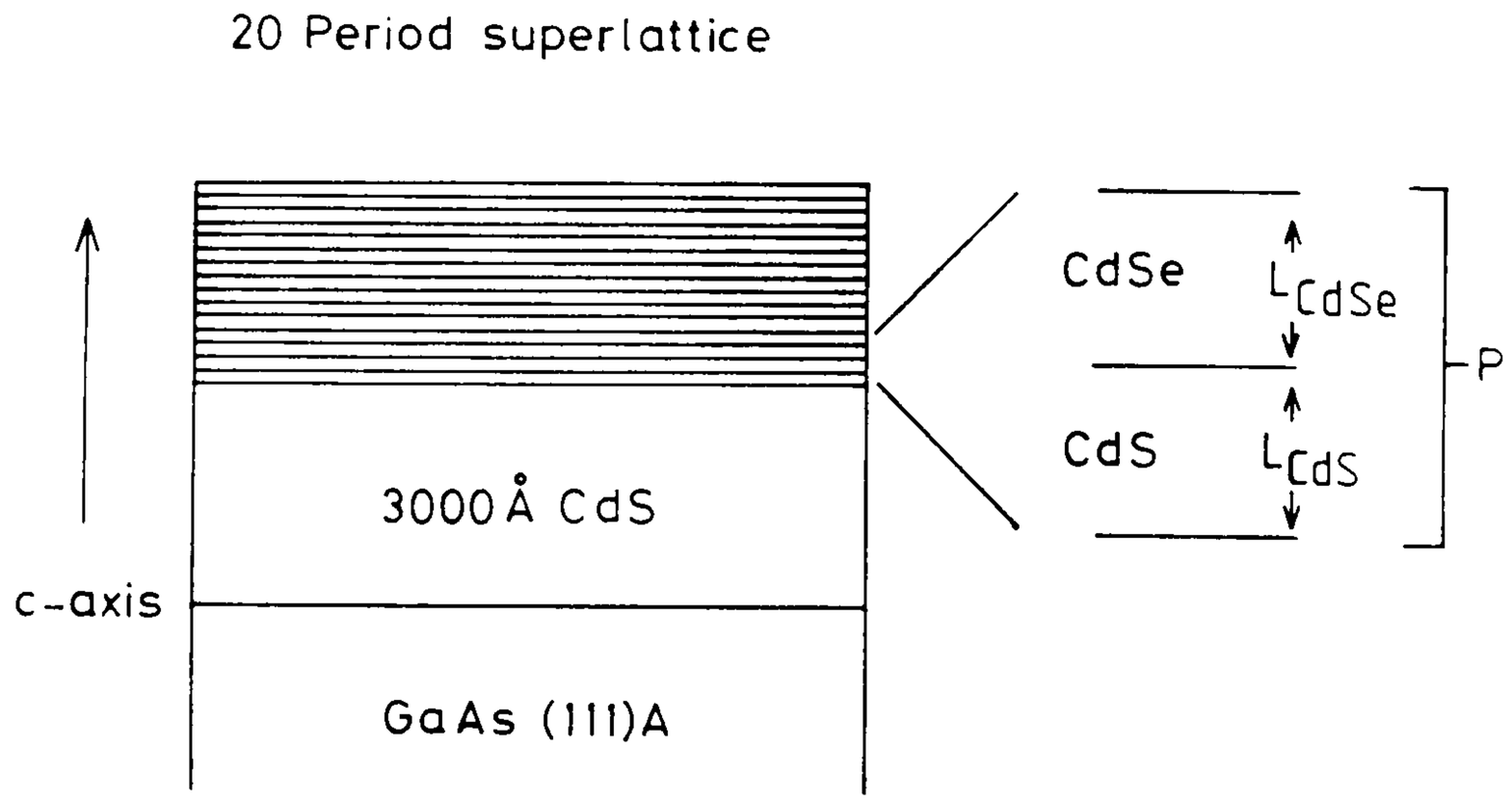

Figure 4.1. Schematic representation of superlattice structures prepared by MOCVD.

The superlattice consists of a 3000Å buffer layer of CdS on GaAs (111)A, followed by twenty repetitions of alternating CdS and CdSe layers. Before any optical studies of the superlattices were attempted they were assessed by transmission electron microscopy. This technique has been used to study the structure of a wide range of semiconductor microstructure systems (for a review see [3]).

4.2.2 Sample preparation

The TEM was conducted by A.G.Cullis using the facilities at R.S.R.E. The samples were prepared in a cross sectional configuration. Layer pairs bonded face to face with epoxy resin were first reduced in thickness normal to the joint by mechanical polishing. Specimen discs, 3mm in diameter, were cut out and were reduced to electron transparency by low voltage ion milling. Most of the thickness reduction was carried out using Ar^+ ion bombardment but, for the final stages of the process, reactive I^+ ion milling was employed to minimise artefact formation [4]. The thinned specimens were examined in a JEOL JEM 4000 EX TEM operated at 400KeV.

4.2.3 Results and discussion

Looking first at the CdS buffer layer, figure 4.2 shows a region of the CdS/GaAs interface. It is immediately evident that the interface is abrupt and that the CdS is growing commensurately with the GaAs. In addition, the CdS is observed to grow with high crystalline quality on the GaAs. Diffraction analysis showed that the buffer layers are orientated with [0001] CdS parallel to the [111] GaAs and with the

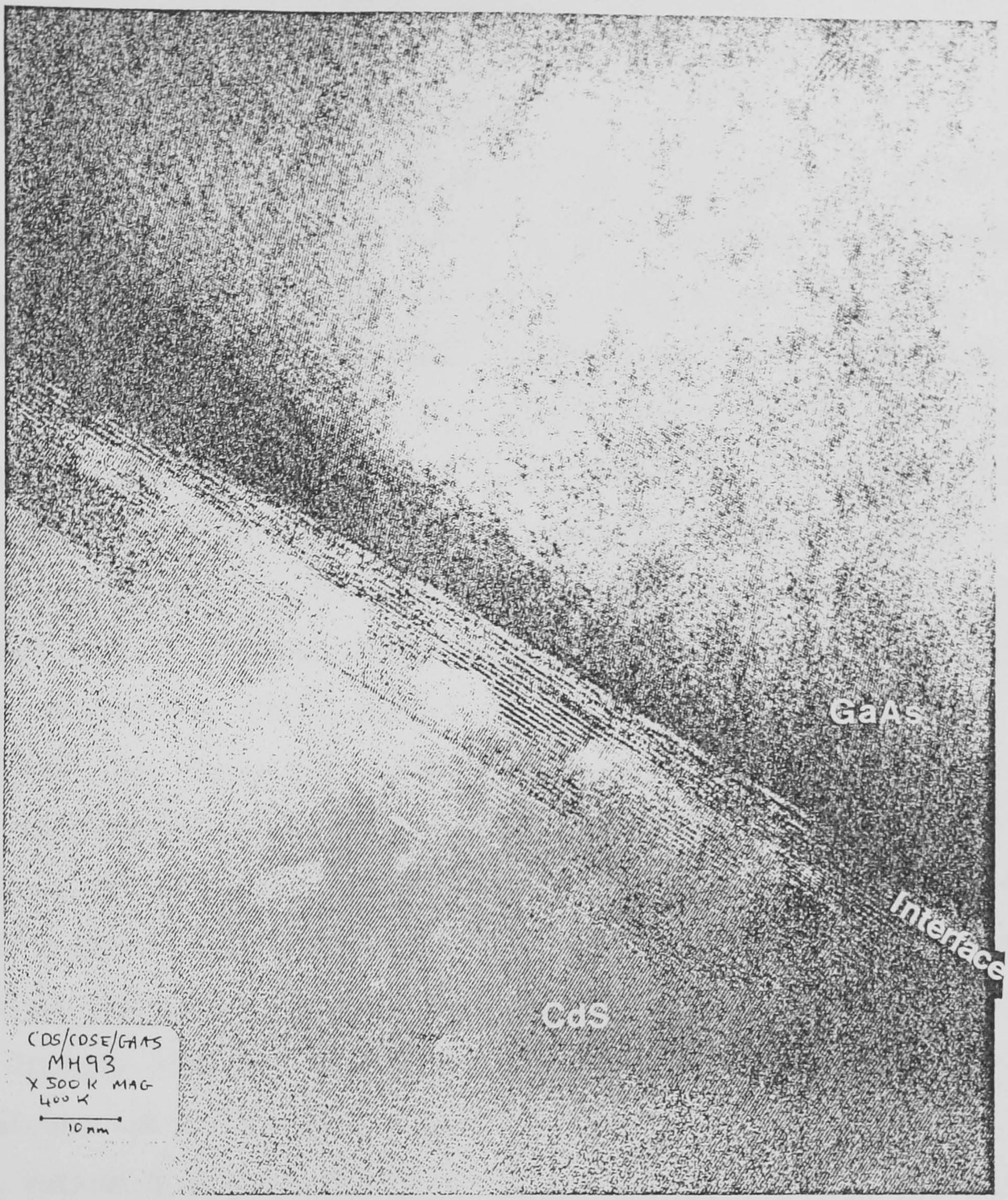

Figure 4.2. Transmission electron lattice image of the CdS/GaAs interface for MH93. The interface and the respective compounds are indicated on the image.

[11$\bar{2}$0] CdS axis parallel to the [110] GaAs.

Figure 4.3 shows another region of the interface. As is (in part) evident, some dislocations, occasional stacking faults and microtwin defects originate at the interface and extend into the CdS buffer. The figure clearly shows a dislocation threading into the buffer layer (left hand side). This dislocation appears to form a loop starting some 250 Å from the interface, below which there are no dislocations. Although this is only a single measurement, it does support the calculated critical thickness of CdS on GaAs of approximately 220Å (see section 3.1.2). Further studies of thin CdS epilayers on this surface have revealed that the strain is relaxed within the first 400Å of epilayer [5]. Figure 4.4 shows the diffraction pattern obtained when the electron beam is passed along the [0001]/[111] axis of a 400Å CdS epilayer on GaAs (111)A (taken from [5]). The six-fold symmetry of the pattern is obvious; in addition, the formation of the spots into rosettes indicates relaxation of the epilayer relative to the GaAs. All the findings from the TEM studies of the CdS buffer layers are consistent with the RHEED analysis for CdS epilayers given in section 3.2. Following this confirmation of the buffer layer's structural quality the superlattices themselves were examined.

Figure 4.5 shows a 'good' region of a 110Å/35Å CdS/CdSe (MH93) superlattice. The alternating layers of the superlattice are clearly revealed. The shading effects are possibly caused by sample stressing during preparation. Diffraction analysis showed that the CdSe in the superlattices was purely wurtzite, in contrast to the CdSe grown directly on GaAs (111)A (see section 3.2.3). The layers were found to be of good structural quality; however, undulations in thickness did occur at some positions. Figure 4.6 shows a region of MH82, a 150Å/70Å CdS/CdSe superlattice grown at 400^{o}C. It can be seen that the

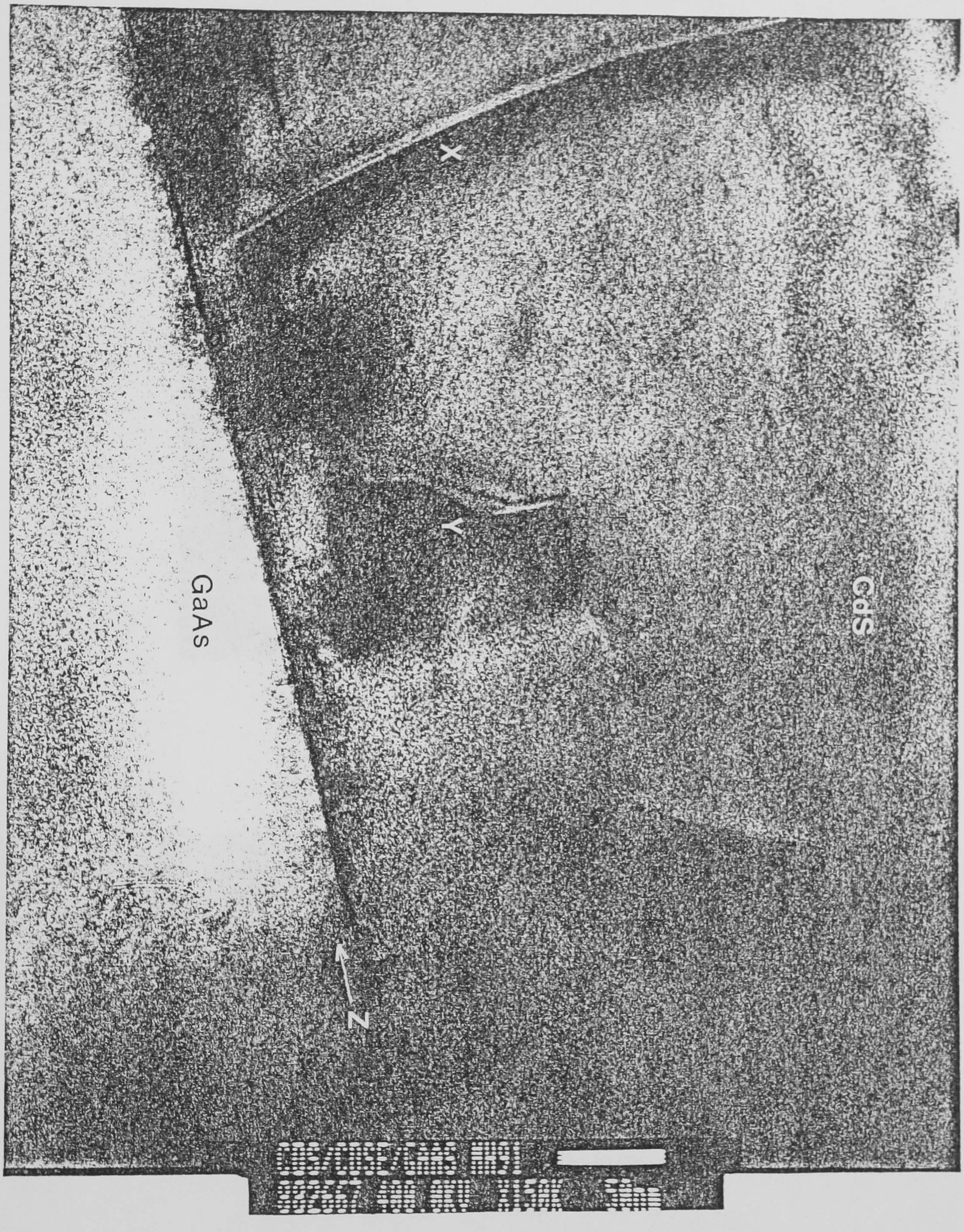

Figure 4.3. Lattice image of CdS/GaAs interface in MH91. The image shows the interface and a number of lattice faults in the CdS epilayer. Marked on the figure are a two threading dislocation lines X and Y, this dislocation appears to originate at a misfit dislocation in the CdS lying parallel to the interface (Z).

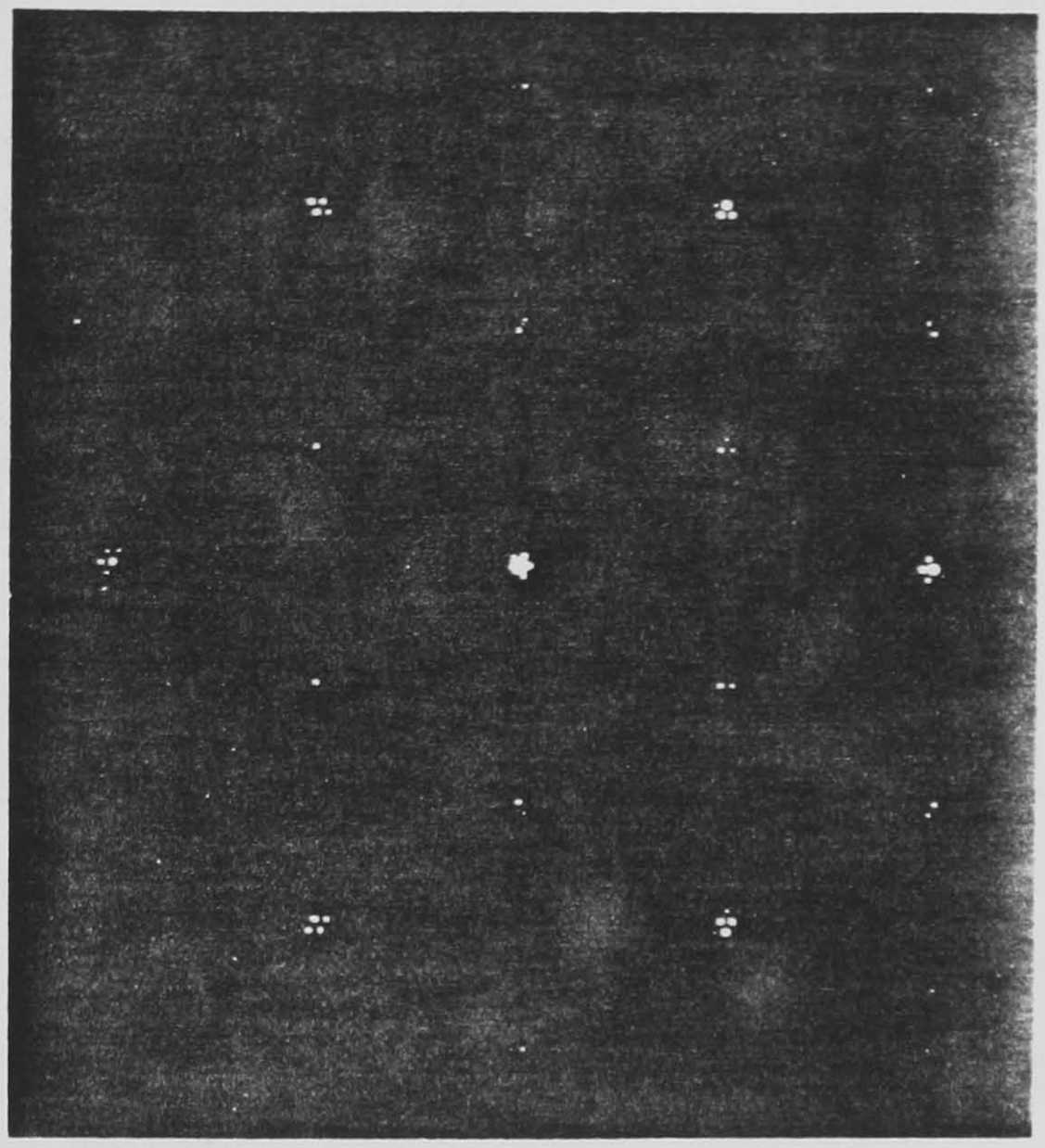

Figure 4.4. Transmission electron diffraction pattern from a 400Å thick CdS epilayer grown on GaAs (111)A. The electron beam is lying parallel to the cubic [001], hexagonal [0001] axis. The formation of the spots into rosettes indicates that the epilayer is relaxed relative to the substrate (see text).

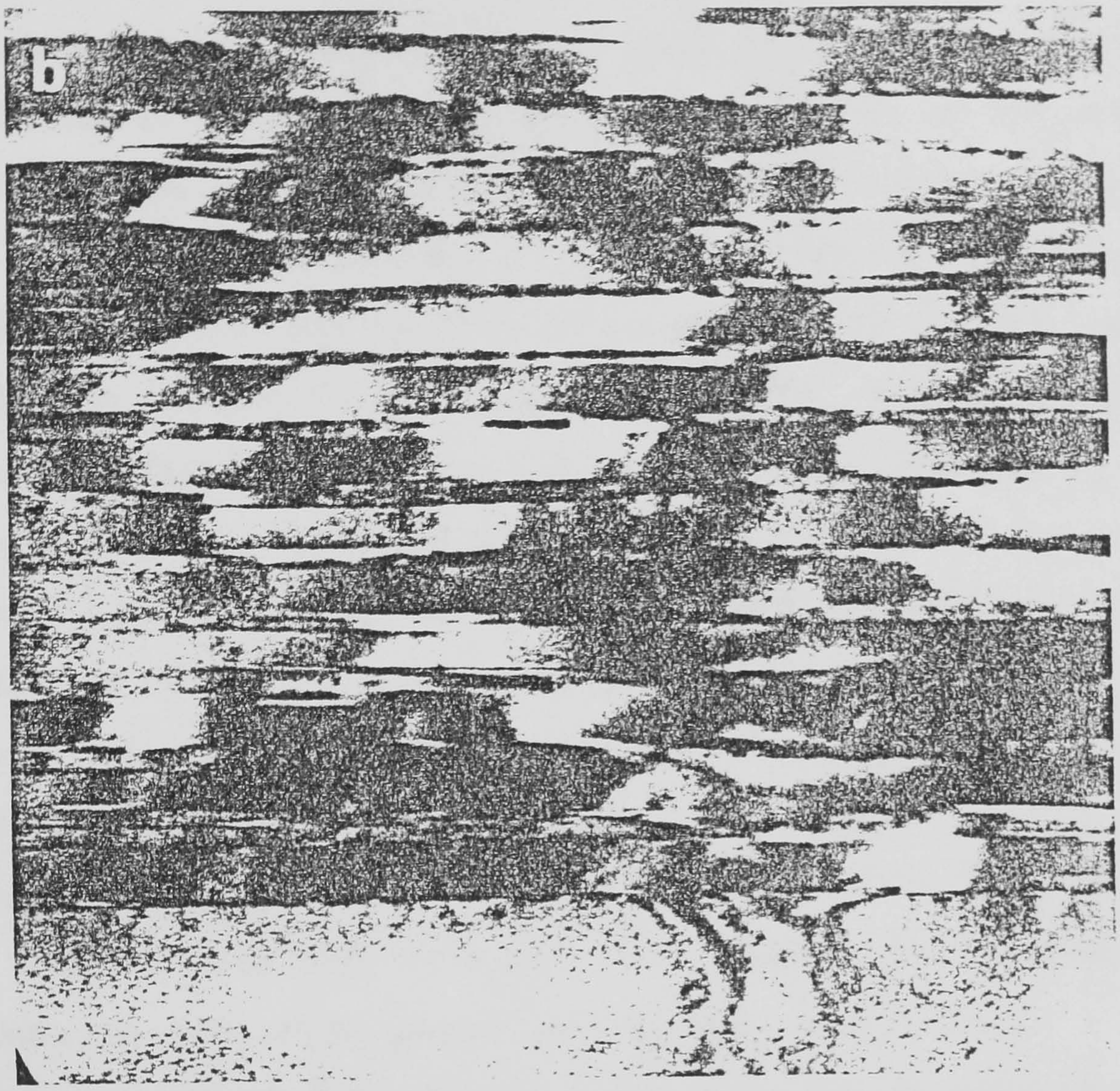

Figure 4.5. Lattice image of CdS/CdSe superlattice (MH93). The component layers are as indicated. The mean thicknesses as measured from the imaging are CdSe 35Å, CdS 110Å.

superlattice shows undulations and, in particular, the top of the CdS buffer layers is not regular. This photograph shows both the buffer and superlattice in their entirety; several dislocations can be seen to extend into the superlattice from close to the interface. Figure 4.7 shows a similar region of MH93, a 110Å/35Å CdS/CdSe superlattice grown at 450°C. This time the top of the CdS buffer is much smoother and the superlattice consequently more planar. From this evidence we believe that the increased growth temperature produces a smoother layer. This assertion is supported by the morphology studies in section 2.4, where it was found that the CdS epilayers became smoother at higher temperatures. Finally, figure 4.8 shows a high resolution image of MH91. By measuring accurately the thickness of a number of periods it was possible to measure the thickness of the component layers. This sample was found to be a 90Å/160Å CdSe/CdS superlattice in variance to the intended 100Å/200Å estimated from growth rates. Appendix 1 indicates the calibration samples used to obtain growth rates.

We can conclude from the TEM measurements that the superlattices are of good structural quality. The interfaces between the component layers being abrupt and acceptably smooth. In addition, the high quality of the CdS buffer layers grown on GaAs (111)A was confirmed. The presence of strain relieving dislocations in the buffer layer was observed, with evidence for the existance of a <400Å critical thickness for CdS on GaAs, in agreement with theory.

As a result of the TEM studies the superlattices were known to be of sufficent structural quality to exhibit quantum size effects in luminescence experiments. The photoluminescence of the layers was then studied.

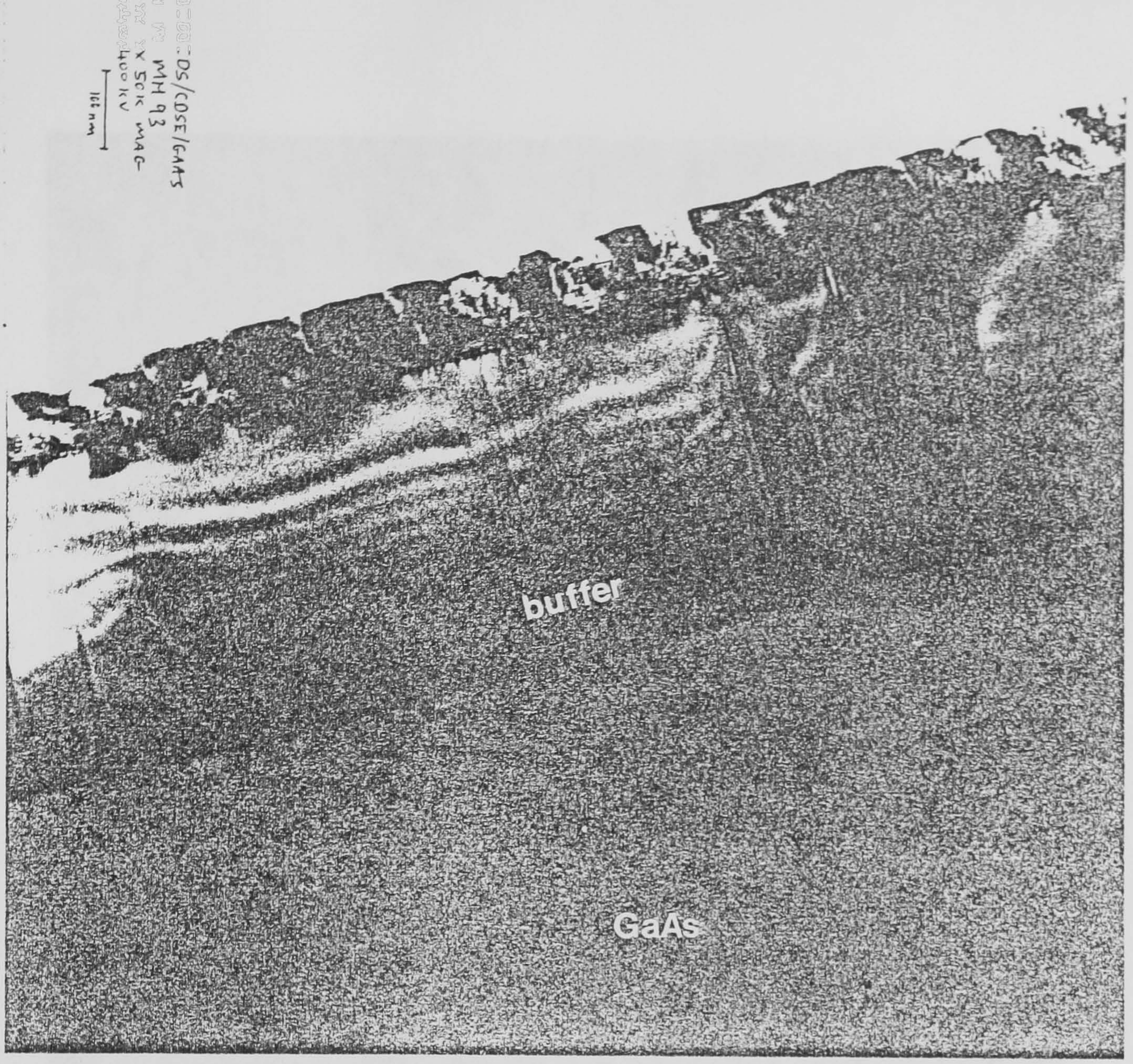

Figure 4.7. TEM image showing substrate, buffer layer and superlattice of sample MH93. This sample was grown at 450°C and shows a smooth and regular interface (c.f. figure 4.6).

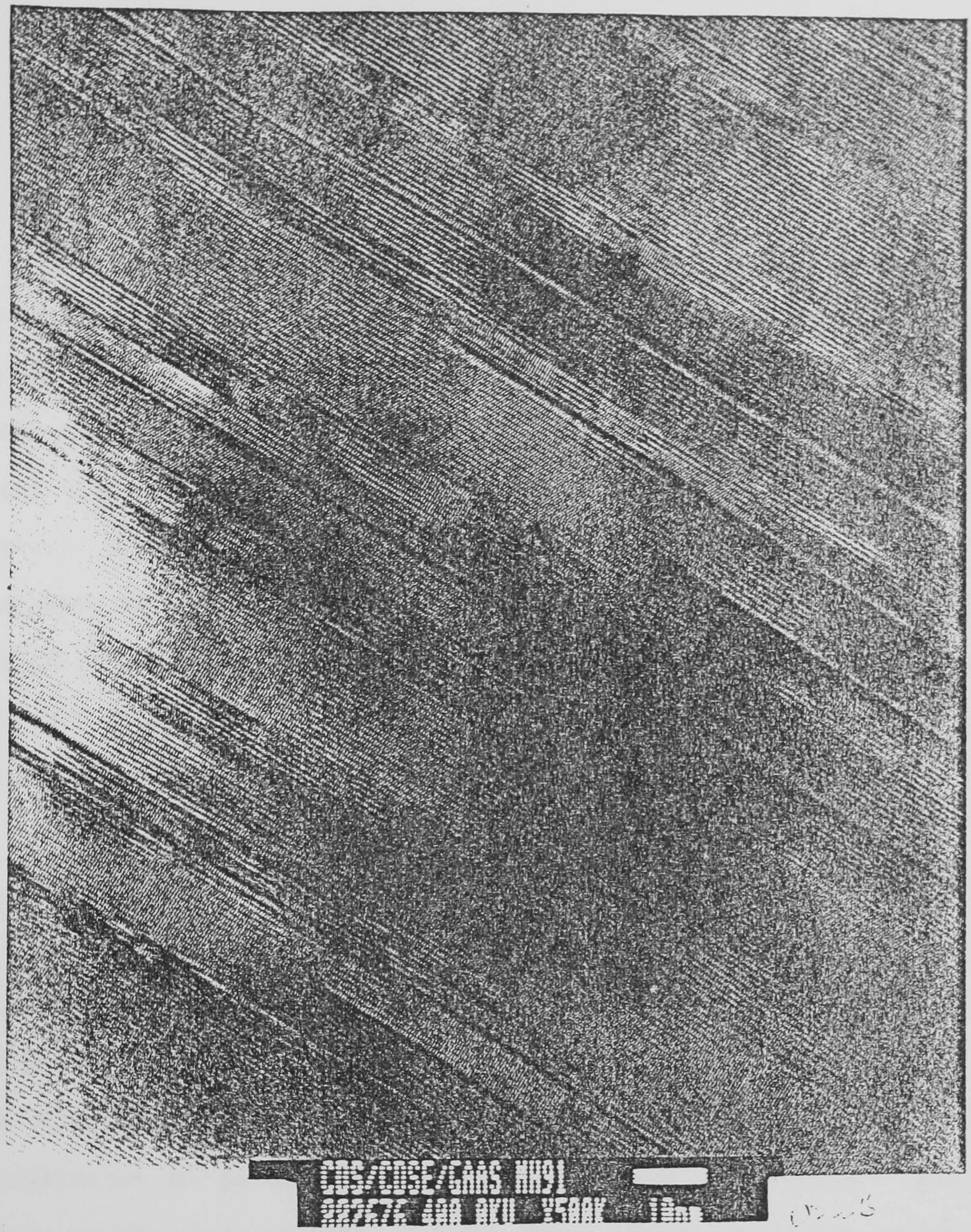

Figure 4.8. High resolution TEM image of superlattice MH91. The layer thicknesses were measured from this to be CdS 160Å, CdSe 90Å.

4.3 Photoluminescence results

Introduction

The technique used to study the electronic states within the CdS/CdSe superlattices was photoluminescence. All II-VI superlattice systems studied by other workers exhibit strong band to band recombination emission (see section 1.7). If the layers are of high purity then this emission is principally excitonic recombination. The observed recombination energy for these transitions allows an assessment of the carrier energy levels within the layers. It was known from TEM that we could grow CdS/CdSe wurtzite superlattices with a high degree of crystalline perfection. We could now proceed to try and determine something of the electronic states within the superlattices.

A number of superlattices were then grown, consisting of 20 periods on a CdS buffer layer as described in the previous section. In light of the TEM evidence it was decided to grow at 450^{o}C as this produced the smoothest layers. Table 4.1 gives a list of all the superlattices studied by photoluminescence in this chapter. The periods were calculated from growth rates calibrated by TEM measurements. The superlattices can be divided into two groups; the constant period series and the constant ratio series. These series were grown to assist the theoretical interpretation in section 4.4. The photoluminescence spectra of all these samples was then recorded with the samples at 2K, as described in section 3.3. The 488nm Ar^{+} laser line was used to excite the luminescence. All spectra were corrected for instrumental response.

Constant ratio series

Name	L_{CdS}	L_{CdSe}	L_{CdS}/L_{CdSe}	Period
MH92	50	60	0.8	110
MH104	45	40	1.1	85
MH95	40	25	1.6	65
MH123	25	25	1	50
MH121	15	15	1	30
MH114	14	14	1	28
MH120	7	7	1	14

Constant period series

Name	L_{CdS}	L_{CdSe}	L_{CdS}/Period	Period
MH109	76	8	0.9	84
MH108	68	20	0.77	88
MH110	40	56	0.58	96
MH111	40	60	0.4	100
MH112	24	84	0.29	108
MH113	12	104	0.1	116

Table 4.1. Superlattices studied by photoluminescence. They are divided into two series as discussed in the text. The dimensions are in angstroms, and are determined from growth rates calibrated by TEM measurements.

4.3.1 Photoluminescence from CdS/CdSe strained layer superlattices

Figure 4.9 shows the spectrum obtained from MH88, a 300Å/400Å CdS/CdSe superlattice. It can be seen that the emission is composed of several bands with structure in the region of the CdSe edge emission (6800-7800Å). In addition to this red emission there is a bright band in the near infrared centred on 9000Å. The infrared emission is not observed from any of the single layers; in particular it is not present in the spectrum from the alloy $CdS_{0.5}Se_{0.5}$. We conclude therefore that this emission is the result of the superlattice structure. As the superlattice period is reduced the structure near the CdSe edge emission position simplifies. Figure 4.10 shows the spectrum obtained from MH90 (160Å/130Å CdS/CdSe). It can be seen that this smaller period sample displays only one, relatively narrow, band in the red centred at 6900Å. The infra-red emission is still present for this sample and is somewhat more intense than for MH88. As the period reduces to 'true' superlattice proportions the emission simplifies further. Figure 4.11 shows the luminescence from MH95 with a period of 65 Å (40Å/25Å CdS/CdSe). The emission for this samples is dominated by the broad band emission. Note that the band is shifted from the infra-red into the red, as expected for quantum confinement effects. The band centred at 8400Å in figure 4.11 is the GaAs edge emission from the substrate.

Subsequently to this series a number of small period samples were grown. These all exhibited one single intense emission band in the red region of the spectrum. Figure 4.12 shows the emission from MH121, a 15Å/15Å CdS/CdSe superlattice. The spectrum shows the band centred at 7000Å. The emission in this case comes from only 600Å of material (the superlattice). It is, however, approximately 10 times brighter than the

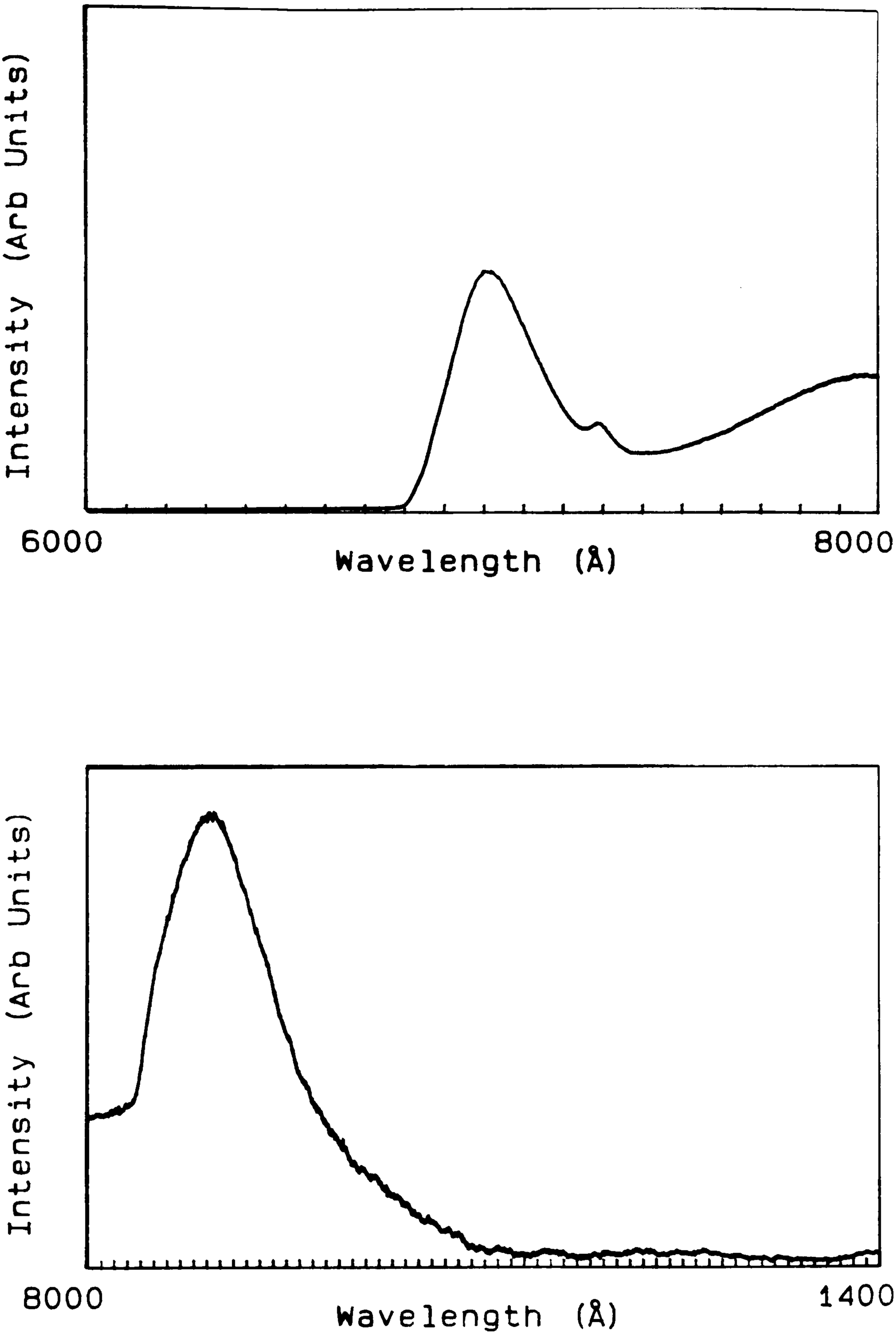

Figure 4.9. Low temperature photoluminescence spectrum from MH88, a 300Å/400Å CdS/CdSe superlattice.

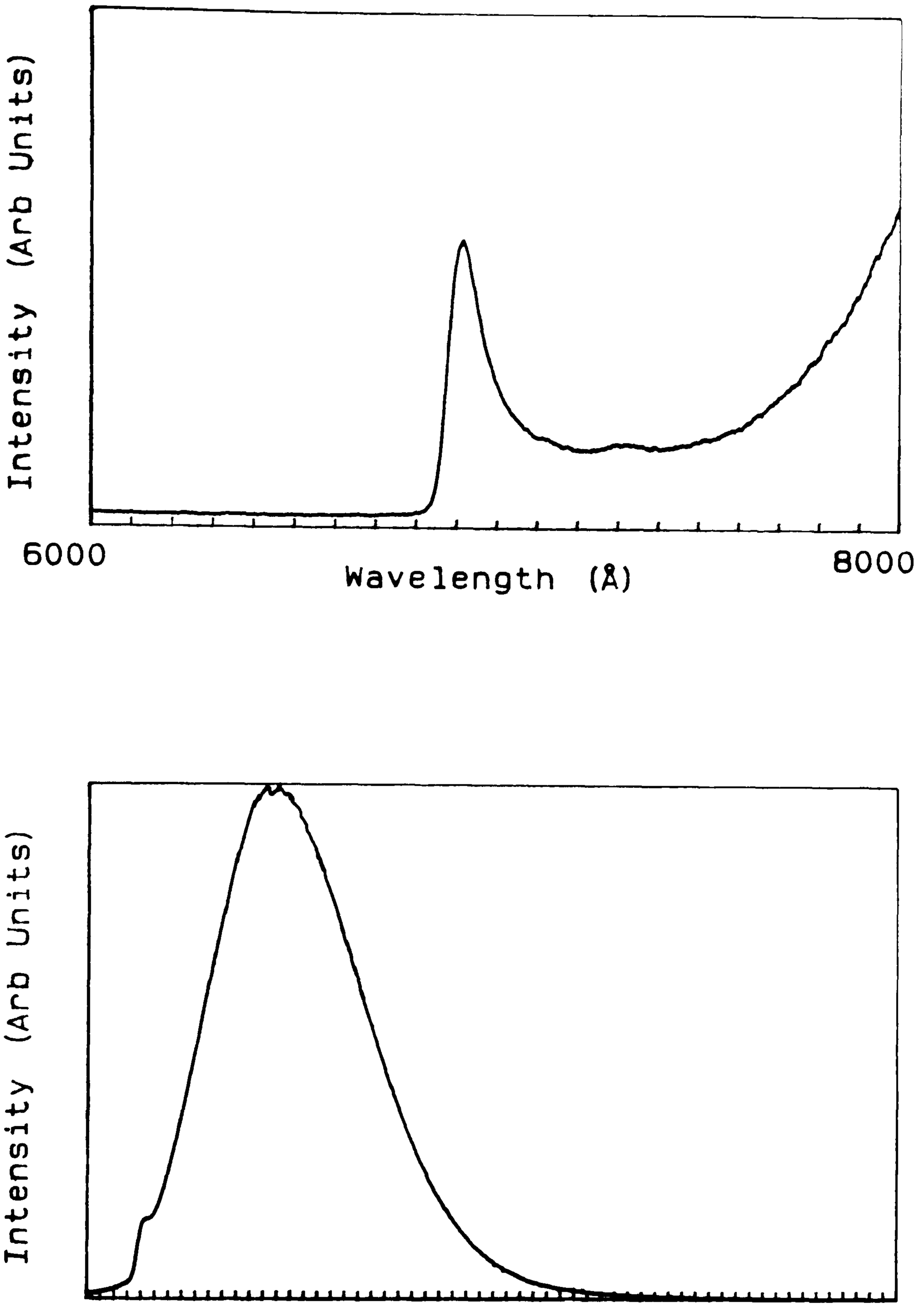

Figure 4.10. Photoluminescence spectrum from MH90 (160/130Å CdS/CdSe).

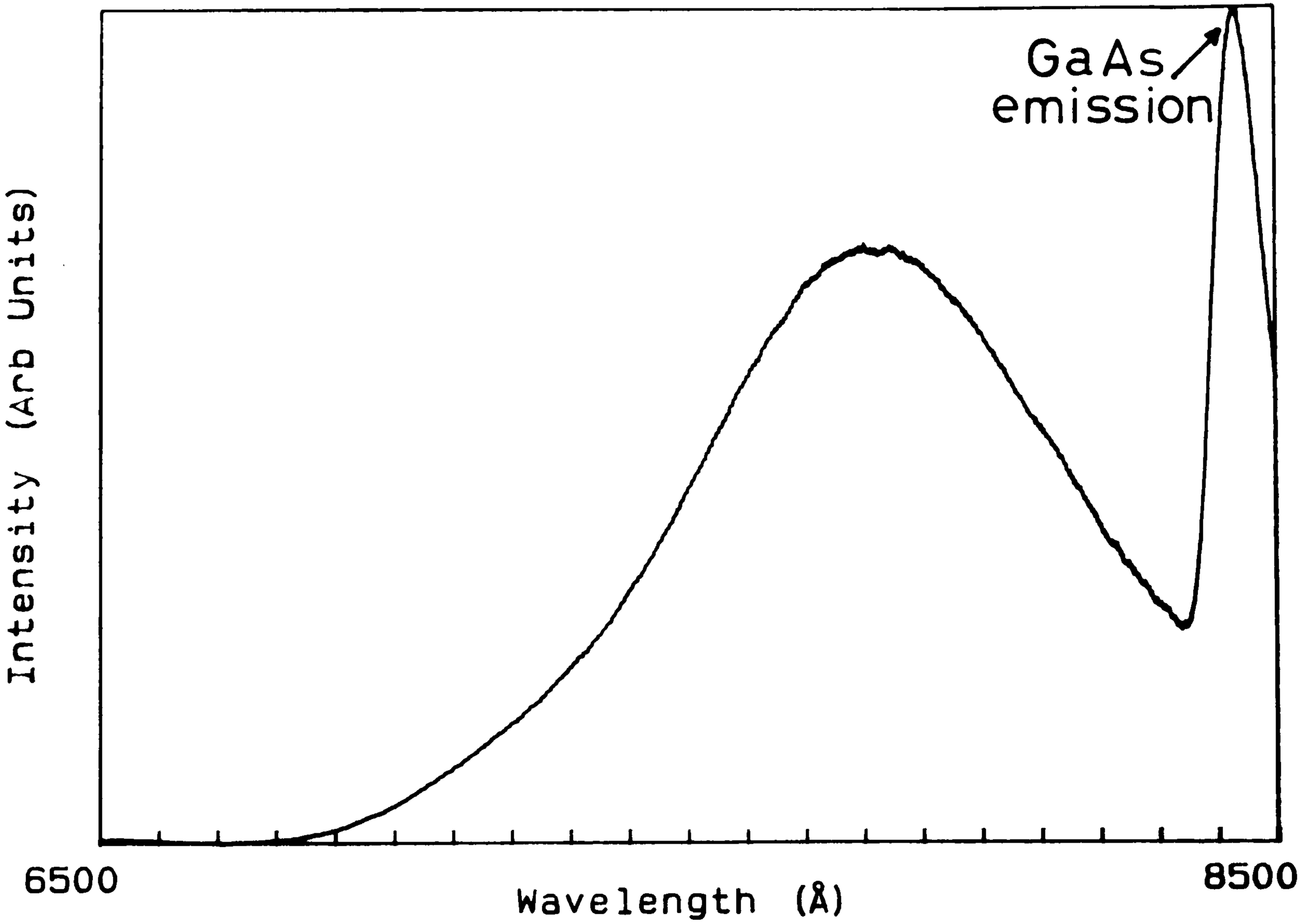

Figure 4.11. Photoluminescence spectrum from MH95 (40Å/25Å CdS/CdSe). For this small period sample the broad band emission is shifted to higher energy relative to the samples in figures 4.9 and 4.10.

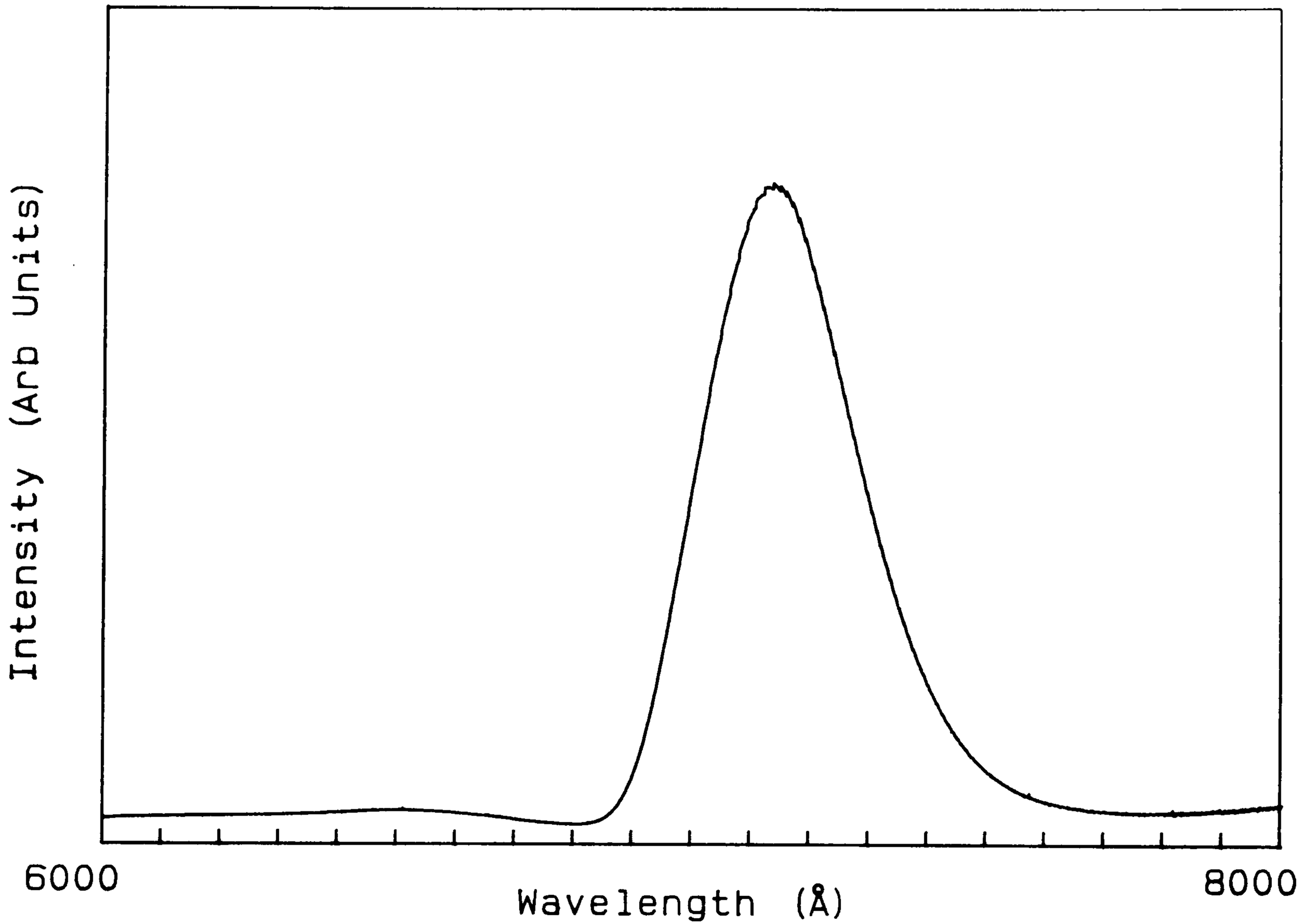

Figure 4.12. Luminescence spectrum from a small period superlattice MH121 (15Å/15Å CdS/CdSe).

excitonic emission observed from a 1μm CdSe epilayer under the same conditions (e.g. MH43 figure 3.31). There is some emission in the region of the GaAs bandedge as indicated by the rise in emission at the low energy end of the spectrum. The red peak is similar (in width and brightness) to that observed from other small period superlattices composed of II-VI semiconductors, for instance ZnSe/ZnTe and ZnS/ZnSe [6,7].

Without studying the theoretical reasons for the emission observed, we can make one simple observation. This concerns superlattices in which the CdS and CdSe layers are of equal thickness. For such a superlattice (in the limit of small period) we expect, intuitively, the emission to become that of the alloy $CdS_{0.5}Se_{0.5}$. Figure 4.13 shows the spectra from MH120 and MH73, a 7Å/7Å superlattice and a $CdS_{0.5}Se_{0.5}$ (see section 3.3.5) alloy respectively; note the different wavelength limits on the spectra. It can be seen that the spectra are still very different even for such a small period superlattice. The large difference suggests that the superlattice structure holds even down to such small periods. That is to say that the absence of 5700Å emission from the superlattice confirms that isotropic alloying does not occur.

We conclude that the spectra from the superlattices show features not observed in single epilayers. That these feature originate from the modulated nature of the structures can be inferred. We can now attempt to identify the emission bands.

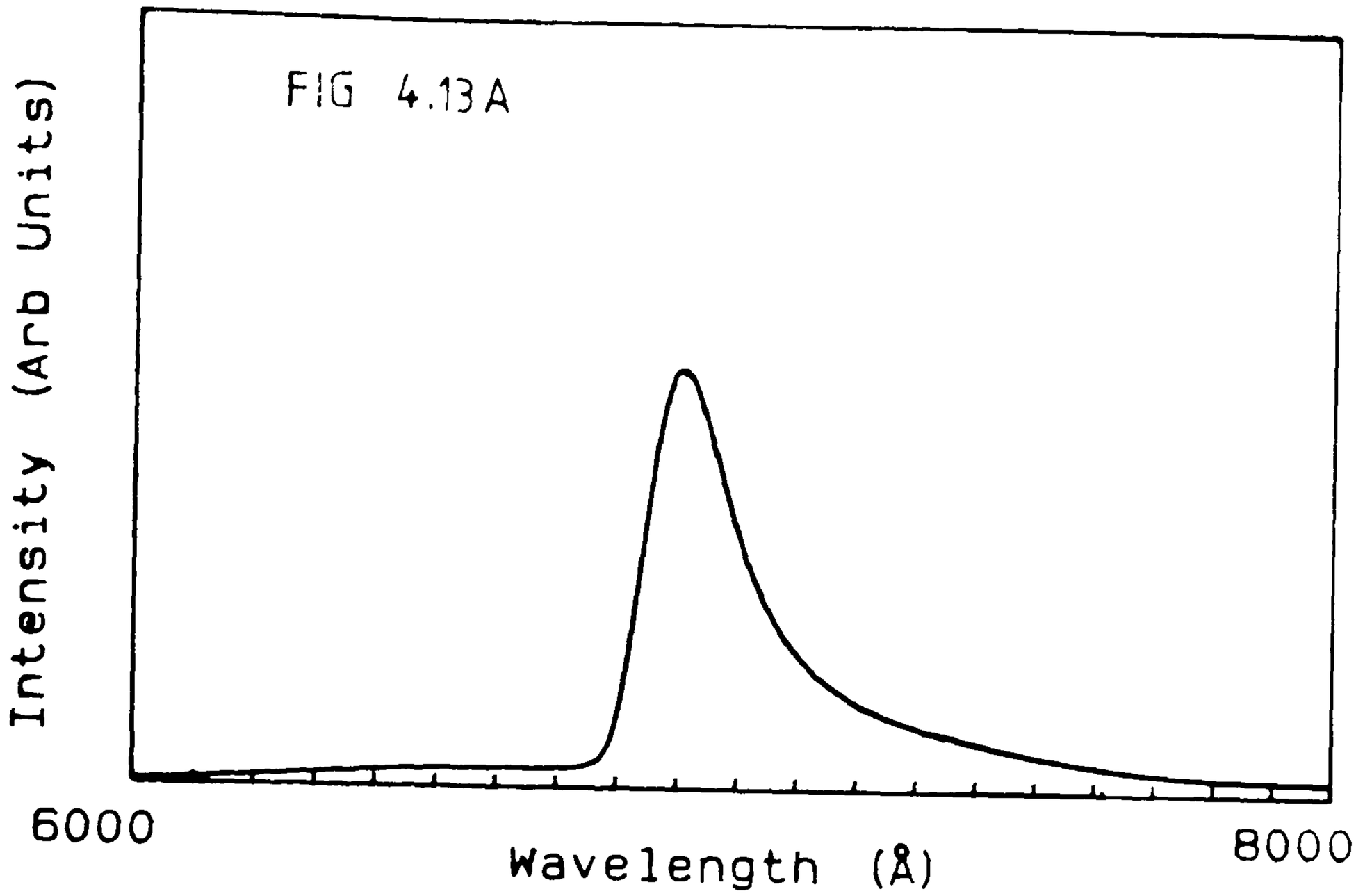

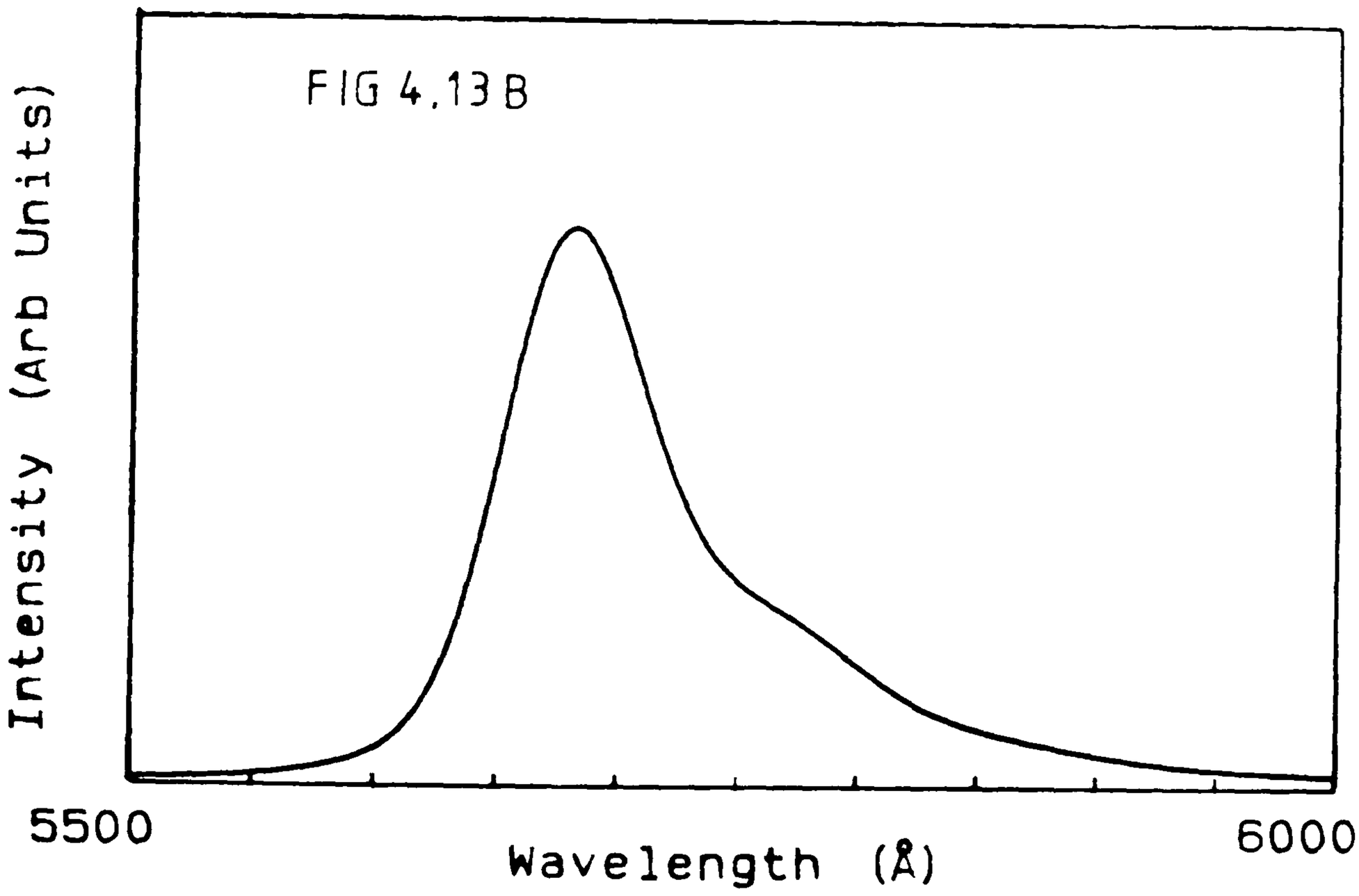

Figure 4.13. Two spectra showing the different luminescence obtained from a superlattice and an alloy. The upper spectra 4.13A is of MH121 a 7Å/7Å superlattice. The lower 4.13B is of MH73 a $CdS_{0.5}Se_{0.5}$ alloy.

4.3.2 Origin of emission bands

The interpretation of superlattice emission was briefly reviewed in section 1.6. The nature of the transitions responsible for the emission from our samples was initially totally unknown. Before any analysis of the CdS/CdSe superlattice system could be attempted it was necessary to identify the origin of the luminescence peaks. In this section we will discuss this identification. In section 4.4 theory is developed to describe the dependence of the luminescence on period for two series of samples.

It is clear from the short period superlattices that the emission band in the near-infrared is the principal emission from the superlattice. As we move to large periods we might expect the luminescence to change to that of bulk CdSe (cf. the CdTe/$Cd_{1-x}Zn_xTe$ system [8]). We therefore expected to be able to identify the luminescence peaks from the thick CdSe layers in terms of the CdSe epilayer emission as studied in section 3.3.4.

Figures 4.14 and 4.15 shows the red emission from MH88 and MH89 with periods of 700Å and 500Å respectively. Both spectra show the same two bands in addition to the deep infra-red emission. The visible red emission from the sample consist of two bands (labelled A and B on the figures), with maxima at 7100Å and 7250Å respectively. We can compare these spectra to those observed from the the CdSe epilayers (section 3.3.4.1). We find that the A and B bands from the superlattices lie close to the wavelength positions of the CdSe epilayer emissions referred to as the Y band (7015Å) and the zero-phonon free to bound emissions (7150Å) respectively (see figure 3.15). Figure 4.16 shows the temperature dependence of the two bands A and B for MH88. The temperature dependence of the A band is identical to that of the Y band from the CdSe epilayers (figure 3.34): they both show rapid quenching

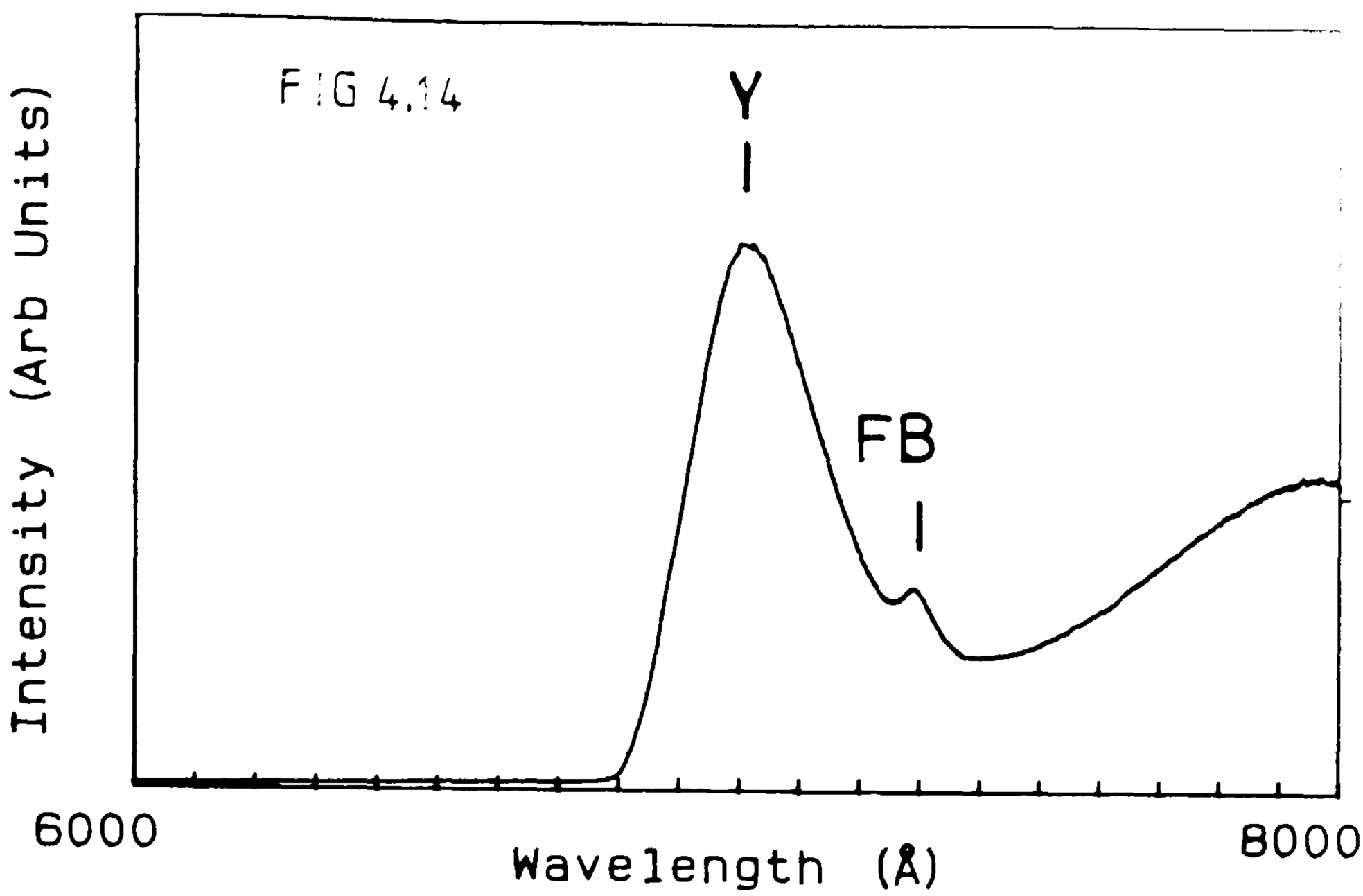

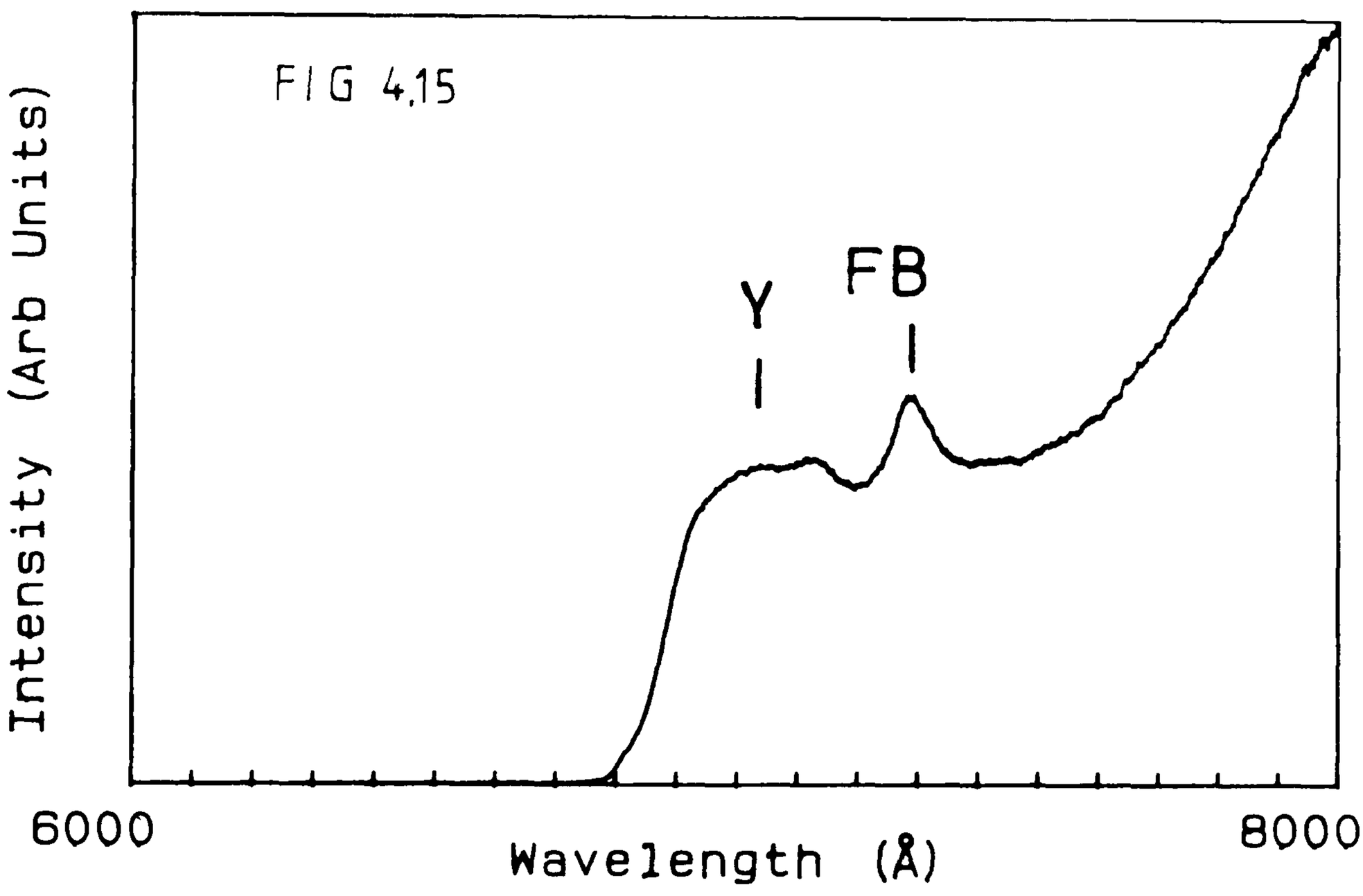

Figures 4.14 and 4.15. CdSe edge emission from large period superlattices. The upper spectra (4.14) shows the luminescence from MH88 (300Å/400Å CdS/CdSe). The lower that from MH89 (300Å/200Å CdS/CdSe). The bands Y and FB are referred to in the text.

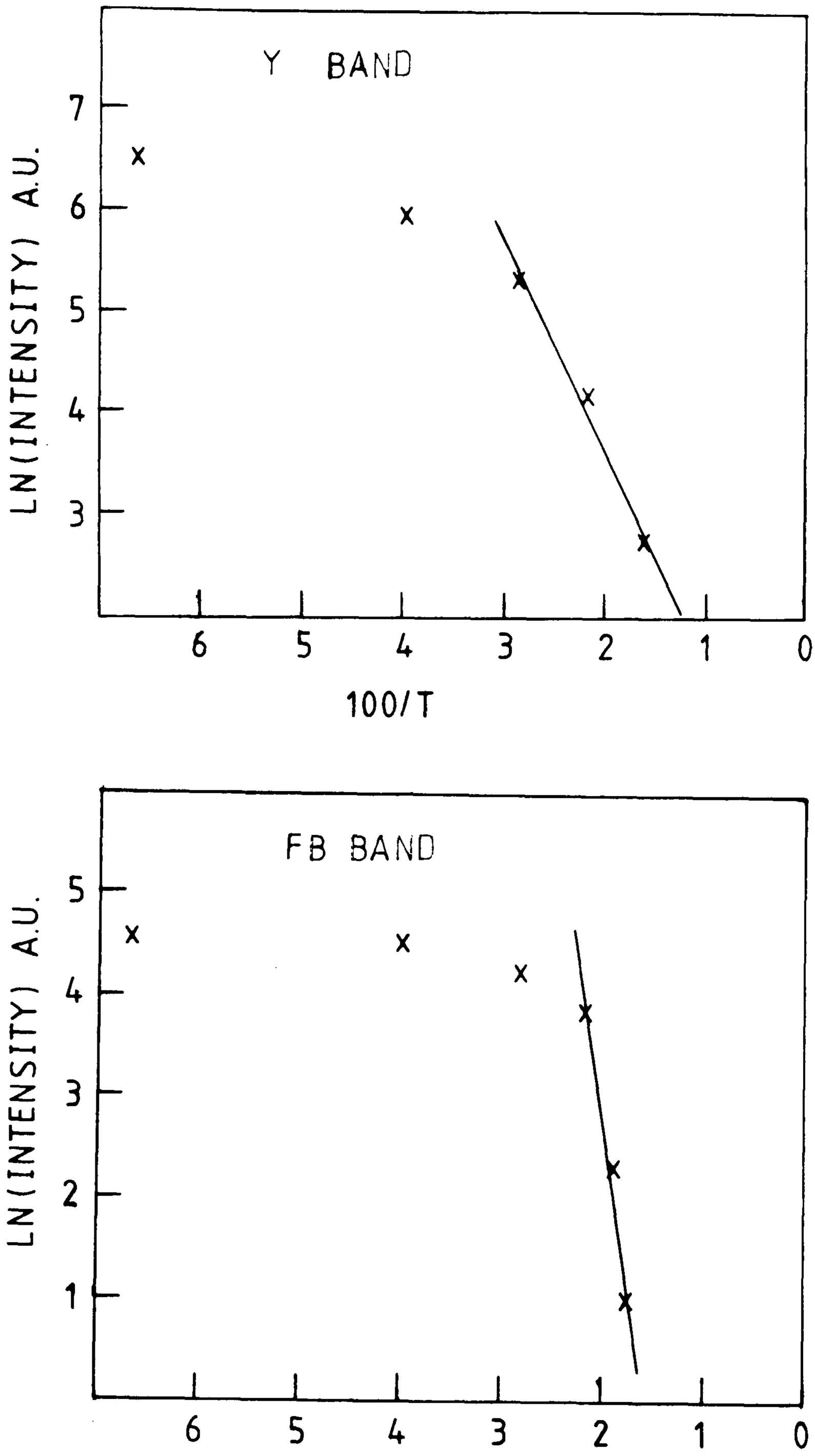

Figure 4.16. Arrhenius plots showing temperature dependance of Y and FB bands from the large period superlattice MH88. The upper graph shows the dependance of the Y band. the line on the right hand side corresponds to an activation energy of 18 meV, precisely tha same as that of the Y band in the CdSe epilayers (figure 3.33). The lower figure shows the dependance of the FB band, this is similar to that of the CdSe free to bound emission (see figure 3.34).

above 35K with the same activation energy of 18 meV. Correspondingly, band B shows identical temperature dependance to the free to bound recombination (figure 3.35). We can conclude that the A and B bands are respectively the same emissions as the Y and free to bound bands observed from the CdSe epilayers. The discrepancy between the wavelength positions observed in epilayers and superlattices is discussed below.

As the sample is warmed, further structure is revealed in the spectra due to the quenching of the Y band at 35K. Figure 4.17 shows three spectra taken from MH88 at 15,50 and 150K. The Y and free to bound bands fade as the temperature is raised, leaving a narrow band at 6850Å (at 45K); this is close to the position expected for the free exciton from CdSe (6797Å [9]) and is marked in figure 4.17 as X_o. This band's temperature dependence is shown in figure 4.18a. The luminescence from the peak at 6850Å persists to high temperature and decays with a small activation energy (29meV). Figure 4.18b shows the temperature dependence of the CdSe free exciton (from MH43). It can be seen that the decays are almost identical, the luminescence decaying with an activation energy of 26meV. We conclude that the band at 6850Å is the free exciton emission from the CdSe layers in MH88. MH89 also showed the same X_o emission at higher temperatures. Figure 4.19 shows the free exciton emission resolved with MH89 at 45K along with the Y band and the free to bound emission (marked FB).

As we move to smaller periods emission spectra changes markedly. Figure 4.20 is a spectra recorded from MH90 at 1.6K. The spectrum shows only the CdSe free exciton emission (X_o) with a very weak free to bound zero-phonon line visible (marked FB on the figure). In order to understand the emission the first thing to note is that the X_o emission from the three samples is shifted to lower energy relative to the bulk

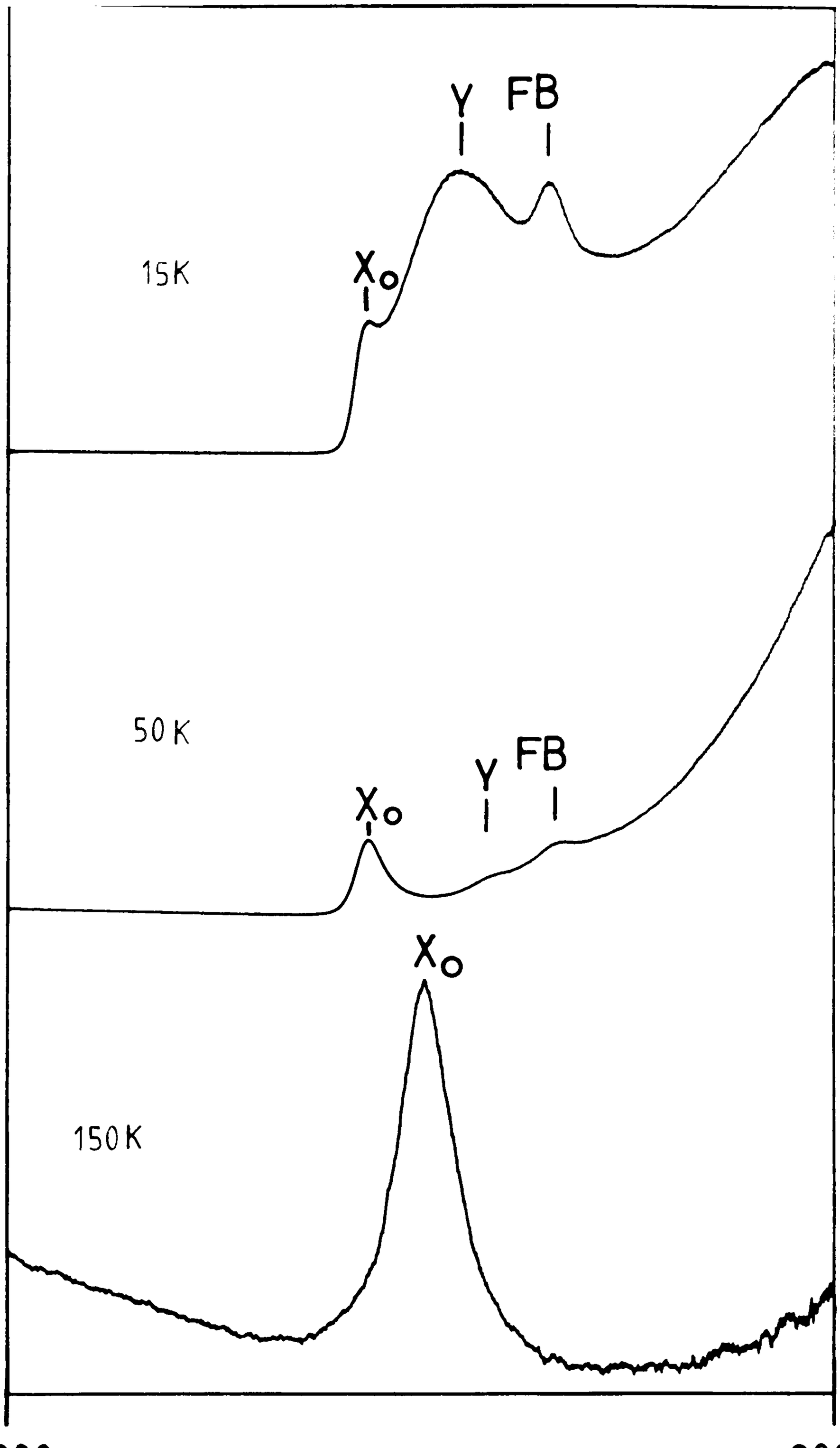

Figure 4.17. Temperature dependance of the emission fro MH88. As the temperature is raised the Y band and the free t bound emission quench, leaving the CdSe free excitoni emission.

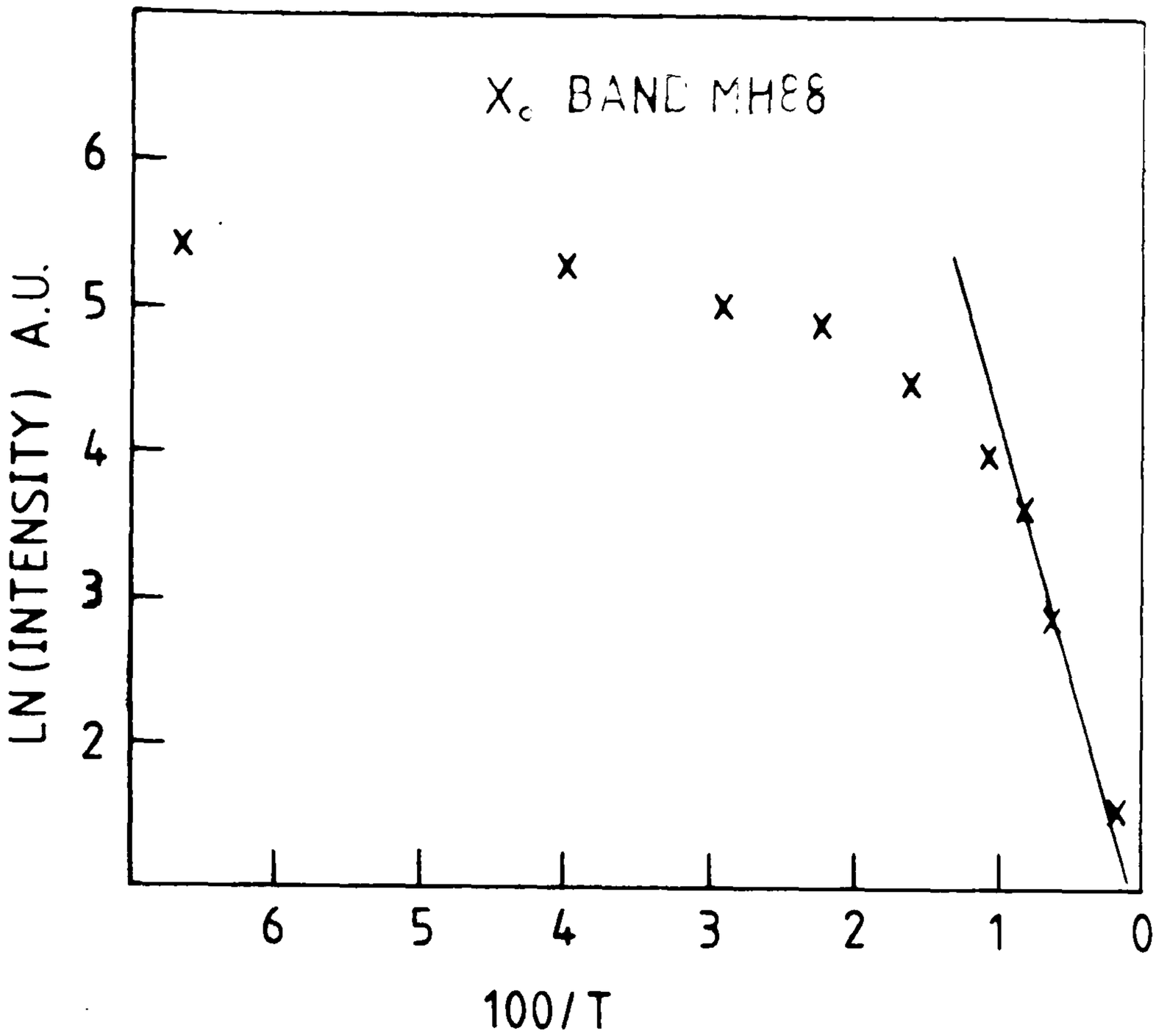

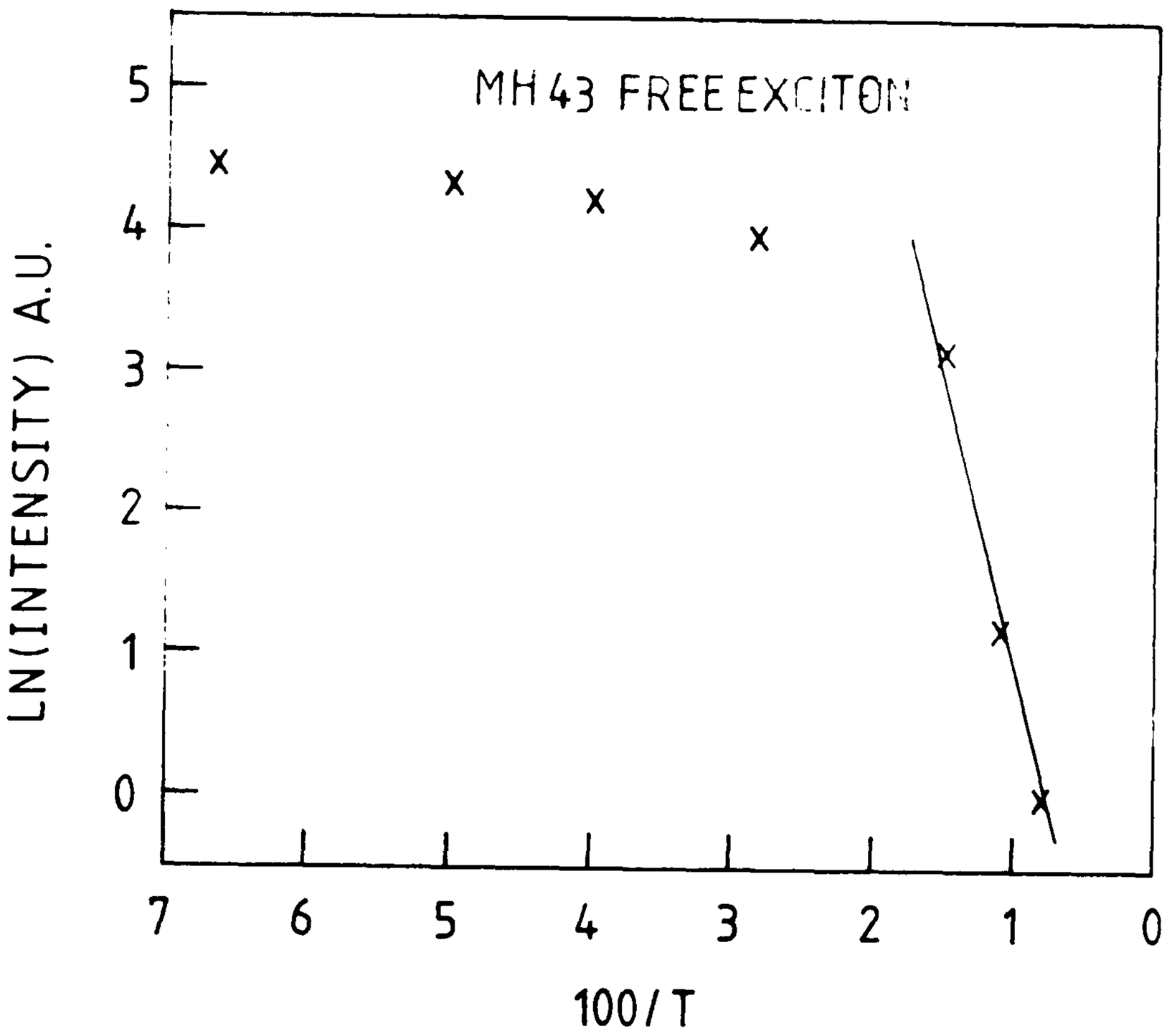

Figure 4.18. Arrhenius plots comparing the temperatur dependance of the Xo band from the superlattice MH88 with th free exciton emission from MH43. The upper graph shows th dependance of the superlattice emission, the lower the CdS epilayer emission. The lines drawn correspond to activatic energies of 29meV and 26meV for the upper and lower diagram respectively.

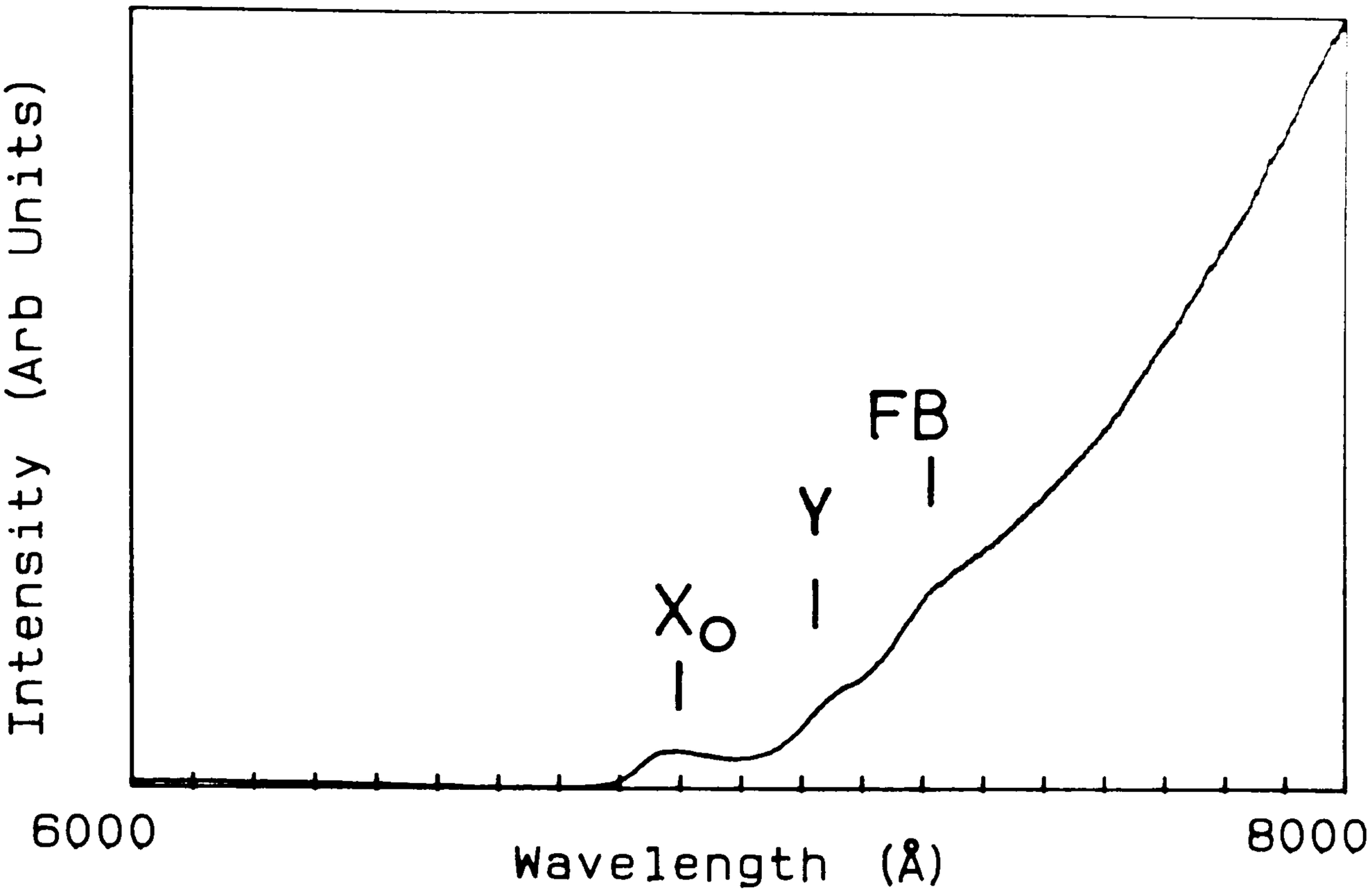

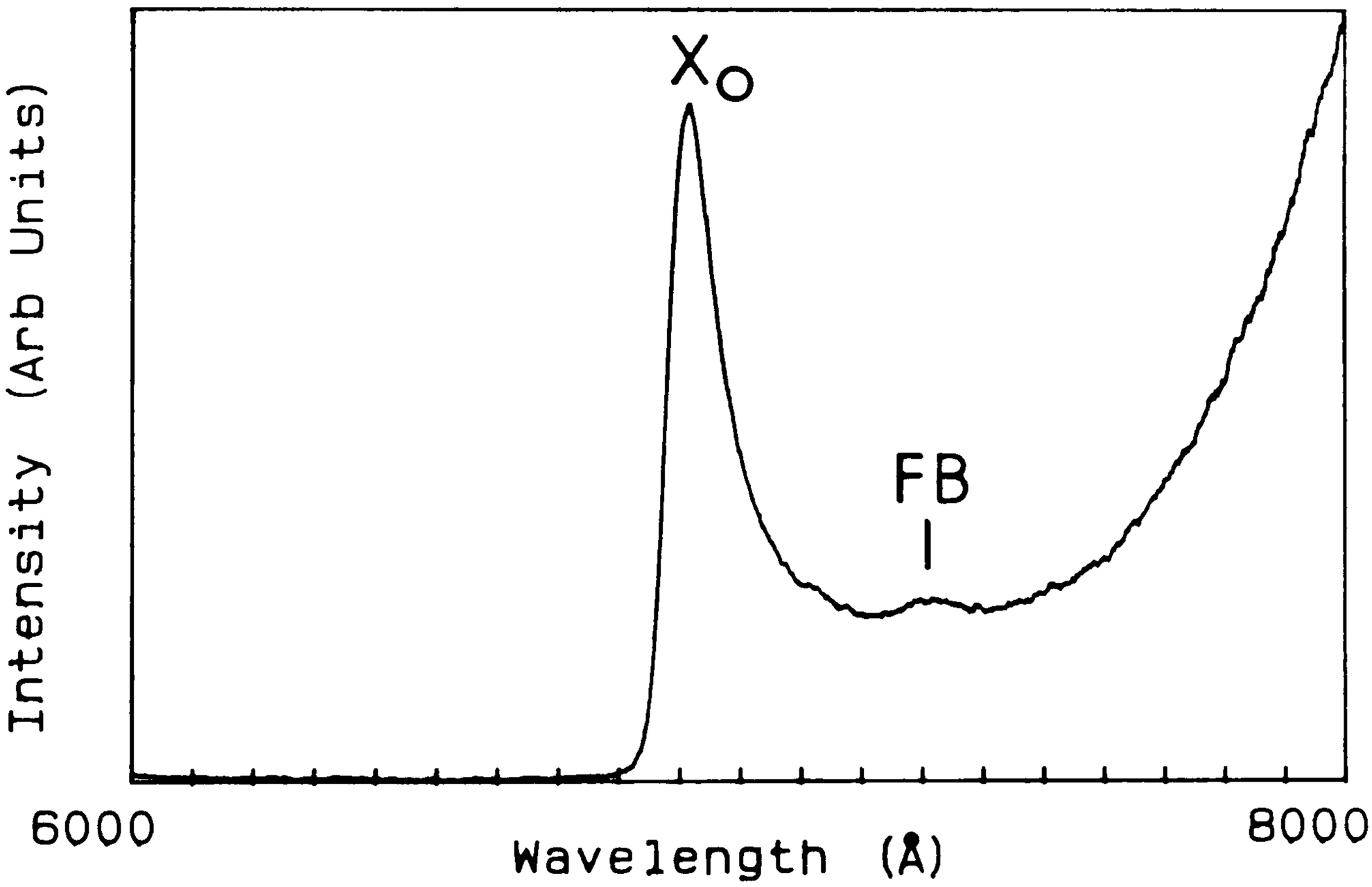

Figure 4.19 (upper spectrum). CdSe edge emission from MH89 at 45K. At this temperature the free excitonic emission is clearly resolved

Figure 4.20 (lower spectrum). Photoluminescence spectrum from MH90 (90Å/160Å CdS/CdSe superlattice). The CdSe edge emission from this sample is dominated by the CdSe free exciton (X_o) with a weak zero-phonon free to bound peak also present.

CdSe free exciton emission. It was shown in section 3.1.4 that elastic deformation of the lattice can produce such a shift. Clearly this could provide an explanation for the red shift observed for the free exciton from these samples.

4.3.3 Strain relaxation in CdS/CdSe superlattices

It is clearly of interest to try and determine whether the superlattices studied above are freestanding or pseudomorphic to the buffer layer. It was shown in section 1.6.3 that a freestanding strained layer superlattice consists of alternating layers under biaxial compression and tension. The lattice constant of such a system was calculated in section 1.6.3. Therefore we can calculate the biaxial compressive strain E on the CdSe in such a freestanding structure. We find it is given by (using equation (xxiii), section 1.6.3)

$$E = 0.039/(1+L_{CdSe}/L_{CdS}) \qquad (i)$$

Where L_{CdSe} and L_{CdS} are the thicknesses of the CdSe and CdS layers respectively and 0.039 is the mismatch between CdS and CdSe. If MH88 is freestanding and the layers of the superlattice are commensurate to each other (without any strain relaxing dislocations) then the CdSe will have a 2.5% compressive strain. We can now use the theory in section 3.1.4 to calculate the energy shift of the CdSe free exciton emission that this strain produces. We find (from equation (xii), section 3.1.4) that we expect a red shift of 26 meV for the A exciton transition energy. The same figures for MH89 and MH90 are 32 and 30 meV respectively. We can compare these shifts to the observed shifts. The shifts measured being 16,23 and 31 meV for MH88,MH89 and

MH90 respectively. We find that the observed shift is less than the calculated shift. However, the values get closer as the period decreases. Indeed, the discrepency for MH90 is well within the limits of experimental error (+_2 meV). MH91 was studied by TEM (see section 4.2), this sample is similar to MH90 with only slightly thinner CdSe layers (90Å compared to 130Å in MH90). MH91 was found to have high crystalline quality, containing very few dislocations. Therefore, we conclude that the samples with larger period than MH90 (290Å) are not freestanding. Moreover, neither are they pseudomorphic as this would produce an even larger red shift. We can therefore conclude that the large period superlattices must contain many dislocations in each CdSe epilayer relaxing the strain. This is supported by the fact that the CdSe layers in these superlattices are close to the critical thickness calculated in section 3.1.2 for CdSe grown on CdS (200Å). We can also conclude that the superlattices with periods <290Å are either freestanding or pseudomorphic.

In section 3.3.4.2 the origin of the Y band was discussed. It was suggested that this band may be associated with the presence of extended lattice defects in the epilayers. This band is absent in the emission from MH90 (160Å/130Å CdS/CdSe) and all superlattices with periods smaller than 250Å. We know that these superlattices are high quality with few lattice defects (section 4.2). We also found above that the thicker superlattices MH89 and MH88 probably contained many such defects. It seems reasonable to suggest that the two observations may be related and that the centres responsible for the Y band are not present in the smaller period superlattices. The evidence from both TEM and luminescence is that the small period superlattices are of high structural quality. The presence of only free excitonic emission from the CdSe in sample MH90 indicates high purity. This is an important

point in view of the analysis in section 4.4. The emission from the CdSe layers in small period structures (<240Å) is free excitonic.

As the period reduces the CdSe edge emission is suppressed and the deep, near-infrared, luminescence dominates. As observed above this emission is not observed from any of the single epilayers, and its intensity increases rapidly as the period decreases. The CdSe edge emission, in contrast, increases in intensity as the period increases. It is found that faint higher energy luminescence is observed for all the smaller period (<150Å) superlattices. An example of this emission is shown for MH108 (68Å/20Å CdS/CdSe) in figure 4.21. This emission is very broad, unlike the CdSe excitonic emission observed from thick samples. The origin of this emission is discussed in section 4.5.4.

We conclude that, as expected, in the limit of long period the emission from the CdS/CdSe superlattices becomes that of bulk CdSe. The CdSe free exciton emission shows clear evidence of red shifting caused by the compressive strain within the superlattice. We can finally conclude that the broad band infra-red emission is the only bright emission which is unique to the superlattice structure.

4.3.4 Effect of laser intensity

It was found that the infra-red emission of the superlattice samples showed large variations with excitation power density. Figure 4.22 shows a series of spectra demonstrating this effect for MH121 15Å/15Å superlattice). The luminescence peak shifts to higher energy by upto 100 meV as the laser power is increased. Accompanying this shift there is a reduction in the FWHM of the peak. Figure 4.23 shows the peak emission energy and FWHM as a function of laser intensity for this sample. The shift to higher energy becomes more pronounced for larger period samples. Figures 4.24 and 4.25 show this shift for MH95 and

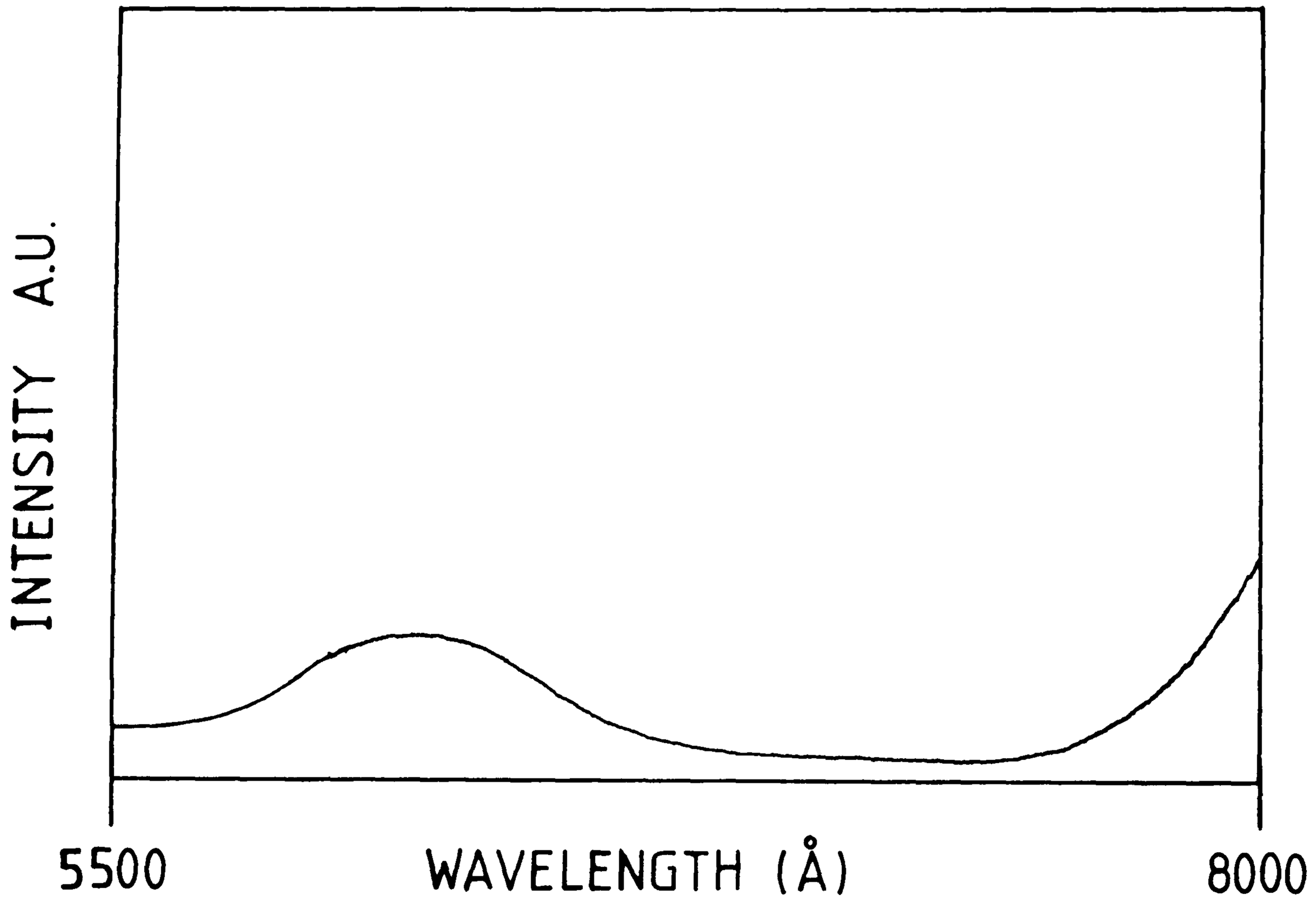

Figure 4.21. Spectrum from MH108 (68Å/20Å CdS/CdSe superlattice). The emission shown is to higher energy of the superlattice emission which peaks at 9000Å (see figure 4.38).

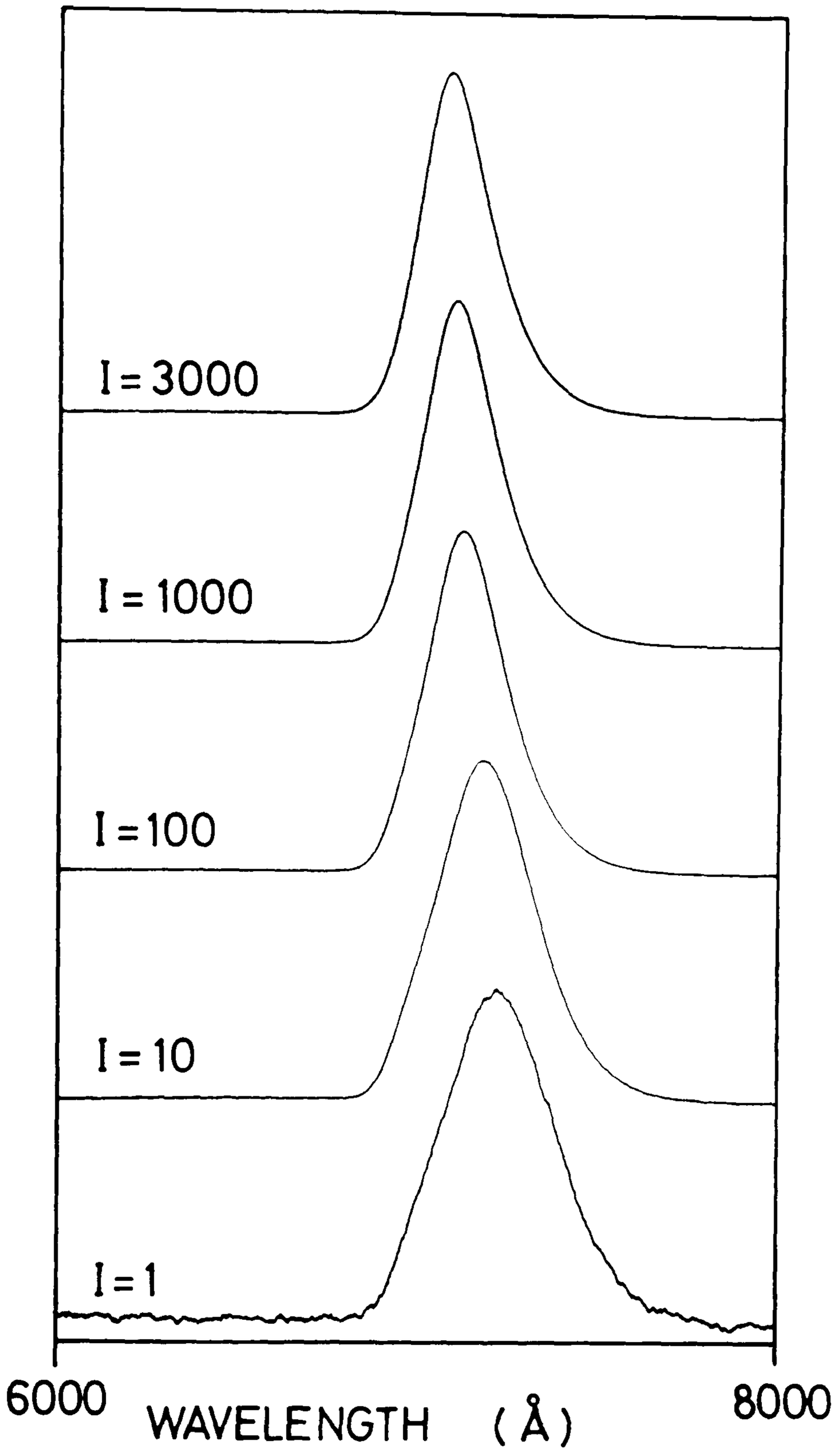

Figure 4.22. Series of photoluminescence spectra showing the effect of laser excitation power on the emission from MH121. The relative laser intensities are indicated on the left hand side in arbitary units.

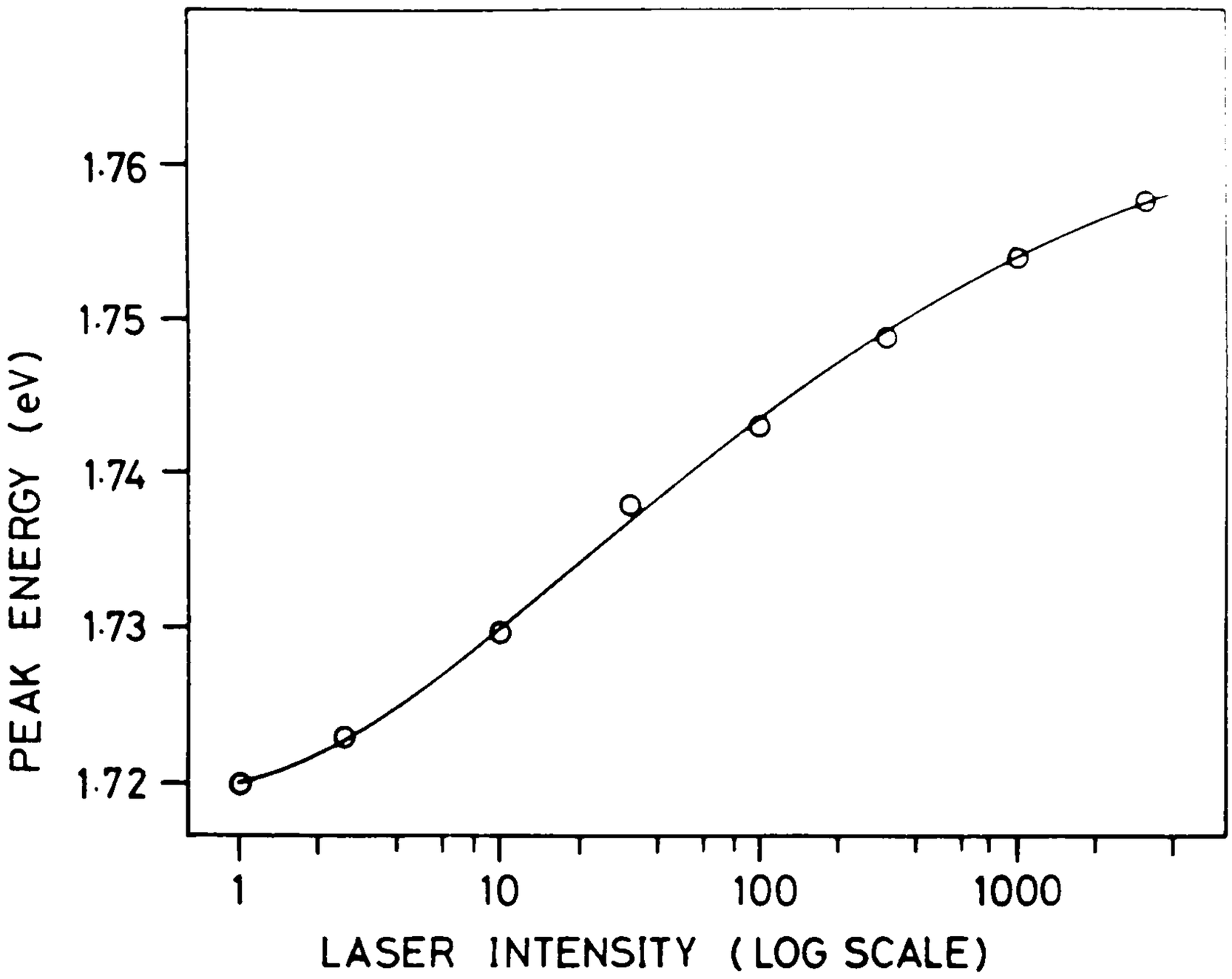

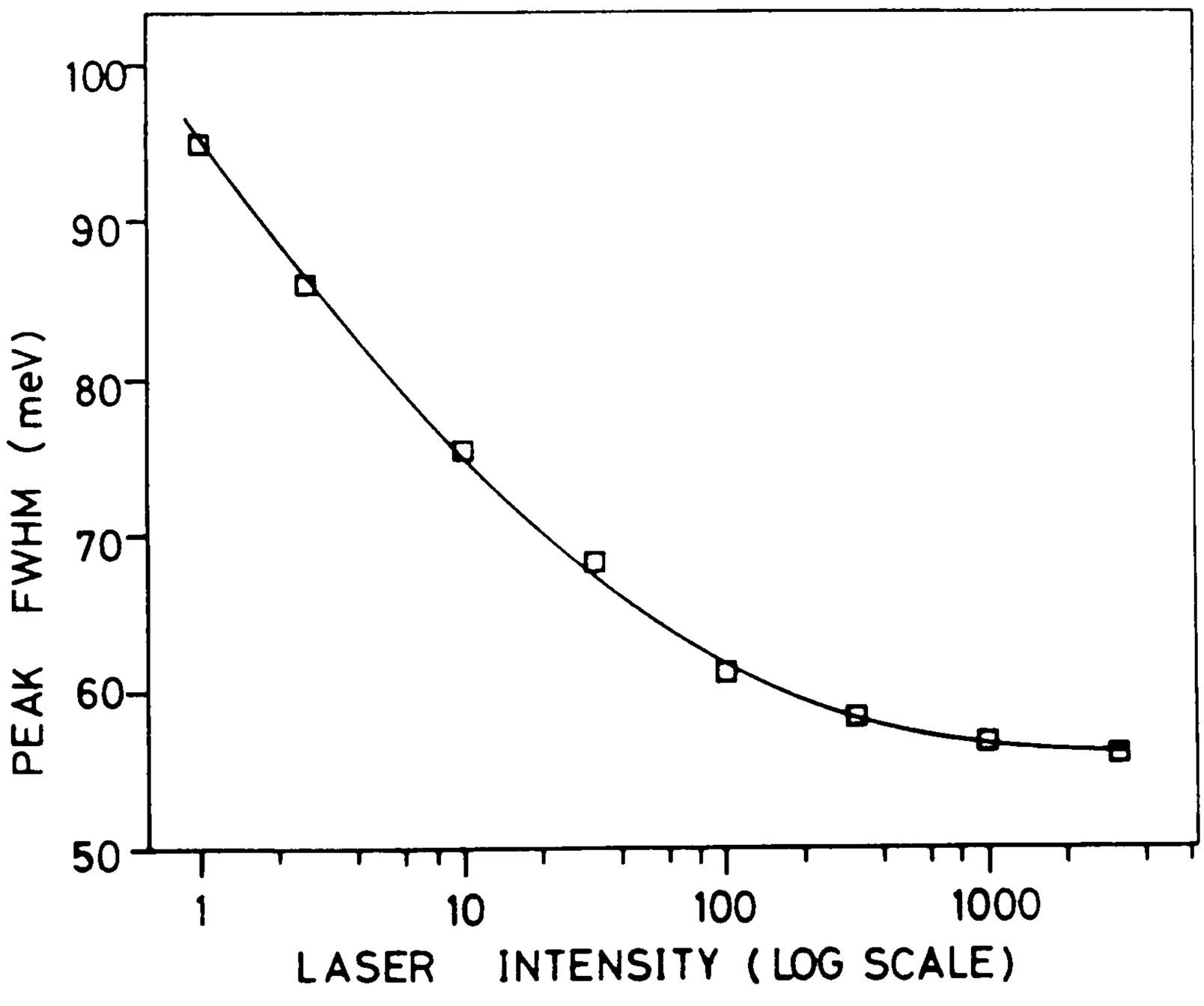

Figure 4.23. two graphs showing the effect of laser excitation intensity on the photoluminescence spectrum for MH121, a 15Å/15Å superlattice. The upper figure shows the variation of the peak position, the lower the FWHM.

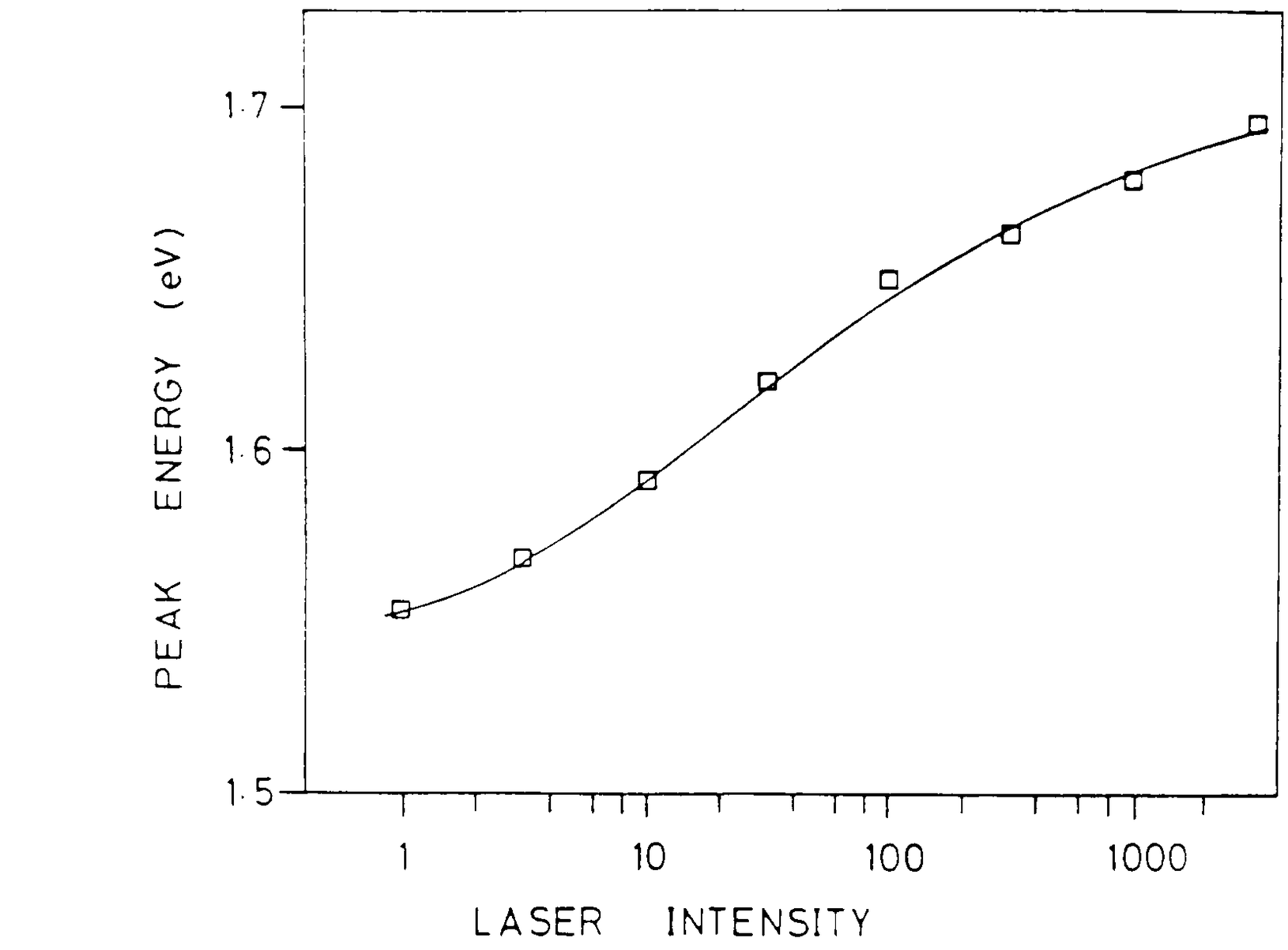

Figure 4.24. The laser power to peak position relationship for MH95 a 40Å/25Å CdS/CdSe superlattice.

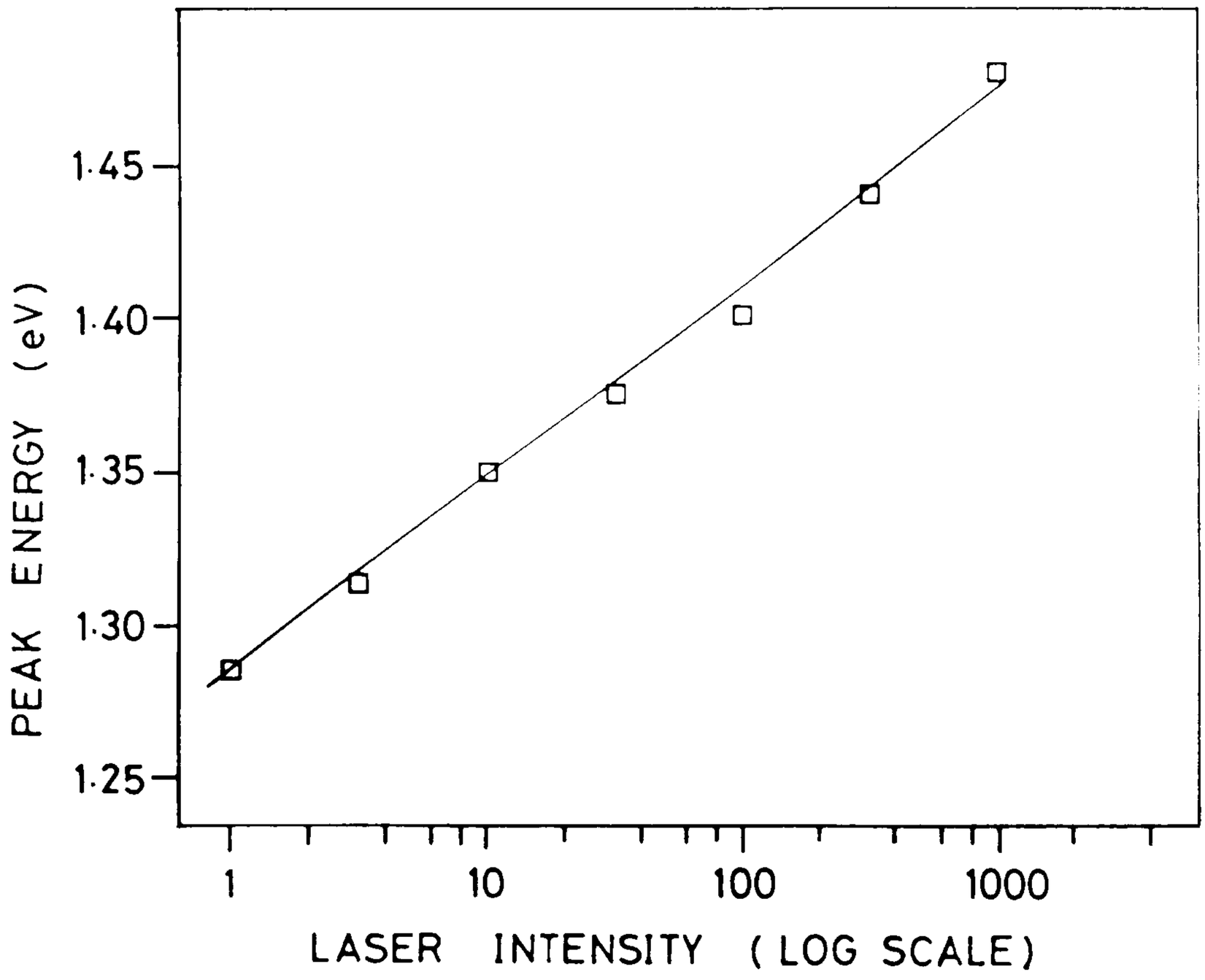

Figure 4.25. Variation of peak position for MH111 a 40Å/60Å CdS/CdSe superlattice. This sample shows a shift of upto 250 meV as the laser intensity increases.

MH111, with periods of 65Å and 100Å respectively. It can be seen that the emission peak from MH95 shifts by up to 300meV as the laser power increases. None of the other peaks observed from the superlattices exhibited this shift. In particular the free to bound, Y band and free excitonic emissions observed from the large period structures did not shift with increasing laser intensity.

Also studied was the intensity of the emission as a function of laser power. This relationship can be useful in determining the origin of superlattice emission. If the emission is impurity driven then it should be possible to saturate the luminescence by increasing the laser power significantly. This results from the presence of only a finite number of impurities to participate in the recombination [10]. In the alternative case of excitonic recombination we expect the luminescence intensity to be proportional to the exciting laser power.

Figure 4.26 shows the $LN(I_{in})$ against $LN(I_l)$ for MH120 (7Å/7Å CdS/CdSe), where I_{in} is the laser excitation power and I_l is the peak emission intensity (i.e. the peak energy emission per unit wavelength). There is no evidence of luminescence saturation and the power N taken from the graph is 1.07 indicating excitonic recombination. This is consistent with, although not conclusive proof of, intrinsic recombination not involving impurities.

4.3.5 Temperature dependence

The temperature dependence of sample MH120 was studied. This sample is a 7Å/7Å superlattice. The red emission from this sample was shown in figure 4.13 and consists of intense superlattice emission at 6800Å. In addition, faint broad band emission in the region 5800-6300Å is observed. This sample, in common with all the superlattices, shows

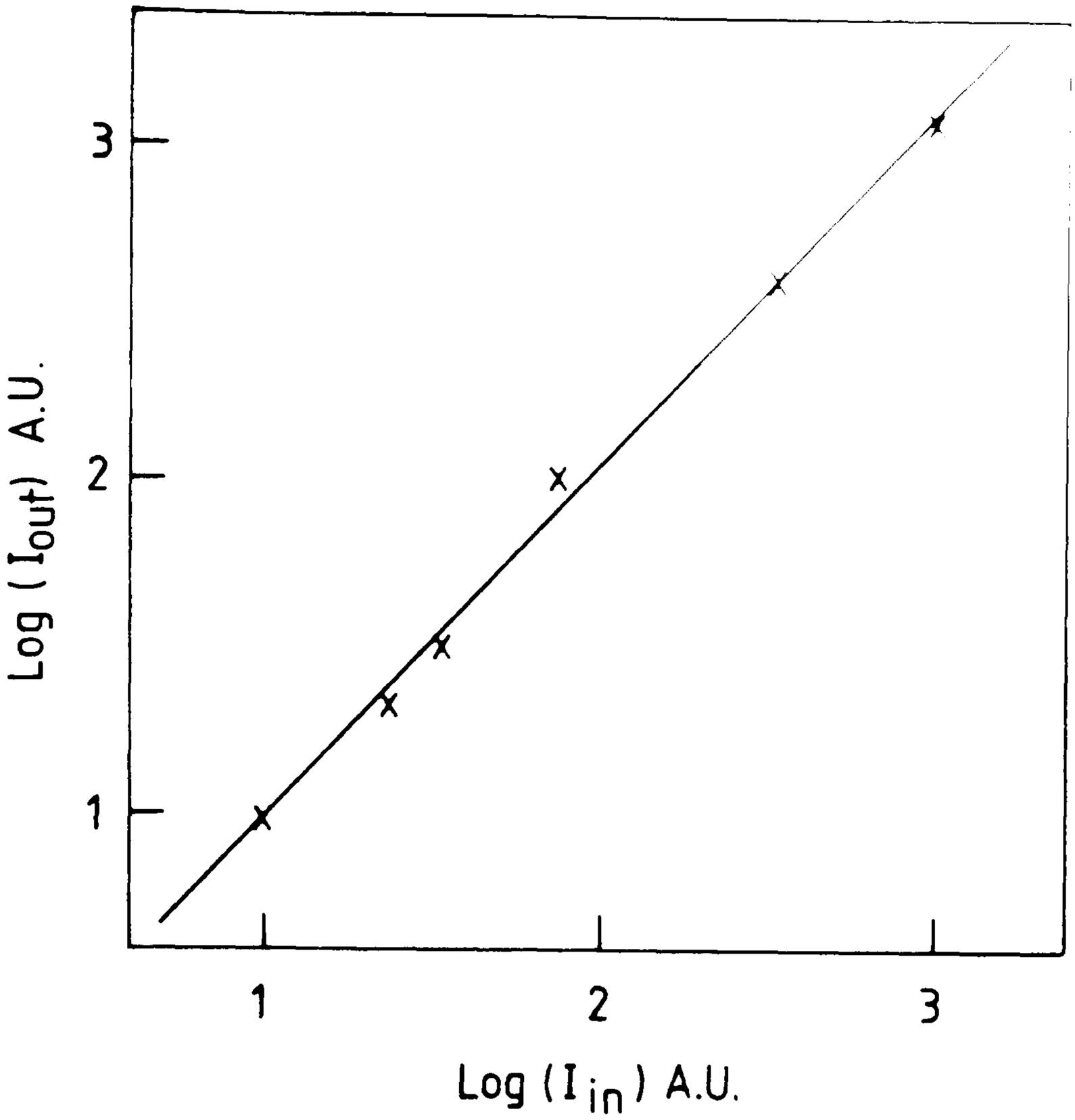

Figure 4.26. Relationship between the laser intensity I_{in} and the peak emission power out I_{out}. Both quantities are in arbitary units.

faint luminescence at a higher energy than the red or infrared 'superlattice' emission. The origin of this band was investigated by examining the temperature dependence of the two bands. Figures 4.27a and 4.27b show this temperature dependence for the 6800Å and 5500Å emissions respectively. It can be seen that both emissions display a remarkable temperature dependence. The intense superlattice emission at 6800Å first reduces in intensity and then increases before quenching totally as the temperature is increased. The emission at 5500Å actually increases initially, reaching a peak at the same temperature as the 6800Å emission is at minimum, before quenching totally as the temperature increases. It is unlikely that the emissions' respective minima and maxima occur at the same temperature by coincidence. It appears that carriers transfer from the superlattice recombination process to the 5500Å emission as the temperature is raised. A similar effect is observed for very small period ZnSe/ZnTe superlattices [11]. In this system the luminescence from a 20Å period superlattice was observed to increase as the temperature was raised. The authors attributed this to thermal detrapping of carriers. Our interpretation of this effect is discussed further in section 4.5.4.

Figure 4.28 shows the temperature dependence of the emission from MH92. The emission from this sample consists of the broad, intense infra-red band observed in all superlattices with periods >50Å. The two curves correspond to laser powers of 50 and 5mw as indicated. The curves show that the luminescence remains fairly constant up to 70K before decaying with an activation energy of 50 meV. The mechanism of the quenching process can not be discerned from these curves. However, the relationships are similar to those observed from other II-VI superlattices with periods in this range (for example ZnSe/ZnTe [11]).

Figure 4.27. Arrhenius plots that show the dependance of the photoluminescence peaks observed from MH121 (a 7Å/7Å superlattice)

Figure 4.27a (upper graph) shows the temperature dependance of the emission intensity for the 6800Å 'superlattice emission'. The points are experimental, the line is drawn to aid the eye.
Figure 4.27b (lower graph) shows the same dependance for the weaker luminescence observed in the region of 5500Å. The points and lines have the same significance as for the previous graph. The peak in emission intensity occurs at the same temperature as the dip in the 6800Å emission intensity (i.e. at 60K).

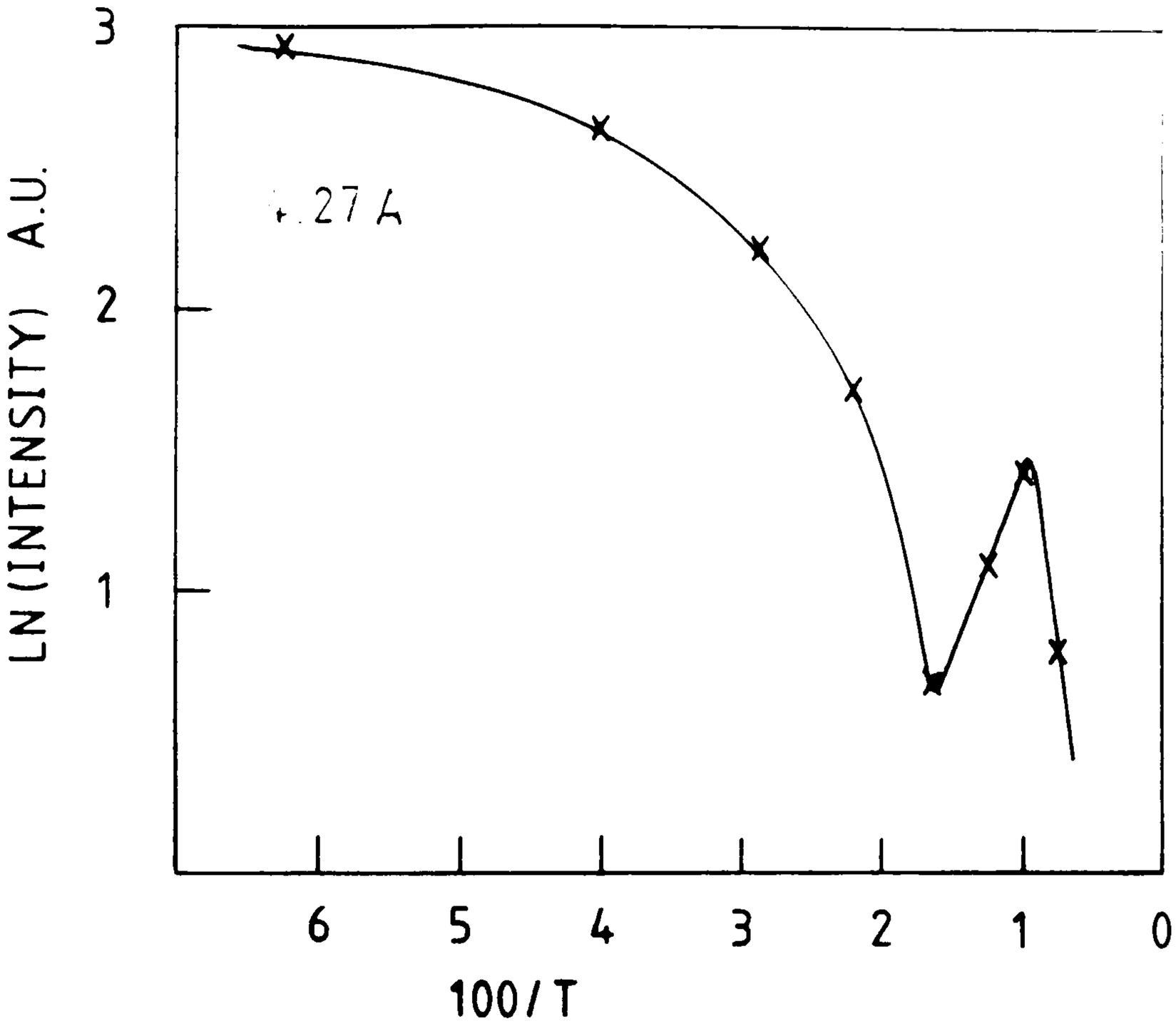
4,27 A
LN (INTENSITY) A.U.
3
2
1
6
5
4
3
2
1
0
100 / T

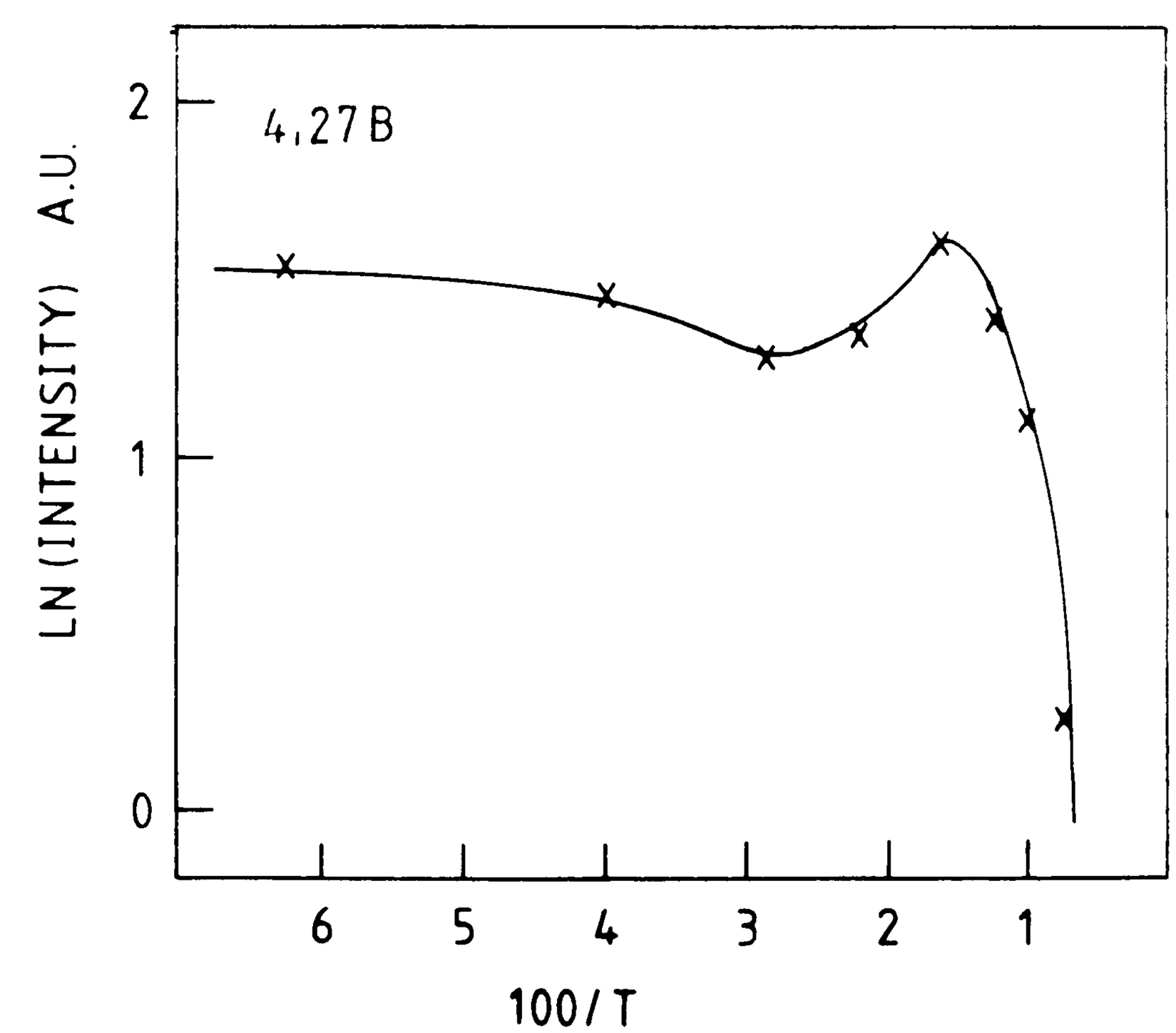
4,27 B
LN (INTENSITY) A.U.
2
1
0
6
5
4
3
2
1
100 / T

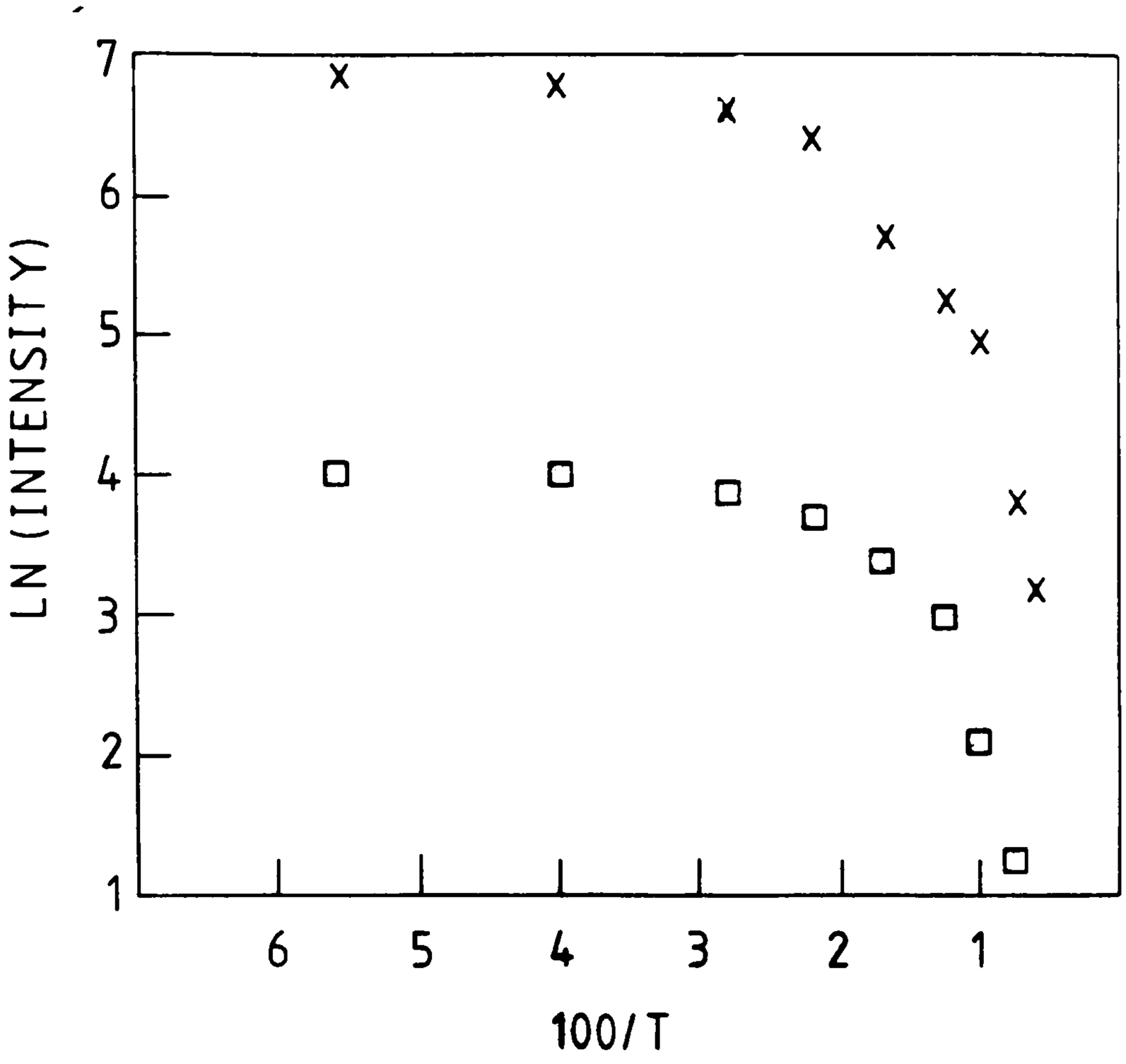

Figure 4.28. Arrhenius plot showing temperature dependance of the superlattice emission from MH92 (60Å/50Å CdS/CdSe superlattice). The crosses correspond to 50 mW laser excitation, the squares 5mW.

4.3.6 Time resolved measurements

The decay time of luminescence can give important information as to its origin. In particular the decay of the luminescence from superlattices has been extensively studied. It has been found these the decay times are very sensitive to the relative positions of the electron and holes within a superlattice [12]. For this reason time decay measurements of the infra-red band from our superlattices were important. These measurements were taken at Strathclyde university by X.Chen and K.P.O'Donnell. The technique used to measure the decay was time correlated photon counting. The details of the technique are described in reference [13]. Here we will simply examine the measured decays for two samples. The samples studied were MH123 and MH93 with periods of 50Å and 145Å respectively. Owing to the limitations of the detector, the time decay measurements were limited to luminescence in the visible region (longest wavelength 7500 Å).

The sample MH123 displayed strong superlattice emission in the region 7000-7500Å. For this sample the time decay was measured at three wavelengths 7000,7300 and 7500Å. The decay curve for for the emission at 7500A is shown in figure 4.29. The decays exhibit different lifetimes, the results are shown in table 4.2. The luminescence decays are not simple exponential. However, the principal decay is a single exponential curve with the given lifetimes. It can be seen that the decay is quite slow for excitonic recombination (16-63ns). This lifetime is long compared to 2.75ns for the free exciton in the alloy $CdS_{0.5}Se_{0.5}$ [13]. The decay is slower at lower energy positions in the peak, indicating a peak shift to lower energy with time. In the case of GaAs the presence of other exponential components in the luminescence decay has been attributed to the presence of impurities [14]. The impurities causes carrier trapping and the consequent alternative

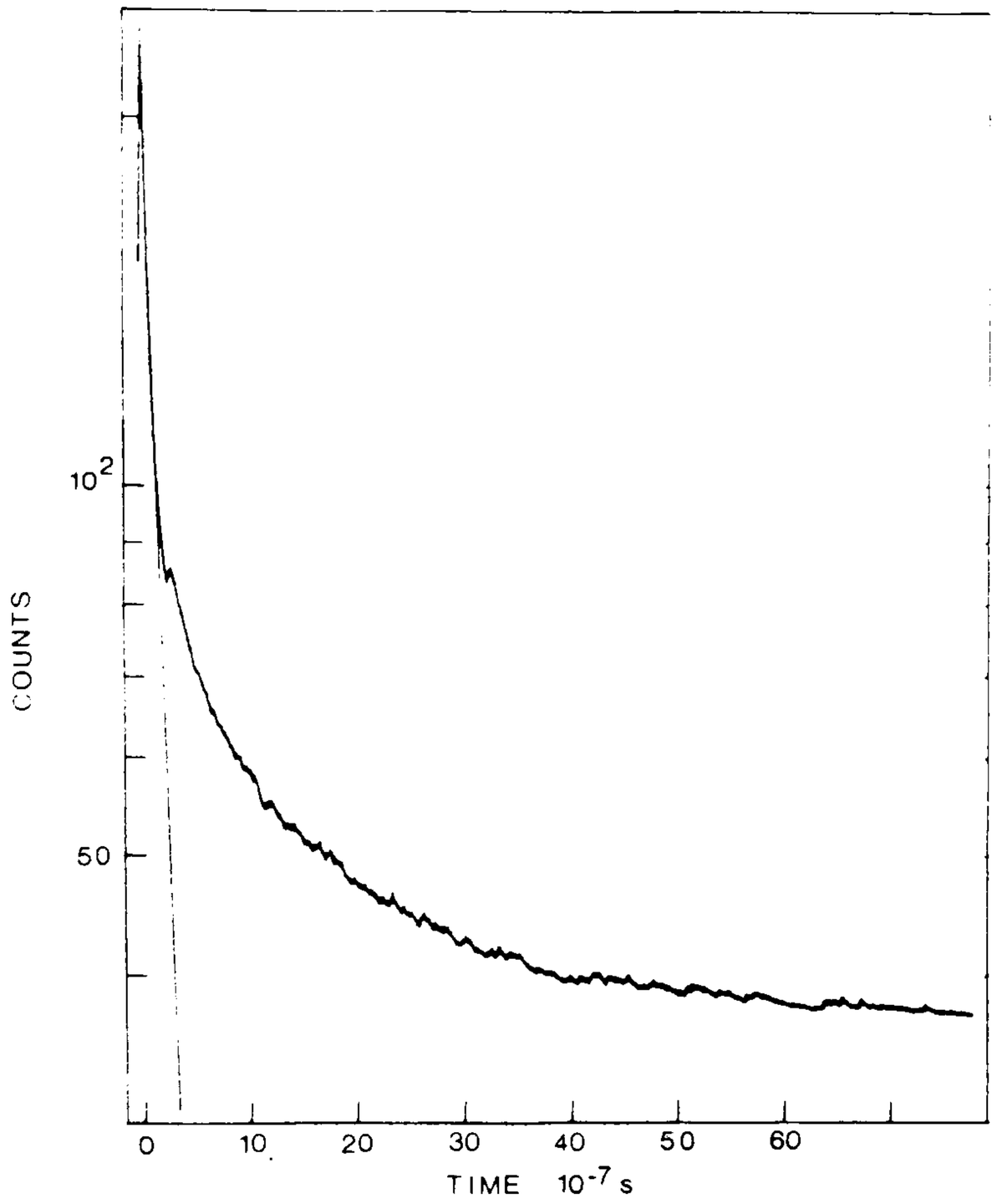

Figure 4.29. Decay curve of luminescence at 7500Å from CdS/CdSe superlattice MH123 (25Å/25Å). The line drawn on the left corresponds to a half life of 63ns.

Wavelength dependance MH123

Wavelength(Å)	7000	7300	7500
Lifetime(ns)	16	58	63

sample	lifetime (ns)	wavelength (Å)
MH93	5	6280
MH123	63	7500

Table 4.2. Summary of time resolved measurements on the luminescence from CdS/CdSe superlattices (K.P.O'Donnell and X.Chen, Strathclyde University).

(slower) recombination processes. Thus the presence of a slow decay process could indicate the presence of impurities in our samples. However, the first decay component accounts for the vast majority of the carrier recombination. Consequently the identification of this luminescence as excitonic recombination is not inconsistent with the observed luminescence decay characteristics. Moreover, the slow recombination time can be explained by confinement of the electrons and holes in separate regions [12].

The other sample studied was MH93 a 110Å/35Å CdS/CdSe superlattice. The band measured was the red band at 6320Å, similar to that from MH120 studied in the previous section. It was found that this band from the sample showed a simple exponential decay, with a half life of 5 ns. This is somewhat longer than that of the CdSe free excition, which has a lifetime of 1.4ns [15]. This emission is discussed in section 4.5.4.

4.4 Theoretical interpretation

4.4.1 Piezoelectric fields

It has been forecast that for cubic strained layer superlattices grown along the [111] axis there should exist within the layers large strain induced piezoelectric fields [16]. It was shown theoretically that these fields should produce a reduction in band gap which might prove of use in non-linear devices [17]. These fields have been indirectly observed in the InGaP/GaAs system by the lifting of the intersubband selection rules [18]. However, in the InGaP/GaAs system the fields involved are of the order of 10^6 V/m. These fields are too small to produce a significant reduction in band gap for superlattices in which the layers are commensurate.

Wurtzite semiconductors are also piezoelectric. Moreover, the highly ionic nature of the II-VI semiconductors leads to a considerable enhancement of the piezoelectric coefficents of these compounds [19]. In light of the work on [111] orientated III-VI systems it was decided to calculate the magnitude of these effects in the CdS/CdSe wurtzite system.

We can calculate the electric fields within the layers of the wurtzite superlattice by use of the wurtzite piezoelectric tensor [20]

	E_{xx}	E_{yy}	E_{zz}	E_{yz}	E_{zx}	E_{xy}	
P_x	0	0	0	0	e_{15}	0	
P_y	0	0	0	e_{15}	0	0	(ii)
P_z	e_{31}	e_{31}	e_{13}	0	0	0	

The P's are electric polarisations in the subscripted directions and the E_{xx} etc are the strains as described in section 3.1.3. The electric polarisation P along the x,y or z axis is now given by

$$P_j = \sum_{i=1}^{6} E_{nm} e_{ji} \qquad \text{(iii)}$$

Where j and i are the row and column respectively and E_{nm} is the appropriate strain component. The components of the strains within a wurtzite epilayer undergoing biaxial strain perpendicular to the c-axis were calculated in section 3.1.3. Using equation (viii)) in section 3.1.3 and equation (iii) above we can obtain the expression for the electric polarization field along the c-axis of the wurtzite layer. We find P_z is given by

$$P_z = 2E([c_{13}e_{33}/c_{33}]-e_{31}) \qquad \text{(iv)}$$

Where E is the biaxial strain and is positive for compression. The values of c_{13}, c_{33}, e_{31} and e_{33} were obtained from reference [19] and are given in table 4.3. The final electric field induced can be obtained from Maxwell's equations. We find, in the absence of free charge, the electric field F is given by

$$F = P_z/\epsilon_o \epsilon_{||} \qquad \text{(v)}$$

Where $\epsilon_{||}$ is the low frequency dielectric coefficent parallel to the c-axis (9.12 for CdS and 10.16 for CdSe [21,22]). Evaluating these two expressions gives us the final simple linear relationships between

	CdS	CdSe
c_{13}	4.6	3.9
c_{33}	9.4	8.45
e_{33}	0.440	0.347
e_{13}	-0.244	-0.160
ε_r	9.12	10.16

Table 4.3. Strain and electroelastic constants of wurtzite CdS and CdSe [22].

the biaxial strain E and the electric field F for both CdS and CdSe of

$$F_{CdS} = 1.05\times10^{10}E \quad V/m \qquad \text{(vi)}$$

$$F_{CdSe} = 7\times10^{9}E \quad V/m \qquad \text{(vii)}$$

In order to use these expressions we need to know the distribution of strain within the superlattice. A further complication is the presence of free charge which can alter the magnitude of the fields.

The easiest strain system to deal with is that of a freestanding superlattice. It was noted in section 4.3.3 that the spectral position of the CdSe free exciton indicated that the thinner superlattices were freestanding. In this case the CdS and CdSe layer have biaxial tension and compression stresses respectively. This will generate fields in opposite directions in the two different layers. The strains in the alternate layers are given by equations (xxiii) and (xiv) section 1.6.3. Figure 4.30 shows the example of a 50Å/50Å CdS/CdSe superlattice with the strains and generated fields. It can be seen that the effect of the strain induced field is to create a sawtooth type potential within the superlattice. However, there is no net polarization field across the whole superlattice because the polarization change across the CdS layers balances the change across the CdSe layers. This balancing of polarizations is simply a convenient property of such a freestanding superlattice, opposite strain induced polarizations are generated in the two component layers. There is in fact a small net field due to the different magnitudes of the CdS and CdSe piezoelectric coefficents, this net field can be allowed for as described below for the pseudomorphic superlattice.

The alternative case of a pseudomorphic (or partially relaxed to

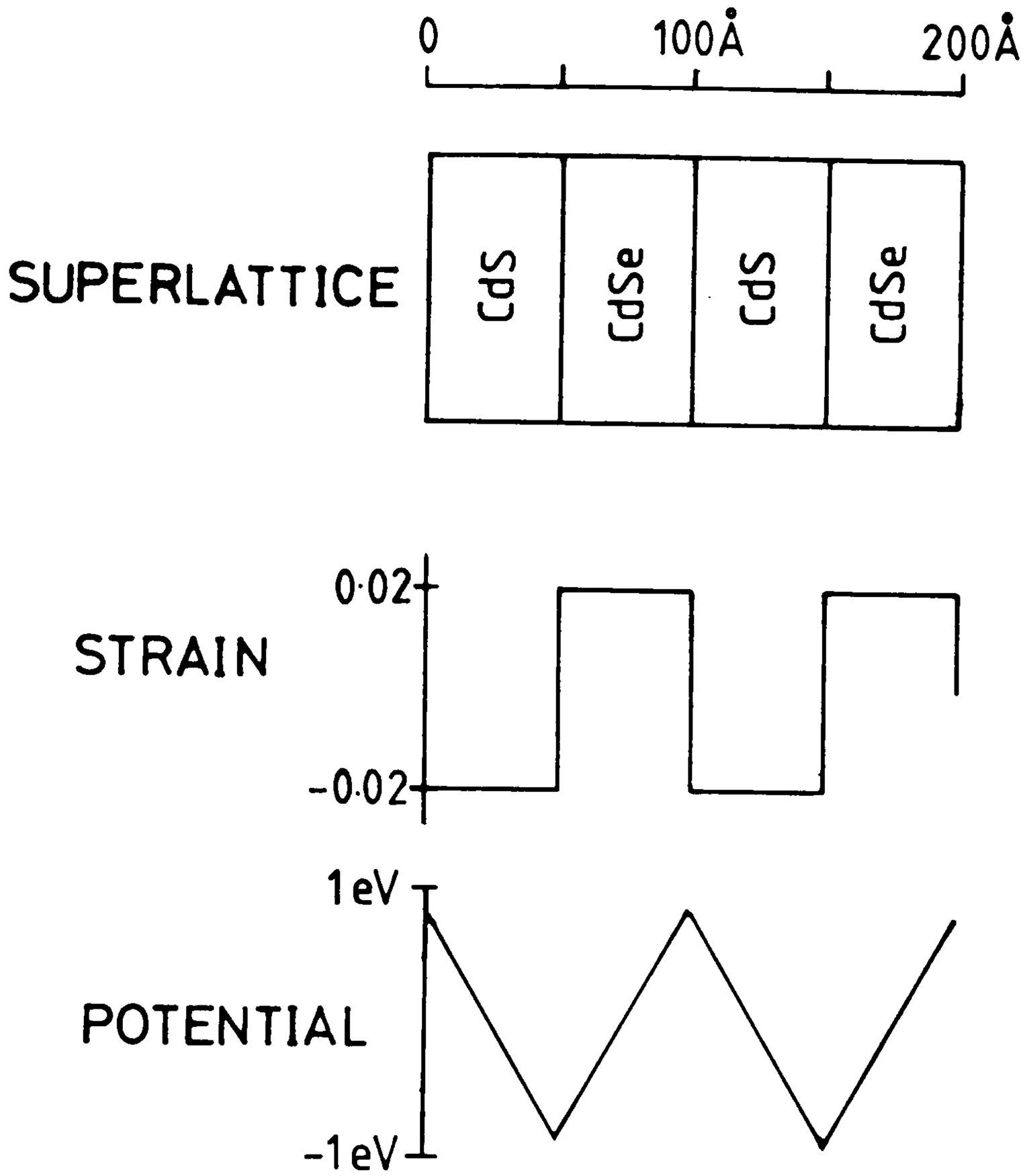

Figure 4.30. Schematic diagram showing a 50Å/50Å CdS/CdSe freestanding superlattice. Below this diagram are two axes showing the variation of the strain and electric potential along the c-axis of such a superlattice.

free standing) superlattice is slightly more complicated. In a pseudomorphic structure the CdS is unstrained. The CdSe layers, however, undergo the full 3.9% mismatch strain (the buffer layer is relaxed relative to the GaAs). Consequently the electric polarization in the CdSe is 0.025 C/m^2. This displacement implies a standing electric field of 2.8×10^8 V/m. This field cannot exist in a steady state because a large potential between the top and bottom of the superlattice would be generated. A good analogy to this structure is a dielectric in a capacitor. Such a dielectric will initially be polarized by an applied electric field and will remain so when the field is removed. However, with time dielectric leakage will occur to neutralise the capacitors stored field by charge displacement. Thus within the superlattice charge must transfer so as to neutralise the net field. This charge will generate a linear electric field analogous to that in a parallel plate capacitor. If we call this field F_{net} we can calculate the field necessary. Using the condition that the F_{net} must be equal and opposite to the total potential drop across each period divided by the period, We find

$$F_{net}=2.8\times10^8\ L_{CdSe}/(L_{CdS}+L_{CdSe})\ V/m \qquad \text{(viii)}$$

$$F_{CdSe}=2.8\times10^8-F_{net}\ V/m \qquad \text{(ix)}$$

$$F_{CdS}=F_{net}\ V/m \qquad \text{(x)}$$

If we calculate these fields over a wide range of L_{CdS} and L_{CdSe} values we find that the result, quantitatively, is the same as the free standing case, i.e. there is a sawtooth potential superimposed in the superlattice potential periodicity. Smith and Mailhot studying the same

problem in the III-V systems came to the same conclusion [17]. Irrespective of the relaxation state of the superlattice, there are large strain induced fields within the layers. As mentioned above, the freestanding case does also have a small net field as the piezoelectric coefficents of CdS and CdSe are not identical. This field is small and can be allowed for in the manner described above. It is interesting to note that the pseudomorphic superlattice can possess a large continuous electric polarization. This 'steady state' internal polarization is analogous to that in ferroelectric crystals [23]; the degree of polarisation being similar to that of a typical ferroelectric, (for example) potassium dihydrogen phosphate, which has a displacement of .0475 C/m^2 (c.f. 0.013 C/m^2 of a superlattice with $L_{CdS}=L_{CdSe}$ grown pseudomorphic to the CdS buffer layer).

Figure 4.31 shows the magnitude of the fields in the layers as a function of the ratio L_{CdS}/Period for the freestanding case. The graph shows that the fields forecast are very large, up to 3×10^8 V/m. This is approximately 20 times greater than expected for III-V superlattices grown on a [111] axis [16]. It was stated above that the fields in the cubic systems were too small to observe directly. We conclude that the CdS/CdSe system, when grown along the wurtzite c-axis, generates much greater fields. It should be possible to observe the effects of these fields in the luminescence, as described in section 4.4.2

The size of these fields may at first sight be difficult to justify. The breakdown field of CdS is approximately 10^8 V/m [24], i.e. less than the fields predicted here. Although we are using macroscopically measured coefficents, there is no reason to believe that the above theory is not applicable. The validity of the calculation for microscopic systems relies on the nature of the piezoelectric effect. The piezoelectric effect originates in the

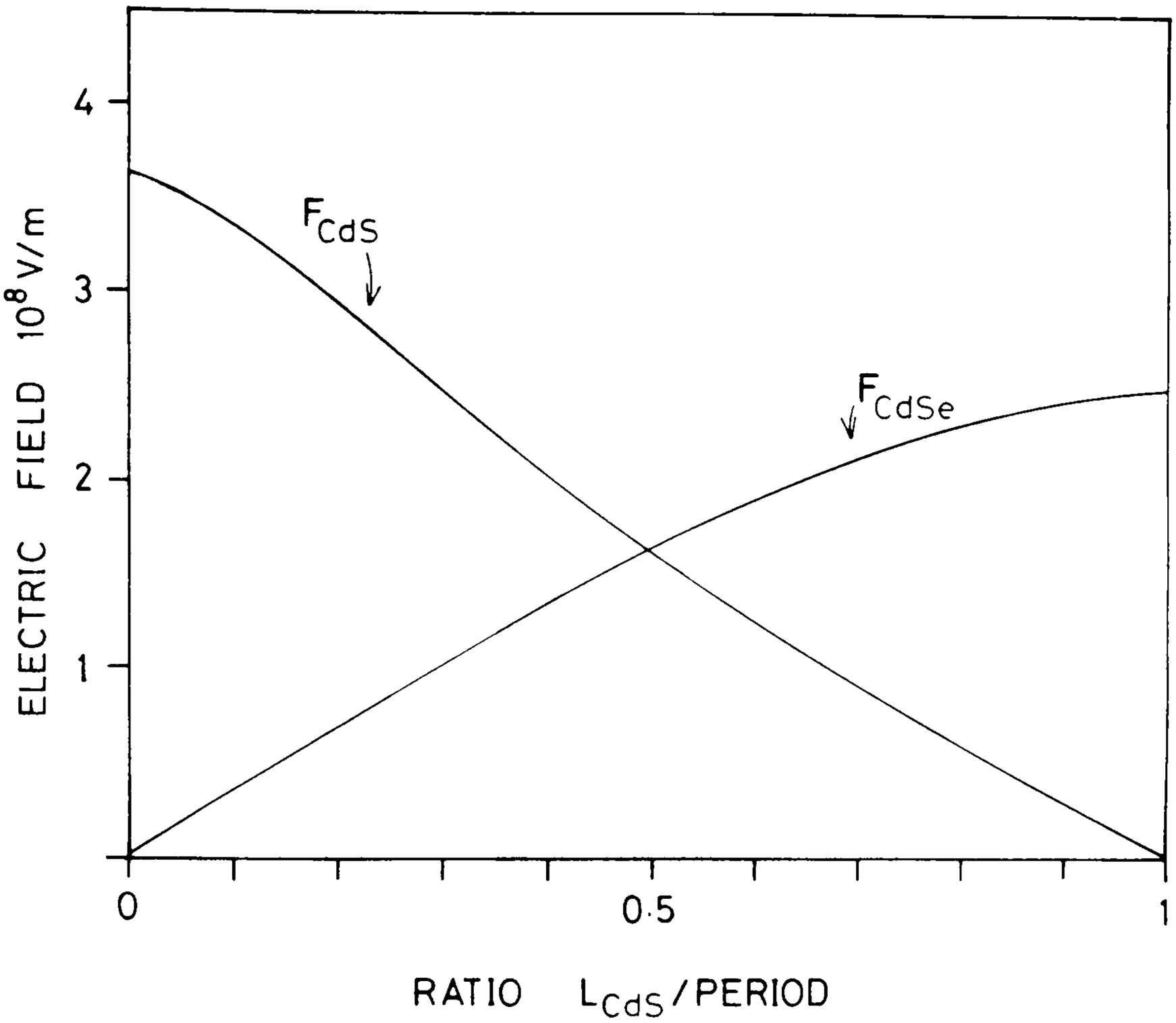

Figure 4.31. Electric fields in a Freestanding superlattice as a function of the ratio LCdS/Period. The diagram indicates the magnitude of the fields in the two compounds, in fact they reversed between CdS and CdSe.

microscopic deformation of the lattice under strain. The charge on the atoms being displaced so as to generate an electric displacement. The correct treatment of this problem would require a full band structure calculation for the appropriate deformed crystal lattices. The difficulty of such a calculation precludes this approach here. However, the approach taken should allow the effect of the internal fields to be discerned from that of the usual compositional type superlattice potential. Moreover, as mentioned above the presence of internal fields has been indirectly observed in III-V compound superlattices.

For the purposes of this study we will assume that the these fields are present and that the electron and hole states are modified accordingly. We can now consider the effects of such fields on the confinement energies within the superlattice.

4.4.2 Effect of an electric field on a quantum well

The use of finite well and Kronig-Penney models for calculating superlattice electron states was described in section 1.6. Clearly for the CdS/CdSe system we expect a similar square well potential from the band offsets. In addition to this, we showed in the previous section that we expect there to be a sawtooth piezoelectric potential superimposed on top of the compositional square well potential. The band offsets for this system are totally unknown. In order to be able to attempt to measure the offset from the luminescence measurements we have to be able to calculate the electron and hole confinement energies.

Figure 4.32 shows the potential well generated by the circumstances described above.

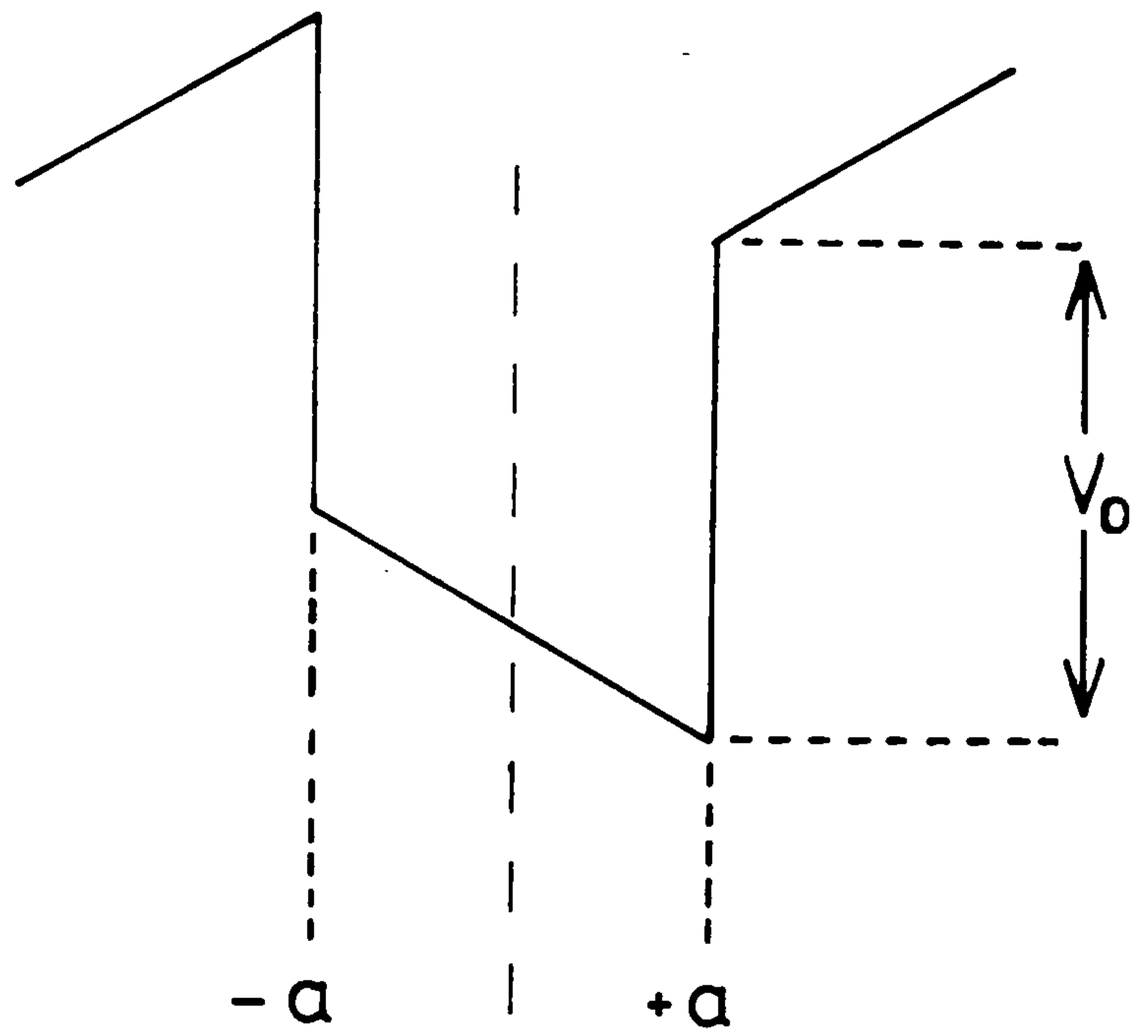

Figure 4.32. Potential well in strained layer system, with strain induced piezoelectric fields. V_o is the appropriate band offset.

This well can by described by the potentials

$$V(z)= V_o+a\ e\ F_w+e\ F_b\ z \quad z>a$$

$$V(z)= e\ F_w\ z \quad |z|<a \qquad \text{(xi)}$$

$$V(z)= V_o-a\ e\ F_w+e\ F_b\ z \quad z<-a$$

Where F_w and F_b are the electric fields in the well and barrier respectively. The problem of the confinement energies for a quantum well in an externally applied electric field has been studied by

several workers [25,26]. Exact solutions of Schrodinger's equations for the electron energy states in this potential can be obtained [27]. However, these solutions involve Airy functions and are difficult and complicated to use. For the purpose of our work a simpler approach was sought. An approximate variational function was tried for the ground state electron (or hole) wavefunction. The problem of the piezoelectric well has not been solved with a variational calculation before. However, the related problem of a finite well in an externally applied electric field has been studied. For such a system the following variational wavefunctions were suggested [25].

$$\psi(z) = A\exp[(q-\beta)z/a] \qquad z<-a$$

$$\psi(z) = B\cos(kz/a)\exp(\beta z/a) \qquad |z|<a \qquad \text{(xii)}$$

$$\psi(z) = C\exp[-(q+\beta)z/a] \qquad z>a$$

Where q and k have their finite well zero field value (see Appendix 2) and β is the variational parameter. From these wavefunctions the variational energy can be obtained from the integral [28]

$$E_{var} = \frac{\int \psi \mathcal{H} \psi^{*} dz}{\int |\psi|^{2} dz} \qquad \text{(xiii)}$$

Where $\mathcal{H}$ is the usual energy Hamiltonian from Schrodinger's equation, the integral on the bottom of the right hand side of (xiii) is the normalization factor. This integral is evaluated in full in

appendix 3. The resulting variational energy was minimised with respect to β by computer. The accuracy of this calculation can be judged by taking certain limits. In the limit of no field the calculation is exact (β is zero and we obtain the finite well solution). In the limit of an infinitely thick well the calculation gives an energy 7% too large (the energy in this case can be calculated from a semiclassical result [29]). We can therefore expect the calculation to give a good approximation over the range of well thicknesses.

We can illustrate the effect of the electric field by taking an example. Figure 4.33 shows the confinement energy of an electron in a 50Å well with 1 eV barriers. The electron effective mass in the well is 0.2 m_o, the fields applied are 10^8 and -10^8 V/m in the well and barrier respectively. It can be seen that the effect of the applied field is to continously reduce the confinement energy as the well width increases. In fact the confinement energy eventually goes 'negative' i.e. falls below the potential at the centre of the well. Included in the figure is the finite well confinement energies (zero field). It can be seen that the finite well confinement energy tends to zero for thick wells. Figure 4.34 shows the variational wavefunctions calculated for the electron in a 50 Å well described above and a hole with a mass 2.5 m_o confined in such a well. It can be seen that the effect of the field is to move the peak probability of the electron's wavefunction towards the lowest point of the potential; the effect is more pronounced for the heavier particle (the hole). We conclude that the effect of strong electric fields on a quantum well is to reduce the confinement energy below that expected for a 'square well' type potential. This effect has been observed in the luminescence from quantum wells in externally applied fields [30], the observed shift to lower energy being in good agreement with the theory above. A small reduction in band gap has also

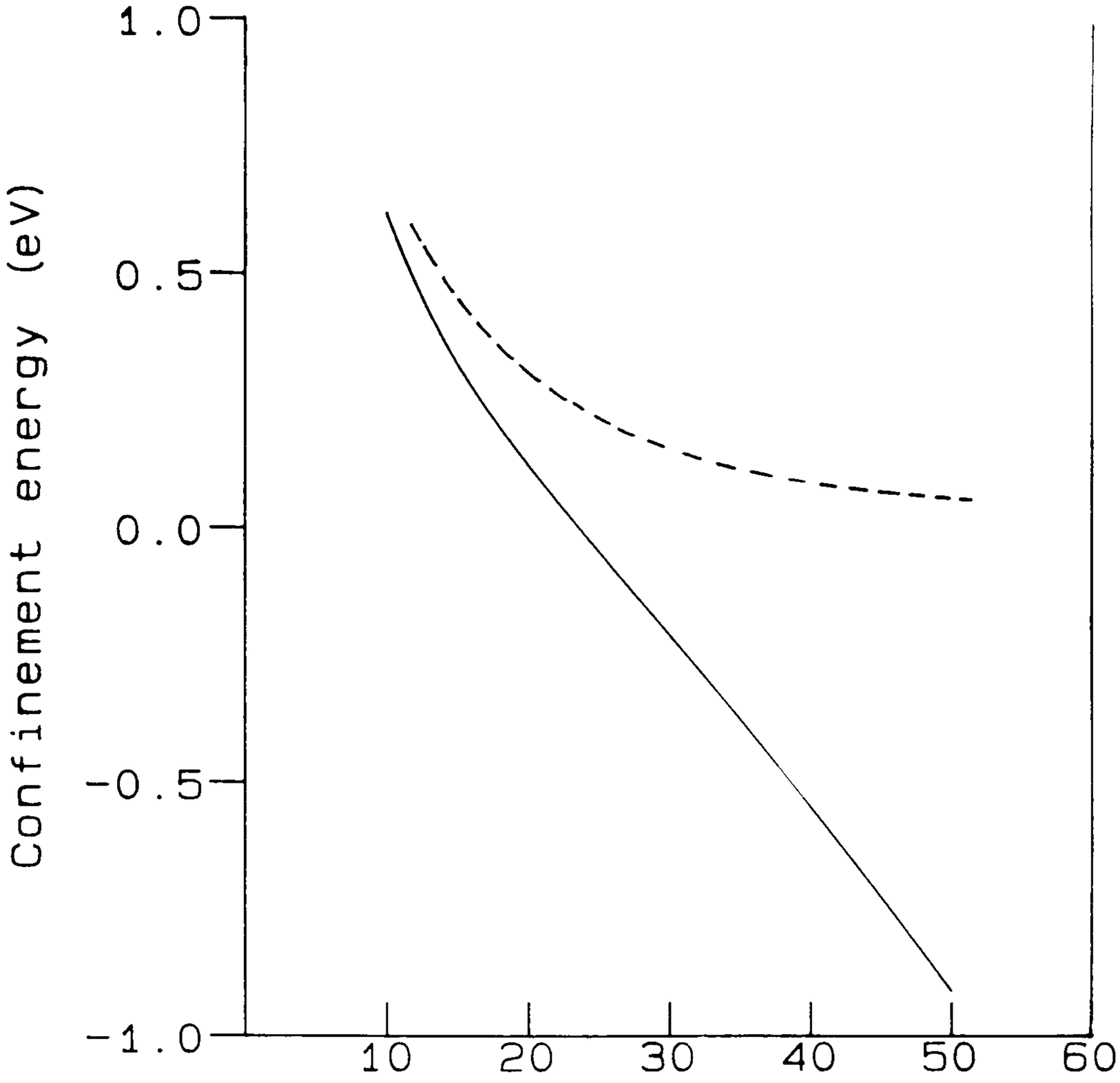

Figure 4.33. Comparison of finite well and piezoelectric well type confinement energy calculations. The curves are calculated assuming a band offset of 1eV, a m* of 2.5×m_o and an electric field of 10^8 V/m.

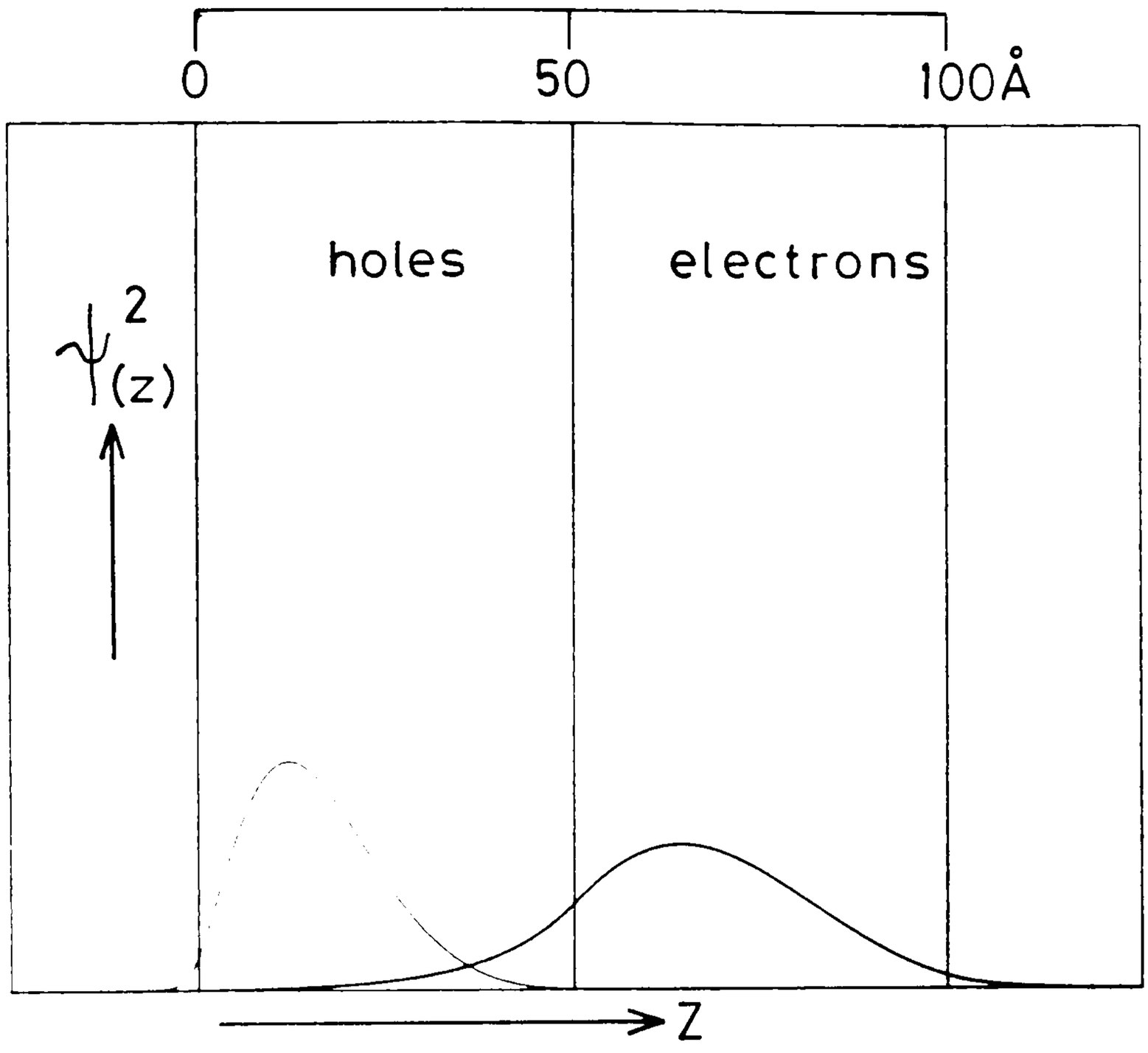

Figure 4.34. Probability density (i.e. $|\psi_{(z)}|^2$) of electrons and holes in a 50Å well in a field of 10^8 V/m as described in the text.

been observed in III-V compounds with internal piezoelectric fields. There is therefore every reason to expect similar effects in the CdS/CdSe system.

It is important to note that the above calculation is only valid for an isolated well. As the barrier thickness reduces the interaction between wells will introduce a non-zero dispersion into the energy level (see section 1.6.1). This will reduce the effective confinement energy below that calculated using the above theory. Also exact treatments would include the effects of excitonic interactions. These interactions however, only introduce small corrections to the calculated confinement energies. Here we are interested in a first order estimate of the carrier confinement energies.

4.4.3 Recombination emission from a superlattice

When the excitonic (or free carrier) recombination emission is observed from a superlattice it is, in general, assumed that the transition observed involves the electron and hole ground states [31]. That is to say that at the low temperatures involved typically (1.6-2K) the carriers will be lying in the lowest energy levels available. This assignment allows the estimation of band offsets by the observation of the recombination energy as a function of superlattice period (e.g. ZnS/ZnSe [32]).

To see how this can be done consider a simple type I superlattice. In a type I superlattice the electrons and holes are confined in the same layer which has a thickness L_1 and a band gap E_1. The corresponding values for the other (barrier) layer are L_2 and E_2. We assume a conduction band potential offset of V_e. Figure 4.35 shows the band structure of such a superlattice.

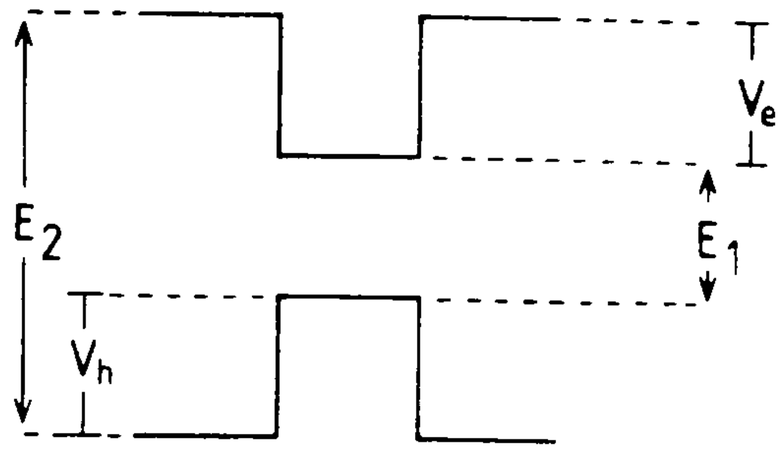

Figure 4.35. Band structure of simple type I quantum well.

For this case the recombination emission energy will be given by (ignoring excitonic binding energies):-

$$E_r = E_1+E_e+E_h \qquad \text{(xiv)}$$

Where E_e and E_h are the confinement energy of the electrons and holes respectively, as derived from the Kronig-Penney relation. There is frequently a splitting of the hole energies due to the presence of both heavy and light holes. For a type I superlattice with piezoelectric fields (see above) the equation (xiv) is the same, but the confinement energies are obtained from the variational calculation above.

In the alternative case of a type II superlattice (see section 1.6) the electrons and holes are confined in seperate layers. This gives two possibilities, either the electrons are in material 1 and the holes in material 2 or vice versa. If we assume $E_1>E_2$ than the two

possibilites are represented in figure 4.36.

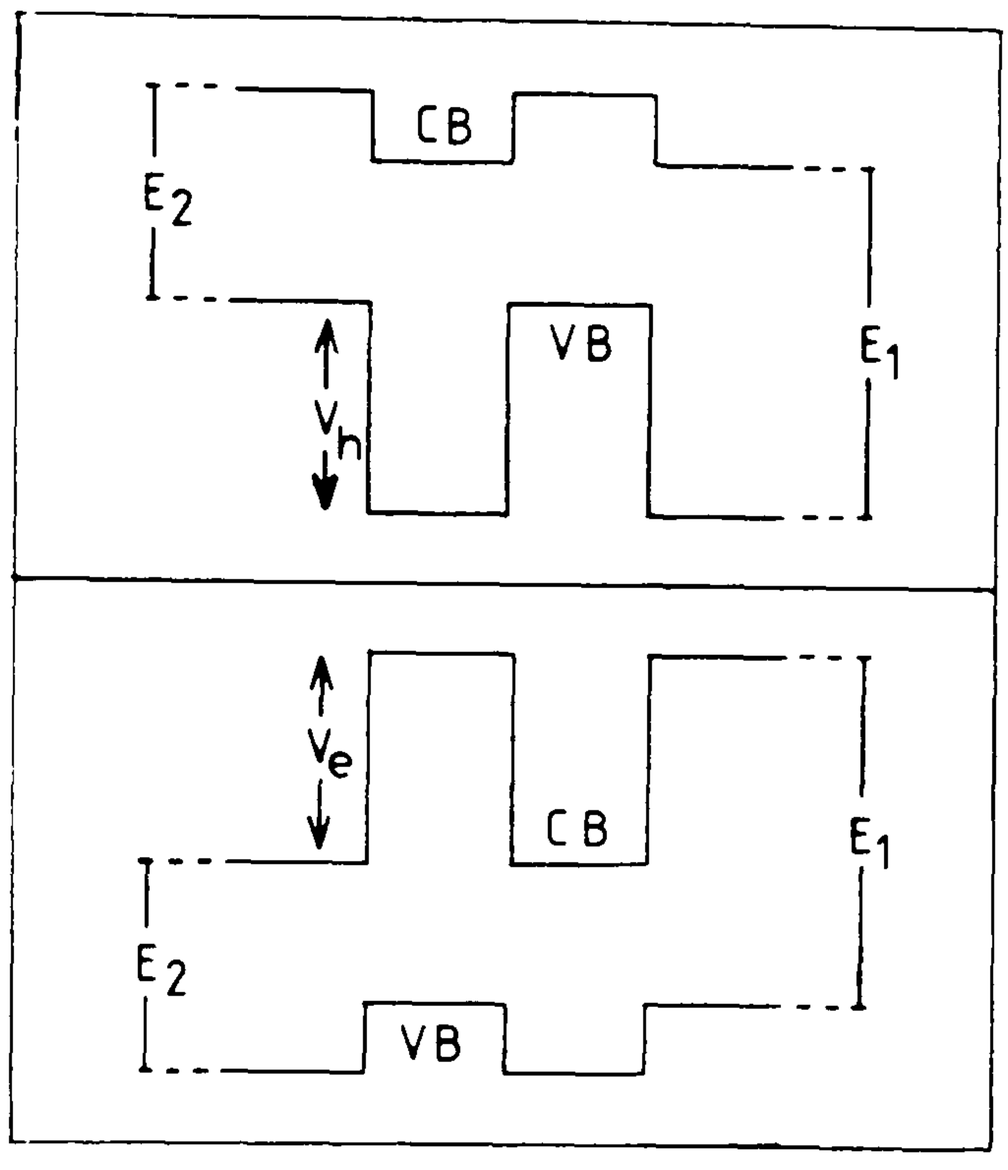

Figure 4.36. Type II superlattice offsets. In the upper case the electrons are confined in material 1 (with band gap E_1). In the lower case the holes are confined in material 1.

The recombination energies are given by the two expressions

$$E_r = E_2 - V_e + E_e + E_h \qquad \text{(xv)}$$

$$E_r = E_1 - V_e + E_e + E_h \qquad \text{(xvi)}$$

For the upper and lower figure respectively. Again the confinement

energies are either given by the Kronig-Penney expression or the variational calculation depending on whether the piezoelectric fields are present. Notice that in the limit of long period the emission from a non-piezoelectric type II superlattice will be given by either E_1-V_e or E_2-V_e depending on the offsets; whilst with the piezoelectric field the band gap will reduce to zero with large enough period.

It is therefore possible, by calculating the recombination energy for the different possibilities, to fit theory to results. Using these relations offsets have been found for a number of different systems. It is in general found that measurement of the ground state luminescence recombination energy is relatively insensitive to the exact value of the band offsets [33]. The lineshape of intersubband recombination emission is subject to a number of difficult to assess factors. These include electron temperature effects and dispersion in the electron E-k relationship [33]. In addition to these effects the exciton binding energy is also function of period and offset. Since the recombination emission observed is usually excitonic in nature this can also affect the measurement of band offsets. However, when dealing with a totally new and unstudied system the considerations above can allow a measurment of the superlattice type and the distribution of the band offsets to reasonable accuracy. Moreover, the variation in the excitonic binding energies in the superlattice will only be of the order of those binding energies in the bulk material. For CdS and CdSe these values are 19 and 29 meV respectively [34,35]. The possible effects of these binding energy uncertainties are discussed in section 4.5.3.

The physical constants used in the calculation of confinement energies are those given in table 1.4, section 1.4. The wurtzite valence band was described in section 1.4. It is composed of three

bands, the holes from each band having different effective masses. It is assumed through out the next section that the holes participating in the transitions were lying in the lowest possible state. The calculation of transition energies was conducted thus. A conduction band offset was assumed for the system. From this the valence band offset was derived for each band, the effect of strain was included in the valence band offset as suggested in [36]. The confinement energies for the carriers was then calculated for each respective periodic potential, using either the Kronig-Penney or piezoelectric model accordingly. Finally the transition energy for the electron-hole recombination was calculated for each band. The band gap of the superlattice was then assumed to be the calculated energy difference between the highest energy valence band states and the lowest energy conduction band states. It was found that, because of the high mass of the J= 3/2 hole along the c-axis of the superlattice, the J= 3/2 valence band was invariably the highest energy valence band. Indeed the high mass of the hole from this band was useful in identifying which compound contains the hole. It requires a very narrow well to produce significant confinement energies for this carrier. Similar considerations were used to identify the offsets in the ZnS/ZnSe and $CdTe/Cd_{1-x}Mn_xTe$ systems [32,38]. In these systems the offsets in one band is very much smaller than in the other.

4.5 Interpretation of luminescence

Introduction

It was observed in section 4.3.1 that the luminescence spectra from the superlattices was dominated by a bright emission band in the red or near-infrared. It was found from luminescence lifetime measurements that this emission was consistent with an excitonic recombination process. Moreover, the high purity of the single epilayers grown by the same process indicated that impurity driven processes were unlikely sources for the emission. If the emission is simple intersubband excitonic emission it should be possible to measure the band offset for this system with our data. In addition, we wanted to observe the effects of the internal fields forecast by the theory in the previous section. For this purpose the series of samples described in section 4.2.1 were grown. This section describes the interpretation of the superlattice emission bands observed from these series. Three problems associated with the system are addressed, the superlattice type (i.e. type I or type II), the magnitude of the conduction band offset and the evidence for the presence of the internal fields.

4.5.1 Constant period series

In chapter 1, two types of offset for superlattices were described. The essential difference between type I and type II superlattices lies in the location of the electrons and holes. In type I superlattices the electrons and holes are confined in the same layer. For type II superlattices the electrons and holes are confined in separate layers. In order to determine the superlattice type a constant period series was grown. This series was composed of 7 samples with a

common period of roughly 100Å (see table 4.1). The ratio of L_{CdS}/Period for these samples was in the range 0.9–0.1.

Similar series of superlattices have been studied in the type II ZnSe/ZnTe system [11]. It should be possible to determine the type of a superlattice by studying the intersubband recombination energies from such a series. The variation in the type I and type II recombination emissions for such a series is illustrated in figure 4.37, in the absence of piezoelectric fields, it can be seen that the curve of superlattice band gap against the ratio L_{CdS}/period is totally different for the two superlattice types. In a type I superlattice the electrons and holes are both confined in the CdSe. Consequently, the emission energy rises as the CdSe well thickness is reduced. In the type II case electrons and holes are confined in the different layers. This separate confinement results in an increase in recombination energy as either layer thickness is reduced. This gives rise to the characteristic U shaped curve for the emission energy versus L_{CdS}/period relationship. Unfortunately the piezoelectric field theory described in the previous section complicates the situation by reducing the band gap further. However, by studying the shape of the emission energy versus L_{CdS}/Period relationship it should be possible to determine which carrier is confined in which layer. This relies on the large difference in effective masses for the two carriers along the c-axis of the component layers. The larger confinement energies being produced by the lighter particle (the electron).

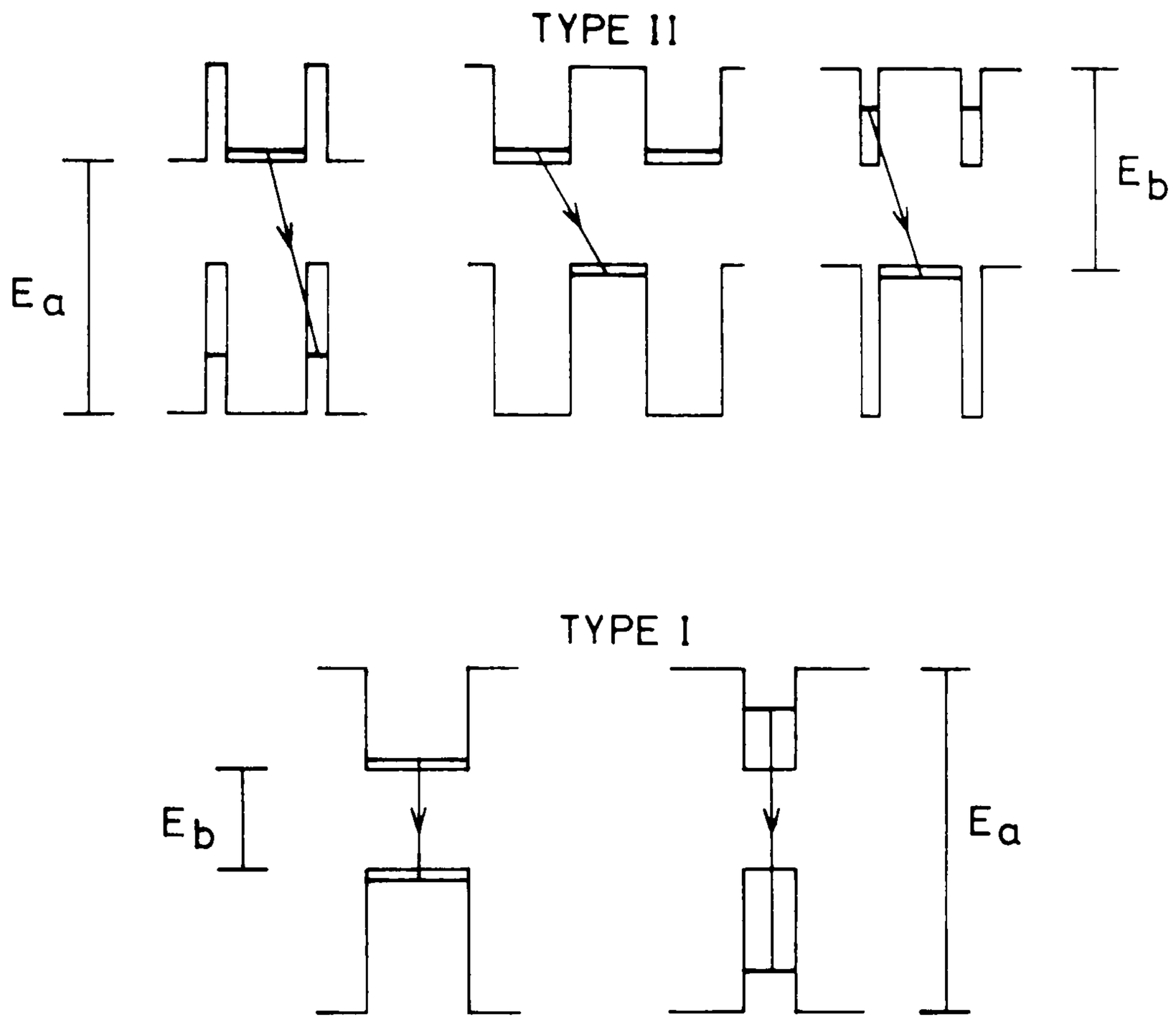

Figure 4.37. Recombination emission from a type II superlattice. This diagram illustrates that the luminescence peak from such a system will shift to higher energy as either of the component layers is reduced in thickness.

Results and discussion

The energy positions of the superlattice bands were measured in the limit of low excitation power. Figures 4.38 and 4.39 show spectra from MH109,MH108,MH112 and MH113 respectively. These four samples show the variation in peak energy across the series, the periods of the samples being indicated on the figure. Sample MH112 displays an asymmetric peak. This is the result of the GaAs substrate absorption edge, which occurs at 8500Å: this change in absorption causes light to be transmitted through the sample and reflected off the copper sample rod. There is consequently a sudden apparent increase in emission intensity at this position. This effect is a hindrance to the measurement of the peak position. For this reason large errors were estimated for the transition energies from samples emitting in this region. The great breadth of the emission in general is apparent in the spectra. For the moment we ignore this: the implications of the width of the bands is discussed in section 4.5.6.

Figure 4.40 shows the recombination energy versus L_{CdS}/period for the constant period series. It can be seen that the curve is bowed in a similar way to that found in the type II ZnSe/ZnTe system [37]. We can now use this curve to assess the superlattice type.

We can eliminate one possibility immediately. The curve is clearly not consistent with the emission from a type I superlattice without internal fields. In this case we would only observe an increase in transition energy as the CdSe layer thickness was reduced. Moreover, the emission is always below the band edge of CdSe (1.84eV). This leaves three possibilities. Type I with internal fields or Type II with or without internal fields. Figure 4.41 shows a calculation using the piezoelectric field theory in section 4.4.2. The transition energies are calculated for the above series in the case of a type I offset with

Figures 4.38 and 4.39 (next two pages). Photoluminescence spectra showing the change in the luminescence from a series of superlattices with common period ($L_{CdS}+L_{CdSe}$=100Å) as the ratio L_{CdS}/period is varied. The thicknesses of the CdS and CdSe layers are indicated on the diagram. The sample numbers are fig 4.38 (top) MH109, (bottom) MH108; fig 4.39 (top) MH112, (bottom) MH113.

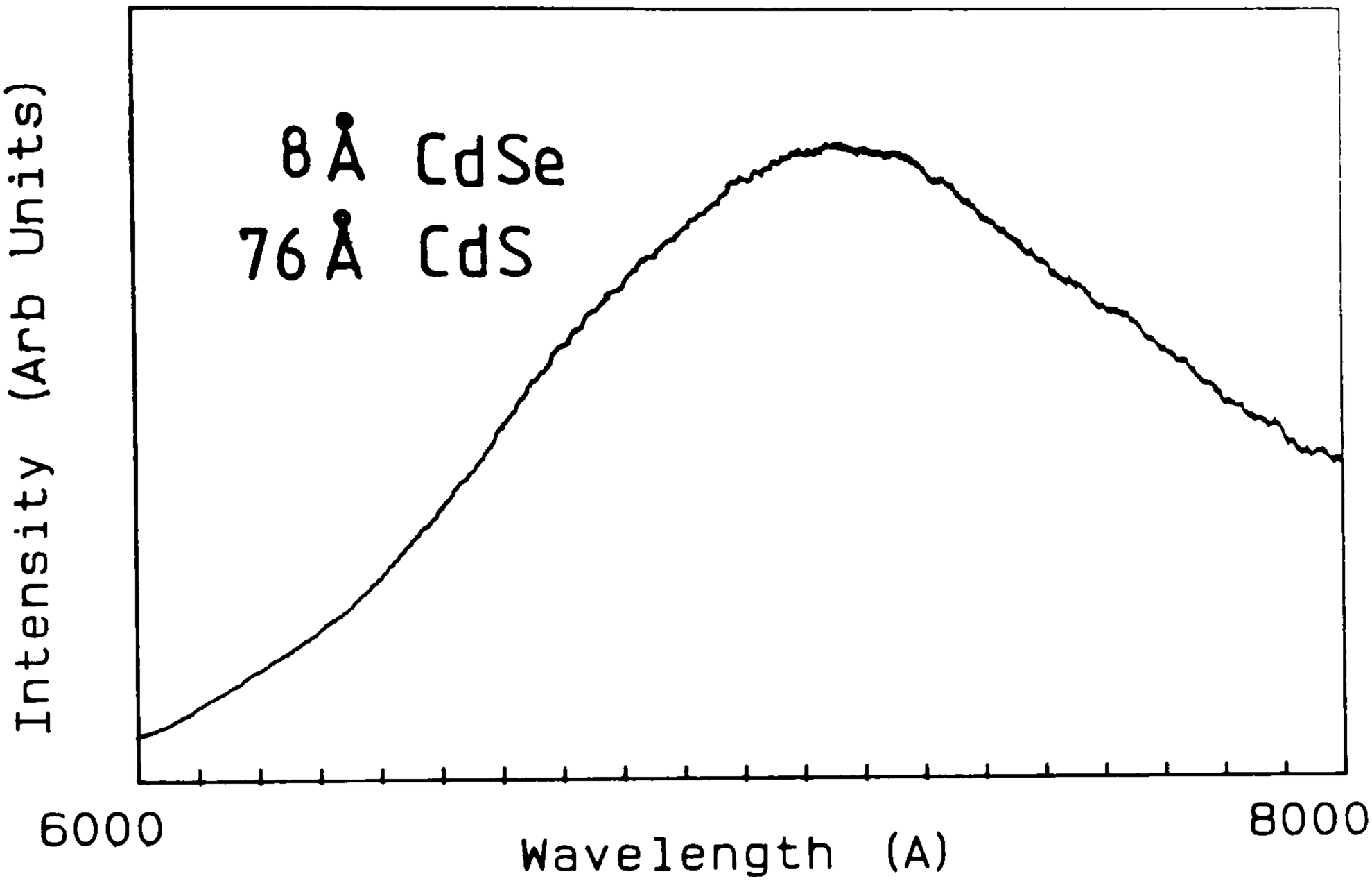
8 Å CdSe
76 Å CdS
Intensity (Arb Units)
6000
8000
Wavelength (A)

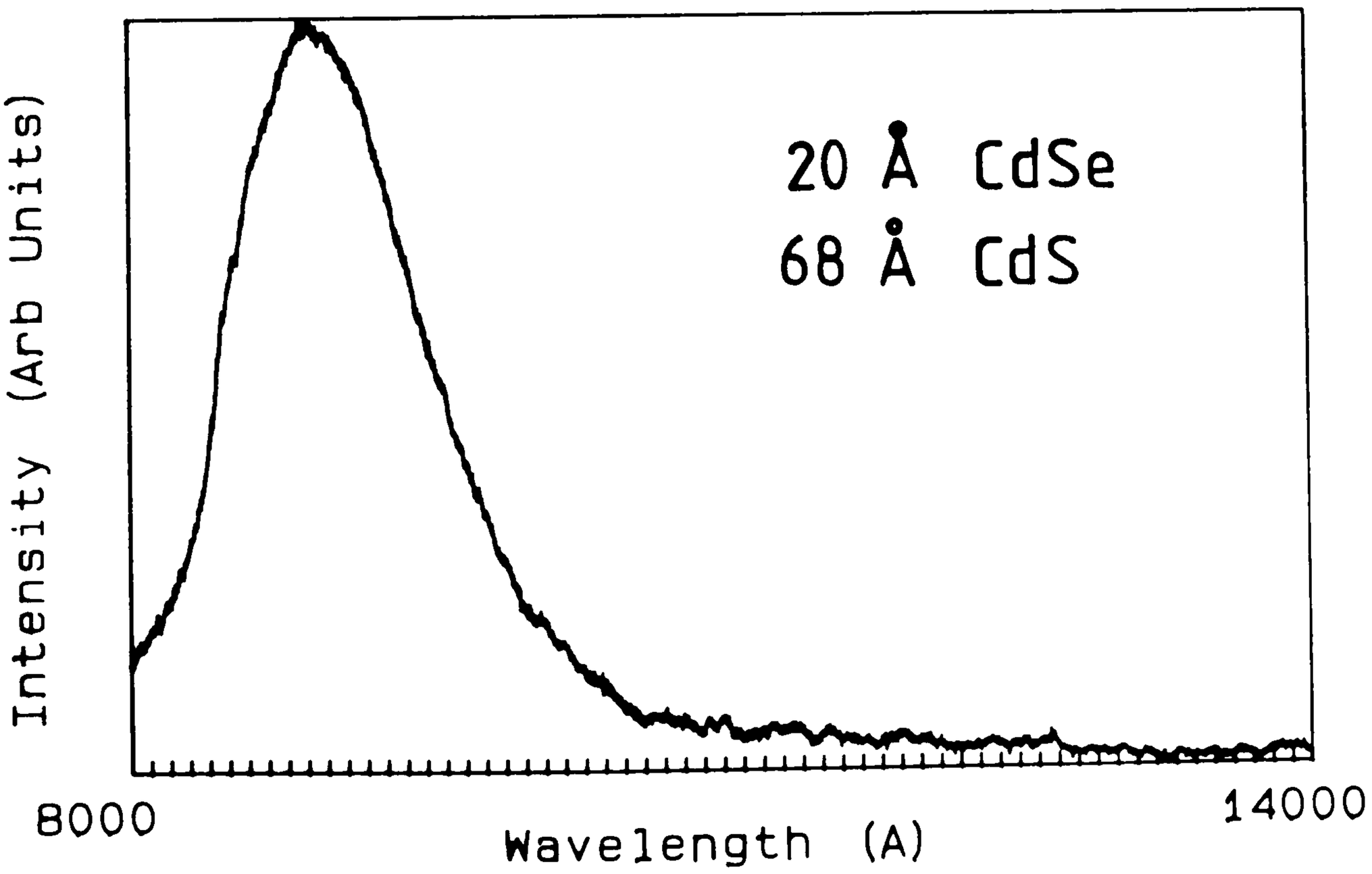
20 Å CdSe
68 Å CdS
Intensity (Arb Units)
8000
14000
Wavelength (A)

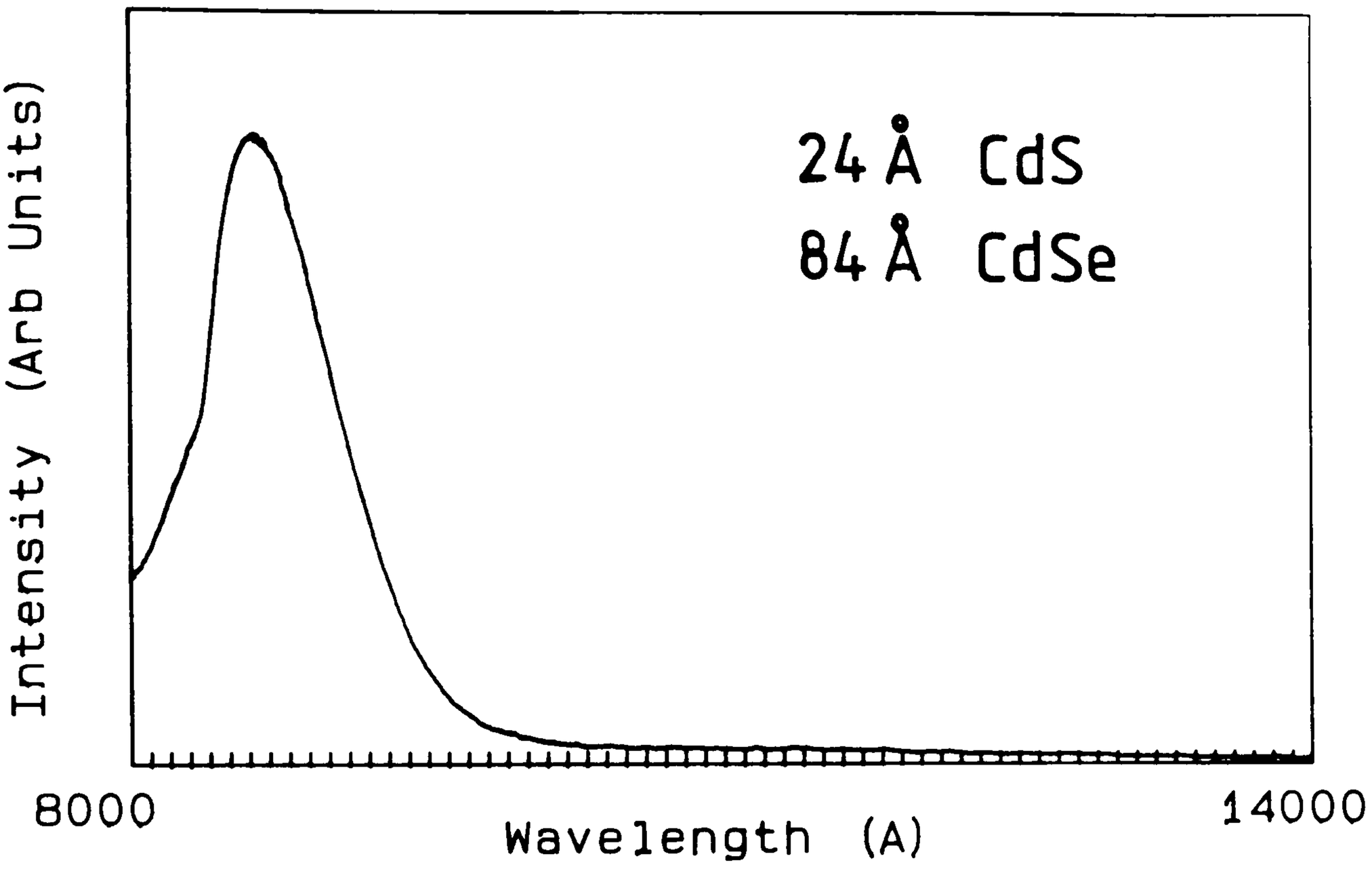
24 Å CdS
84 Å CdSe
Intensity (Arb Units)
8000
14000
Wavelength (A)

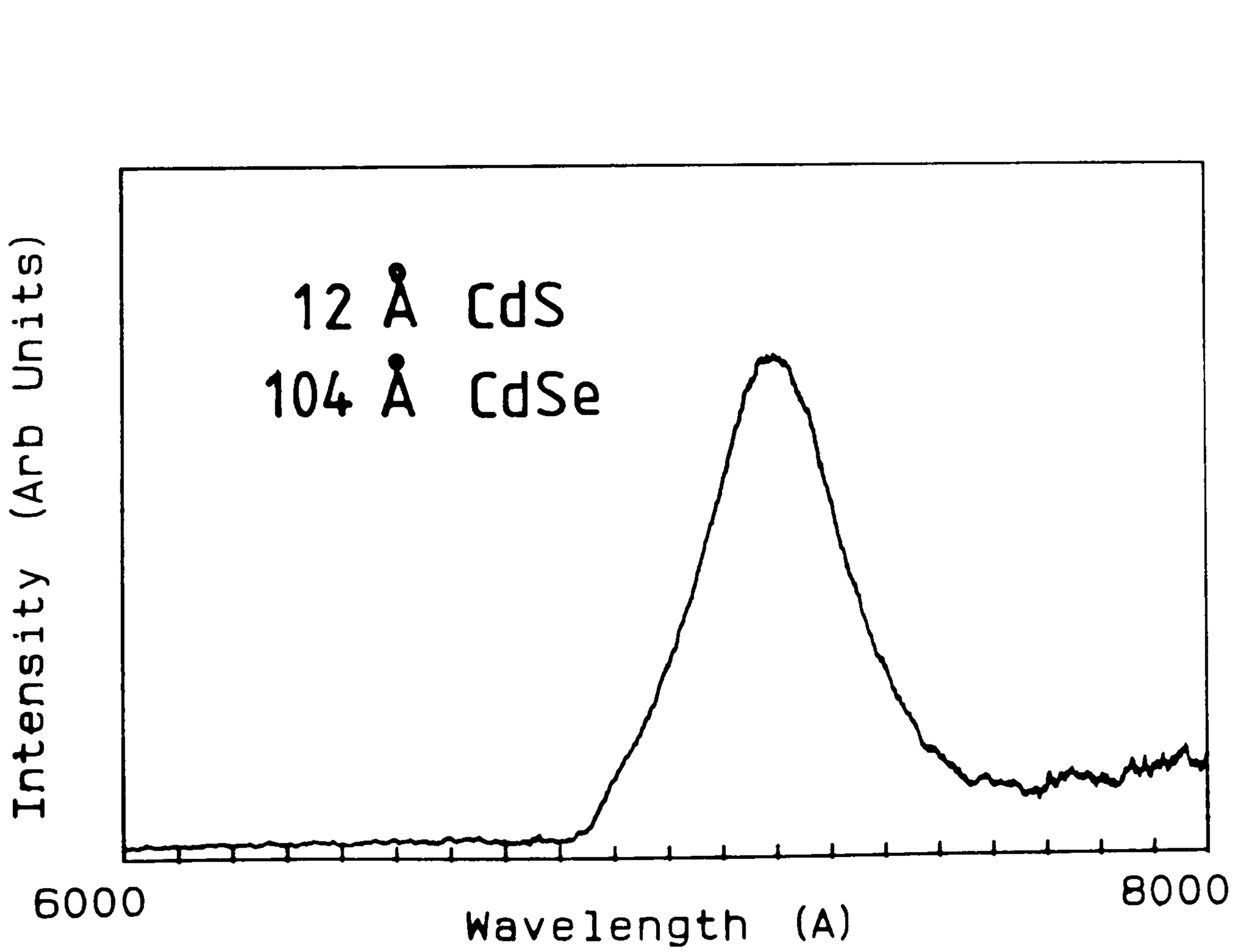
12 Å CdS
104 Å CdSe
Intensity (Arb Units)
6000
8000
Wavelength (A)

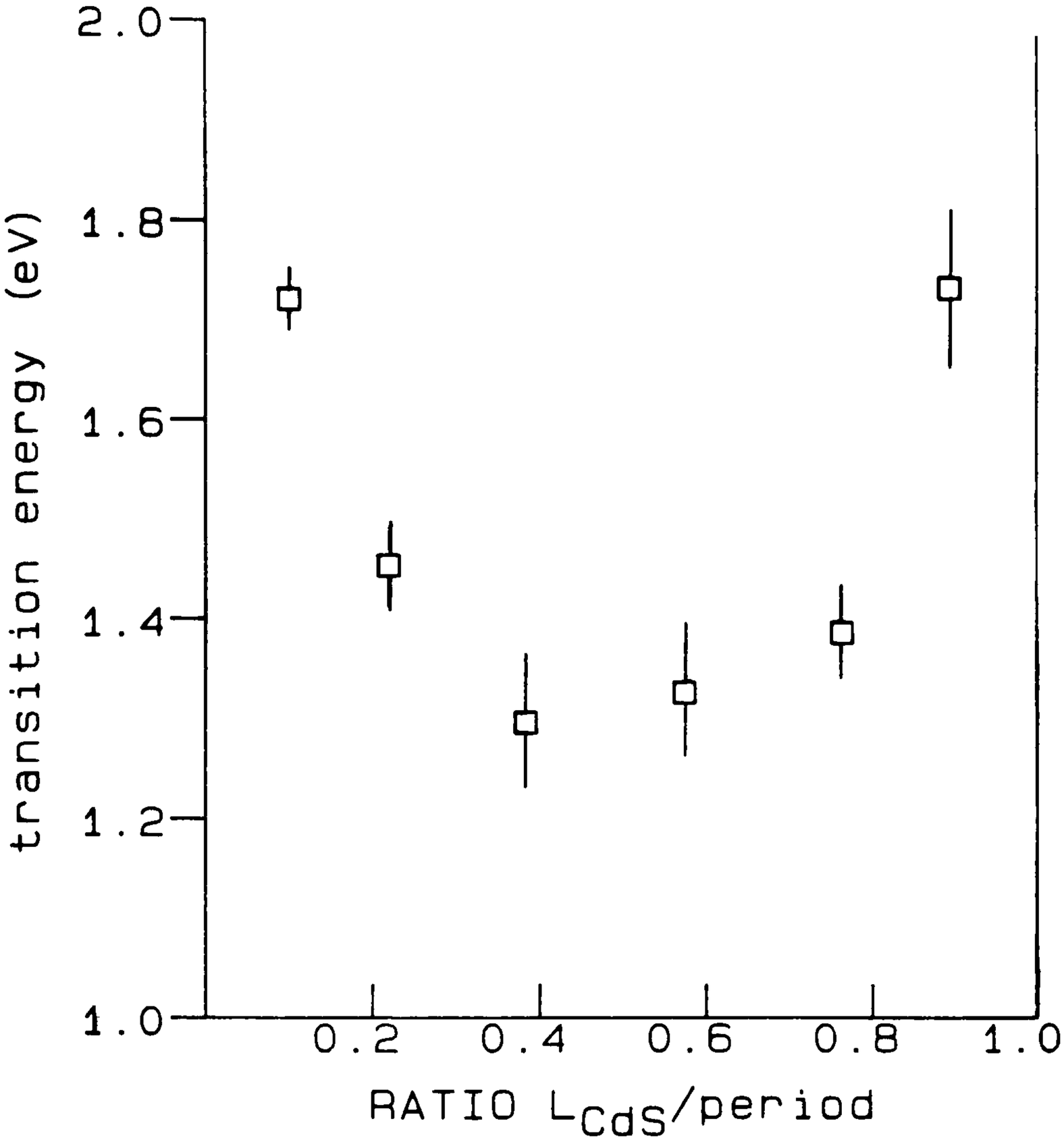

Figure 4.40. Recombination energy versus ratio LCdS/period for the constant period series. The points are experimental and the length of the error bars indicates the full width half maxima.

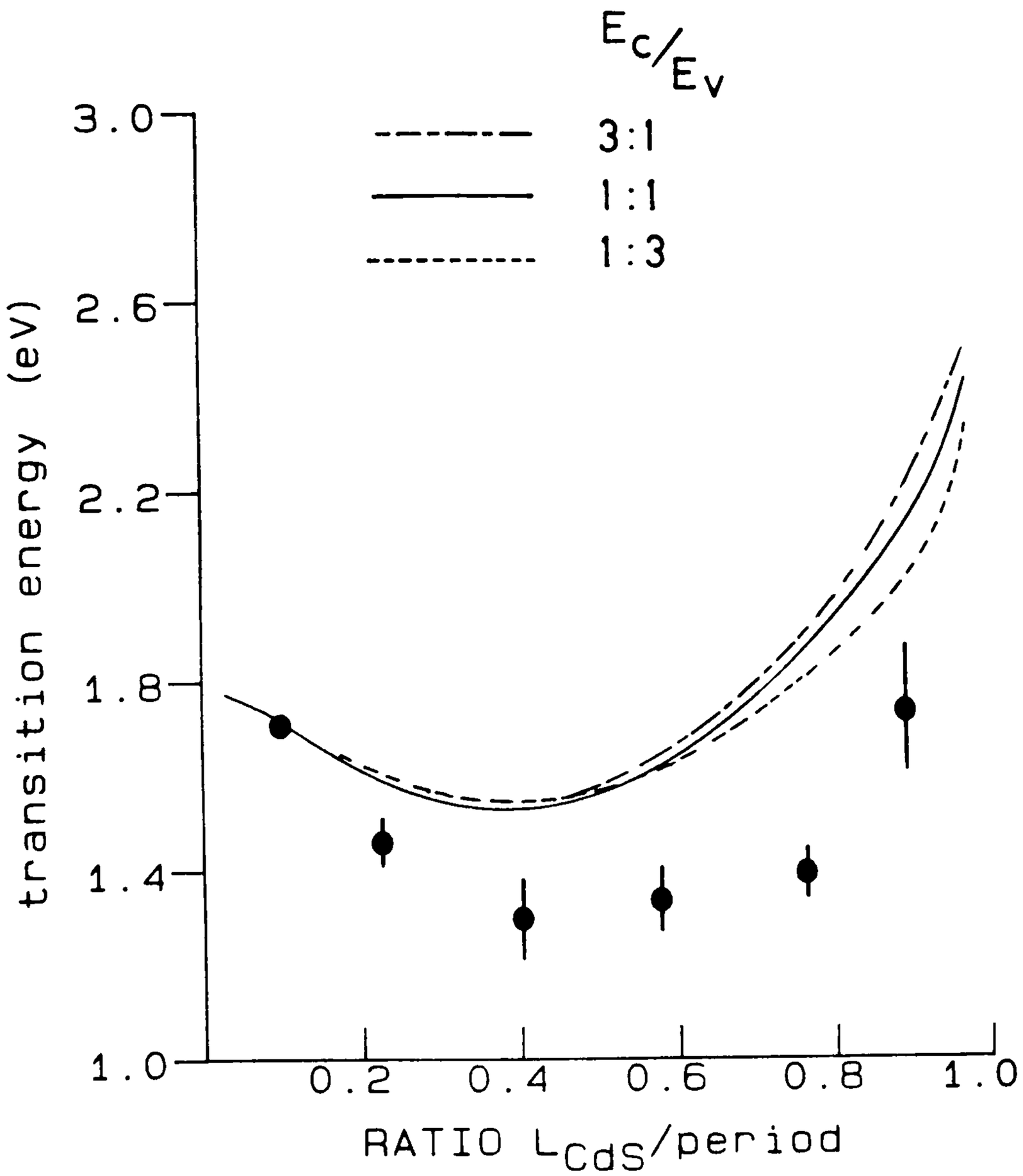

Figure 4.41. Calculated curves for constant period series in the case of a type I superlattice with piezoelectric fields. The lines correspond to the conduction band offset to valence band offset ratios indicated (Ec/Ev). The curves were calculated using the piezoelectric theory. The points are experimental.

piezoelectric fields. The curves correspond to the conduction band to valence band offset ratios indicated. It is obvious that none of the curves lies close to the observed transition energies. We therefore exclude the possibility of a type I offset for the system. In section 4.5.5 further evidence against a type I offset is presented.

We therefore now consider a type II offset. The electron can be confined in either the CdS or CdSe in such a superlattice. It was suggested earlier that the large mass of the hole along the c-axis of CdS and CdSe should allow us to deduce which compound confines this carrier. We note in figure 4.40 that when L_{CdS}/period =1 and 0 (i.e. pure CdS and CdSe respectively) the emission is at 2.56 and 1.82 eV respectively, corresponding to the intrinsic edge emission for the pure compounds. There is therefore a marked asymmetry in the curve in figure 4.40, the sample MH109 with 10Å CdSe layers in 90Å CdS layers produces emission 0.8eV lower in energy than the CdS band gap. The corresponding sample MH113 with 10Å CdS layers in 90Å CdSe layers produces emission at 1.74eV, almost exactly at the CdSe band edge (1.82eV). This certainly suggests that the hole is confined in the CdSe. We therefore consider the case of a type II system with the hole confined in the CdSe. Figures 4.42 and 4.43 shows a series of curves for this case with and without piezoelectric fields respectively. It can be seen that both theories can provide reasonable agreement with experiment. The curve corresponding to a conduction band offset of 0.25 eV with piezoelectric field effects is particularly close. The alternative case of electrons confined in the CdSe cannot produce a curve that lies remotely near the observed transition energies. This is a result of the large conduction band offset in this model, the CdSe electron being light and producing high confinement energies. In all these theoretical fits a J=3/2 hole mass of 2.5 m_o in CdSe is assumed. It was noted in

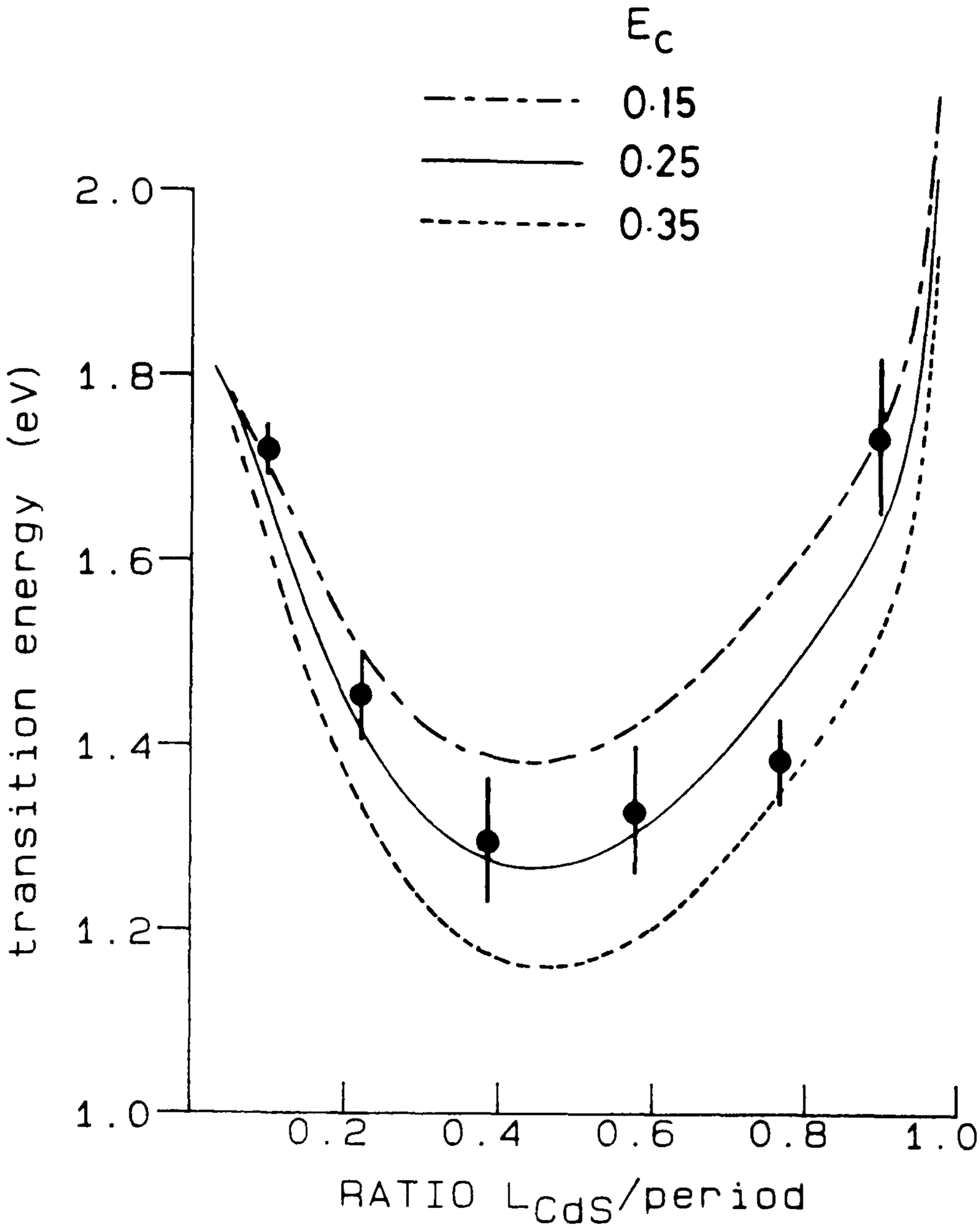

Figure 4.42. Curves indicating the calculated recombination energy in the case of a freestanding piezoelectric superlattice with type II offsets (the electron being confined in the CdS) for the constant period series. The calculation of the curves for each of the conduction band offsets indicated is described in the text. the points are experimental.

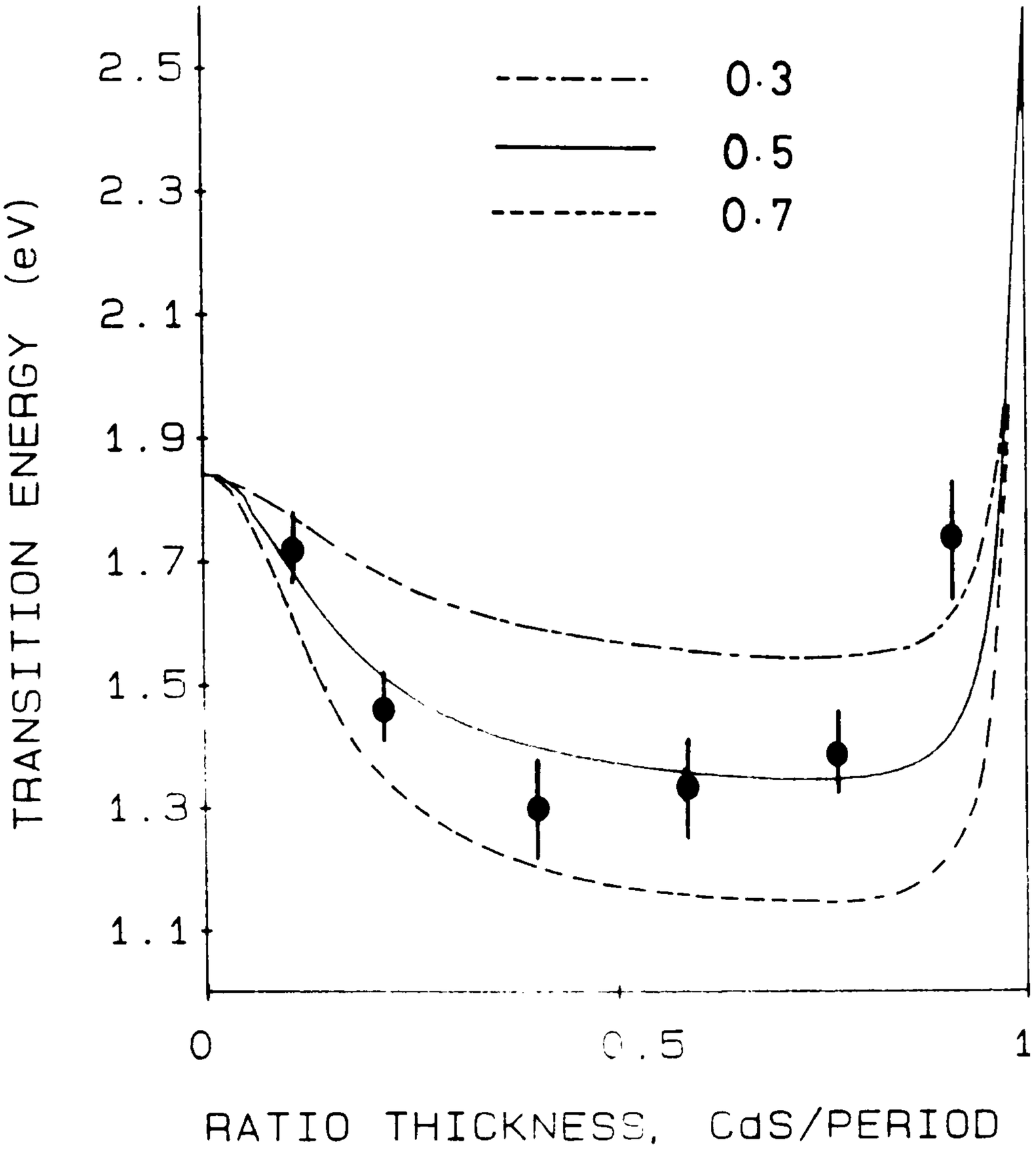

Figure 4.43. Calculated recombination energies for a simple type II superlattice without internal fields for the constant period series. The curves were calculated using the Kronig-penney relations as described in the text. The curves correspond to the conduction band offsets indicated. The points are experimental.

section 1.4 that this value was uncertain and in fact lied in the range 1-2.5 m_o. In practice it was found that these two limiting values gave very similar fitting curves and that this problem did not interfere with the previous analysis.

We conclude from this series that the evidence of the confinement energies is that the superlattice offset is type II. We cannot, from these data alone, be sure that the internal fields expected are present. The transition energies can be accounted for by either a large type II offset with no piezoelectric effect (E_c approximately 0.6 eV); or a small type II offset with internal fields (E_c approximately 0.25 eV). Unfortunately there is considerable error expected in the measured thickness of the layers. This problem is especially acute for small thicknesses (i.e. the extrema of the curve). To be able to demonstrate the presence of the internal fields, samples with different periods must be studied

4.5.2 Constant ratio series

Introduction

The constant ratio series were grown with layers of CdS and CdSe of equal thickness (see table 4.1). The periods were in the range 14-120Å. The growth of such a series should allow the measurement of the offsets. In addition, as was pointed out in section 4.4.2, piezoelectric effects should result in a continuous decrease in the effective band gap as the period increases. Such a series of superlattices should show the effects of the piezoelectric fields. This would provide direct evidence for the existence of such fields, previously only forecast theoretically.

Results and discussion

The peak emission energies of the constant ratio series were taken at low temperatures. As before, the spectra were recorded in the limit of low laser excitation. Figure 4.44 shows three spectra from superlattices in the series with periods of 13Å/13Å, 25Å/25Å and 45Å/40Å. It can be seen that the FWHM of the peaks increases rapidly as the period increases. Figure 4.45 shows the relationship of the peak emission energy versus period. It can be seen that the emission energy decreases as the period increases, as expected for either model.

The first analysis we can apply is by studying the limit of small period. For vanishingly small period superlattice emission must become that of the alloy $CdS_{0.5}Se_{0.5}$. In this limit the piezoelectric field effects become insignificant (see section 4.4.2). This should produce an excitonic emission at 2.15 eV. It can be seen from the figure 4.45 that the even the 14Å period sample only emits at 1.8eV. The mass of the hole along the c-axis of CdSe is very large ($1\text{-}2.5*m_o$). The low energy of the 14Å period superlattice emission is entirely consistent with the hole being confined within the deepest well (see figure 4.36 upper diagram). Moreover, the depth of the emission is entirely consistent with a type II offset system (cf ZnS/ZnTe and ZnSe/ZnTe [39]). This supports the model proposed in the previous section of a type II system with the hole confined in the CdSe.

We can now try to fit the theoretical curves to this data. Figure 4.46 shows the data points with two Kronig-Penney type fitting curves. Curve A assumes a 0.23 eV conduction band offset, whilst curve B assumes a 0.51eV conduction band offset. It can be seen that the two curves give reasonable agreement at either long or short period. However, it is impossible, assuming a simple square well type potential, to account for all the observed recombination energies.

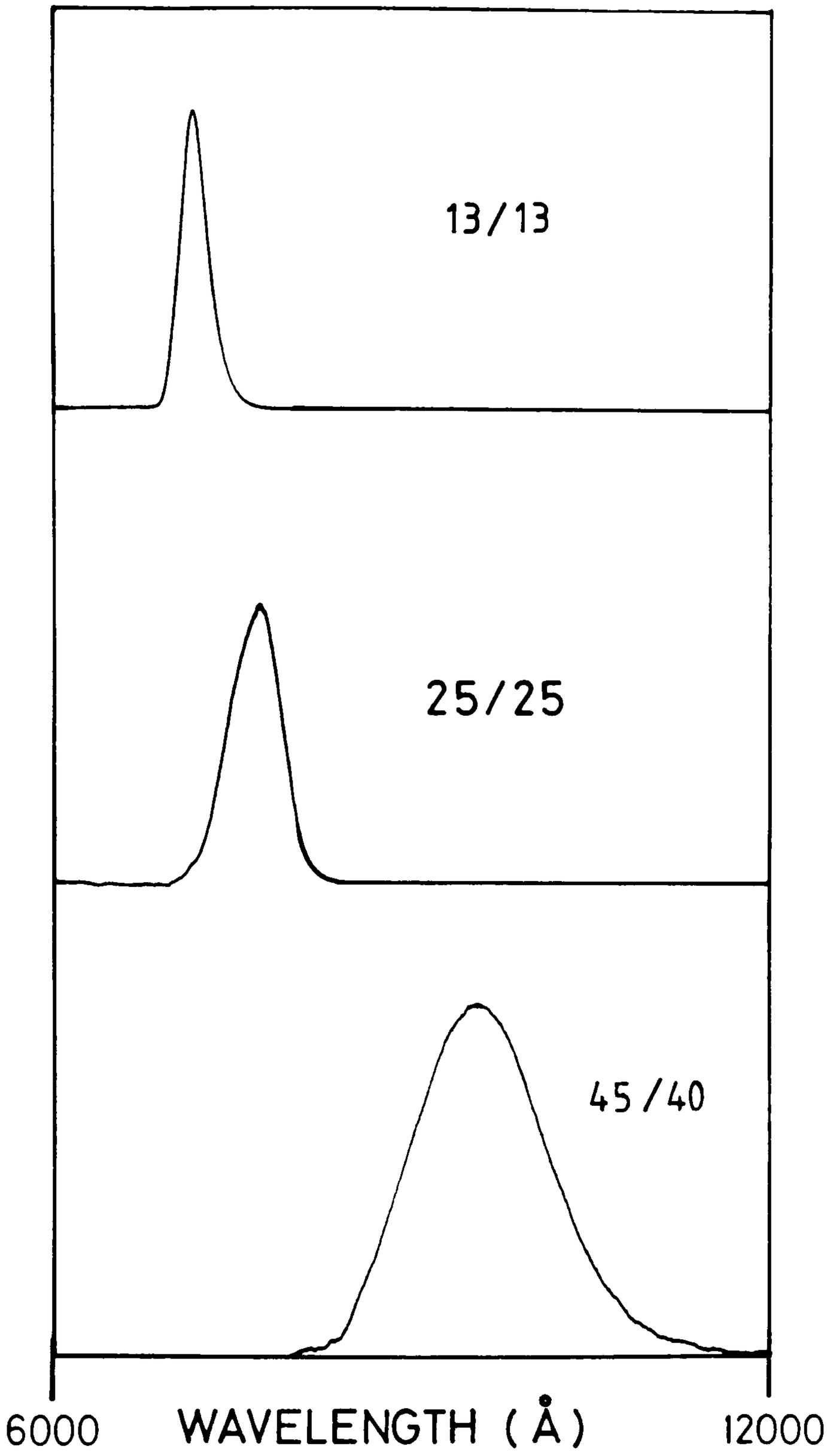

Figure 4.44. Variation of photoluminescence spectra within the L_{CdS}=L_{CdSe} series of superlattices with the periods indicated.

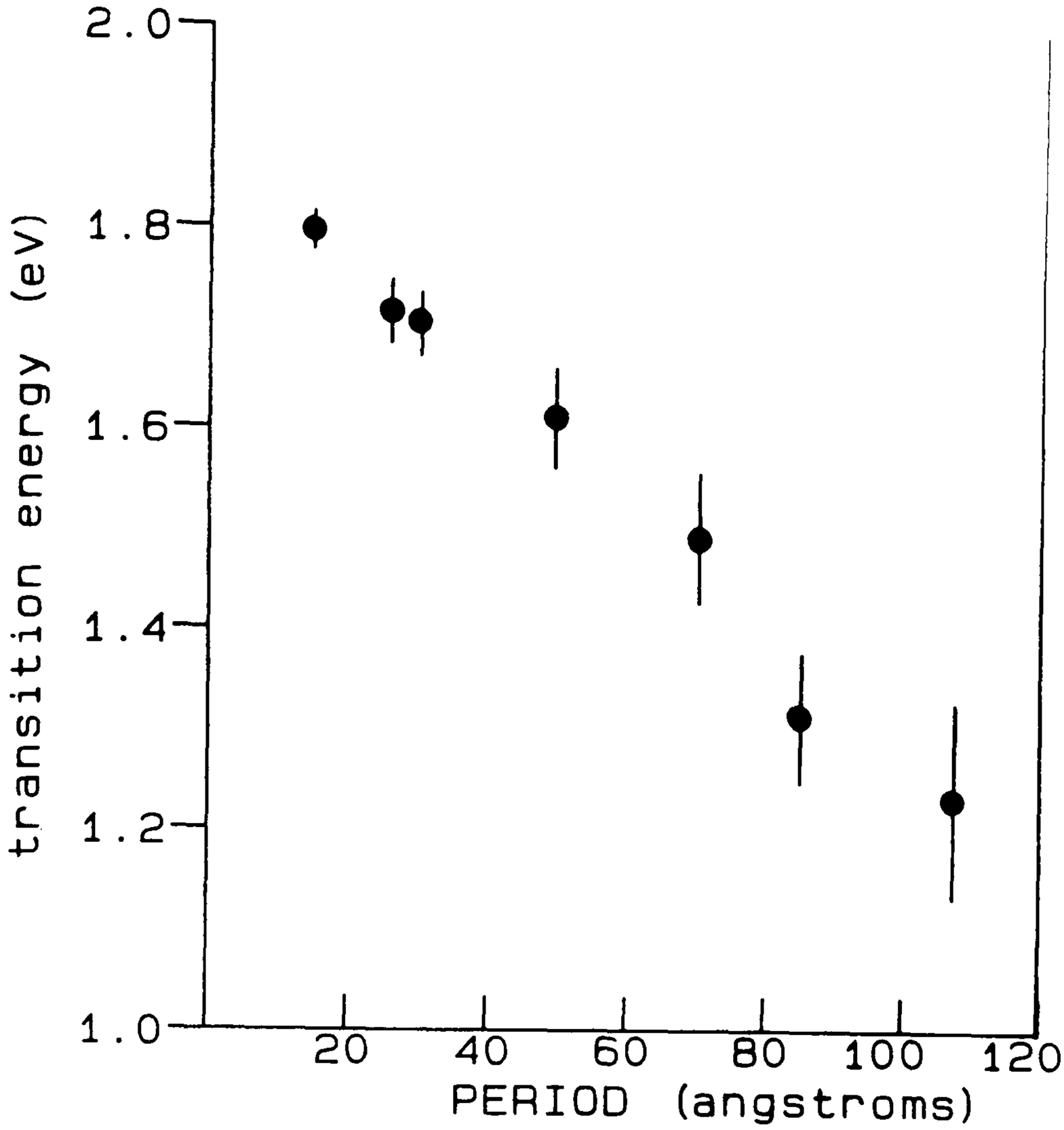

Figure 4.45. Transition energies as a function of period for samples with (approximately) $L_{CdS}=L_{CdSe}$. The points are experimentally measured in the limit of low excitation intensity. The error bars indicate the FWHM of the peaks.

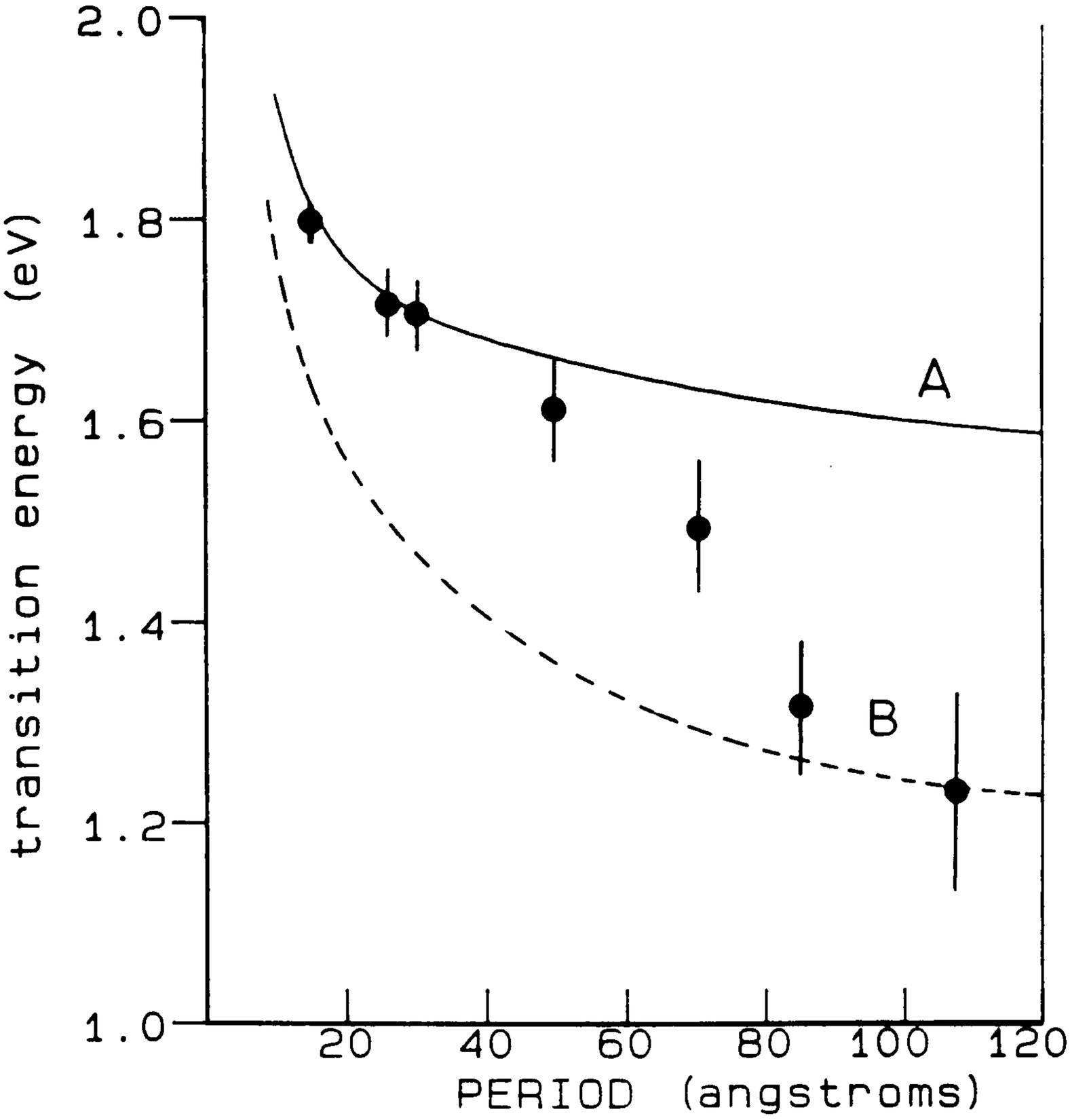

Figure 4.46. Fitting curves for the case of a simple Type II superlattice without internal fields for the second series of superlattices as calculated by the Kronig-penney model. The curves A and B correspond to the conduction band offsets of 0.23 and 0.51 eV respectively, the points are experimental.

To account for the shape of this curve we use the piezoelectric theory. Figure 4.47 shows data with two fitting curves, A and B. Curve B is the variational calculated transition energies, curve A is the Kronig-Penney curve A from figure 4.46. Both curves assume the same 0.23 eV conduction band offset. It can be seen that, as expected, the Kronig-Penney model gives a good fit to the data in the limit of small period. The piezoelectric theory assumes no interaction between adjacent wells and so is innaccurate for small period. However, for large period superlattices the piezoelectric theory gives good agreement with the observed value.

We conclude that the curve fitting for the two series studied presents direct evidence for the presence of piezoelectric fields within this system. This represents the first direct observation of the presence of such fields within strained layer superlattices. In addition the luminescence recombination energies indicate that the system is type II with a conduction band offset of approximately 0.23 eV. For this calculation we assume that the excitonic binding energy is zero. The effect of binding energy on our calculations would be to decrease the measured offset. Therefore we conclude that our measured offset is an upper limit value.

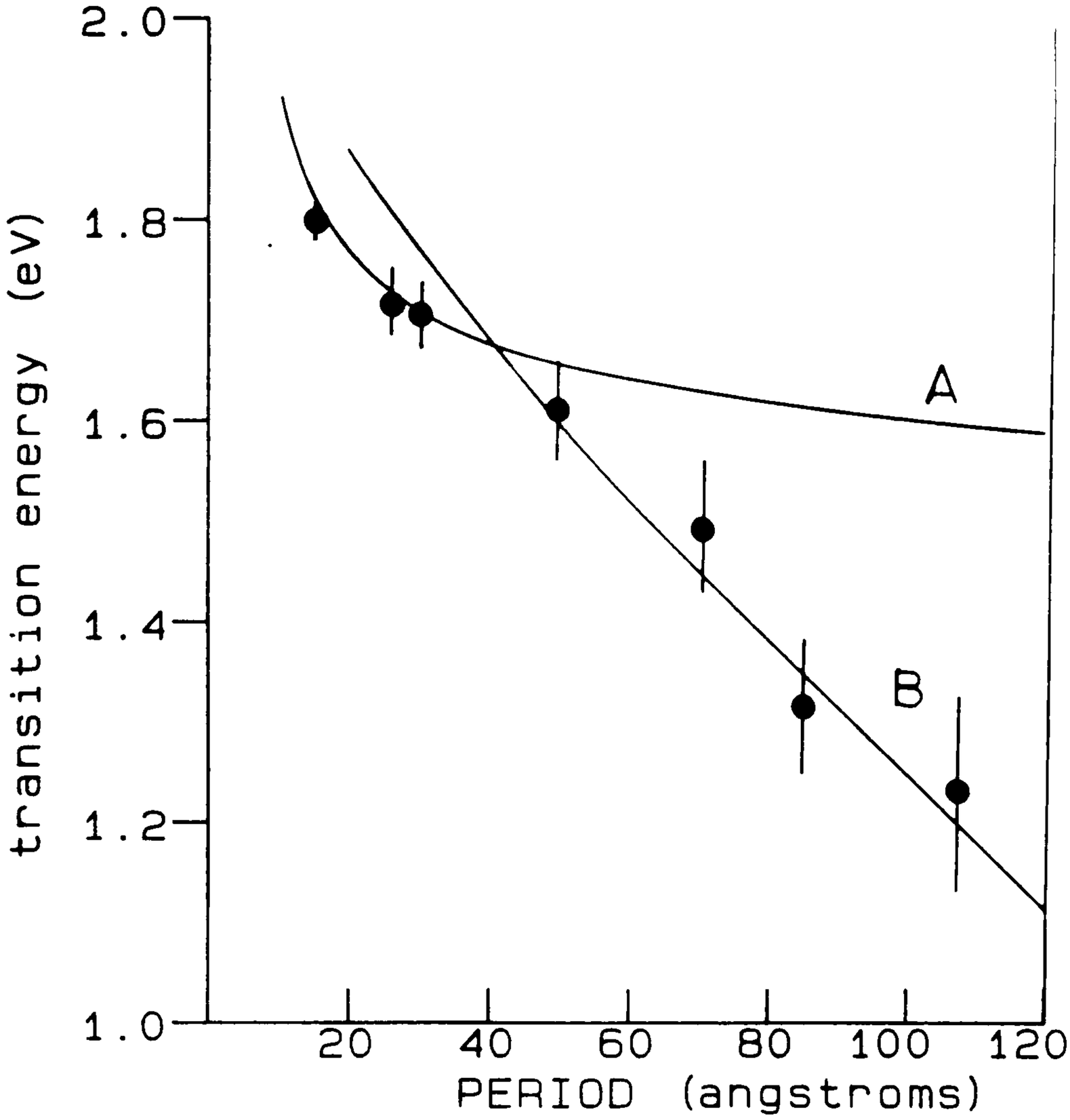

Figure 4.47. Fitting Curves for the transition energy as a function of period. Curve A is the Kronig-Penney calculation assuming a conduction band offset of 0.23 eV. Curve B is calculated using the piezoelectric theory, but assuming the same 0.23 eV conduction band offset. The points are experimental.

4.5.3 Band structure of a CdS/CdSe superlattice

The luminescence from the CdS/CdSe superlattice samples is unlike that reported for any other superlattice system. In the theoretical section possible reasons for this were proposed. In the previous section the luminescence was interpreted. We can now use this intepretation to propose a model for the system. It is important that this model be able to account for all the observed properties of the system

We now have the final model for the band structure of a CdS/CdSe superlattice when grown with the c-axis vertical. The analysis above suggests a type II structure with a 0.23 eV conduction band offset (1.02 eV E_v). We also found that the presence of the piezoelectric internal fields had to be assumed to account for the depth of the emission from large period superlattices. The small conduction band offset is in line with that expected from the 'common cation rule' [40]. The value of the conduction band offset measured is subject to a number of unknowns. These include the exact mass of the hole in CdSe parallel to the c-axis, excitonic binding effects, and problems associated with well width fluctuations. By considering the limiting values of the hole mass and realistic uncertainties in the superlattice periods an error can be estimated in E_c. In addition to these unknowns there are also excitonic binding effects. Such excitonic effects will lower the transition energy by the magnitude of the binding energy. Without considering the calculation of excitonic binding energies in quantum wells we can make a few simple observations. For a type I quantum well, in the limit of small period, the excitonic binding energy is increased above that in the bulk (by upto four times the 3 dimensional value [41]). Therefore without calculating the possible magnitude of the electron-hole interaction energy we will simply

estimate a possible error in the measured offset of twice the excitonic binding energy in CdSe i.e. approximately 40 meV. As this energy will be subtracted from the conduction band offset, we note that the measured offset is an upper limit. Combining this error with the error due to uncertainties in the effective masses and well widths we ascribe E_c in this system a value of 0.23+_0.1 eV. We can now use our measurement to draw our predicted band structure for the system.

Figures 4.48 and 4.49 show the periodic potential along the c-axis of CdS/CdSe superlattices with periods of 14,50,100 and 200 angstroms. Included in the diagrams are the calculated ground state transition energies. It is obvious from the diagram that the band gap of this superlattice should actually reduce to zero at some point. This is shown for the 200 angstrom period superlattice in figure 4.49, this superlattice has a band gap of 0.2 eV. The CdS/CdSe system therefore has a band gap which is tunable in the region 0-1.8 eV.

The theory used is straightforward, and the results above support it. However, the system is clearly very unusual and it is important to justify this interpretation in as many ways as is possible.

4.5.4 Origin of higher energy emission

It was described in the luminescence section how, in the large period superlattices, CdSe free excitonic emission was observed. Furthermore, for smaller periods there was still some higher energy emission observed. Considering the model developed above we can explain this higher energy emission in terms of direct (in real space) recombination. It is observed in the next section that the laser intensity effects are very similar to those seen from GaAs nipi doping superlattices. These structures are doping superlattices as described

Figures 4.48 and 4.49. Series of schematic diagram showing the potential distribution along the c-axis of CdS/CdSe superlattices with various periods. The periods are indicated by the scale markers. Also indicated on the diagrams are the electron and hole confinement energies in their respective wells.

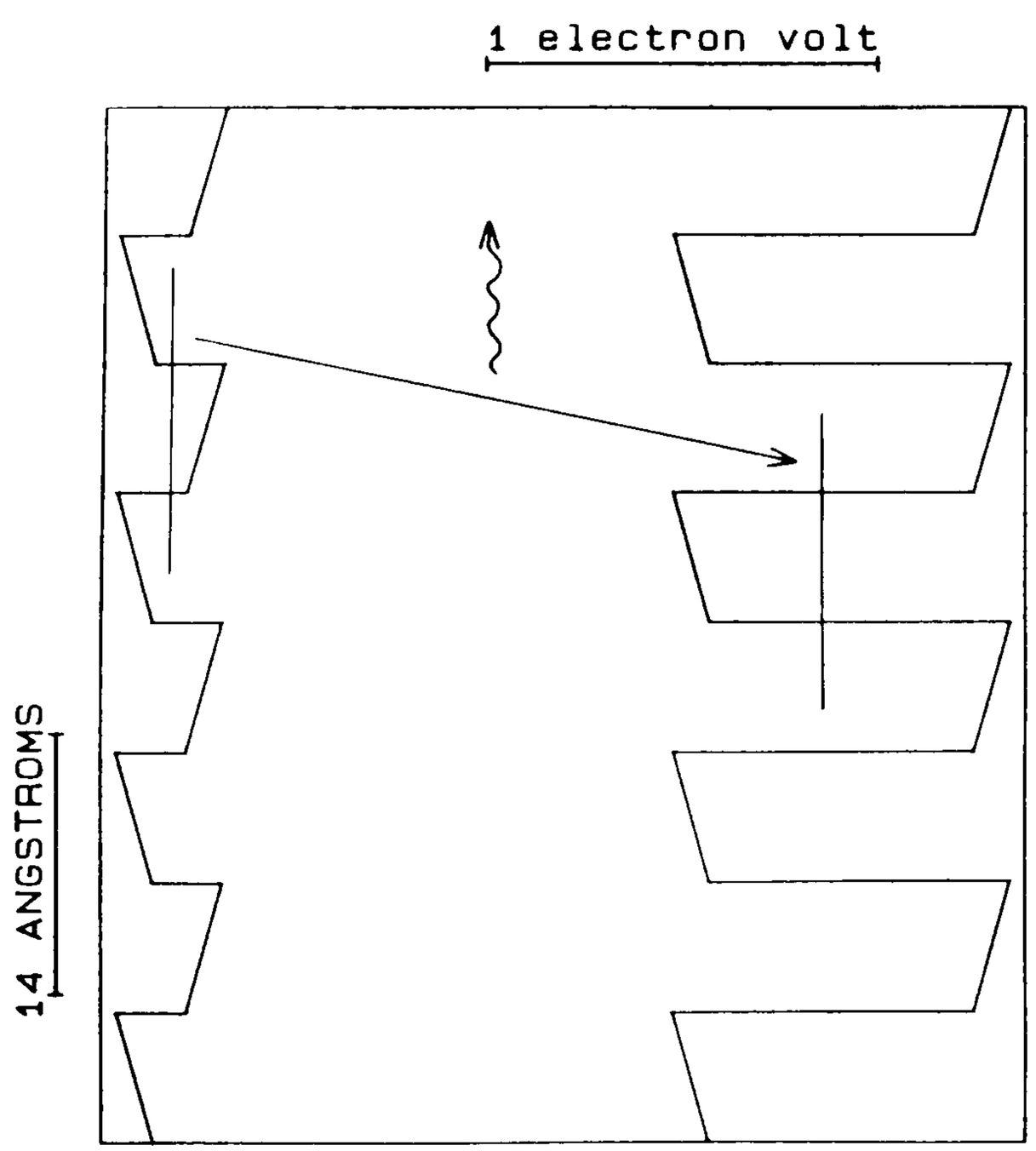
1 electron volt
14 ANGSTROMS

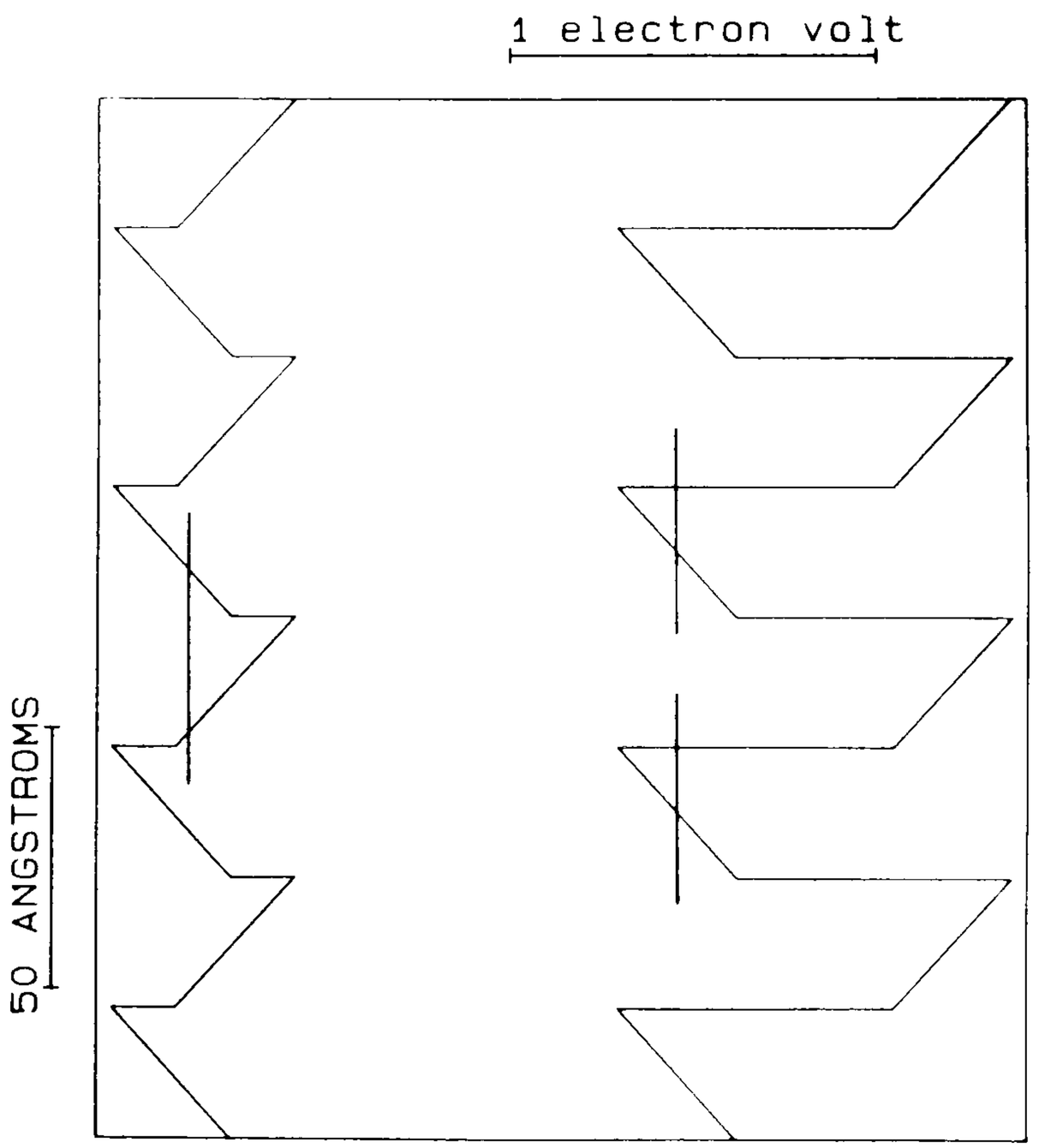
1 electron volt
50 ANGSTROMS

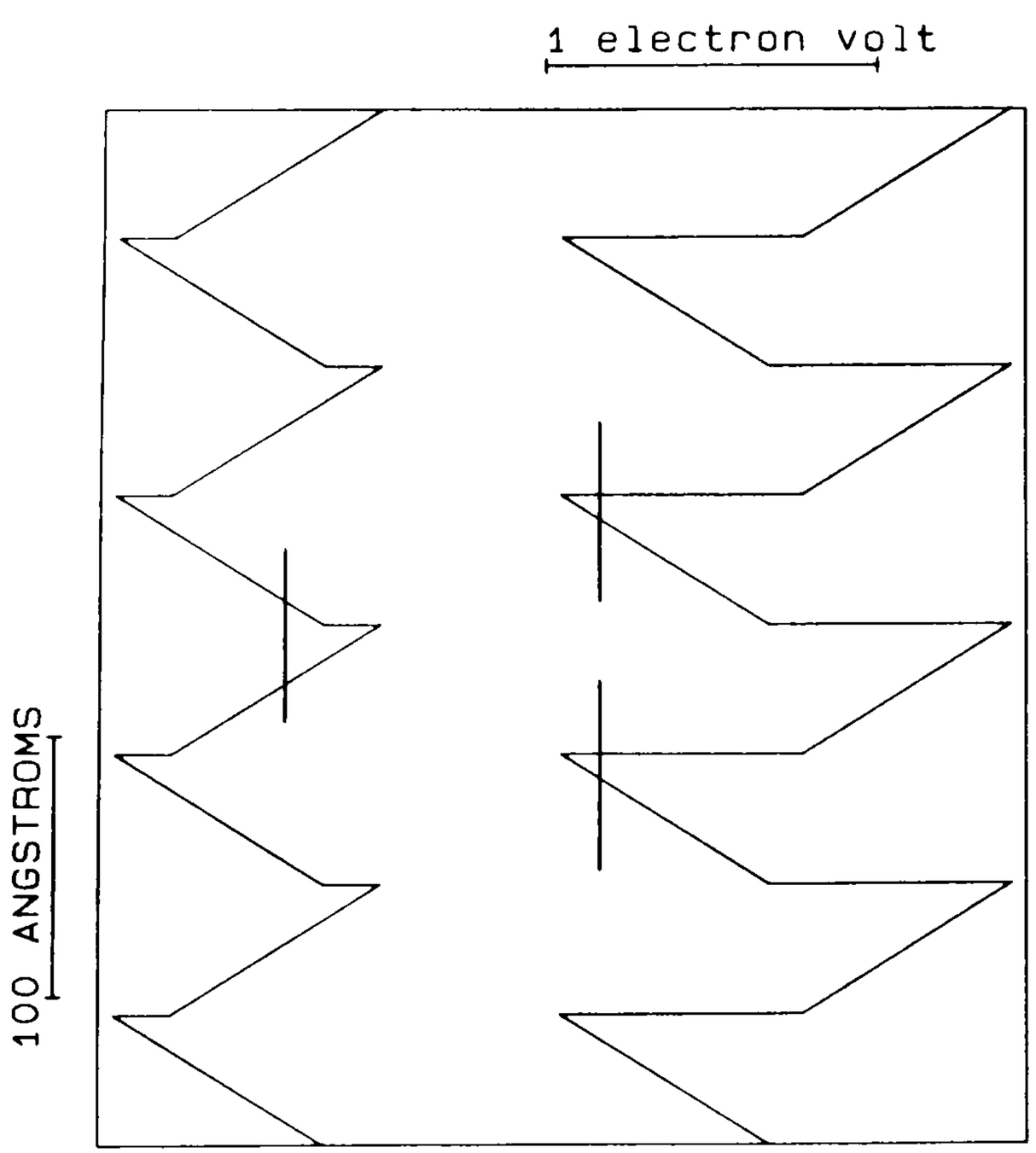
1 electron volt
100 ANGSTROMS

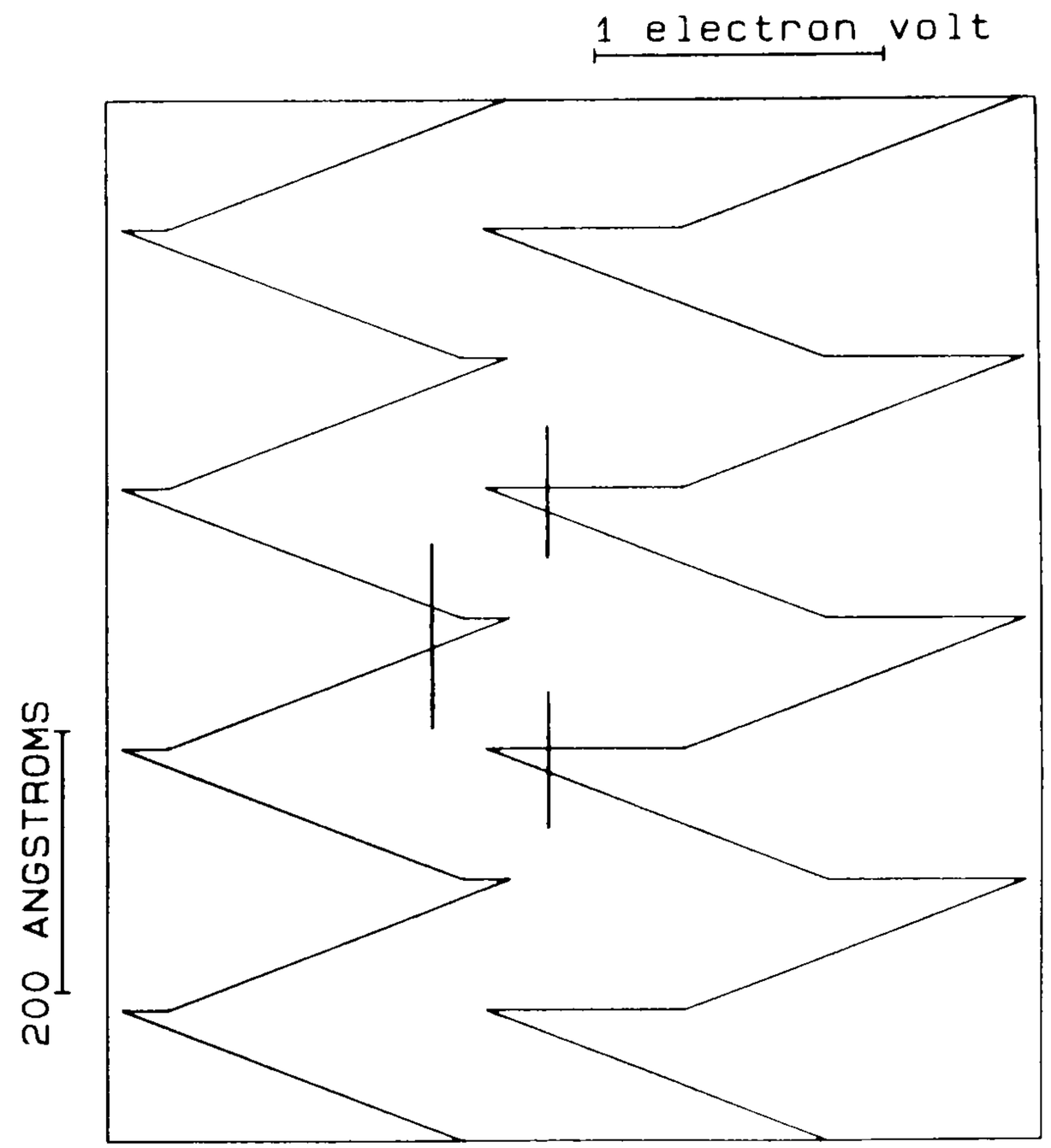
1 electron volt
200 ANGSTROMS

in section 1.6.2. GaAs nipi structures also display broad band emission below the GaAs band edge. Moreover, with increasing laser power the emission shifts to higher energy and the FWHM decreases. For this system the effect is due to the charge separation effects within doped layers (for a review see [42]). Within the structures the carriers lie in separate parabolic wells. Figure 4.50 is taken from [42] and it illustrates the origin of the luminescence seen from these structures (the notations refer to that paper). It can be seen that there are two principal processes, the direct in space hw(60) and the indirect in space hw(54). These give rise to two emissions from the superlattice, one at the GaAs band edge and one at much lower energy. Figure 4.51 (taken from [43]) illustrates the mechanism behind this. The photoexcited carriers either thermalise (via phonon emission) into their respective wells and then recombine via the low energy process or, before reaching the wells, recombine directly across the GaAs bandedge. We can understand our observed high and low energy emissions in terms of similar processes. The equivalent of the transition hw(60) in our system is the high energy emission which is observed from all the superlattices. The intense near-infrared emission is the indirect recombination as assigned in the previous theoretical treatment.

To support the above analysis we can make three observations. Firstly it is observed that the intensity of the direct recombination increases relative to the indirect as the exciting intensity increases. This is also observed for the equivalent emission in the nipi structures [43]. Support also comes from our temperature dependence work. In section 4.3.5 such emission from a 7Å/7Å superlattice was studied. It was found that as the temperature was raised the high energy (direct) emission intensity increased, whilst the superlattice (indirect in space) emission's decreased. This is precisely what is

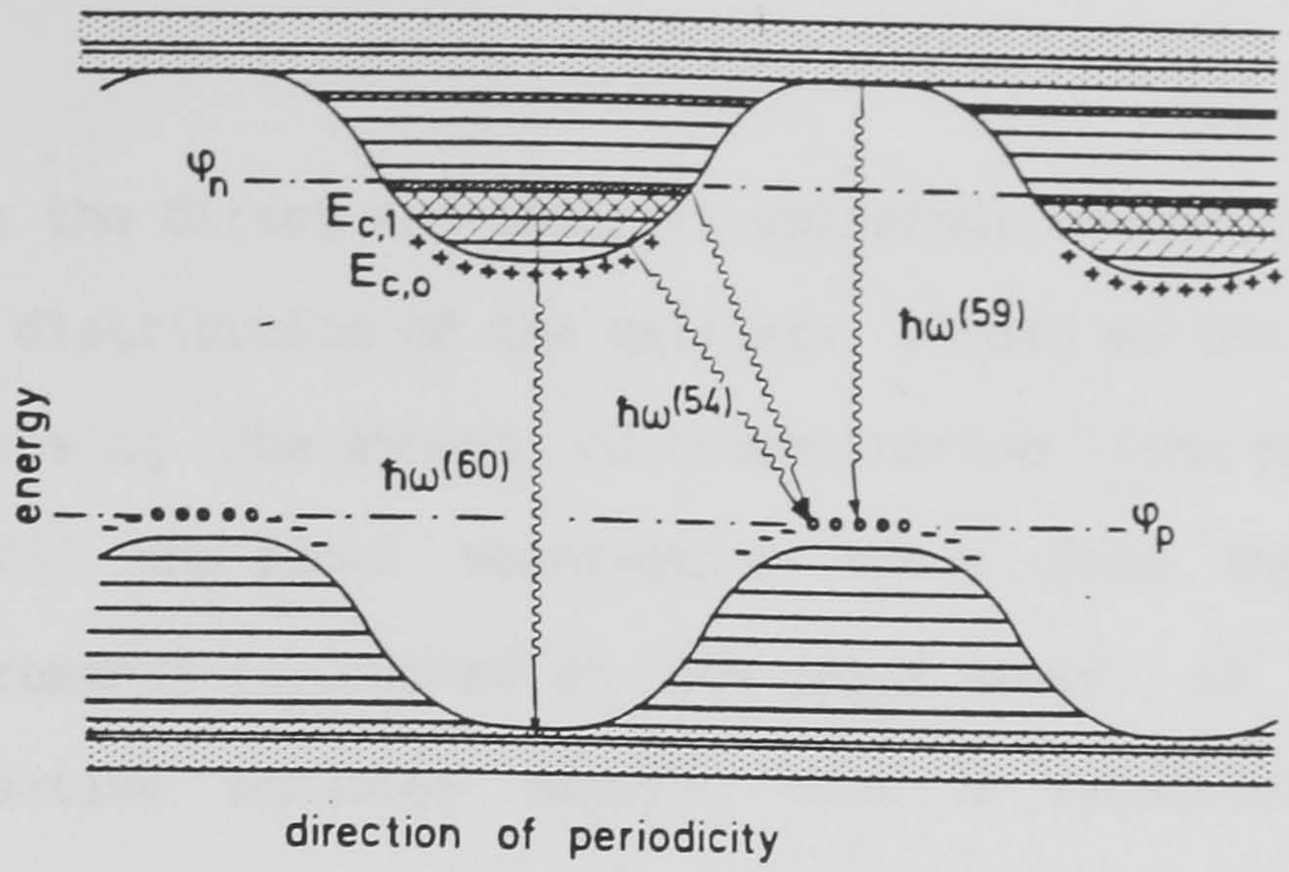

Figure 4.50. Origin of luminescence from GaAs nipi doping superlattices. The notation refers to reference [39]. Two principal type of emission are observed the indirect in space hw(54) and the direct in space hw(59).

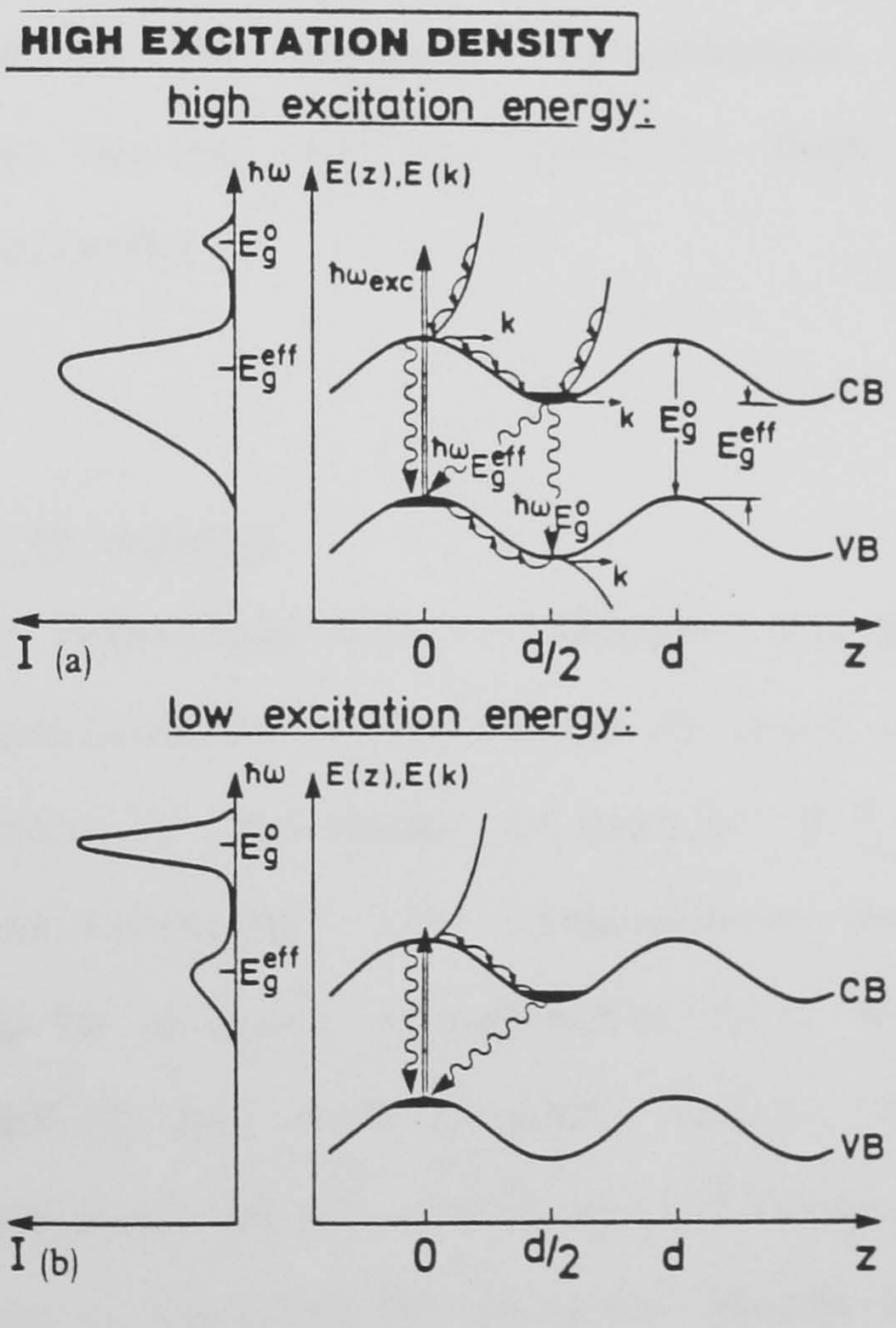

Figure 4.51. Schematic diagram taken from reference [40] illustrating photoluminescence processes in GaAs nipi structures. The upper diagram illustrates the production of electrons at high k values by the laser excitation. These electrons then decay by phonon emission (arrows) to recombine with holes in the valence band either directly or indirectly in space (see text).

observed for the direct and indirect emissions in GaAs nipi stuctures. The thermal distribution of the carriers alters as the temperature is raised, increasing the amount of recombination from carriers in the same layer [42]. The final observation comes from the luminescence decay measurements (conducted at low temperature). It was found that the superlattice emission decayed with a relatively long decay half-life of 16-63ns for a 25Å/25Å superlattice. In contrast the higher energy emission (6280Å) from a 145Å period superlattice decayed in only 5ns. This is what is expected from the process discussed above. The carriers rapidly thermalise into their respective wells to recombine via the low energy process, with a longer decay. Figure 4.52 shows our model for the origin of the observed luminescence for a 50Å/50Å CdS/CdSe superlattice. The hw_1 and hw_2 refer to high and low energy recombinations respectively.

4.5.5 Space charge effects

One of the most remarkable effects observed for the luminescence from the CdS/CdSe superlattices is the effect of laser intensity on the emission peak position. It was found in section 4.3.4 that, as the laser excitation power increased, the luminescence peak shifted to higher energy by up to 0.3 eV. Accompanying this shift there is a reduction in the FWHM of the emission peak. Similar effects are also observed for the GaAs nipi structures discussed above. The effect in the doping structures is produced by the space charge fields developed between the electron and hole confining layers. When carriers are photoexcited into the wells a space-charge potential develops between the doped layers raising the energy difference between the electron hole recombining pairs. This produces an increase in emission energy.

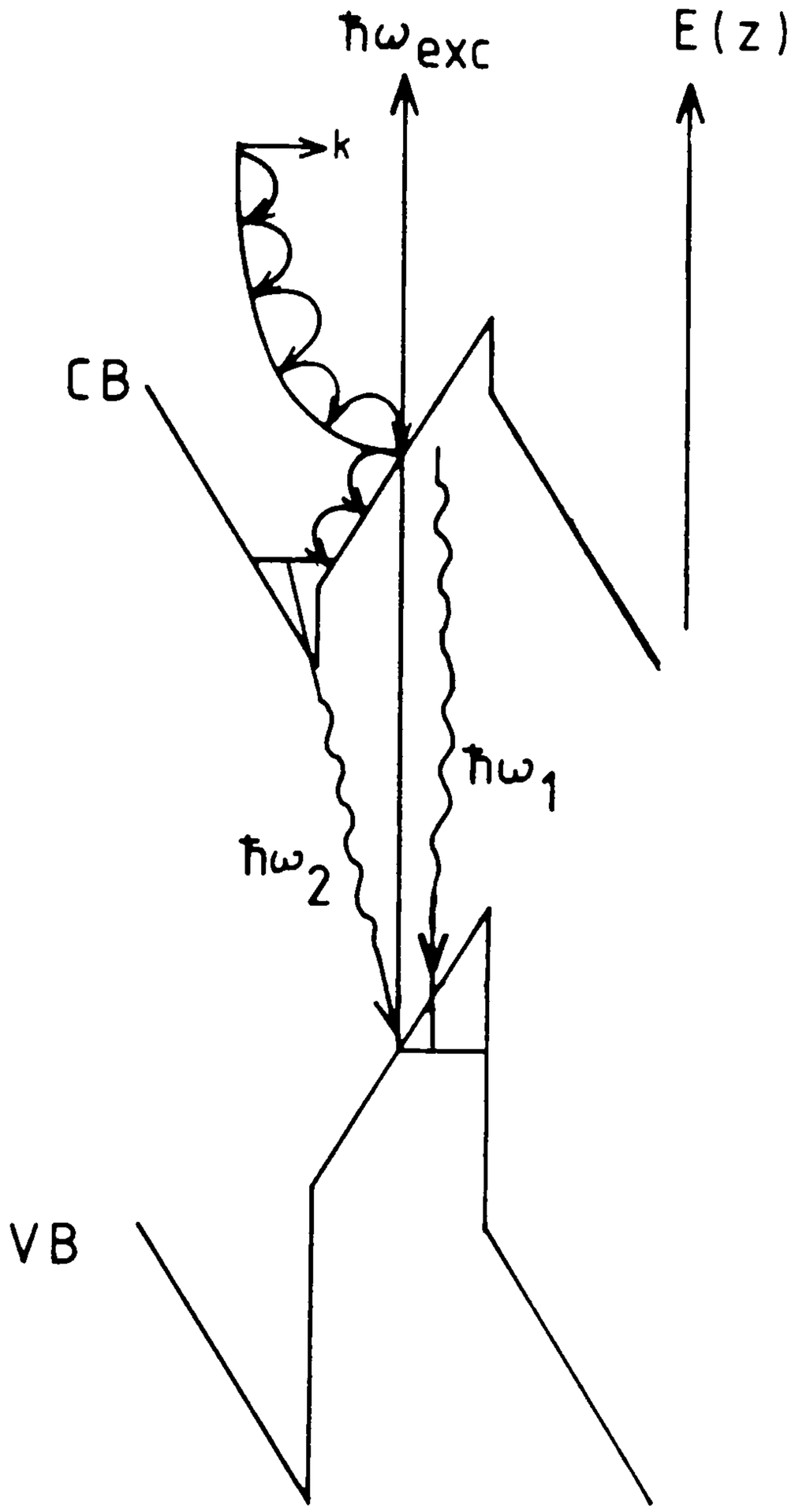

Figure 4.52. Physical model for red emission observed from CdS/CdSe superlattice. The incoming exciting photon hwexc creates an electron in the conduction band at elevated energy (i.e significantly above the bottom of the conduction band). This electron can then either decay by phonon emission into the piezoelectric well before recombining or recombine directly (in space) within the CdSe. The two resulting emissions are labelled hw1 and hw2. Similar effects are observed in GaAs nipi structures (see text and figure 4.51).

Clearly such a mechanism could explain the observed peak shift in the CdS/CdSe superlattices. If this is the case then carriers must be confined in separate layers. This can be easily verified by observing the effect of laser power on luminescence originating from carriers within the same layer. The spectrum obtained from MH90 (160Å/130Å CdS/CdSe) was studied at two different excitation densities (one 1000 times more intense than the other). It was observed that the deep superlattice emission shifted by 0.3 eV under the increased excitation. However, the CdSe excitonic emission energy did not shift at all between the two laser powers.

A process that could explain a shift in emission energy was simple band filling. However, such a process would affect the CdSe excitonic recombination, broadening and shifting the peak and no such shift is seen. We conclude that the peak at 6900Å, as expected, originates from recombination between carriers within the same layer. This is to be expected if the recombination is a result of excitons existing wholly in the CdSe, with no significant degree of band filling occuring. The superlattice emission, however, does shift and the only satisfactory explanation for this is the presence of space charge effects.

As carriers are photocreated within the layers of a CdS/CdSe superlattice they will be thermalise into the lowest energy state lying (mostly) in the ground state of their respective potential wells. The approximate wavefunctions for carriers in these potentials were calculated in section 4.4.2. These carriers can now be thought of as producing a 2 dimensional sheet of charge within the layer. It was shown in [44] that such a superlattice is analogous to a parallel plate capacitor, with the plates positioned along the z-axis at the positions :-

$$z = \langle z \rangle = \int \psi_{(z)} z \, \psi^{*}_{(z)} \, dz \qquad \text{(xviii)}$$

The fields between the plates can be calculated trivially to be given by

$$F = Ne / \epsilon_o \epsilon_{11} \qquad \text{(xix)}$$

Where N is the areal charge density within the layers of the superlattice. Figure 4.53 shows schematically the plates and the resulting electric fields. It can be seen that the effect of the charge generated field is to neutralise the internal piezoelectric fields. This effect was recognised in [17] where the pieozelectric superlattice was first envisaged. The situation is actually more complex as the <z>'s are not exactly located at the interfaces. Moreover, as the charge density increases the fields are neutralised and the wavefunction will alter. However, qualitatively the effect is to reduce the internal fields.

Figure 4.54 shows the change in potential distribution which can be expected from carrier seperation in a superlattice described in section 4.5.3. The shift to higher energy from the emission that is observed can therefore be understood in terms of the field neutralisation. The low energy of the emission for low laser powers being a result of the piezoelectric fields.

With the piezoelectric field theory, we calculate a transition energy of 0.7 eV for MH91 (160/90Å CdS/CdSe). In practice we observe a transition energy of 1.1 eV. This clearly represents an anamolous result. This can be understood in terms of the charge effects. Figure 4.25 shows the shift of emission peak with laser power for MH111

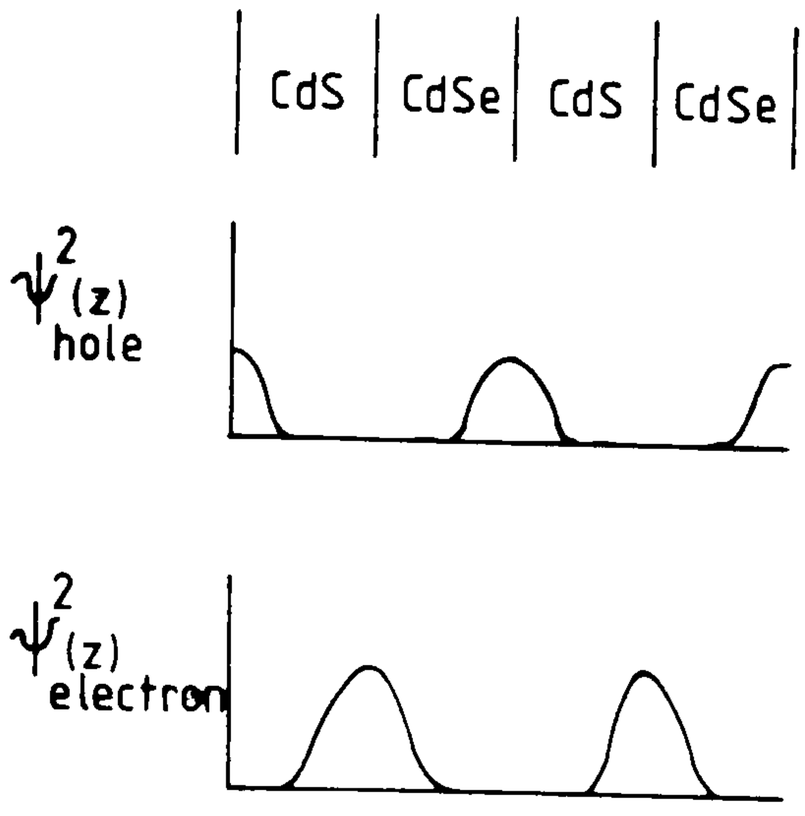

Figure 4.53. Schematic illustration of the seperation of charge in a CdS/CdSe superlattice with piezoelectric fields. The charge seperation results in a parallel capacitor type potential which opposes the internal fields.

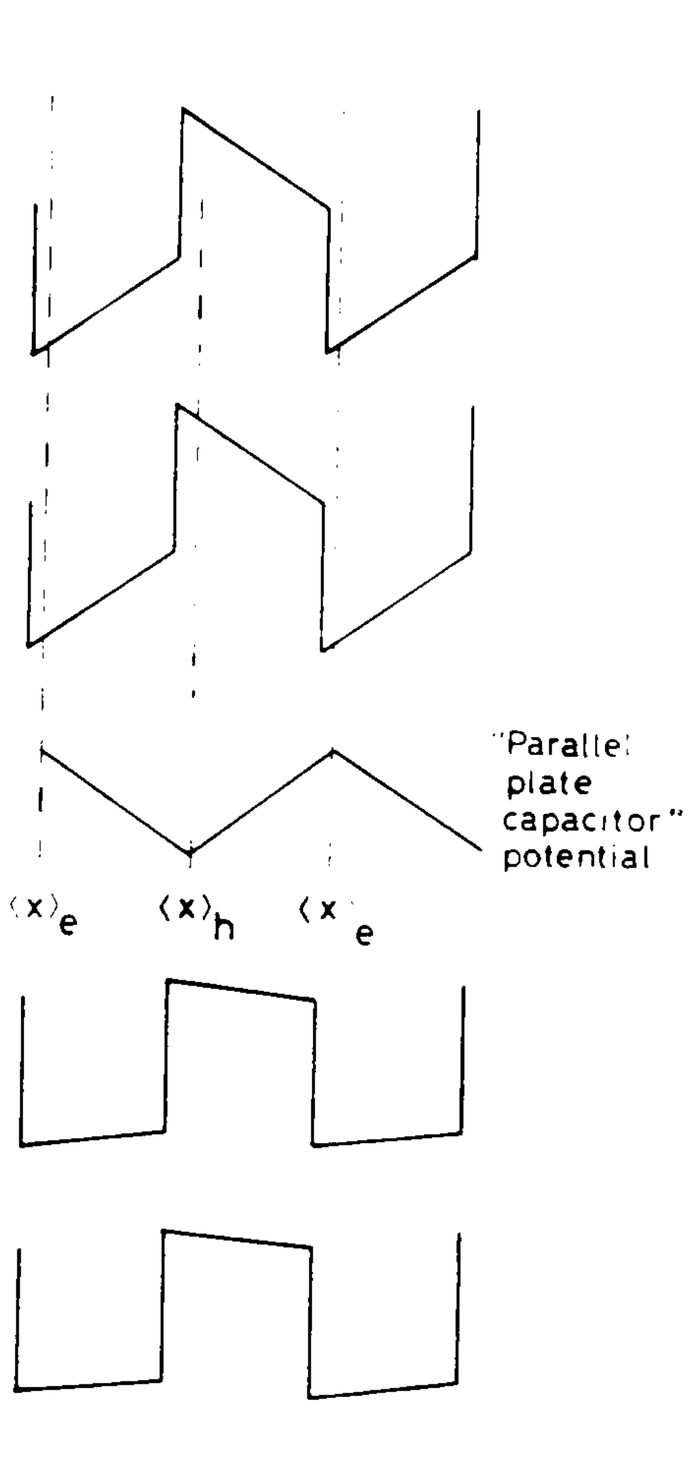

Figure 4.54. Effect of light-excited space charge field on internal fields in piezoelectric superlattice.

(40Å/60Å CdS/CdSe). It can be seen that at the low excitation limit the gradient of the graph is still steep; at this limit the laser power was as low as was possible to still detect a luminescence signal. We conclude that the actual low excitation limit of the emission energy is not being observed. The intensity of the luminescence will be proportional to the inverse of the carrier lifetimes for decay by the luminescence process. For very large periods the recombination rate of the electron and hole pairs is very small. Consequently the luminescence cannot be observed before significant charge has accumulated. It is important to compare figure 4.24a with figure 4.25 which shows a similar graph for a 15Å/15Å sample. In this case the graph shows a clear tailing off at the low excitation limit. We conclude that for the small period sample we are observing the unperturbed transition energy.

4.5.6 Emission band line shape

For small superlattice periods the emission from the samples studied here is similar to that observed from other II-VI superlattices. However, as we move to large periods the emission band becomes very broad, with a FWHM of upto 200 meV. Clearly to justify our intepretation we must be able to account for this observed emission breadth. In this section we will consider mechanisms that can cause such linewidths in luminescence from superlattices.

Spectral broadening in semiconductor excitonic recombination has a number of causes. The main contributions are from phonon interaction and hot electron effects [45]. In superlattices both these can occur and, in addition, well width variation effects can contribute. Considering phonon interaction first, we can see direct evidence for

such interaction in figure 4.55. This figure shows the emission from mh122, a 7Å/7Å superlattice. It can be seen that phonon replicas are clearly visible on the low energy tail of the superlattice emission, the phonon energy being 27.5 meV. We are not concerned with calculating phonon energies within superlattices here. However, this energy is close to that of the CdSe LO phonon and is consistent with the believed nature of the structure [46]. We can conclude that phonon broadening occurs and is a major factor in the linewidths for small period superlattices, causing a FWHM of 40-70meV. Strong phonon interaction is not observed in type I superlattices. However, in type II superlattices we might expect, qualitatively, the seperation of the carriers in real space to encourage phonon assisted recombination. We can only assume that similar phonon interaction occurs in the larger period structures. However, in this case the phonon replicas are obscured by other broadening mechanisms.

The principle broadening mechanism observed in superlattice emission is due to well width fluctuations [47]. The fluctuations in well width cause variations in the recombination energy, broadening the observed luminescence band. It can be shown trivially that the energy broadening is proportional to the differential dE/dl, where E is the transition energy [48] i.e:-

$$\Delta E \propto \frac{\delta E}{\delta L} \qquad \text{(xx)}$$

Consequently, for a simple superlattice without electric fields, the line width reduces as the period increases. This is indeed observed in a wide range of systems. The CdS/CdSe system is unusual in that a large increase in FWHM is observed for increasing period.

To explain the FWHM we consider first the effect of width

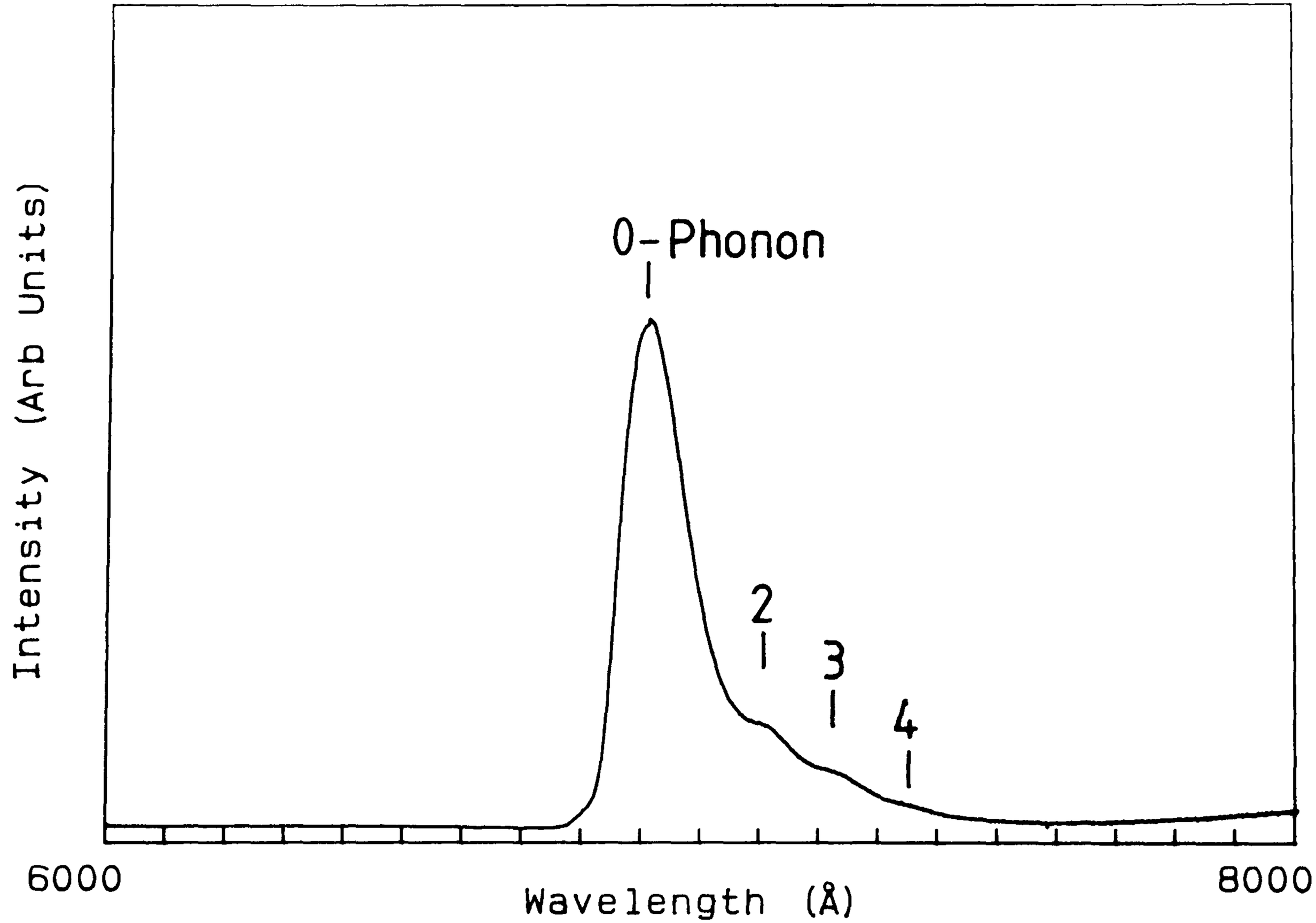

Figure 4.55. Photoluminescence spectrum of MH122 (7Å/7Å CdS/CdSe superlattice). Phonon replicas are clearly visible on the lower energy tail of the superlattice emission. The 1st phonon replica appears to be obscured by the main peak.

fluctuations. For a conventional superlattice, in the limit of wide wells, a change in well width will not affect the confinement energy. However, with internal fields, such fluctuations will produce large changes in the recombination energy. This is illustrated by figure 4.56.

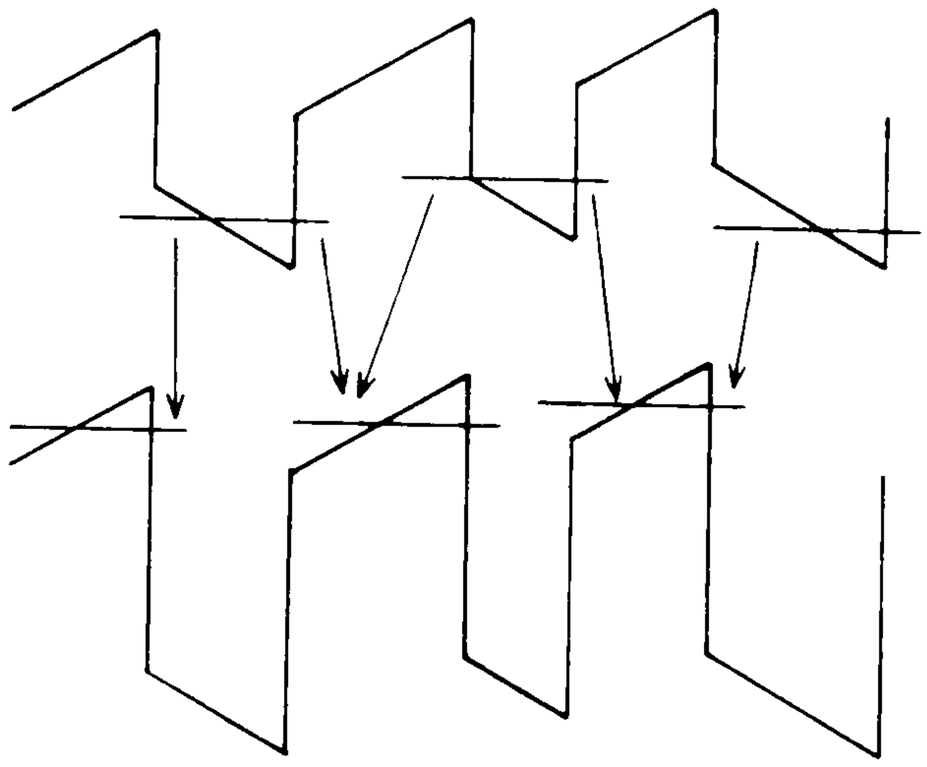

Figure 4.56. Effect of layer thickness variations on emission energy.

It can be seen that variations in layer thickness not only produce variations in confinement energy but also alter the potential energy at the centre of the wells. The variations in the well thickness are quantized into multiples of c/2 (c is the wurtzite lattice constant and corresponds to two monolayers). The difference in recombination energy thus produced is given by dE_r=de+c*F/4; where de is the change in confinement energy, c is the wurtzite lattice constant and F is the electric field. Similar effects have been observed in AlGaAs/GaAs multiple quantum wells in an externally applied electric field [49]. It was observed in this system that the FWHM of the recombination emission

was proportional to the applied field.

Therefore in a piezoelectric system the slightest fluctuation in well width will cause large variations in emission energy. We consider MH111 a 40Å/60Å CdS/CdSe superlattice, with an emission band FWHM of 230 meV. We can do a naive calculation by subtracting the 70 meV due to phonon broadening and estimate a 'thickness fluctuation' band width of 160 meV. This width could be caused by a fluctuation in the interfaces of only two monolayers (7Å). Fluctuations larger than this are actually observed in the TEM images (for example see figure 4.8).

It also relevant to compare the luminescence from MH113 (12/104Å CdS/CdSe) and MH109 (76/8Å CdS/CdSe) (figure 4.15). The sample with the thin CdS layers shows a much smaller luminescence line width (54 meV) compared with the equivalent sample with thin CdSe layers (260 meV). The model developed above has the hole confined in the CdSe, at the bottom of a 1.012 eV deep potential well. For sample MH109 a change in the CdSe thickness of only one atomic monolayer (3.5Å) will change the recombination energy by 185 meV (calculated from the variational wavefunction). The same figure for MH113 (variation in the CdS well of one monolayer) is approximately 60 meV. The last figure was estimated from the Kronig-Penney model, since it is essential for this sample to include the effects of dispersion on the confinement energies. The small value of the second figure is a result of the lower mass of the electron and the smaller depth of the electron potential well. This observation provides very strong support for the model developed earlier, as it is difficult to account for by other processes.

The well width fluctuation mechanism in itself can explain the observed emission width. However, the observed reduction in FWHM with increased laser power may indicate another mechanism. Such a reduction is also observed for the emission from nipi structures. The change in

this case is attributed to laser penetration effects [43]. The emission from different depths will be shifted to different extents. The net effect is to broaden the observed band. As the laser power is increased the emission from the layers at all depths will shift to occur in the same spectral region. Hence a reduction in linewidth occurs. It is interesting to note that the effect of injected charge is to neutralise the internal fields. This in itself might reduce the FWHM by making thickness variations less significant. Although this effect could (in fact should) occur, it is indistinguishable from the laser penetration effect. We conclude that the great breadth of the emission is a result of the presence of the piezoelectric fields. However, this is not inconsistent with a good quality superlattice structure.

4.5.7 Luminescence decay time

The subject of superlattice luminescence decay rates has been widely studied. It has been found that the half life of the excitonic emission from type I superlattices is typically very short, e.g. 600ps ZnS/ZnSe [50]. This is a result of the close confinement of the electron hole pairs in these structures. However, for type II systems and GaAs nipi structures, the decay times are found to be considerably longer. The calculation of absolute carrier recombination rates in superlattices is a non-trivial problem (see for example [51]). However, one result that we can apply to this problem is that the recombination rate is proportional to the square of the electron hole wavefunctions 'overlap integral' I_o defined by [51]:-

$$I_o = \int \psi_e(z)\,\psi_h(z)\,dz \qquad \text{(xxi)}$$

Electrons and holes confined in the layers of a Type I superlattice will have an overlap integral of approximately 1. Hence the recombination rate is fast. This is essentially the reason for the slow recombination rates in type II and doping superlattices. In these systems the electrons and holes are separated spatially. It is found that in the type II superlattices the recombination rate can be orders of magnitude longer than in bulk [52]. Simlarly, in doping superlattices the electrons and holes lie in well separated, deep potential wells (see figure 4.50) and thus the overlap integral is very small. Consequently nipi structures display very long recombination times, up to microseconds [53]. It was noted in section 4.5.3 that there are certain similarities between the piezoelectric superlattice and GaAs nipi structures. We expect the recombination rate in the piezoelectric superlattice to be long as well, the electron hole overlap integrals being very small for this system.

In section 4.3.6 the time decay of the luminescence was measured. It was found that the recombination rate from a 25Å/25Å CdS/CdSe superlattice was 16ns and 63ns at 700 and 750 nm respectively. These lifetimes are significantly longer than measured for the type I II-VI compound superlattices (for example 3ns for CdSe/ZnSe [54]). We conclude that they are consistent with separate carrier confinement within the superlattice. It was also reported that the luminescence decay was not simple exponential. It was suggested there that the presence of impurities could cause a complex exponential decay [14].

To explain the wavelength dependence of the decay times we must examine the origin of the luminescence. We found in sections 4.3.2 and 4.3.6 that the luminescence was entirely consistent with excitonic recombination. In the last section the breadth of the luminescence band was attributed to a combination of phonon interaction, layer thickness

variations and laser power effects. Consider a system in which the superlattice layers are perfectly smooth: We expect to get one band which is broadened by phonon-interaction alone. In this case the luminescence decay rate is the same at any point in the band, this has been observed in other systems (e.g. ZnS/ZnSe [54]). Considering a system with well width fluctuations: now the low energy tail of the emission band is principally emission from longer period regions of the superlattice (see previous section). Figure 4.57 shows the relationship between the square of the electron hole overlap integral and the period for a $L_{CdS}=L_{CdSe}$ superlattice (calculated from the variational wavefunctions). The graph shows that the larger the period the smaller the overlap integral and hence, the slower the recombination. For our system we therefore expect the low energy tail to display longer lifetimes as the emission from longer periods dominates on this side, as is observed in MH123 (25Å/25Å).

We conclude that the measured lifetimes are consistent with the piezoelectric model. We can do a simple calculation in support of this analysis. The emissions at 700nm and 750 nm correspond (using the theory described in section 4.4.3) to superlattices with periods of 15Å/15Å and 23Å/23Å respectively. The square of the electron hole overlap integrals calculated for these superlattices are 0.186 and 0.05 respectively. We can therefore estimate the relative recombination rate for carriers in the two superlattices to be 0.186/0.05=3.10. This compares with the observed 63ns/16ns=3.94. Considering the naivety of this calculation the theory is in good agreement with experiment for this case.

There is another way to estimate recombination rates for the long period superlattices based on the observed space charge effects. It is obvious that in a superlattice being studied under continuous wave

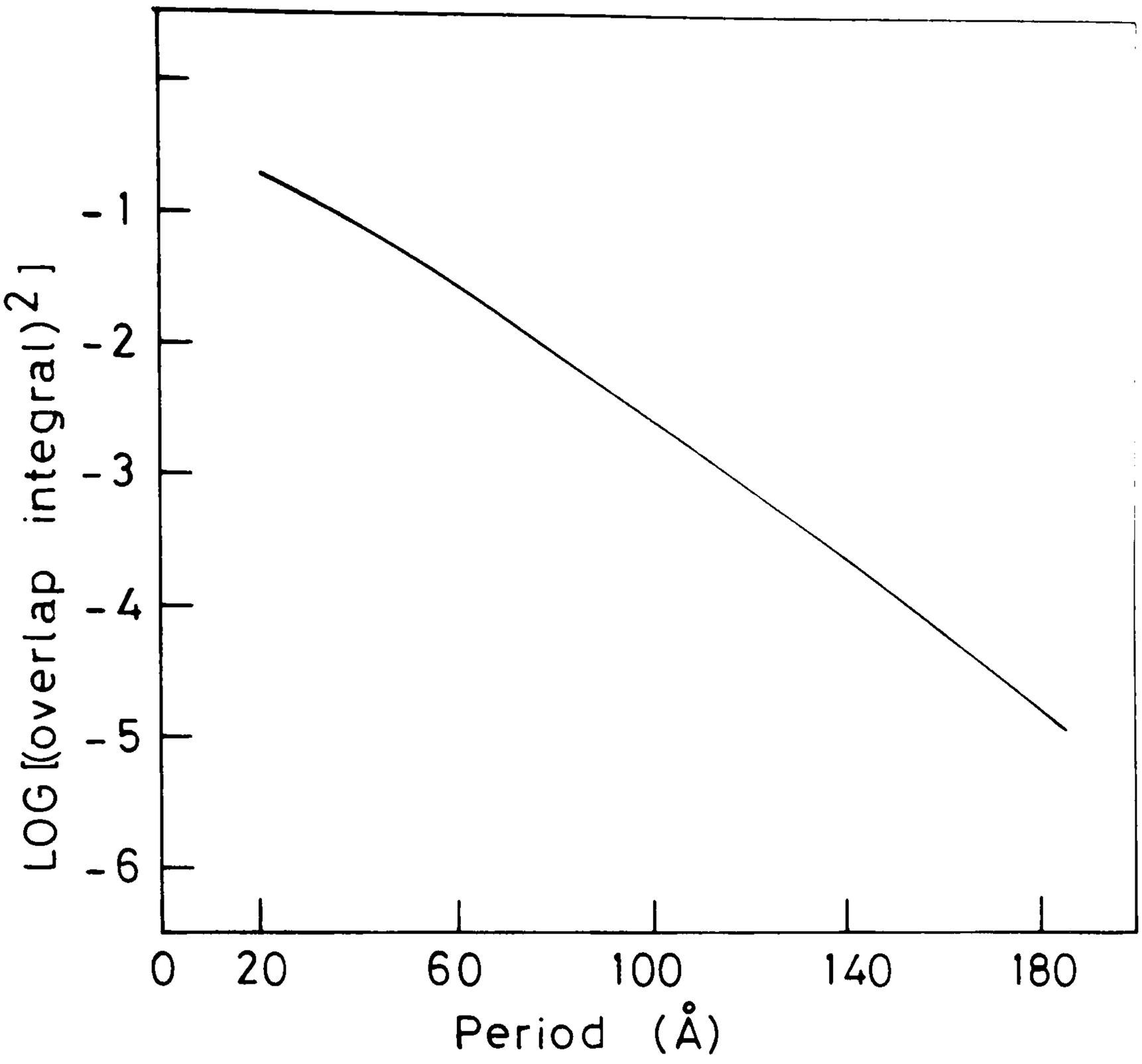

Figure 4.57. Relationship between the square of the electron hole wavefunction overlap integral and superlattice period for the case LCdS=LCdSe. The curve was calculated using the piezoelectric theory, no allowance was made for excitonic interactions.

illumination the rate of carrier creation is equal to the rate of carrier recombination. Now if the probability of recombination per carrier pair per unit time is Y, then we can express the recombination rate R as

$$R = NY \qquad \text{(xxii)}$$

Where N is the number of electron hole pairs (assuming excitonic recombination). We consider the superlattice MH111 (40Å/60Å CdS/CdSe). It was found that the luminescence intensity was proportional to the excitation intensity for this sample. Therefore we believe that the above expression for the recombination rate is valid for this superlattice. It was observed for this superlattice that as the excitation density was altered from $1mw/mm^2$ to $10mw/mm^2$ the luminescence shifted by 60 meV. The model we have for this shift is that the increased laser power creates carriers that do not recombine quickly enough to prevent charge accumulating in the respective layers. This process continues until the resultant space charge field neutralises the internal fields. When this occurs the electron-hole overlap integral increases until the recombination rate is sufficently fast to balance equation (xxii), i.e. Y will increase.

We can use this model to estimate recombination times. Taking the above example, we calculate (using the variational calculation) a change in the areal charge density of $2\times10^{16}e/m^2$ is necessary to produce the observed shift in MH111. $10mw/mm^2$ corresponds to 2.5×10^{22} photons/m^2/sec. Clearly we do not know how many of these photons create carriers in which layers. However, we can consider the limiting case in which all the photons are absorbed by one period of the superlattice (the upper limit of N). Y is now given by

$$2.5\times10^{22} = 2\times10^{16}Y \qquad \text{(xxiii)}$$

The half life of a carrier is thus given by

$$T_{1/2} = \ln(2)/Y > \ln(2)/10^{6} \qquad \text{(xxiv)}$$

$$T_{1/2} > 7\times10^{-7}\ S \qquad \text{(xxv)}$$

N is an upper limit, therefore $T_{1/2}$ is a lower limit. We conclude that the carrier half-life in a 40Å/60Å CdS/CdSe superlattice is at least 0.7μs. This is a very long lifetime and is in excess of what we would expect from a type II superlattice in the absence of the piezoelectric effect [52]. We conclude that the lifetime measurements are consistent with the seperation of the electron hole pairs. In addition, the apparent very long lifetimes associated with large periods supports the presence of the internal fields.

4.6 Summary and conclusions

This chapter described the studies conducted on CdS/CdSe multilayer structures grown by MOCVD. These were the first such structures reported and the first wurtzite multilayer epitaxial structures grown. The structures were investigated initially by transmission electron microscopy. It was vital that something of the structural quality of the structures could be observed directly. The lattice images show that the structures are of high quality and are wurtzite throughout, with no twinning. This is in contrast to the observed twinning in CdSe epilayers. Diffraction analysis indicated a critical thickness for the CdS on GaAs of <400Å. The TEM high resolution lattice images showed abrupt interfaces and allowed accurate calibration of the growth rate for a series of samples.

We conclude from this structural assessment that the layers are of high crystalline quality. Furthermore, despite the high growth temperature (450^{o}C), the constituent compounds have not interdiffused significantly. From this assessment we concluded that our superlattices are of as high a quality as other II-VI superlattices known to exhibit quantum size effects.

The other technique applied to the superlattices was photoluminescence. It was observed in the luminescence that for large period structures the luminescence was composed of CdSe edge emission shifted to lower energy by strain effects. The other emission observed was an infra-red band which dominated the emission as the period was reduced. This band shifted into the visible for small period superlattices. In addition, it was found that the infrared emission shifted to higher energy by up to 0.3 eV as the laser exciting power was increased, the largest shifts being observed in the larger period

samples.

In order to explain the observed luminescence the theoretical background to the system was investigated. It was found that the system should contain large strain induced piezoelectric internal fields. The magnitude of the calculated fields was so large that the effects should be readily observable in the luminescence. In order to study this effect some elementary confinement energy calculations were carried out using a variational approximation. The kind of band structure expected and the interpretation of the luminescence was discussed. The conclusion of this theoretical work was that the CdS/CdSe system should show almost unique properties in terms of the electron and hole confinement energies.

The final section used the theory developed to model the recombination energies in the superlattices. It was found, by studying two different series of samples, that the band offsets of the system were type II. The conduction band offset was determined to be in the range 0.23+_0.1 eV with the electron confined in the CdS and the hole in the CdSe. It found that it was essential to assume the presence of internal fields to explain the observed luminescence. This provided the first reported direct evidence for the presence of such fields in a superlattice. Finally the potential distribution along the c-axis of the superlattices was discussed. The observed laser power effects and time decay of luminescence were interpreted in terms of the model developed.

In conclusion, the photoluminescence from these samples is highly unusual. In fact it does not bear resemblance to that observed to date from any other II-VI superlattice system. In some manners it resembles doping superlattice emission (power shifts and indirect recombination), in others II-VI compositional superlattices (small period emission). We

believe we have demonstrated that this is a result of the strain induced fields. The induced fields dominate at large periods, producing recombination reminiscent of doping structures (e.g. GaAs nipi structures). At small periods the compositional superlattice type emission dominates. We find that every aspect of the superlattice emission can be explained by our model. The principle result of this chapter is that the CdS/CdSe superlattice system is type II with a conduction band offset of 0.23+_0.1 eV. In addition the expected piezoelectric effects occur and cause substantial reduction in the effective band gap as the period increases.

We conclude that this system present unique properties. The band gap of the superlattice is tunable from 0-1.8 eV. This system presents new and previously unobserved effects to the field of semiconductor superlattices.

REFERENCES FOR CHAPTER 4

[1] N.Samarth, H.Luo, J.K.Furdyna, S.B.Qadri, Y.R.Lee, R.Alonso E.L.Suh, A.K.Ramdas and H.Otsuka. To be published in Surface Science

[2] P.J.Gowers, Proc. Nato Advanced Research Workshop Thin Film Growth Techniques for Low Dimensional Structures (New York: Plenum)

[3] M.P.Halsall, J.J.Davies, J.E.Nicholls, B.Cockayne, P.J.Wright and G.J.Russell J. Cryst. Growth 91 (1988) 135

[4] N.G.Chew and A.G.Cullis Ultramicroscopy 23 (1987) 175

[5] A.G.Cullis, P.W.Smith, P.J.Parbrooke, B.Cockayne, P.J.Wright and G.M.Williams in press

[6] M.Kobayashi, N.Mino, H.Katagiri, R.Kimura, M.Konagai and K.Takahashi Appl. Phys. Lett. 48 (1986) 296

[7] T.Yokogawa, M.Ogura and T.Kajiwara, Appl. Phys. Lett 49 (1986) 1702

[8] H.Tuffigo, R.T.Cox, F.Dal'Bo, G.Lentz, N.Magnea, H.Mariette and C.Grattepain Superlattices and Micro. 5 (1989) 83

[9] R.G.Wheeler and J.O.Dimmock Phys. Rev. 125 (1962) 1805

[10] D.L.Rosen, Q.X.Li and R.R.Alfano Phys. Rev. B 31 (1985) 239

[11] M.Kobayashi, N.Mino, M.Konagai and K.Takahashi Surf. Science 174 (1986) 550

[12] G.H.Dohler Surf. Sci. 73 (1980) 97

[13] K.Shum, G.C.Tang, R.Junnarkar and R.R.Alfano Appl. Phys. Lett. 51 (1987) 1839

[14] J.E.Fouquet and R.D.Burnham, IEEE J. Quantum Electron 22 (1986) 1799

[15] C.Gourdon, P.Lavallard and M.Dagenais Phys. Rev. B 37 (1988) 2589

[16] D.L.Smith, Solid State Commun. 57 (1986) 919

[17] D.L.Smith and C.Mailhot Phys. Rev. Lett. 58 (1987) 1264

[18] B.S.Yoo, X.C.Liu, A.Petrou, J-P Cheng, A.A.Reeder, B.D.McCombe, K.Elcess and C.Fonstad

[19] D.Berlincourt, H.Jaffe and L.R.Shiozawa Phys. Rev. 129 (1963) 1009

[20] see for example "The physical properties of crystals" J.F.Nye (Oxford university press, Oxford, 1960).

[21] N.K.Abrikosov, V.F.Bankina, L.V.Poretskaya, L.E.Shelimova and E.V.Skudnova; Semiconducting II-VI,IV-VI and V-VI compounds, Plenum, New York, 1969, 27

[22] R.Geick and C.H.Perry J. Appl. Phys. 37 (1966) 1994

[23] see for example "Ferroelectric crystals" F.Jona and G.Shirane Pergamon, New York (1962)

[24] not available however compare for ZnS ($2*10^8$ V/m) T.D.Thompson and J.W.Allen J. Phys. C 20 (1987) L499

[25] G.Bastard, E.E.Mendez, L.L.Chang and L.Esaki Phys. Rev. B 28 (1983) 3241

[26] E.J.Austin and M.Jaros Phys. Rev. B 31 (1985) 5569

[27] D.Ahn and S.L.Chuang Phys. Rev. B 34 (1986) 9034

[28] see for example "Quantum mechanics" L.I.Schiff McGraw-Hill, New York (1955).

[29] Wlodek Zawadzki, J. Phys. C 16 (1983) 229

[30] E.E.Mendez, G.Bastard, L.L.Chang, L.Esaki, H.Morkoc and R.Fischer Phys. Rev. B 26 (1982) 7101.

[31] R.Dingle: in Festkorperproblem ed. by H.J.Queisser (Pergamon-Vieweg, Braunschweig 1975) Vol XV p.21

[32] K.Mohammed, D.J.Olego, P.Newbury, D.A.Cammack, R.Dalby and H.Cornelissen Appl. Phys. Lett. 50 (1987) 1820

[33] P.Voisin, G.Bastard and M.Voos Phys. Rev. B 29 (1984) 935

[34] J.Voight, F.Spiegelberg and M.Senoner, Phys. Stat. Sol. 91 (1979) 189

[35] C.W.Litton, D.C.Reynolds and T.C.Collins, Phys. Rev. B 6 (1972) 2269

[36] H.Fujiyasu and K.Mochizuki J. Appl. Phys. 57 (1985) 2960

[37] M.Kobayashi, N.Mino, H.Katagiri, R.Kimura, M.Konagai and K.Takahashi J. Appl. Phys. 60 (1986) 773

[38] L.A.Kolodzieski, R.L.Gunshor, N.Otsuka, W.M.Becker and V.Nurmikko IEEE J. Quantum Elect. 22 (1986) 1666

[39] H.Fujiyasu, K.Mochizuki, Y.Yamazaki, M.Aoki, A.Sasaki, H.Kuwabara, Y.Nakanishi and G.Shimoaka Surf. Science 174 (1986) 543

[40] S.Wei and A.Zunger Phys. Rev. Lett. 59 (1987) 144

[41] R.C.Miller, D.A.Kleinmann, W.T.Tsang, and A.C.Gossard, Phys. Rev. B 24 (1981) 1134

[42] for a review see K.Ploog and G.H.Dohler Advances in Physics 32 (1983) 285.

[43] H.Jung, H.Kunzel, G.H.Dohler and K.Ploog, J. Appl. Phys. 54 (1983) 6965

[44] P.Voisin, J.A.Brum, M.Voos, L.L.Chang and L.Esaki Surf. Science 174 (1986) 255

[45] see for example J.L.Pankove 'Optical processes in semiconductors' (Dover publications, New York 1971) chpt 6.

[46] see for example A.K.Ramdas, Superlattices and Micro. 4 (1988) 69

[47] H.Jung, A.Fischer and K.Ploog Appl. Phys. A 33 (1984) 97

[48] J.Singh, K.K.Bajaj and S.Chaudhari. Appl. Phys. Lett. 44 (1984) 805

[49] F.Y.Juang, J.Singh, P.K.Bhattacharya, K.Bajema and R.Merlin Appl. Phys. Lett. 48 (1986) 1246.

[50] D.Lee, Q.Fu, A.V.Nurmikko, L.A.Kolodziejski and R.L.Gunshor Superlattices and Micro. 5 (1989) 345

[51] G.H.Dohler Phys. Stat. Sol. (b) 52 (1972) 533

[52] E.Finkman, M.D.Sturge and M.C.Tamargo. Appl. Phys. Lett. 49 (1986) 1299

[53] W.Rehm, H.Kunzel, G.H.Dohler, K.Ploog and P.Ruden Physica 117B & 118B (1983) 732
(1986) 709.

[54] K.P.O'Donnell, P.J.Parbrooke, B.Henderson, C. Trager-Cowan Chen.X, Yang.F, M.P.Halsall, P.J.Wright and B.Cockayne J. Cryst. Growth in press.

APPENDIX 1: Samples grown

NAME	Material	Substrate	Bakeout	(^{o}C,mins)		T_g (^{o}C)	R_g(μm/hr)	T(μm
MH1	CdS	GaAs (100)	500	10	H	300	equipment failure	
MH2	CdS	GaAs (100)	500	10	H	300	3.4	1.7
MH3a	CdS	GaAs (100)	500	15	H	300	3.4	1
MH3b	CdS	GaAs (110)	500	15	H	300	3.4	1
MH3c	CdS	GaAs (111)A	500	15	H	300	3.4	1
MH3d	CdS	Glass	500	15	H	300	3.4	1
MH4a	CdS	GaAs (100)	550	10	H	300	3.4	3
MH4b	CdS	GaAs (110)	550	10	H	300	3.4	3
MH4c	CdS	GaAs (111)A	550	10	H	300	3.4	3
MH5a	CdS	GaAs (100)	550	15	H	300	5.1	10
MH5b	CdS	GaAs (110)	550	15	H	300	5.1	10
MH5c	CdS	GaAs (111)A	550	15	H	300	5.1	10
MH6a	CdSe	GaAs (100)	500	10	H	300	3.4	1
MH6b	CdSe	GaAs (110)	500	10	H	300	3.4	1
MH6c	CdSe	GaAs (111)A	500	10	H	300	3.4	1
MH6d	CdSe	Glass	500	10	H	300	3.4	1
MH7a	CdSe	GaAs (100)	550	15	H	300	3.4	3
MH7b	CdSe	GaAs (110)	550	15	H	300	3.4	3
MH7c	CdSe	GaAs (111)A	550	15	H	300	3.4	3
MH8a	CdS	GaAs (100)	500	10	H	350	1.7	2
MH8b	CdS	GaAs (111)A	500	10	H	350	1.7	2
MH9a	CdS	GaAs (100)	500	10	H	250	1.7	2
MH9b	CdS	GaAs (111)A	500	10	H	250	1.7	2
MH10a	CdS	GaAs (100)	550	10	H	400	1.7	2
MH10b	CdS	GaAs (111)A	550	10	H	400	1.7	2
MH11	CdS	GaAs (111)B	550	10	H	350	equipment failure	
MH12	CdS	GaAs (111)B	550	10	H	350	1.74	0.87
MH13	CdS	GaAs (111)B	550	10	H	350	1.74	0.1
MH14	CdS	GaAs (111)B	550	10	H	350	1.74	0.4
MH15	CdS	GaAs (111)B	550	10	H	350	1.74	0.8
MH16	CdS	GaAs (111)B	550	10	H	350	1.74	2
MH17	CdS	InP (111)B	none			350	1.74	0.1
MH18	CdS	InP (111)B	none			350	1.74	0.25
MH19	CdS	InP (111)B	none			350	1.74	0.5
MH20	CdS	InP (111)B	none			350	1.74	1
MH21	CdS	InP (111)B	none			350	1.74	2.5
MH23	CdS	GaAs (111)A	550	10	H	350	1.6	1.2
MH24	CdS	GaAs (111)A	550	10	H	350	1.6	0.4
MH25	CdS	GaAs (111)A	550	10	H	350	1.6	4
MH26	CdS	GaAs (111)A	550	10	H	350	1.6	0.7
MH27	CdS	GaAs (111)A	550	10	H	300	1.6	1.5
MH28	CdS	InP (111)B	none			200	2	2
MH29	CdS	InP (111)B	none			250	2	1.5
MH30	CdS	InP (111)B	none			300	1.7	1.5
MH31	CdS	InP (111)B	none			350	1.6	1.2
MH32a	CdS	InP (111)B	500	10	H_2S	300	1.7	0.9
MH32b	CdS	GaAs (111)A	500	10	H_2S	300	1.7	0.9
MH33a	CdS	InP (111)B	600	10	H_2S	300	1.7	1
MH33b	CdS	GaAs (111)A	600	10	H_2S	300	1.7	1
MH34a	CdSe	InP (111)B	550	1	H_2Se	300	2	1.5
MH34b	CdSe	GaAs (111)A	550	1	H_2Se	300	2	1.5
MH34c	CdSe	InAs (111)A	550	1	H_2Se	300	2	1.5
MH35a	CdSe	InP (111)B	550	5	H_2Se	350	2	1
MH35b	CdSe	GaAs (111)A	550	5	H_2Se	350	2	1
MH35c	CdSe	InAs (111)A	550	5	H_2Se	350	2	1
MH36	CdS	GaAs (111)A	550	10	H^2	350	1.4	0.7

MH37	CdS	GaAs	(111)A	550	10	H	350	1.4	0.3
MH38	CdS	GaAs	(111)A	550	10	H	350	1.4	0.1
MH39a	CdSe	InAs	(111)A	none			300	2.4	1.8
MH39b	CdSe	GaAs	(111)A	none			300	2.4	1.8
MH40	CdSe	GaAs	(111)A	550	10	H	350	2	1
MH41	CdSe	GaAs	(111)A	550	10	H	400	equipment failure	
MH42	CdSe	GaAs	(111)A	550	10	H	400	1.5	0.9
MH43	CdSe	GaAs	(111)A	550	10	H	450	1.2	1
MH44	CdSe	GaAs	(111)A	550	10	H	250	3	1.5
MH45	CdSe	GaAs	(111)A	550	10	H	450	1.2	1
MH46	CdS/CdSe	GaAs	(111)A	550	10	H	350	2	1/1
MH47	Alloy	GaAs	(111)A	550	10	H	350	2	0.7
MH48	CdSe/CdS	GaAs	(111)A	550	10	H	350	2	1/1
MH49	Alloy	GaAs	(111)A	550	10	H	350	2	1
MH50	CdS	GaAs	(111)A	550	10	H	350	0.8	0.4
MH51	CdS	GaAs	(111)A	550	10	H	350	0.8	0.15
MH52	CdS	GaAs	(111)A	550	10	H	350	equipment failure	
MH53	CdS	GaAs	(111)A	550	10	H	350	0.8	0.035
MH54	CdS	GaAs	(111)A	550	10	H	350	0.8	0.07
MH55	CdS	GaAs	(111)A	550	10	H	350	0.8	0.02
MH56	CdSe/CdS	GaAs	(111)A	550	10	H	350	0.8	0.16/0.6
MH57	CdS	GaAs	(111)A	550	10	H	350	0.8	0.4
MH58	CdSe/CdS	GaAs	(111)A	550	10	H	300	0.8	0.03/0.3
MH59	CdS	GaAs	(111)A	550	10	H	350	0.8	0.46
MH60	Alloy	GaAs	(111)A	550	10	H	350	0.8	0.6
MH61	Alloy	GaAs	(111)A	550	10	H	350	0.8	0.8
MH62	CdS	GaAs	(111)A	550	10	H	325	0.8	0.4
MH63	CdS	GaAs	(111)A	550	10	H	400	0.8	0.8
MH64	CdS	GaAs	(111)A	550	10	H	400	0.8	1
MH65	CdS/CdSe/CdS	GaAs	(111)A	550	10	H	400	0.8	0.4/0.2/0.2

After these samples the subsequent ones were all grown with the fast gas flow system described in section 2.3.2. The substrates used were all GaAs (111)A baked out for 10 minutes at 550°C under hydrogen. The next samples listed are divided into single layers and superlattices, with the single epilayers listed first. The flow rates are included as these relate to the alloy growth described in section 3.3.4, the growth rates were in the range 1-2 μm/hr.

Sample	Material	Flow rates (cc/min) H_2S	H_2Se	T_g (°C)	thickness (μm)
MH66	CdSe	0	50	350	2
MH67	Alloy	20	80	350	1
MH68	Alloy	40	60	350	1
MH69	Alloy	60	40	350	1
MH70	Alloy	80	20	350	1
MH71	CdS	100	0	350	1
MH72	Alloy	90	10	350	1
MH73	Alloy	95	5	350	1
MH74	Alloy	60	40	400	1
MH75	Alloy	80	20	400	1
MH76	Alloy	90	10	400	1
MH77	Alloy	93	7	400	1
MH78	Alloy	90	10	450	1

MH79	Alloy	97	3	450	1	

Superlattices

Samples marked * were imaged by TEM.

Sample	Buffer layer	Layer thicknesses CdS	CdSe	n	T_g	Period (Å)
MH80	None	150	70	20	350	220
MH81	CdS 5000	150	70	20	350	220
MH82*	CdS 5000	150	70	20	400	220
MH83*	CdS 3000	100	50	20	450	150
MH84	CdS 5000	150	70	20	400	220
MH85	CdS 5000	150	20	20	400	170
MH88	CdS 4000	300	400	10	450	660
MH89	CdS 4000	300	200	10	450	460
MH90	CdS 4000	160	130	20	450	260
MH91*	CdS 4000	160	90	20	450	220
MH92	CdS 4000	50	60	20	450	110
MH93*	CdS 4000	110	35	20	450	100
MH94	CdS 4000	equipment failure				
MH95	CdS 4000	40	25	20	450	55
MH96	CdSe 3000	60	90	20	450	150
MH97	none	60	90	20	450	150
MH98	CdS 3000	60	alloy 130?	20	450	150
MH99	CdS 3000	60	alloy 130?	20	450	230
MH100	CdS 3000	60	alloy 130?	20	450	230
MH101	CdS 3000	60	alloy 130?	20	450	230
MH104	CdS 3000	45	40	25	450	100
MH105	CdS 3000	76	7	20	450	83
MH106	CdS 3000	68	20	20	450	88
MH107	CdS 3000	equipment failure				
MH108	CdS 3000	68	20	20	450	88
MH109	CdS 3000	76	8	20	450	84
MH110	CdS 3000	56	40	20	450	96
MH111	CdS 3000	40	60	20	450	100
MH112	CdS 3000	24	84	20	450	88
MH113	CdS 3000	12	104	20	450	116
MH114	CdS 3000	14	14	20	450	28
MH115	CdS 3000	60	30	10	450	90
MH116	CdS 3000	60	30	5	450	90
MH117	CdS 3000	60	30	2	450	90
MH118	CdS 3000	60	30	1	450	90
MH119	CdS 3000	40	60	20	450	90
MH120	CdS 3000	7	7	20	450	14
MH121	CdS 3000	15	15	20	450	30
MH122	CdS 3000	7	7	20	450	14
MH123	CdS 3000	25	25	20	450	40

Subsequently to this a number of CdS epilayers were grown on GaAs (111)A at different growth rates the ones studied for surface morphology were.

MH134	1.6μm of CdS	grown at 3.5	μm/hr
MH135	1.5μm of CdS	grown at 1.6	μm/hr
MH136	1.5μm of CdSe	grown at 1.6	μm/hr
MH137	2.6μm of CdS	grown at 2.6	μm/hr
MH138	2 μm of CdS	grown at 2.6	μm/hr

APPENDIX 2

Particle confined in a finite well

The quantization condition for such a particle was given in chapter 1 (pg 25) as:-

$$k^2-q^2 = 2kq\ \mathrm{Cot}(ka) \qquad \text{(i)}$$

$$q^2=2m^*(V-E)/\hbar^2 \qquad \text{(ii)}$$

$$k^2=2m^*E/\hbar^2 \qquad \text{(iii)}$$

Where a is half the diameter of the well, V is the depth of the potential well and E is the total energy of the electron. The other constants take their usual physical values. This relation can be solved graphically by plotting the curves of k/q, Cot(ka) and -Tan(ka) against E on the same graph. The crossing points corresponding to the solutions [1]. However, an easier numerical approach can be taken by computer. This is achieved by assuming a solution at an arbitary energy E and then iterating

$$k_{m+1} = (1/a)\mathrm{ArcCot}([k_m^2-q_m^2]/[2qk]) + n\pi$$

where m is the iteration number and n is the quantum number of the transition. The energy E_m is calculated from (iii) and the corresponding q_m is derived from (ii). In order to avoid infinities at the asymptotes of the Cot function the initial E should be chosen to lie above the previous transition but below the value being sought.

This is best achieved by starting with E=0 for the first transition and then using each transition in turn as the starting point for the interation to find the next. A program to perform this calculation was written in pascal on a Victor IBM compatible equipped with a maths coprocessor. The energies so derived were used for the calculation described in appendix 3.

Kronig-Penney dispersion relation

The Kronig-Penney relations were given on page 26 as :-

$$k_a^2 = 2m_aE/\hbar^2 - k^2 \qquad \text{(iv)}$$

$$k_b^2 = 2m_b(V-E)/\hbar^2 - k^2 \qquad \text{(v)}$$

$$x = m_ak_b/m_bk_a \qquad \text{(vi)}$$

$$\text{Cos}(dk_{sl}) = \text{Cos}(ak_a)\text{Cosh}(bk_b) - \tfrac{1}{2}[x-1/x]\text{Sin}(ak_a)\text{Sinh}(bk_b) \qquad \text{(vii)}$$

Where m_a and m_b are the effective masses of the carriers in the respective wells. For a full description of how this relation produces the minibands and parabolic dispersion see any good solid state text book (for instance [2]). Here we are only interested in solving this equation. The important solutions required are when the right hand side of equation (vii) takes the values of -1 or +1 as these represent the top or bottom of subbands; we will refer to the right hand side of equation (vii) as g(E). We now have two alternative conditions to satisfy:-

$$g(E) + 1 = 0$$

or

$$g(E) - 1 = 0$$

These conditions were solved by simply starting with E=0 and increasing it in increments of dE until a condition is observed where

$$g(E+n\times dE) + 1 < 0 \quad \text{and} \quad g(E+(n+1)\times dE) + 1 > 0$$

with -1 substituted for +1 to obtain the alternative solution. The two values E+n dE and E+(n+1)dE are then passed to a midpoint solving routine to obtain precise values for the energies at the subband extrema. This is illustrated by the flow diagram below.

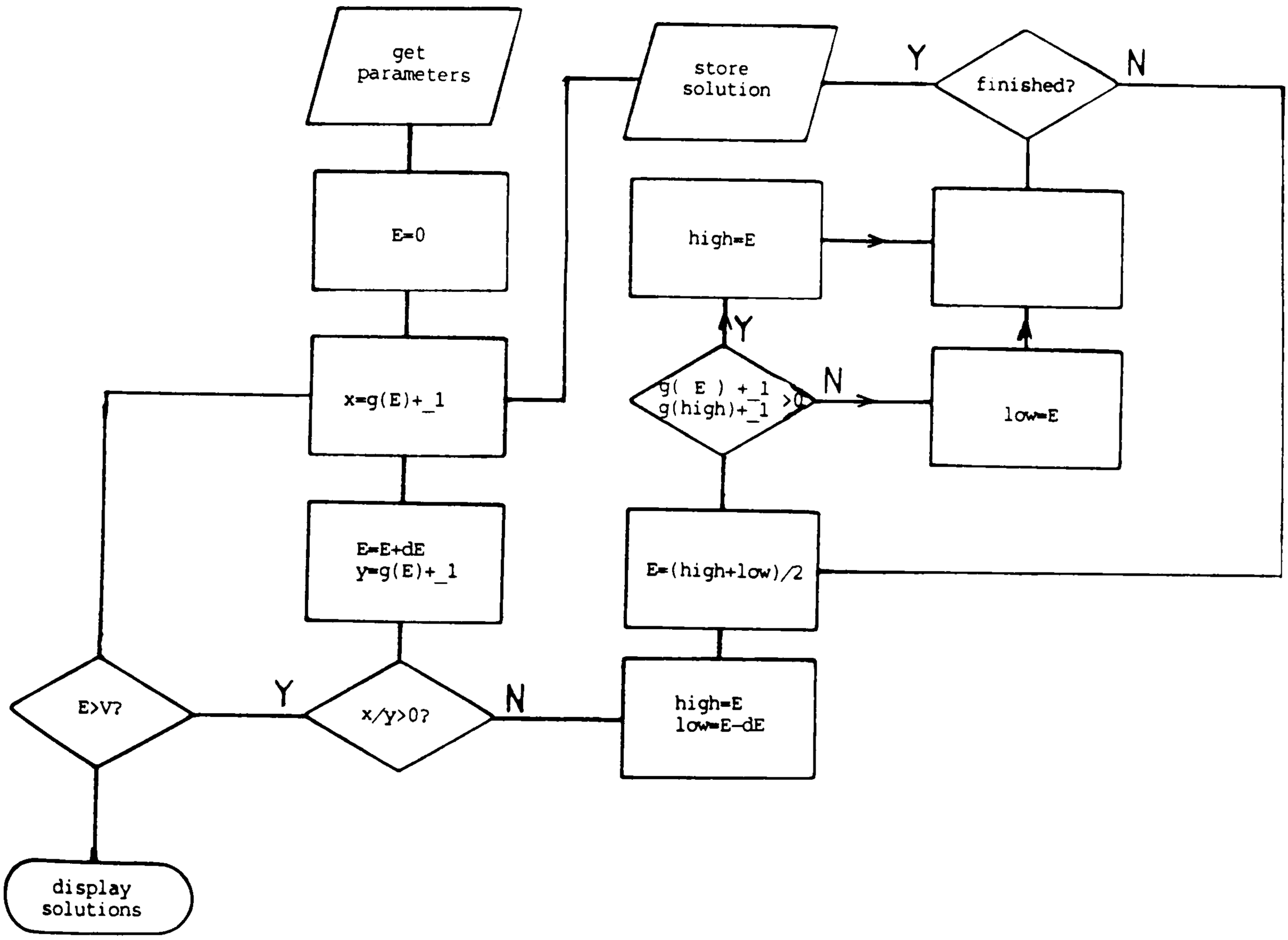

After solving the solutions are ordered so as to produce the energy positions of bottom and top of each subband in order from the lowest energy state up. The energies of the bottom of the subbands corresponding to g(E)= +1,-1,+1,-1,+1 etc from the first band upwards. It is important to note that if dE exceeds the energy difference between any two solutions then the routine will miss solutions. This can be prevented by choosing a small enough dE. This was expressed in terms of V for our program and set at V/400. This provided a good compromise between time taken to calculate the subbands and the possible missing of solutions. In practice the confinement energies calculated were greatly in excess of V/400.

REFERENCES

[1] L.I.Schiff 'Quantum Mechanics' McGraw-Hill, 1968 chpt 2

[2] see for example A.J.Dekker 'Solid State Physics'
MacMillan publishing Ltd. London 1952

APPENDIX 3

Evaluation of variational energy

The variational wavefunctions tried for the piezoelectric well were given on page 129 as:-

$$\psi(z) = A\exp[(q-\beta)z/a]$$

$$\psi(z) = B\cos(kz/a)\exp(\beta z/a) \qquad \text{(i)}$$

$$\psi(z) = C\exp[-(q+\beta)z/a]$$

Where A,B and C are normalizing constants, q and k are the zero field finite well parameters, β is the variational parameter and a is half the width of the well (see figure 4.32). The variational energy E_{var} is given by

$$E_{var} = \frac{\int \psi \mathcal{H} \psi^*}{\int \psi \psi^*} \qquad \text{(ii)}$$

Where $E_{var} > E_o$, E_o being the exact energy eigenvalue. The expression (ii) is therefore minimized with respect to β to give the closest value to the exact eigenvalue. The Hamiltonian $\mathcal{H}$ is the usual Schrodinger one :-

$$\mathcal{H} = \frac{-\hbar^2}{2m}\frac{\partial^2}{\partial x^2} + V(z) \qquad \text{(iii)}$$

Where V(z) is the potential given by (pg 128)

$$V(z) = V_o + aF_w e + eF_b z \qquad z>a$$

$$V(z) = eF_w z \qquad |z|<a \qquad \text{(iv)}$$

$$V(z) = V_o - aF_w e + eF_b z \qquad z<-a$$

The matrix element $\int \psi \mathcal{H} \psi^*$ can therefore be broken into three integrals. To assist with these integrals the wavefunction was rewritten in a different form :-

$$\psi(z) = A\exp[(q-\beta)(z/L+1/2)] \qquad z<-L/2$$

$$\psi(z) = B\sin[kz/L+\delta]\exp[-z/L] \qquad |z|<L/2 \qquad \text{(v)}$$

$$\psi(z) = \exp[-(q+\beta)(z/L-1/2)] \qquad z>L/2$$

where $\delta = k/2 + \text{ArcTan}(k/q)$ and $L=2a$ (i.e L=width of well)

The purpose of this is simply to simplify the integration. After the Hamiltonian operation the three expressions to be evaluated are now (after considerable simplification and use of integration by parts):-

$$(1) \qquad A^2 \int_{-\infty}^{-L/2} \left(\frac{-\hbar^2 (q-\beta)^2}{2m \quad L^2} + V_n + eF_b z \right) \exp[2(q-\beta)(z/L+1/2) \quad dz$$

$$(2)\quad \left\{ B^2\left[\left(\frac{\hbar^2}{2m}\,\frac{\beta^2+k^2}{L^2}+eF_wz\right)\int_{-L/2}^{L/2}\mathrm{Sin}^2(kz/L+\delta)\exp(-2\beta z/L)\;dz\right.\right.$$

$$+\frac{\hbar^2}{2mL}\,\mathrm{Sin}^2(kz/L+\delta)\exp(-2\beta z/L)$$

$$\left.\left.-eF_w\int_{-L/2}^{+L/2}\int_{-L/2}^{+L/2}\mathrm{Sin}^2(kz/L+\delta)\exp(-2\beta z/L)\;dz\;dz\right]\right.$$

$$(3)\qquad C^2\int_{+L/2}^{\infty}\left(\frac{-\hbar^2}{2m}\,\frac{(q+\beta)^2}{L^2}+V_p+eF_bz\right)\exp[-2(q+\beta)(z/L+1/2)]\;dz$$

Where $V_p = V+eF_wa$ and $V_n = V-eF_wa$

(1) and (3) are easily integrated by parts to give:-

$$(1)\quad I_{z<-a} = \frac{\hbar^2}{4m}\,\frac{(q-\beta)}{L} - \frac{V_nL}{2(q-\beta)} - \frac{zeF_bL}{2(q-\beta)} + \frac{eF_bL^2}{4(q-\beta)^2}$$

$$(3)\quad I_{z>a} = \frac{-\hbar^2}{4m}\,\frac{(q+\beta)}{L} + \frac{V_pL}{2(q+\beta)} + \frac{zeF_bL}{2(q+\beta)} + \frac{eF_bL^2}{4(q+\beta)^2}$$

These expressions were checked by comparison with numerical integrations and found to be correct.

Integral (2) gives rise to a very complicated expression which will not be presented in full here. However, the important integrals were evaluated by repeated integration by parts and are expressed below:-

$$\int\mathrm{Sin}^2(kz/L+\delta)\exp(-2\beta z/L)\;dz=$$

$$\left(\frac{-L}{2\beta}+\frac{L/(2\beta)\mathrm{Cos}(2kz/L+2\delta)-kL/(2\beta^2)\mathrm{Sin}(2kz/L+2\delta)}{2[1+k^2/\beta^2]}\right)\exp(-2\beta z/L)$$

$$\int\int \mathrm{Sin}^2(kz/L+\delta)\exp(-2\beta z/L)\ dz^2 =$$

$$\left(\frac{L^2}{8\beta^2} + \frac{kL^2(2\beta^3)\mathrm{Sin}(2kz/L+2\delta)+[k^2L^2/(4\beta^4)-L^2/(4\beta^2)]\mathrm{Cos}(2kz/L+2\delta)}{2[1+k^2/\beta^2]^2}\right)\exp(-2\beta z/L)$$

These two integrals allow (2) to be evaluated exactly, again the resulting expression was checked by both differentiation and numerical analysis and found to be correct.

To get the variational energy the normalization integral $\int \psi\psi^*$ must be evaluated. This, it turns out, can be done using integrals already evaluated from (1),(2) and (3). However, use must be made of the wavefunction continuity conditions linking the constants A,B and C (by matching the wavefunctions at $z = \pm L/2$).

(i) $A = B\mathrm{Sin}(-k/2+\delta)\exp(-\beta/2)$

(ii) $C = B\mathrm{Sin}(k/2+\delta)\exp(\beta/2)$

With these the normalization factor B is the same for all the three wavefunctions. A computer program was written in pascal on an IBM compatible to evaluate the variational energy for a wide range of well and field parameters. To find the E_{var} minima with respect to β the usual approach would be to analytically differentiate the E_{var} expression with respect to β. However, this was impossible in this case due to the compexity of the final expression, so the resulting energy was numerically differentiated with respect to β and a midpoint method was used to find the energy minima with respect to this parameter. It was found that for all realistic field and well parameters only one minima occured in the range β=0 to q. Therefore the program simply

started at these limits and calculated the variational energy to any desired accuracy. This is illustrated by the flow diagram below.

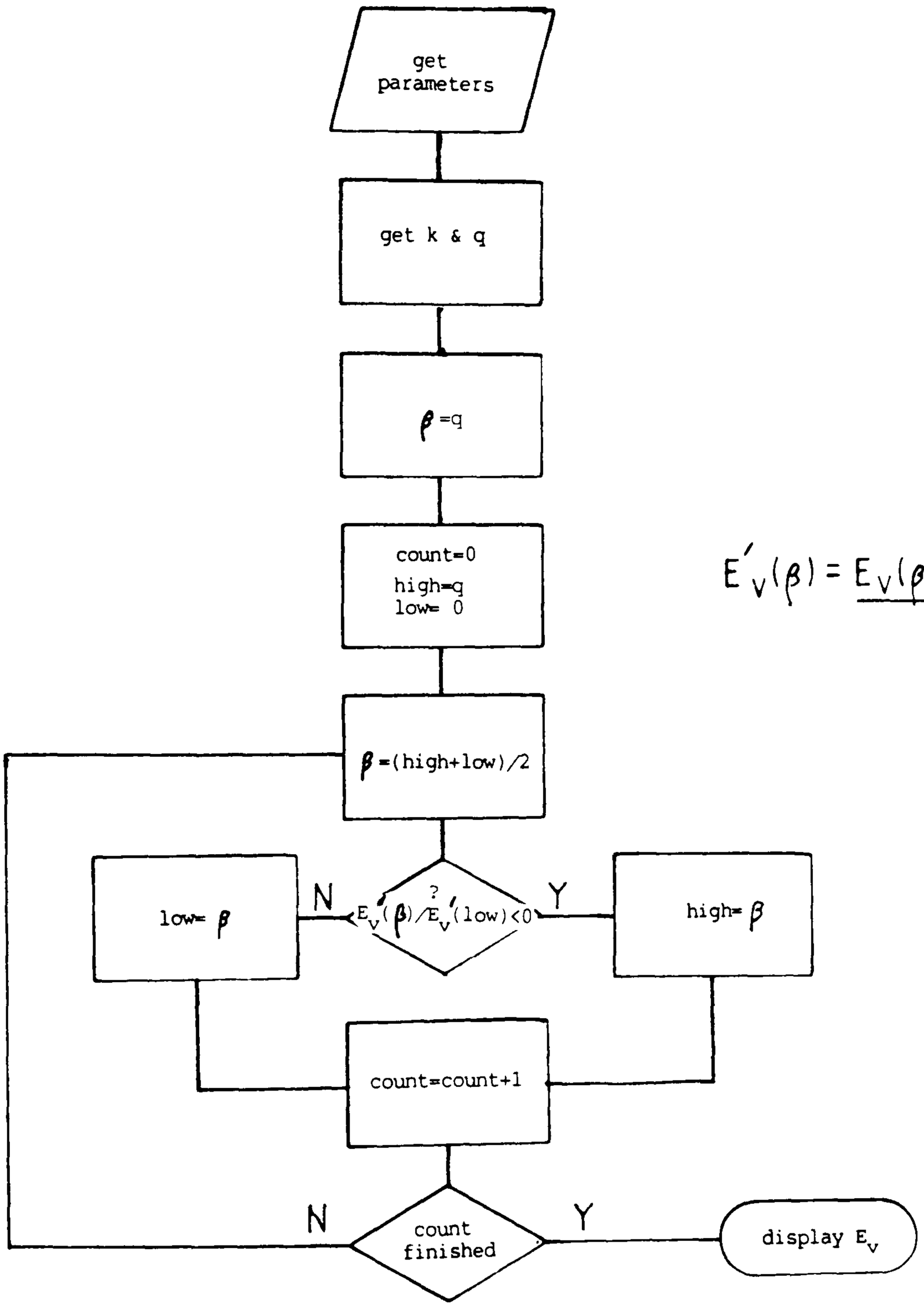

$$E'_V(\beta) = \frac{E_V(\beta) - E_V(\beta+\Delta\beta)}{\Delta\beta}$$